Window Layers for Silicon Heterojunction Solar Cells: Properties and Impact on Device Performance

THÈSE N^{O} 6659 (2015)

PRÉSENTÉE LE 26 JUIN 2015

À LA FACULTÉ DES SCIENCES ET TECHNIQUES DE L'INGÉNIEUR
LABORATOIRE DE PHOTOVOLTAÏQUE ET COUCHES MINCES ÉLECTRONIQUES
PROGRAMME DOCTORAL EN SCIENCE ET GÉNIE DES MATÉRIAUX

ÉCOLE POLYTECHNIQUE FÉDÉRALE DE LAUSANNE

POUR L'OBTENTION DU GRADE DE DOCTEUR ÈS SCIENCES

PAR

Johannes Peter SEIF

acceptée sur proposition du jury:

Prof. J. Brugger, président du jury
Prof. C. Ballif, Dr S. De Wolf, directeurs de thèse
Prof. E. Kessels, rapporteur
Dr B. Strahm, rapporteur
Prof. P. Muralt, rapporteur

ÉCOLE POLYTECHNIQUE
FÉDÉRALE DE LAUSANNE

Suisse
2015

Abstract

Currently, crystalline silicon (c-Si) wafer-based solar cells dominate the photovoltaic market (80–90%). In this thesis we concentrate on silicon heterojunction (SHJ) solar cells that—in contrast to diffused homojunction cells—rely on the application of amorphous silicon (a-Si:H) thin films. Unlike standard homojunction devices, which are typically limited by their highly recombination-active semiconductor-to-metal contacts, SHJ devices exhibit excellent surface passivation enabled by intrinsic and doped a-Si:H films. These a-Si:H layers, however, entail drawbacks for optical performance and carrier transport, two topics that will be addressed in this work. To this end we investigate *non-traditional* materials for SHJ devices, with the goal of replacing the a-Si:H or the transparent electrodes. These materials include micro-crystalline silicon (μc-Si:H) and organic semiconductors for contact formation; amorphous silicon suboxides (a-SiO_x:H) for surface passivation; and transparent electrodes applied by atomic layer deposition (ALD) as protective layers against subsequent processing steps. Along with the optical and electrical properties of these materials, we study the impact on device performance associated with their deposition. For this we test the devices under standard testing conditions (25 °C) and at elevated temperatures closer to those encountered in the field.

For the investigations on μc-Si:H layers, we change process parameters (including temperature, pressure, power, excitation frequency and hydrogen dilution) as well as pre-treatments, gas variations and nucleation layers. We assess the suitability of these approaches for SHJ solar cells and apply selected measures in devices. Thereby we demonstrate a gain in short-circuit current density in the range of 0.5–1 mA cm^{-2} and good fill factor values of up to 79.2% using either *n*- and *p*-type μc-Si:H layers. Furthermore, with the goal of reducing optical losses, we test wide-bandgap a-SiO_x:H layers for passivation. In terms of current gain without negative side effects on transport, we argue that these layers are best applied to the electron-collecting contact—put at the front of the device—as their application to the hole-collecting contact introduces a transport barrier for holes. This barrier deteriorates the device performance at 25 °C, but shows a beneficial effect on the temperature coefficient of the device, yielding coefficients as low as −0.1%/ °C. In some cases—compared to standard devices—devices with a-SiO_x:H layers exhibit superior performance at elevated temperatures, which can be of interest in warmer climates. In parallel to these main topics we also study aluminum-doped zinc oxide (ZnO:Al) layers deposited by ALD as a protective layer against sputter-induced damage and organic semiconductors as transparent electrodes for the hole-collecting contact. In both cases we observe a gain in terms of surface passivation, which indicates that these

materials may be beneficial for the contact formation in future device structures. In addition to these material-related investigations, we unravel the temperature-dependence of each individual cell parameter and present a brief comparison of state-of-the-art technologies and their respective temperature dependence.

Keywords: high-efficiency, crystalline silicon heterojunction solar cells, optical losses, window layers, transport losses, contact formation, temperature coefficient.

Résumé

Le marché du photovoltaïque est actuellement dominé par les cellules solaires à base de wafers de silicium cristallin (c-Si), avec 80–90% des parts du marché. Cette thèse se concentre sur les cellules solaires à hétérojonction de silicium (SHJ), qui—contrairement aux cellules à homojonction diffusées—reposent sur l'application de couches minces de silicium amorphe (a-Si:H). Contrairement aux dispositifs standards à homojonction, qui sont typiquement limités par leurs contacts métal/semi-conducteur très recombinants, les dispositifs SHJ présentent une excellente passivation de surface obtenue grâce aux couches intrinsèques et dopées de a-Si:H. Cependant, ces couches de a-Si:H engendrent des inconvénients pour les performances optiques et pour le transport des porteurs de charge, deux aspects qui sont principalement traités dans ce travail de thèse. À cette fin, nous étudions des matériaux *non-traditionnels* pour des dispositifs SHJ, dans le but de remplacer le a-Si:H ou les électrodes transparentes. Ces matériaux sont notamment : le silicium microcristallin (μc-Si:H) et les semiconducteurs organiques pour la formation des contacts, les sub-oxydes de silicium amorphes (a-SiO_x:H) pour la passivation de surface, et les électrodes transparentes déposées par procédé de dépôt de couches atomiques (ALD) pour jouer le rôle de couches protectrices lors des étapes ultérieures de fabrication. Nous étudions les propriétés optiques et électroniques de ces matériaux, ainsi que l'impact du procédé de dépôt sur les performances du dispositif. Pour ce faire, nous testons le dispositif aussi bien dans les conditions standards de test (25 °C) qu'à des températures plus élevées, qui sont plus proches de celles véritablement rencontrées sur le terrain.

Pour l'étude des couches μc-Si:H, nous varions les paramètres des procédés de dépôt (cela comprend des variations de température, pression, puissance, fréquence d'excitation et dilution d'hydrogène), ainsi que des prétraitements, l'utilisation de différents gaz et de couches de nucléation. Nous estimons la pertinence de ces approches pour les cellules solaires SHJ et en choisissons certaines pour la fabrication de dispositifs. Les utilisant, nous démontrons un gain de 0.5 à 1.0 mA cm^{-2} en densité de courant de court-circuit et de facteurs de forme jusqu'à 79.2% en utilisant des couches de μc-Si:H de type *n* ou *p*. De plus, afin de réduire les pertes optiques, nous testons des couches de passivation au a-SiO_x:H à large bande interdite. Le gain en courant confirmé, nous mettons en évidence qu'il est préférable d'utiliser ces couches pour le contact collectant les électrons—placé sur la face avant du dispositif—car leur application en tant que contact collecteur de trous introduit une barrière au transport des trous. Bien que cette barrière détériore les performances du dispositif à 25 °C, elle produit un effet bénéfique pour le coefficient de température du dispositif, permettant d'obtenir des coefficients aussi bas

que −0.1 %/°C. Dans certains cas—comparées aux dispositifs standards—des performances supérieures sont observées à température élevée pour les dispositifs présentant les couches spécifiques susmentionnées, ce qui peut présenter un intérêt pour les climats chauds. En parallèle de ces deux thématiques principales, nous étudions également des couches d'oxyde de zinc dopé à l'aluminium (ZnO:Al) déposées par ALD, comme couches protectrices contre les dégâts engendrés lors de la pulvérisation cathodique, et des semiconducteurs organiques comme électrodes transparentes pour le contact collecteur de trous. Dans les deux cas nous observons un gain par rapport à la passivation de surface, ce qui indique le potentiel de ces couches en dispositif. Additionnellement à ces études relatives aux matériaux, nous découplons la dépendance en température de chacun des paramètres individuels de la cellule solaire, et présentons une brève comparaison des technologies de l'état de l'art et l'influence de la température sur ces derniers.

Mots clefs : haute efficacité, cellules solaires à hétérojonction de silicium cristallin, pertes optiques, couches transparentes, pertes de transport, formation de contact, coefficient de température

Contents

List of abbreviations and symbols

semiconductors	
α	absorption coefficient [cm^{-1}]
D^0, D^+, D^-	amphoteric defect states (dangling bonds) containing one, no or two electrons
E_{04}	bandgap [eV] defined with respect to $\alpha = 1 \times 10^4$ cm^{-1}
$\sigma_{n,\,p}$	capture cross-sections for electrons or holes
CB	conduction band
CBO, ΔE_c	conduction band offset [eV]
CZ	Czochralski grown crystalline silicon
DB	dangling bond
S_{eff}	effective surface recombination velocity
e^- and h^+	electron and hole
Δn or Δp	excess carrier density of electrons or holes [cm^{-3}] also called injection-level
E_F	Fermi level
FZ	float-zone grown crystalline silicon
FCA	free-carrier absorption
$\tau_{eff}(\Delta n)$	injection-dependent effective minority-carrier lifetime [s] (short: τ_{eff})
τ	lifetime [s], optionally with subscript *SRH* = Shockley-Read-Hall, *rad.* = radiative, *Auger*, *bulk*, or *surf.* = surface for different recombination pathways.
E_g	optical bandgap [eV]
SHJ	silicon heterojunction
T	ambient-temperature
T_{dep}	deposition temperature
VB	valence band
VBO, ΔE_v	valence band offset [eV]

deposition techniques	
ALD	atomic layer deposition
LPCVD	low-pressure chemical vapor deposition
PVD	physical vapor deposition
PECVD	plasma enhanced chemical vapor deposition
RF	radio frequency (typically 13.56 MHz)
VHF	very high frequency (here all frequencies: ≥40.68 MHz)

gases	
CO_2	carbon dioxide
D_2	deuterium
Si_2H_6	disilane
H_2	hydrogen (molecular, alternatively atomic: H)
PH_3	phosphine
SiH_4	silane
SiF_4	silicon tetrafluoride
TMB	trimethylborane [$B(CH_3)_3$]

materials	
ZnO:Al	aluminum-doped zinc oxide
ip/*in*	cell (precursor) with *in*- and *ip*-stacks on either side *in*/*ip* same with *ip* at the rear, here *i*, *p* and *n* refer to amorphous silicon layers with different doping.
c-Si	crystalline Silicon, *p*-type(c-Si(*p*)) or *n*-type(c-Si(*n*))
DSP	double-side polished wafer with orientation (111) or (100)
HCl	hydrochloric acid
HF	hydrofluoric acid
a-Si:H	hydrogenated amorphous silicon optionally intrinsic a-Si:H(*i*) or doped a-Si:H(*p* or *n*)
a-SiO_x:H	hydrogenated amorphous silicon suboxide (also SiO_x)
IO:H	hydrogenated indium oxide
μc-Si:H	hydrogenated microcrystalline silicon optionally intrinsic μc-Si:H(*i*) or doped μc-Si:H(*p* or *n*)
μc-SiO_x:H	hydrogenated microcrystalline silicon oxide optionally doped μc-SiO_x:H(*p* or *n*)
ITO	indium tin oxide
Ip	stack of a-Si:H(*i*)/a-SiO_x:H(*i*)/a-Si:H(*p*)
In	stack of a-Si:H(*i*)/a-SiO_x:H(*i*)/a-Si:H(*n*)
TCO	transparent conductive oxide
PVK	poly(N-vinylcarbazole)
PEDOT:PSS	poly(3,4-ethylenedioxythiophene):poly(styrenesulfonate)
ZnO	zink oxide

characterization	
η	conversion efficiency [%]
J-V	current-voltage measurement optionally also temperature- or illumination-dependent *J-V*(*T*) or *J-V*(suns)
iJ-V	implied *J-V* (reconstructed curve from PCD)
J	current density [$\mathrm{mA\,cm^{-2}}$]
EQE	external quantum efficiency
FF	fill factor [%]
FTIR	Fourier transform infrared spectroscopy
iJ	implied current density [$\mathrm{mA\,cm^{-2}}$]
iFF	implied *FF* (from PCD) [%]
iV_{oc}	implied open-circuit voltage (internal voltage from PCD) [V]
IR	infrared light
IQE	internal quantum efficiency
mpp	maximum power point
V_{mpp}	maximum-power voltage [V]
J_{mpp}	maximum-power current density [$\mathrm{mA\,cm^{-2}}$]
oc	open-circuit
V_{oc}	open-circuit voltage (external voltage) [V]
PCD	photoconductivity decay measurement optionally temperature-dependent PCD(*T*)
PL	photoluminescence measurement
pFF	pseudo *FF*(from suns-V_{oc} measurement) [%]
χ_{c}	Raman crystallinity [%]
R	reflection [%]
SEM	scanning electron microscopy
R_{s}	series resistance [$\Omega\,\mathrm{cm^2}$]
sc	short-circuit
J_{sc}	short-circuit current density [$\mathrm{mA\,cm^{-2}}$]
R_{sh}	shunt resistance [$\Omega\,\mathrm{cm^2}$]
AM1.5g	solar spectrum with air-mass 1.5 (at a latitude of 45°) AM = $1/\cos(\theta)$, with incidence angle with respect to normal (θ)
SE	spectroscopic ellipsometry
STC	standard testing conditions (25 °C, AM1.5g, $0.1\,\mathrm{W/cm^2}$)
TC	temperature coefficient (relative) [%/ °C] optionally with subscript: V_{oc}, iV_{oc}, J_{sc}, *FF*, *iFF*, η
tc	temperature coefficient (absolute) [parameter unit/ °C] optionally same subscripts as for TC
TDS	thermal desorption spectroscopy
TEM	transmission electron microscopy optionally high-resolution (HR) or energy-filtered (EF)
UV	ultraviolet light

1 Introduction

1.1 Photovoltaics: *towards sustainable energy*

In order to satisfy the world's ever-increasing hunger for energy for generations to come, mankind has to find more sustainable ways to produce energy than relying on conventional sources. Fossil fuels (coal, oil and natural gas) and nuclear fuels (uranium) both share the same downsides: (1) they will run out eventually and (2) their usage entails significant negative effects on the environment (global warming, nuclear waste, etc.). This explains the call for more sustainable and cleaner solutions.

Over the last ten years worldwide investments in renewable power sources have increased by a factor of approximately 2.5 [van der Hoeven 2014]. Most of these renewable sources, be they wind, hydro or biomass, rely on *indirect* conversion of the energy supplied by the sun. In contrast, power generation based on photovoltaic devices converts solar energy *directly* into electricity which—after conversion to alternating current, which, for some applications is not even necessary as they work with direct current—is immediately ready for use. Furthermore—once installed—photovoltaic devices do not emit harmful greenhouse gases and the byproducts of their fabrication are much easier to handle as they are by far less hazardous. Tapping into the power of the sun is also the most logical thing to do, as on the human timescale the sun represents an almost infinite source of energy.

Additionally, there is a geopolitical benefit to solar power. Despite the fact that there is an irradiation gradient[1] and that climatic conditions (numbers of hours of sun, temperature, humidity, etc.) differ with different geological circumstances and location, in principle solar power is accessible around the globe and hence does not discriminate against any countries. This is not true for conventional sources, which are located only in specific places, which has led to conflicts and inequality in wealth among peoples and nations.

Furthermore, the sun supplies more than enough energy for everyone. *Every day* the earth

[1] Moving from the poles towards the equator the power density increases as the path the sunlight has to travel through the absorbing atmosphere to reach the surface is reduced.

receives approximately 4'140 PWh of energy,[2] which corresponds to almost 80'000 times the daily (220 times the annual) electricity consumption or 14'000 the daily (40 times the annual) total energy consumption of mankind in 2012 [OECD 2014] p. 28. Needless to say, if it were possible to harvest only a fraction of this energy, mankind's energy problem would be solved.

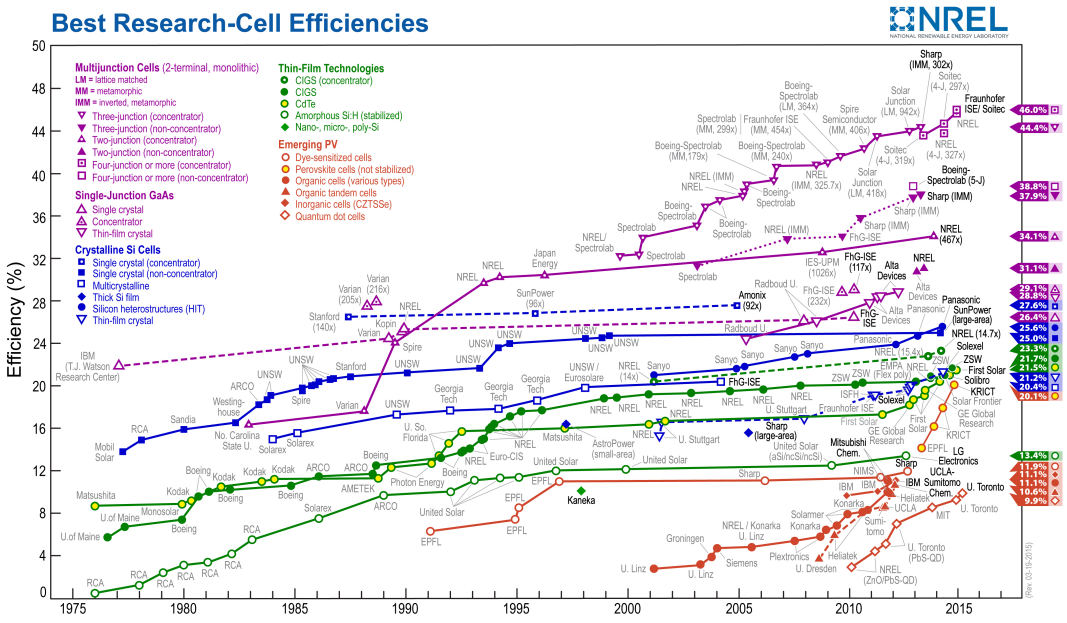

Figure 1.1 – Record efficiency chart published by the National Renewable Energy Laboratory (NREL, status 19-03-2015) as an overview of all the different photovoltaic technologies [NREL 2015].

1.2 Photovoltaic technologies

The record efficiency chart published by the National Renewable Energy Laboratory (NREL, USA), shown in Fig. 1.1 [NREL 2015], shows the wide spectrum of different solar cell technologies. Their main differences are mainly material- and production process-related but they obviously differ also in their record conversion efficiencies. Current technologies are based on crystalline silicon (c-Si)—which dominates the worldwide production capacity [Fraunhofer ISE 2014]—crystalline gallium arsenide (GaAs); thin-film technology [cadmium telluride (CdTe), copper indium gallium selenide (CIGS), and silicon (amorphous and microcrystalline)], and organic technology (*e.g.* organic dye-sensitized or organic-inorganic Perovskites). Despite their differences, these technologies share a common ground with respect to the basic physics involved in the generation of power. We elucidate this in the next section, discuss limiting factors (focusing mainly on c-Si technology) and briefly describe the structure of silicon heterojunction solar cells (SHJ)—the technology this thesis focuses on—in section 1.2.3 (p. 16).

[2] Calculated from the AM0 spectrum, *i.e.* the solar spectrum just outside the earth's atmosphere. Hence, this figure does not correspond to the usable energy, since part of it is absorbed within the earth's atmosphere.

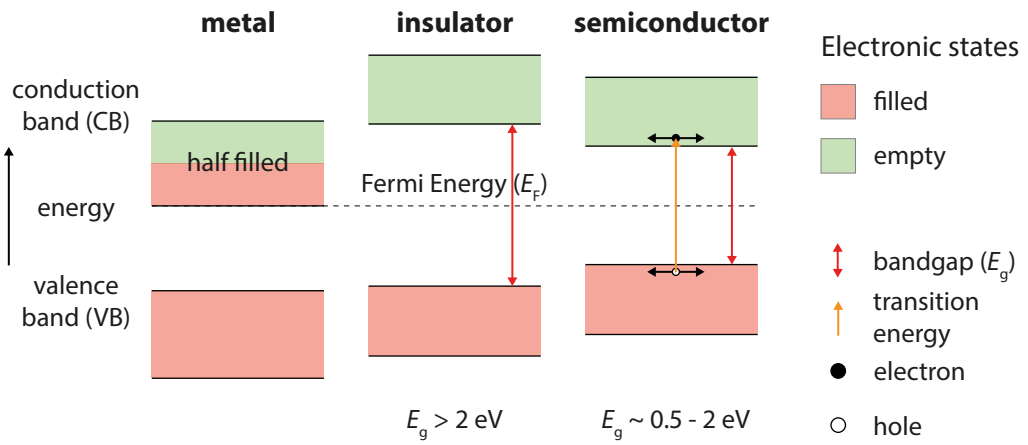

Figure 1.2 – Simplified representation of the band structures for metals, insulators and semiconductors.

1.2.1 Semiconductors and solar cells

The generation of electric energy in photovoltaic devices relies on the direct conversion of light (typically sunlight) into an electric potential via the photovoltaic effect, which is able to drive a current. In order for an electron to reach a conducting state, it has to absorb a certain amount of energy, which can be supplied either thermally or by irradiation. For metals, as shown in Fig. 1.2, no energy is required to excite an electron. Insulators and semiconductors on the other hand exhibit a so-called *bandgap*, a region in energy space, in which no electronic states are available. Typical values for the bandgap energy (E_g, the width of the bandgap) of semiconductors are on the order of 0.5–2 eV, matching the energies associated with light of the spectral range from ultraviolet (UV, $\lambda \leq 400$ nm), over visible, to infrared (IR, $\lambda \geq 700$–1050 nm). To cross the bandgap from the valence band (VB) to the conduction band (CB) and enable carrier transport, the electrons have to absorb at least an energy equal to E_g. Photons with an energy less than E_g are not absorbed and do not contribute to current generation; the material appears transparent to these photons.[3] Conversely, photons with an energy greater than E_g excite electrons to states high up in the CB, from where they return to the lower edge of the CB by thermalization and their excess energy is lost. Hence, for the spectral range of interest, there is an optimum E_g, which happens to be close to that of c-Si [Shockley 1961], the material investigated in this work.

The excitation of electrons from the VB to the CB always leaves behind an equal amount of net positive charges in the VB which are called *holes*; a hole is a quasi-particle representing the lack of an electron. Just like the electrons in the CB, these holes are able to move in the VB as shown schematically in Fig. 1.3. This is a crucial point for photovoltaic cells as the mere excitation of charge carriers is not sufficient to generate an electric potential. The cell has

[3] This is of great importance when designing window layers for the front side of a device (see section 1.2.2.3, p. 13; chapter 3, p. 37; and chapter 6, p. 99).

to be able to efficiently separate the two types of charge carriers before they recombine—*i.e.* before an electron falls back into the VB and fills up a hole—and are lost to build up the electric potential (see section 1.2.2.2, p. 7). This is achieved by giving the charge carriers an incentive to move in opposite directions: either by setting up an electric field across the absorber,[4] like it is done for thin-film devices, or by applying carrier-selective contacts at the interfaces that collect only one type of carriers and repel the other, as *e.g.* done for SHJ solar cells. In Fig. 1.4 we show in a simplified way how one can imagine this process. We compare a solar cell—driven by the sun—to two water-filled buckets, separated by a wall but connected by a sun-driven pump which lets the water pass in only one direction. This pump stands for the incentive for charge separation.

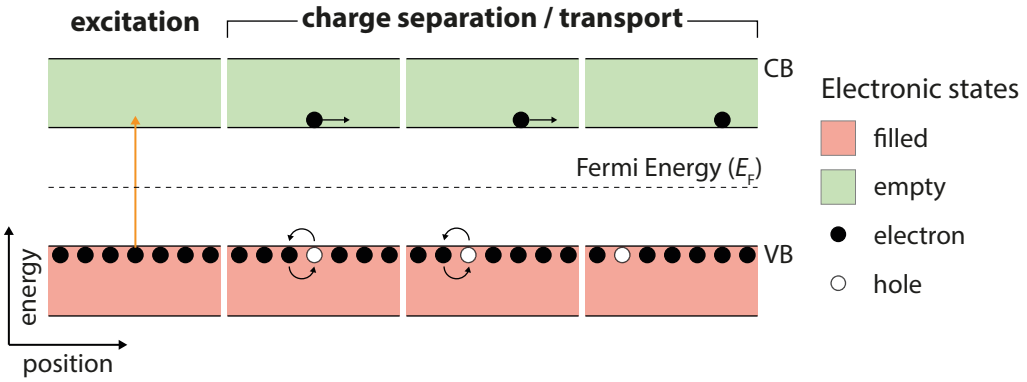

Figure 1.3 – Schematic representation of carrier transport in a semiconductor.

In the dark only a small number of free charge carriers are present in the absorber—due to external excitation—and the water levels are equal in both buckets, see Fig. 1.4(a). If however the cell is illuminated, electron-hole pairs are generated and, ideally, separated immediately. This corresponds to water being pumped from the left bucket to the right bucket. This gives rise to an electric potential which is represented by the different water levels and is maximized in open-circuit (oc) conditions in which no external current (water) is flowing [see Fig. 1.4(b)].

The electric potential can be reduced in two ways: (1) as mentioned before, by recombination of charge carriers (see section 1.2.2.2, 7), which can be imagined as tiny holes present in the wall that separates the two sides of the bucket, allowing the water to flow back to the left side. In the fabrication of solar cells it is important to reduce this effect as much as possible as we discuss in the next section, and (2) by connecting the two sides of the device via an external circuit as shown in Fig. 1.4(c). In this so-called short-circuit (sc) condition, the electrons flow through the electric circuit, equilibrating the electrical potential on both sides of the cell, *i.e.* the water level. This is the condition of maximum current and zero potential, or voltage.

[4] The absorber of a solar cell is the part in which the light is supposed to be absorbed. Depending on the technology this can be a layer (*e.g.* a silicon thin film) or substrate (*e.g.* a c-Si wafer).

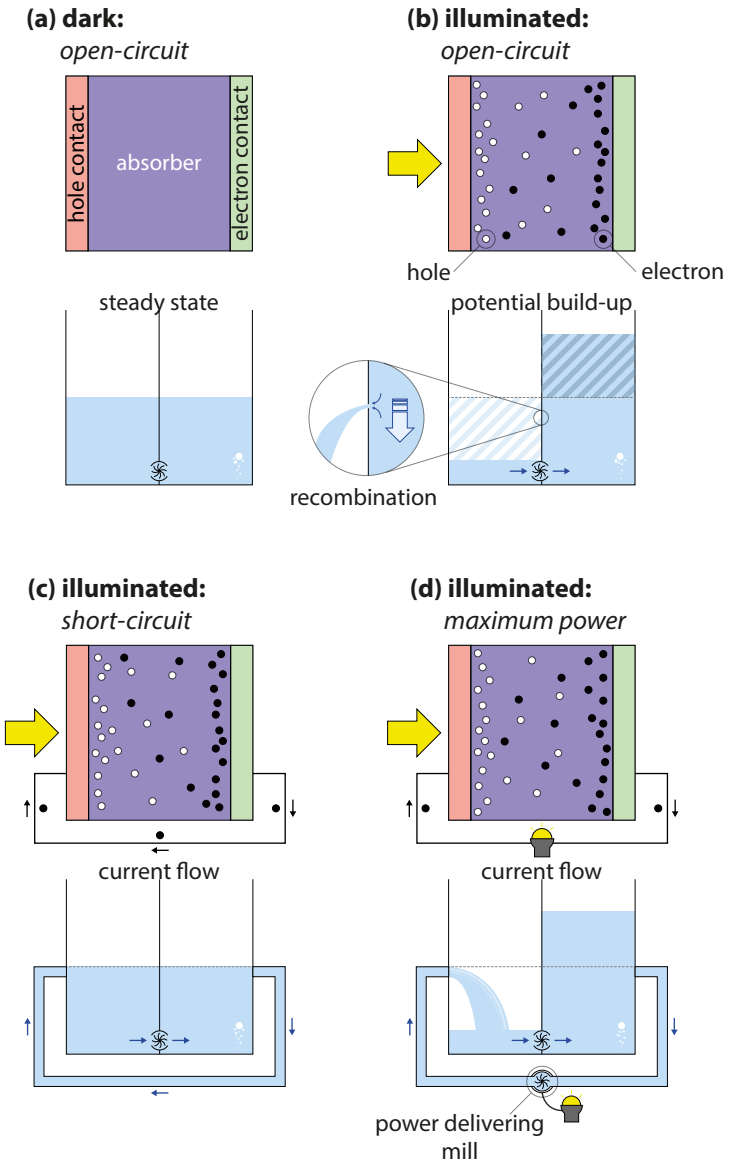

Figure 1.4 – General function of a photovoltaic cell in different conditions (top row): (a) in the dark and under illumination: (b) in open-circuit conditions, (c) in short-circuit conditions, and (d) in operation conditions with an external load symbolized by the small lamp. Ideally this load makes the cell operate at maximum power. The lower part of each figure shows a simplistic representation of a photovoltaic cell in the form of a water-filled bucket. The yellow arrow indicates the direction of the light.

In the field, a photovoltaic cell is preferably in neither of these conditions as the product of the current and the voltage determines the output power of the device. In both oc- and sc-conditions, either the current or the voltage is nil, and so is the power drawn from the cell. For practical purposes, the cells are preferably operated at the maximum power point (mpp), at which the product of current and voltage is maximized. For this condition to be satisfied, a load is introduced in the electric circuit, keeping the voltage at a higher level as shown in Fig. 1.4(d).

In the following section we discuss different limiting factors acting on the solar cell's performance, *i.e.* on the relevant cell parameters. Then we discuss the fundamental limitations that apply to solar cells in general and finally focus on SHJs, discussing the limitations of the main cell parameters in this type of solar cell (which may also apply to other technologies).

1.2.2 Limiting factors

1.2.2.1 Fundamental limitations

The performance of solar cells in general depends on three factors: (1) the voltage, (2) the current output of the device and (3) the carrier transport properties within the device. However, maximizing all three at the same time is a difficult task. There are often trade-offs, as maximizing one of them often comes at the expense of lowering the others.

The fundamental limit of the obtainable voltage with a solar cell is the bandgap (E_g) of the absorber material. This is, however, never attained as the *quasi Fermi levels*[5]—related to the excess density of electrons or holes—cannot move arbitrarily close towards the band edges. For instance there will always be radiative recombination, needed to obey thermodynamic principles, which limits the maximum attainable carrier density. This will be discussed in more detail in the next section (p. 8). The maximum quasi Fermi level splitting represents the maximum internal voltage that can be expected. Hence, any processes that affect the excess carrier densities may affect the maximum voltage (see next section). Now, in order to increase the voltage it is possible to use an absorber material with a wider bandgap. This, however, has a negative effect on the current, as fewer of the low-energy photons are absorbed ($E_{h\nu} < E_g$). And vice versa, decreasing E_g increases the current—thanks to more absorption—but at the same time lowers the voltage and moreover all the excess energy of high-energy photons is lost to thermalization. Hence there is an optimal bandgap for the spectrum of the sun, which in fact is close to that of c-Si as mentioned before (section 1.2.1, p. 3) [Shockley 1961].

According to Shockley and Queisser—who used a detailed balance approach—this compromise between current and voltage, leads to a theoretical limit of 30% using the spectrum of a 6000 K blackbody [Shockley 1961] or 33% for a spectrum of AM1.5 [Swanson 2005]. This detailed balance approach only considers radiative recombination, the only *real* fundamental

[5] The quasi Fermi levels for electrons and holes represent the Fermi level with respect to either of the charge carrier types separately [Sze 1981].

recombination path, representing the inverse of absorption. However, for silicon as an indirect semiconductor other recombination mechanisms have to be accounted for as well. The Shockley-Queisser-limit is therefore an overestimation. Assuming a perfect absorber, Tiedje, Yablonovitch and Cody extended the calculations by the AM1.5 spectrum, and included non-radiative recombination processes, namely Auger recombination (see next section). Doing so, they obtained 29.8% as the new device limit [Tiedje 1984]. More recently the Auger coefficients have been updated leading to the most recent efficiency limit of 29.43% for c-Si-based devices (110 μm-thick, undoped wafer) [Richter 2013].

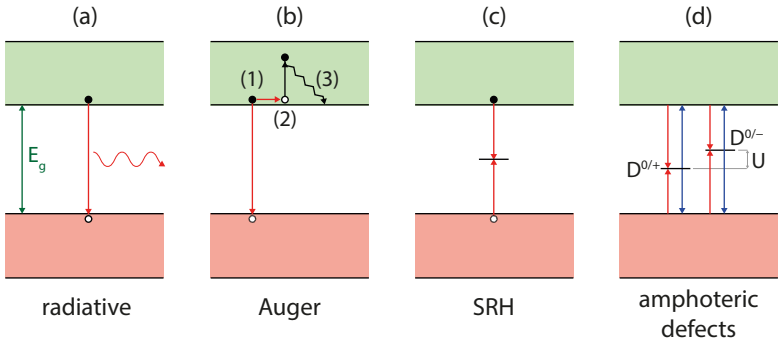

Figure 1.5 – Recombination processes in semiconductor materials.

1.2.2.2 Limits: *voltage — recombination*

One of the aspects limiting solar cell performance the most—mainly acting on the voltage—is carrier recombination. Besides intrinsic recombination processes (*radiative* and *Auger recombination* [Auger 1923])—which are inherent to the material and cannot be avoided—there is recombination via defect states located within the bandgap of the material. This is referred to as *Shockley-Read-Hall recombination* [Shockley 1952, Hall 1952] (in the bulk and at the surface[6]). All three recombination pathways shall be briefly discussed in this section, especially with respect to their behavior at low and high injection levels, *i.e.* excess carrier densities (Δn) that are much lower than the equilibrium densities (n and p): $\Delta n = \Delta p \ll n, p$, or higher than the latter: $\Delta n = \Delta p > n, p$). This is of particular importance for the understanding and interpretation of lifetime data obtained by photoconductivity decay measurements (see section 2.2, 27). Note that it is possible to associate a so-called minority-carrier lifetime (τ) with each of these recombination pathways, and which combined determine the *effective* minority-carrier lifetime (τ_{eff}) in a device.

Recombination rate and lifetime In *thermal equilibrium and darkness* generation and recombination cancel each other out, *i.e.* carriers that are thermally excited, recombine

[6] At the surface the situation is more complex as will be discussed later.

eventually. Both rates (generation G_{th} and recombination R_{th}) are given in units of [$\text{cm}^{-3}\text{s}^{-1}$].

$$G_{\text{th}} = R_{\text{th}} \text{ and } n_i^2 = np \tag{1.1}$$

Impinging light generates electron-hole pairs, thus the carrier densities n and p increase compared to their values in the dark. In the first few μs a steady state develops, where recombination and generation again cancel out. Under illumination or generally with carrier injection, the carrier densities are given by the following relations, where n_0 and p_0 are the carrier densities before illumination or carrier injection and n_i the intrinsic carrier density.

$$n = n_0 + \Delta n \tag{1.2}$$
$$p = p_0 + \Delta p \tag{1.3}$$
$$np > n_i^2 \tag{1.4}$$

With the net recombination rate[7] $U = R - R_{\text{th}}$ the so-called *bulk lifetime* τ_{bulk} [s] can be defined, which is given for each carrier type separately.

$$\tau_n = \frac{\Delta n}{U} \tag{1.5}$$
$$\tau_p = \frac{\Delta p}{U} \tag{1.6}$$

The bulk lifetime is influenced by different processes, which shall be discussed in the following. Note that the net recombination rate U increases with increasing excess carrier density. As shown in Eq. 1.5 and 1.6, the lifetime depends on the injection level (Δn and Δp), which we discuss in more detail for each recombination pathway in the following.

Radiative recombination: An electron residing in the conduction band can recombine directly, via band-to-band recombination, with a hole in the valence band. In this *two-particle* process, the energy that the electron loses (equivalent to the bandgap energy E_{g}) is emitted in form of a photon [see Fig. 1.5(a)]. This is in fact the inverse of light absorption. The process is more probable for direct bandgap materials (*two-particle process*) than for indirect bandgap materials such as c-Si. For indirect bandgap materials, a third particle—a phonon—is required for the transition to take place (*three-particle process*).

The radiative recombination rate R_{e} is given by the following formula, where r_{ec} is the recom-

[7] This is the recombination (R) devoid the recombination in thermal equilibrium (R_{th}). Typical values: $U \approx 10^{18}\,\text{cm}^{-3}\text{s}^{-1}$ and $\Delta n = 10^{14}\,\text{cm}^{-3}$.

bination coefficient and G_{th} is the thermal generation rate (no illumination):

$$\begin{aligned} R_{\text{e}} &= r_{\text{ec}} \cdot n \cdot p \quad \text{general rule} \\ &= r_{\text{ec}} \cdot n_i^2 \; = \; G_{\text{th}} \quad \text{in equilibrium} \end{aligned} \tag{1.7}$$

The net radiative recombination rate on the other hand is given by the deviation from thermal equilibrium:

$$U_{\text{rad.}} = R_{\text{e}} - G_{\text{th}} = r_{\text{ec}} \left(np - n_i^2 \right) \tag{1.8}$$

Here the carrier concentrations are given by equations 1.2 (electrons) and 1.3 (holes). As the recombination rate depends on the injection level, it is necessary to distinguish between high and low injection levels. More details are given in appendix 7.2 (p. 131).

At low injection levels the minority-carrier lifetime for this radiative recombination path ($\tau_{\text{rad.}}$) depends on the inverse of the doping concentration (N_0) as $\tau_{\text{rad.}} \propto N_0^{-1}$. In contrast, for high injection levels it is linked to the excess carrier density (Δn) and $\tau_{\text{rad.}} \propto \Delta\text{n}^{-1}$.

Radiative recombination shows a distinct temperature dependence for temperatures below 300 K as discussed elsewhere [Trupke 2003, Nguyen 2014]. However, it shows only a minor impact on τ_{eff} as for silicon this parameter is dominated by either Auger or Shockley-Read-Hall recombination as can be seen in Fig. 1.6 and as discussed in the following. More information on radiative recombination can be found in the literature [Altermatt 2005].

Auger recombination: This recombination process involves *three particles*: two electrons (or holes) and one hole (or electron). The first charge carrier recombines via a direct band transition [see Fig. 1.5(b), process (1)], transmits its energy to a second charge carrier near the conduction (valence) band edge and excites it to a higher (lower) energy level in the conduction (valence) band [see Fig. 1.5(b), process (2)]. From this state it gradually loses its energy by thermalization [see Fig. 1.5(b), process (3)] and returns to the band edge, which results in a lost electron-hole pair. Essentially a three-particle process, the recombination rate for the Auger process is given by [Sze 1981]:

$$U_{\text{Auger}} = C_n n^2 p + C_p p^2 n \tag{1.9}$$

$C_{n,p}$ are the Auger coefficients. The fact that a n^2 appears in the electron term and a p^2 in the hole term accounts for the contribution of two particles (electrons or holes) as described above.

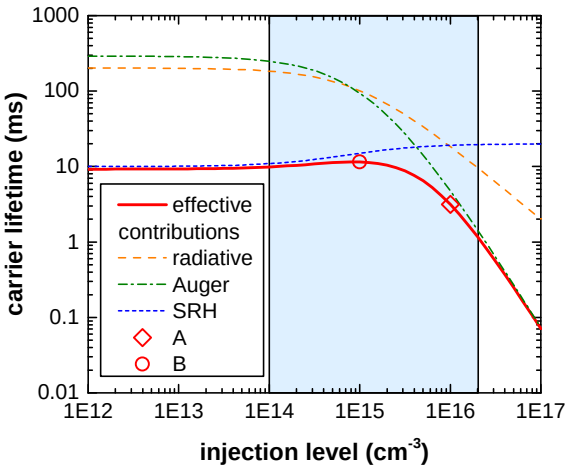

Figure 1.6 – Effective carrier lifetime as a function of the injection level (carrier density) and its three contributions: (1) radiative, (2) Auger and (3) Shockley-Read-Hall. This data was obtained for an n-type wafer with a doping density of 1×10^{15} and $\tau_n = \tau_p = 1000\,\mu$s and a mid-gap trap level ($E_i - E_t = 0$). The lifetimes were calculated using the software available on PV-Lighthouse [McIntosh 2015]. The shaded area indicates the injection range typically accessible by lifetime measurements (using our standard tool, see 2.2.2.2, p. 32), whereas (A) and (B) indicate points of interest, their position (Δn value) determining the maximum voltage both in open-circuit and operating conditions, respectively. Note that the exact position of these points are sample-dependent.

As for the radiative path, it is important to consider the injection dependence of Auger recombination. At low injection levels τ_{Auger} is proportional to N_0^{-2}, while at high injection levels the relation is $\tau_{\text{Auger}} \propto \Delta n^{-2}$. More information can be found in the literature [Dziewior 1977, Sinton 1987, Kerr 2002, Richter 2012].

Shockley-Read-Hall and surface recombination: Electronic defect states within the bandgap can capture both electrons and holes from their respective bands and thereby lead to recombination [see Fig. 1.5(c)]. This process is known as Shockley-Read-Hall (SRH) recombination. However, whether a defect acts like a *recombination center* depends on its energetic position (E_t) within the bandgap.

Defects that are close to the band edges are typically referred to as *trap states*. For this type of defect the capture cross-sections—σ_n for electrons or σ_p for holes (determining the capture probabilities for each carrier type)—for one type of charge carrier is much larger than for the other. Additionally, owing to being close to one of the band edges, the re-emission probability of the captured carrier is also larger than the probability to capture its counterpart from the opposite band. Hence these defects do not contribute to recombination.

Defects that are closer to mid-gap on the other hand are referred to as *recombination centers*. For the most efficient recombination center the capture cross-sections are equal $\sigma_n = \sigma_p$. Hence, if an electron is captured, the same is very likely to happen to a hole, which completes the recombination process. But in general, if the re-emission probability for a captured carrier

is smaller than the capture probability for its counterpart, the defect leads to recombination.

The net recombination rate for this pathway is given by the following equation:

$$U_{\mathrm{SRH}} = \frac{v_{\mathrm{th}} N_{\mathrm{t}} \left(np - n_i^2\right)}{\frac{1}{\sigma_p}\left(n + n_1\right) + \frac{1}{\sigma_n}\left(p + p_1\right)} \tag{1.10}$$

Here v_{th} is the thermal velocity of the charge carriers, N_{t} is the defect density and $n_1 = n_i \exp\left((E_{\mathrm{t}} - E_{\mathrm{F}}^i)/k_{\mathrm{B}}T\right)$ and $p_1 = n_i \exp\left((E_{\mathrm{F}}^i - E_{\mathrm{t}})/k_{\mathrm{B}}T\right)$.

In high injection ($\Delta n = \Delta p > n_0$ and p_0 as well as $\Delta n = \Delta p > n_1$ and p_1) the carrier lifetime is given by the sum of the intrinsic carrier lifetimes and is independent of the doping or the injection level.

$$\tau_{\mathrm{SRH}}^{n,p} = \frac{\Delta n}{U_{\mathrm{SRH}}} = \tau_{n0} + \tau_{p0} \tag{1.11}$$

$$\text{with} \qquad \tau_{n0,p0} = \frac{1}{\sigma_{n,p} v_{\mathrm{th}} N_{\mathrm{t}}} \tag{1.12}$$

For the case of low injection (with $n \sim N_{\mathrm{D}}$ and equal capture cross-sections: $\sigma = \sigma_n = \sigma_p$) the lifetime is given by the following equation, which can be determined from the general equation (Note: τ_{SRH} is doping dependent):

$$\tau_{\mathrm{SRH}} = \frac{\Delta n}{U_{\mathrm{SRH}}} = \frac{1 + \frac{2n_i}{N_{\mathrm{d}}} \cosh\left(\frac{E_{\mathrm{t}} - E_{\mathrm{F}}^i}{k_{\mathrm{B}}T}\right)}{\sigma v_{\mathrm{th}} N_{\mathrm{t}}} \tag{1.13}$$

The lifetime associated with SRH recombination, τ_{SRH}, consists of two parts: a *bulk* (τ_{bulk}) and a *surface* ($\tau_{\mathrm{surf.}}$) contribution. τ_{bulk} is related to impurities, *e.g.* metal atoms that diffuse into the material where they create defect states and thus—depending on their position in the bandgap—recombination centers. These types of defects can be detrimental to the carrier lifetime and minute amounts are sufficient to reduce the carrier lifetime to close to zero [Davis 1980].

The *Shockley-Read-Hall formalism* for bulk recombination described above, can also be applied to the c-Si surface, assuming a simple defect state at a discrete energy. For the SHJ solar cells, however, this simple model does not hold. Similar to bulk amorphous silicon (a-Si:H), the interface of a c-Si silicon wafers exhibits so-called *dangling bonds* (DB). These electronic states are the result of the rupture of the crystal lattice resultant unsatisfied bonds. These states

can hold one (D^0), two (D^-) or no electrons (D^+) and are referred to as *amphoteric defects*.[8] Hence, to describe the recombination at this a-Si:H/c-Si interface a different model has been proposed in [Olibet 2007] and studied further by [Leendertz 2010]. For more information see also [Shockley 1952, Hall 1952].

In contrast to radiative or Auger recombination, SRH recombination can be avoided with (1) high-quality materials [*e.g.* float-zone (FZ) wafers] with extremely low amounts of impurities and (2) schemes for surface passivation, which rely on *chemical* or *field-effect passivation* [see Fig. 1.7(a) and (b)]. Chemical passivation relies on the application of a material which reduces N_t and hence increases τ. Typical examples for this type of passivating material are a-Si:H for SHJ solar cells [Fujiwara 2009] and derivatives such as oxides (a-SiO_x:H) [Mueller 2010]. In contrast, passivation by field-effect takes advantage of band bending in the absorber material—induced by fixed charges—and prevents one type of charge carrier from reaching the interface which increases τ as well. Materials that are used for this type of passivation are *e.g.* thermally grown oxides [Mark 2002], amorphous silicon nitrides (a-SiN_x) and aluminum oxide (Al_2O_3) [Agostinelli 2006, Hoex 2006, Saint-Cast 2009]. These two effects can also be combined.

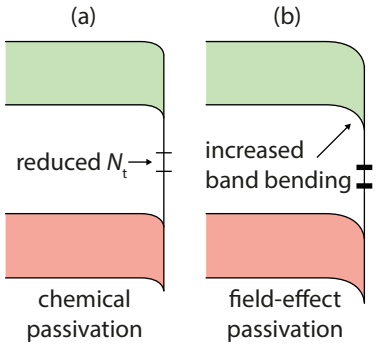

Figure 1.7 – Means for passivation of semiconductor surfaces.

Effective minority-carrier lifetime Since all the three recombination processes (index i) occur at the same time and their recombination rates are additive, the effective rate is given by:

$$U_{\text{eff}} = \sum_i U_i = U_{\text{rad.}} + U_{\text{Auger}} + U_{\text{SRH}} \tag{1.14}$$

[8] Due to Coulomb repulsion, the addition of a second electron to the DB state demands an additional amount of energy (U), hence, D^- is located higher in energy [see Fig. 1.5(d)].

From this the effective minority-carrier lifetime can be expressed as follows:

$$\frac{1}{\tau_{\text{eff}}} = \sum_i \frac{1}{\tau_i} \tag{1.15}$$

$$= \frac{1}{\tau_{\text{rad.}}} + \frac{1}{\tau_{\text{Auger}}} + \frac{1}{\tau_{\text{bulk}}} + \frac{1}{\tau_{\text{surf.}}} \tag{1.16}$$

From this equation it is evident that the shortest lifetime dominates the others and thus limits τ_{eff}. As the different recombination mechanisms show some injection dependence, different injection ranges are dominated by different recombination pathways. A typical lifetime curve, as measured by photoconductivity decay (see section 2.2.2.2, p. 32) is shown in Fig. 1.6 with all the contributions discussed above. It is important to note that for high cell performance there are two points of interest [(A) and (B)] indicated in the figure. These points are associated with the maximum voltage in (A) open-circuit and (B) operating conditions. These voltages are driven by the corresponding injection level Δn at the two points (A) and (B). It is directly influenced by recombination and is ideally maximized.

1.2.2.3 Limits: *current — parasitic absorption*

We now turn to the limitations of the current. Besides excellent surface passivation obtained with a-Si:H layers, SHJ solar cells exhibit a limitation in extractable current density [Holman 2012]. At the front of the device the main optical losses are attributed to light absorbed in the transparent conductive oxide (TCO), in the doped a-Si:H and—to a lesser extent—in the intrinsic a-Si:H layers. The intrinsic and doped a-Si:H layers, with a bandgap of approximately 1.7 eV, mainly absorb high-energy photons. However, due to the high defect density within these layers, the generated electron-hole pairs are not separated efficiently before they recombine and therefore do not contribute to the current generation. TCO layers in general typically exhibit a wide bandgap, yet, at the front, the TCO acts not only as an anti-reflective coating, but also as a transport layer enabling lateral transport to the metallic grid. Hence it has to be conductive enough, which is assured by a high conductivity σ.

$$\sigma = q \cdot \mu \cdot n \tag{1.17}$$

As can be seen from this formula, to maximize σ either the mobility μ or the carrier density n has to be increased. Increasing n, however, results in increased free-carrier absorption (FCA) which leads to optical losses in the long-wavelength range [Holman 2013c]. For this reason, it is preferable to optimize μ and find a trade-off between optical and electrical losses. These optical losses can easily be quantified by quantum efficiency measurements (described in section 2.2.2.4, p. 34).

Optical losses are, however, not limited to layers applied at the front. The layers at the rear of the device play an important role as well. While short wavelengths are absorbed in the first few tens of nanometers at the front, longer wavelengths can travel through the wafer several times before being absorbed or escape at the front. Assuming perfect internal reflection and hence light trapping, no losses in the long-wavelength range would be expected. Unfortunately this is not the case in a real device. It has been shown for textured devices that light that reaches the metallic rear reflector can excite surface plasmon polaritons which represent the major loss mechanism for near-bandgap light [Holman 2013a]. Based on these findings, novel rear reflectors have been developed that use a stack of indium tin oxide (ITO) and magnesium fluoride (MgF_2) and local contacts at the rear [Holman 2013b].

Besides all these losses associated with the layers implemented into a SHJ device, one important source for optical losses is shadowing by the metallic grid, which is needed for carrier extraction at the front of a both-side-contacted device. There are several approaches to reduce these losses. One obvious way is to reduce the amount of the surface covered by the grid to a minimum. In fact, reducing the width of the metallic fingers *e.g.* by using copper-plating instead of screen-printing has shown the potential of this approach [Hernández 2012, Papet 2013, Geissbühler 2014]—with the added benefit of replacing the costly silver by the much cheaper copper. Another approach is to completely remove the front grid and collect both holes and electrons at the rear. That way the front layers can be optimized for passivation and increased light transmission, without any restraints in carrier transport. These so-called inter-digitated back-contacted cells have proven highly efficient, also thanks to their increased current [Masuko 2014, Tomasi 2014]. However, for these devices certain current losses are present as well [Paviet-Salomon 2015].

In terms of optical performance, in the present work, we concentrated mainly on the front side silicon layers and assessed the potential of different window layer materials to improve their transparency. This is discussed in chapters 3 (p. 37) and 6 (p. 99).

1.2.2.4 Limits: *transport*

In c-Si solar cells, besides being dependent on the passivation quality of the wafer surface—dark saturation currents—carrier transport depends on device-inherent resistances, namely *shunt resistance* (R_{sh}) and *series resistance* (R_s). Empirical and analytical studies have investigated transport limiting factors [Green 1983, Khanna 2013]. A shunt is a connection of both sides of a solar cell via an alternative current path, which can cause signification power losses. Shunts are attributed mostly to manufacturing defects or the cell design and have to be avoided, *i.e.* R_{sh} has to be maximized for high-performance devices. Thanks to the cell design used in this work (see Fig. 2.2), R_{sh} is very high and losses associated with it can be neglected. R_s on the other hand plays an important role. It is linked to (1) transport of the carriers through the solar cell: the absorber and the different layers, and includes *ohmic* and *non-ohmic* contributions stemming from the bulk properties of each layer or the interactions between the layers that possibly lead to the formation of Schottky barriers [Tung 2014]; (2)

contact resistance between the materials used in the cell, *e.g.* the metal and the TCO; and (3) resistance in the external metallic contacts. In contrast to R_{sh}, R_s should be minimized in order to allow for highest conversion efficiencies.

Contacts — *a brief discussion*: As stated before, the contacts are one of the most critical parts of a photovoltaic device. Recently several authors discussed fundamental points of contacts [Cuevas 2013, Wurfel 2015, Bullock 2014, Holman 2015]. They argue that for a photovoltaic device to work, the contacts have to be: (1) passivating, *i.e.* reduce the losses due to recombination (see section 1.2.2.2, p. 7); (2) carrier-selective, (3) and majority-carrier conductive. Here, minority- or majority-carrier refers to the respective carrier type *in* the contact, *i.e.* for the hole-collecting contact, holes are majority-carriers and hence electrons are minority-carriers. These three requirements can be achieved by introducing carrier-selective resistances, whereby the current of one type of charge carrier towards the electrode is reduced. This is schematically shown in Fig. 1.8. So considering the electron contact (analogous for the hole contact), the collected electron current (hole current) $J_{\text{coll.}}{}^{n}$ ($J_{\text{coll.}}{}^{p}$) has to be maximized while the recombination currents $J_{\text{rec.}}{}^{n}$ and $J_{\text{rec.}}{}^{p}$ are ideally reduced to a minimum. Notably, all of these requirements have to be fulfilled in order to have a well-behaving device. It is for instance not viable to optimize the passivating aspect at the expense of the majority-carrier conductivity of a contact, which brings us back to what we discussed earlier (section 1.2.2.1, p. 6).

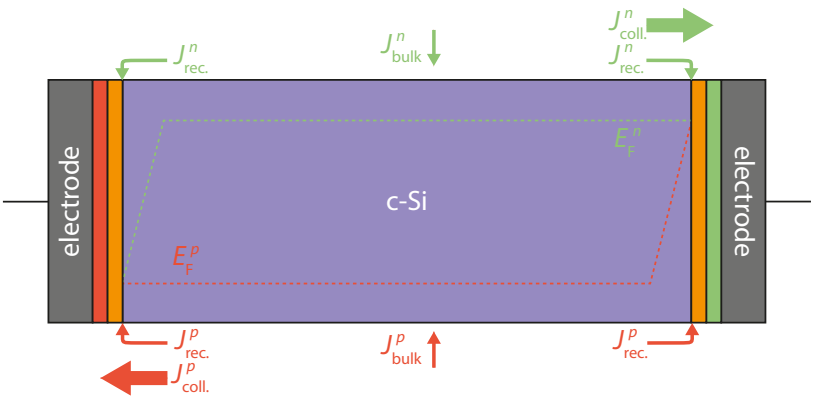

Figure 1.8 – Schematic of the contacts and charge carrier currents in a SHJ device. Adapted from Holman *et al.* [Holman 2015].

Due to their different electronic properties, adjacent materials can have a significant effect on one another as the contact forms. This can lead to the bending of the electronic bands and as a result barriers may form as depicted in Fig. 1.9 for a metal-semiconductor contact. In this specific case, the height of this barrier depends on the work function of the metal ($q\varphi_m$)—the energy it takes to extract an electron from Fermi energy to the vacuum level—and the

electron affinity of the semiconductor ($q\chi_s$). The barrier height is then simply given by $q\varphi_B = q(\varphi_m - \chi)$. This barrier represents a hurdle for majority carriers in the semiconductor and, depending on its height or width, it can be either overcome by thermionic emission or crossed by tunneling for sufficiently thin barrier width. In this case the contact would be referred to as *ohmic* otherwise we speak of a *Schottky contact*. These barriers give therefore rise to the *contact resistivity* (ρ_c). For ohmic contacts ρ_c is negligible compared to the series resistance. For non-ohmic contacts, however, it can be significant and impede carrier transport. Hence, ideally it also has to be minimized to enhance device performance. However, as shown in [Bullock 2014] in order to optimize the performance, a trade-off has to be found between ρ_c and passivation. More information on the topic can also be found in [Sze 2002] or [Demaurex 2014a].

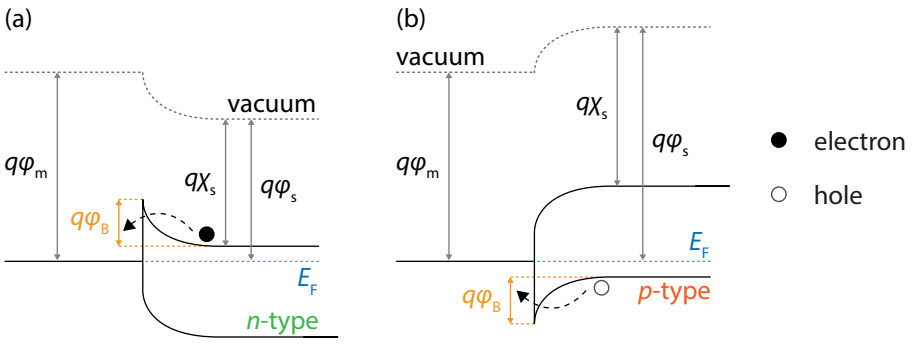

Figure 1.9 – Metal-semiconductor contacts for (a) *n*-type and (b) *p*-type semiconductors. Adapted from [Sze 2002].

The concepts briefly presented here are important to keep in mind for the development of new SHJ structures. In particular when replacing the standard a-Si:H layers by different materials (chapter on a-SiO_x:H, p. 37; or chapter 6, p. 99) but also for applying additional layers for protective purposes (chapter on atomic layer deposited protective layers, p. 83).

1.2.3 Silicon heterojunction solar cells: *concept & status*

Since the pioneering days of SHJ solar cells—developed by Taguchi and Tanaka *et al.* at SANYO, Japan, in the early 1990s [Tanaka 1992]—many groups and companies have studied this promising technology on both *n*-type and *p*-type silicon wafers. A summary can be found in De Wolf *et al.* [De Wolf 2012b]. In contrast to standard devices, which rely on the diffusion of dopant atoms into the crystalline bulk material to form the *p*-*n* junction, SHJ solar cells use intrinsic and doped a-Si:H layers. Even though this technology is already being commercialized by Panasonic, Japan, there are still a number of points that remain unclear and its potential is not fully exploited. Judging by the most recent results from Panasonic [Taguchi 2014, Masuko 2014], which show maximum voltages close to the fundamental limit of c-Si (769 mV for a 100 μm wafer [Tiedje 1984], or around 749 mV for a 110 μm wafer [Richter 2013]), it is fair to say that the main challenges now are the improvement of both the

current and the transport properties in this type of device, while keeping high voltage values.

The SHJ concept has the potential for high efficiency at competitive production costs, and in combination with recently emerging technologies like *e.g.* perovskite solar cells, even for ultra-high-efficiency devices [Loper 2014]. In 2014 Panasonic announced two new record efficiencies (see Fig. 1.1): 24.7% for their standard both-side-contacted SHJ device [Taguchi 2014], and an interdigitated back-contacted (IBC) device. With an efficiency of 25.6% [Masuko 2014] this IBC device passed the record efficiency of 25% held until then by the University of New South Wales [Zhao 1999, Green 2009] for the previous 15 years. This result was obtained on so-called passivated emitter, rear locally diffused (PERL) solar cells. Yet, they were not the only ones to reach 25%. SunPower commercialized an IBC solar cell and reached conversion efficiencies 25% on five-inch wafers as well [Cousins 2010] as did SHARP (25.1%) on lab-scale devices [Nakamura 2014].

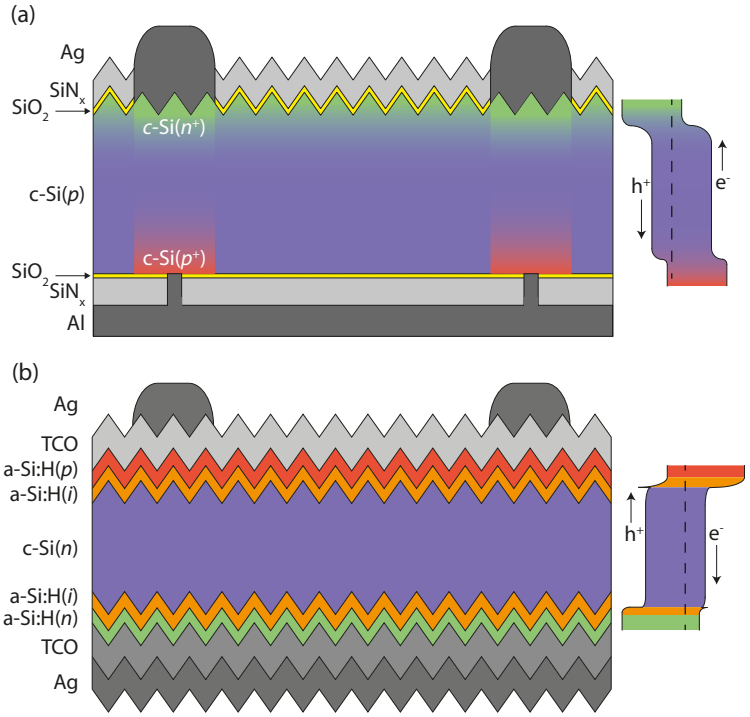

Figure 1.10 – Comparison of the structure of (a) a PERL and (b) a SHJ solar cell.

Even though currently both SHJ and PERL devices reach similar conversion efficiencies, there are fundamental differences. In order to maintain a high voltage, both technologies rely on high-quality surface passivation to suppress recombination of charge carriers (see section 1.2.2.2, p. 7). This, in fact, marks the most crucial difference. In standard cells—we use the PERL cell as reference [Zhao 1999, Green 2009]—the metallic contacts are plated at local openings of the anti-reflective coating (*e.g.* silicon nitride, SiN_x) and the passivation layer (*e.g.* silicon dioxide, SiO_2) to form a direct metal-semiconductor contact [see Fig. 1.10(a)]. Even

though this type of contact provides good transport properties it is likely the most performance-limiting aspect of this technology as it is recombination-active and hence significantly lowers the maximum voltage.

The advantage of the SHJ concept is the displacement of the metallic contacts away from the c-Si interface, thereby limiting recombination. This is achieved by inserting a stack of wide-bandgap intrinsic (*i*) and doped (*n* or *p*) a-Si:H layers, as well as a TCO layer—necessary for optical and electrical reasons—between the c-Si absorber and the metallic contacts [see Fig. 1.10(b)]. This device architecture enables high voltages at open-circuit conditions close to the theoretical limit [Tiedje 1984] as mentioned before [Taguchi 2014, Masuko 2014]. Recently, so-called *passivating contacts* [Demaurex 2014a, Tous 2014a], which try to combine the best of both worlds, have been investigated [Cousins 2010, Smith 2012].

However, as mentioned before, the gain in surface passivation is achieved at the expense of the current output [Holman 2012]. This is easily understood, comparing the structure of the two technologies shown in Fig. 1.10. As the metallic fingers at the front directly contact the absorber through local openings in the stack of highly transparent dielectrics (SiO_2 and SiN_x)—enabling high passivation between the fingers *and* good light incoupling—transport is not a limiting factor for the PERL solar cell. The SHJ solar cell on the other hand relies on transport through the intrinsic and doped a-Si:H layers capped with a TCO. These layers, give rise to *parasitic absorption* as discussed earlier (see section 1.2.2.3, p. 1.2.2.3) and challenges in carrier transport (see section 1.2.2.4, p. 14; and chapter 3, p. 37).

For a more complete introduction to SHJ solar cells, the reader is referred to the literature [De Wolf 2012b].

1.3 Objectives and structure

1.3.1 Motivation and goal of this work

The objectives of the present thesis are twofold. The main *scientific* goal is to understand how the material properties of intrinsic a-Si:H, and doped silicon and their interfaces to the TCO layers impact device performance. For this purpose materials like hydrogenated microcrystalline silicon (μc-Si:H) and hydrogenated amorphous silicon suboxides (a-SiO_x:H) are investigated focusing on the influence of the individual layers on transport and optical properties. The goal is to minimize optical and electrical losses. The latter goes hand in hand with the more *technological* objective, namely the development of processes for the implementation of these non-standard materials into SHJ devices.

1.3.2 Structure

The structure of this manuscript is as follows:

- **Chapter 2** describes the main experimental techniques used, *i.e.* all the processing steps and sample characterization.
- **Chapter 3** discusses the advantages and drawbacks of implementing wide-bandgap a-SiO_x:H layers in SHJ devices. Furthermore, the impact of the band offsets' asymmetry on cell performance is studied using as a show case wide-bandgap oxide layers. This supports the trend towards hole-collection at the rear of the device.
- **Chapter 4** discusses the temperature-dependence of the interface passivation and its impact on individual cell parameters.
- **Chapter 5** presents alternative materials for transparent electrodes which could enhance the optical performance of a device. In the first part the effect of atomic-layer-deposited TCO layers on the minority-carrier lifetime are investigated, while the second part focuses on similar effects associated with organic semicoductors.
- **Chapter 6** discusses strategies of how to obtain thin, *p*- or *n*-doped but highly microcrystalline layers on an a-Si:H substrate and assesses the suitability of these methods for SHJ devices. Furthermore the impact of different μc-Si:H-deposition regimes on the effective minority-carrier lifetime at different stages of the cell fabrication process are reported. Finally, the benefits of μc-Si:H layers in terms of current and transport are discussed on the basis of device results.
- The **Conclusion** summarizes the results obtained during the course of this thesis and gives an outlook for further developments.

1.4 Contribution to the research field

The present work contributes mainly to the field of SHJ solar cells but also to the field of c-Si-based solar cells in general. The main scientific results are described hereafter. Note that the technical terms will be introduced in chapter 2 (p. 23).

Aiming at optical improvements, we investigated a-SiO_x:H layers and their suitability for SHJ solar cells. Even though these materials—as all wide-bandgap materials—may have the potential for higher current values—we report on an increase of 0.43 mA cm^{-2}—their position in the cell structure has to be considered carefully. We found that, in contrast to electrons, holes can suffer from transport barriers introduced by enhanced valence band offsets, which tend to be larger than the offsets found in the conduction band. This increase in valence band offset mainly acts on the fill factor. Even though this might be a strong argument against the application of a-SiO_x:H, temperature-dependent measurements have shown that these barriers can lead to improved temperature coefficients—as low as −0.1%/ °C compared to the −0.2 to −0.25%/ °C reported for SHJ solar cells—and hence better performance at higher temperatures. This will be discussed in more detail in chapters 3 (p. 37) and 4 (p. 63). In a subsequent study, we investigated the impact of asymmetric band offsets in SHJ and show that electrons are less affected by wide-bandgap materials than holes. From this we conclude that SHJ devices may benefit from the collection of holes at the rear.

The already mentioned temperature behavior of SHJ solar cells, and especially the effect of elevated temperatures on the wafers' surface passivation, was studied in detail. We found that both the maximum voltage and the transport properties are slightly influenced by the temperature-induced variations in effective minority-carrier lifetime, while the current is not. We argue that the temperature coefficient of a c-Si-based solar cell depends not only on the maximum voltage—as proposed by other authors [Green 1985, Taguchi 2008, Mishima 2011]—but also on the passivation dependence on temperature and of the cell structure, namely *e.g.* the presence of barriers, as mentioned above. In order to gain a deeper insight into the temperature behavior of different device technologies, we compared a set of cells—obtained from imec (Leuven, Belgium)—to a standard SHJ solar cell. Both these topics are discussed in chapter 4 (p. 63).

Focusing more on enhancing the maximum voltage of a device, the potential of protective atomic-layer-deposited TCO layers was assessed. These layers are meant to shield the underlying a-Si:H(*i*) passivation layers and the c-Si interface against damage induced by the subsequent sputtering step. A clear indication was found such layers can prevent sputter damage. Yet, despite an enhancement in implied voltage (the upper bound for the maximum voltage after deposition of the a-Si:H layers) after sputtering, this difference could not be conserved in a finished device, likely due to the use of a-Si:H layers optimized to be thick enough to prevent permanent damage from sputtering. For the layers used in this study, the transport properties were negatively affected which could be linked to an increase in series resistance, associated with the presence of an a-SiO_x:H layer—formed during processing—at

the a-Si:H/ALD TCO interface. Here we studied the advantages and drawbacks of these ALD layers with respect to the passivation at carrier injection levels found at the operation point of a SHJ solar cell. Even though, applied to the hole contact, the layers used here do not show an improvement, the opposite is true for the electron contact. These results will be discussed in chapter 5, section 5.1 (p. 83). Applying the same methodology, we investigated polymer layers, this time to improve the hole contact. Indeed, we observe a beneficial effect on the effective passivation of this contact. This will be presented in 5, section 5.2 (p. 90). In addition to their beneficial electrical properties these materials may also help to improve the optical performance thanks to their low refractive indices [Holman 2013b].

Our study of charge-collecting layers for SHJ solar cells focused on doped microcrystalline silicon layers (μc-Si:H(p) and μc-Si:H(n)). This material has the potential for higher current values, thanks to it better transparency compared to standard a-Si:H layers. Yet, its application in SHJ solar cells is linked to a number of technological challenges. For the deposition of thin (~10 nm), sufficiently doped and microcrystalline layers on a-Si:H(i)-coated substrates, precise process control is crucial. In the course of this thesis we explored various strategies to obtain μc-Si:H layers and assessed their suitability for SHJ solar cells. Furthermore, we investigated the impact of different deposition regimes on the passivation quality of SHJ devices and report on cell results obtained the latter, assessing the optical benefits of μc-Si:H layers. Remarkable gains in current of up to 1 mA cm^{-2}, excellent fill factor values of up to 79.2% and conversion efficiencies of 20.9% were obtained. This will be discussed in chapter 6 (p. 99).

Apart from the topics summarized here, contributions to other investigations were provided in the framework of in-house collaborations. These contributions helped to understand the nature and importance of parasitic absorption in a-Si:H layers [Holman 2012]; to assess the potential of hydrogen-plasma treatments of a-Si:H layers for improved passivation of c-Si surfaces [Descoeudres 2011]; as well as plasma etching for the patterning of a-Si:H layers for advanced cell designs [Geissbühler 2013]; to develop homo-epitaxial layers deposited by PECVD [Demaurex 2014b]; and to understand the links between lifetime, ideality factor—at both low and high illumination—and the fill factor of a device [Tomasi 2015].

2 Experimental details

In this chapter we will briefly review the most important processes and methods to both fabricate and characterize SHJ solar cells and the associated materials.

2.1 Process flow for silicon heterojunction solar cells

2.1.1 Wet chemistry: *cleaning, texturing and oxide removal*

SHJ solar cells are based on c-Si wafers. In this work high-quality float-zone (FZ) wafers were used. Compared to the Czochralski technique—which relies on pulling single crystals from a melt and impurities from the crucible may be incorporated into the ingot—the float-zone technique enables much higher resistivities (lower contamination levels) [Sze 2002]. These single crystals are sawn into thin plates by wire sawing, with a thickness typically on the order of 200–300 μm. As-cut wafers exhibit sawing damage (micro-cracks at the surface), which is subsequently removed by etching. In order to ensure good light trapping properties, an anisotropic potassium hydroxide (KOH) etch is used to form micron-scale pyramids on each side of the wafer. The wafers are then cleaned to avoid contamination. Before cell processing the native oxide (1–2 nm) present at the wafer surface after the cleaning step, is stripped using a diluted hydrofluoric acid (HF, 5%) solution. If not stated otherwise, we applied HF for 60 s. This is sufficient to terminate the c-Si surface by hydrogen, which makes it hydrophobic and provides good passivation.

Note that for the supply of textured wafers we relied on either Meyer Burger Research Switzerland or the PV-Center of the Swiss Center for Electronics and Microtechnology (CSEM).

2.1.2 Layers: *deposition methods*

2.1.2.1 Plasma-enhanced chemical vapor deposition

Following the wet chemistry steps, the next processing step for standard devices is the deposition of a-Si:H(*i*), a-Si:H(*p*) and a-Si:H(*n*) layers. The intrinsic layers represent the core of this technology, as they provide excellent surface passivation and therefore enable high V_{oc} values. The doped layers are needed to form the carrier-selective contacts for either electrons [a-Si:H(*n*)] or holes [a-Si:H(*p*)].

The technique used in this work to deposit these layers is plasma-enhanced chemical vapor deposition (PECVD). This process takes place within a PECVD reactor as depicted in Fig. 2.1. Such a reactor consists of a vacuum chamber into which a second, smaller chamber—the plasma reactor—is inserted, in which the actual deposition takes place. The plasma reactor is typically pumped down to pressures as low as 10^{-6} to 10^{-7} mbar, to avoid contamination of the layers, and heated to the processing temperature (150–200 °C). Prior to the deposition of device-relevant layers the chambers are preconditioned, *i.e.* pre-coated with silicon.

Here we relied on three types of PECVD reactors: (1) an industrial-sized large-area system (KAI-M, developed by unaxis, which was transferred to Oerlikon Solar that was bought by TEL Solar), (2) a medium-sized research and development cluster tool (Octopus I, 1st generation, INDEOtec) and (3) a large-area cluster tool (Octopus II, 2nd generation, INDEOtec). Their specifications are listed in Tab. 2.1 (p. 25).

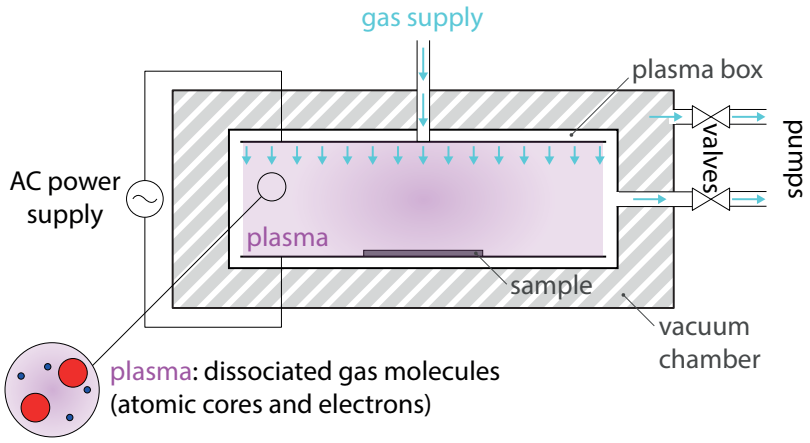

Figure 2.1 – Schematic of a PECVD reactor.

During the deposition process, precursor gases (silane, SiH_4; disilane, Si_2H_6; or silicon tetrafluoride, SiF_4), dilution gases (hydrogen, H_2 or deuterium, D_2), and optionally doping (phosphine, PH_3 or trimethylborane, $B(CH_3)_3$) or alloying gases (carbon dioxide, CO_2) are introduced into

the plasma reactor through one of two capacitor plates, the shower electrode. The other capacitor plate holds the substrate, typically a piece of glass or a c-Si wafer (Fig. 2.1) on which the layers are deposited. These plates are connected to a power-supply unit coupled to a frequency generator and driven by an alternating electrical field at a specific excitation frequency and power. Within this alternating electric field electrons are accelerated and gain sufficient energy to collide inelastically with gas molecules. This marks the ignition of a plasma, within which an increasing number of molecules is dissociated and whose constituents—atoms, radicals ions and electrons—are able to move. This represents also the main advantage of this technique (plasma enhanced), namely the fact that it allows us to run processes that typically necessitate high temperatures (to dissociate the precursor gas molecules) at relatively low temperatures of around 200 °C. The radicals formed in the plasma move to the reactor surface, where they react with one another and induce the film growth of the desired material. For more details the reader is referred to the literature, *e.g.* [Smith 1995].

Depending on the requirements for the layer properties (*e.g.* bandgap, crystallinity, doping, hydrogen content etc.), the deposition parameters, namely pressure (p), incoupled power (P), temperature (T), frequency, and gas flow ratios, are varied. Each of these parameters has a specific influence on the plasma composition and hence on the properties of the growing thin film. The layer thickness is controlled by the deposition time. The precise control of the process is essential for the deposition of the different layers, in particular for the a-Si:H(i) passivation layers, where it is crucial to avoid epitaxy at the crystalline interface [De Wolf 2012b] or the μc-Si:H layers that were investigated here (6, p. 99).

Table 2.1 – Reactor specifications.

Reactor	**Plate size** [mm×mm]	**Interelectrode gap** [mm]	**Frequency** [MHz]	**Chambers**
KAI-M	612 × 502	13	40.68	2
Octopus I	163.35 × 153.35	15	13.56–81.36	4
Octopus II	350 × 450	15	40.68	2

2.1.2.2 Sputter deposition: *TCO and metallization*

Magnetron sputtering deposition belongs to the class of physical vapor deposition (PVD) techniques. Similar to PECVD, this method relies on high vacuum and plasma technology as well. However, in contrast to PECVD, the gases used do not supply the precursors for the layer growth. Instead they are supplied by a slab—the target—of the material one wants to deposit. For the deposition, argon is mixed with additional doping gases like *e.g.* oxygen and a plasma is ignited either by a direct current (DC) or alternating current (AC) power supply, as in the case of PECVD. The ionized atoms or molecules are accelerated towards the target. Upon

impact, they eject material from the target's surface which is deposited on the sample.

In this work, we used this technique to deposit indium tin oxide (ITO) as transparent electrodes and silver (Ag), which serves as both electrical contact and rear reflector.[1] Depending on their position, the TCO layers have to fulfill different requirements. The front TCO acts as anti-reflective coating, provides a contact to the metallic front grid and ensures—at least to some extend—lateral transport towards the fingers (Fig. 2.2), which is not provided by the doped a-Si:H layers. Recently, however, it has been argued that a part of the lateral current might actually be transported within the c-Si bulk [Geissbühler 2014]. If the rear of the device is textured, the TCO applied on this side helps to avoid plasmonic losses in the metallic reflector [Holman 2013a, Holman 2013b] and provides a good contact to the latter.

In contrast to other deposition techniques, the deposition conditions during sputtering can be harsh and may damage the layers already present on the substrate or the substrate itself. This sputtering-induced damage has been found to be associated with the ion bombardment by ions and with the UV irradiation occurring during the process [Demaurex 2012] and is one aspect limiting the efficiency (section 1.2.2.2, p. 7).

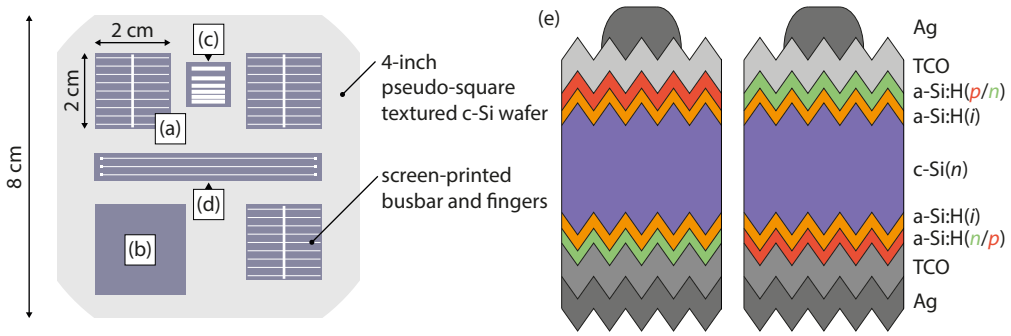

Figure 2.2 – Standard wafer design used in this work, with three (a) $2\times2\,cm^2$ screen-printed SHJ solar cells; (b) a spectral response pad; (c) a transfer-length-measurement pad; and (d) a pad for line resistivity measurements. (e) Schematics of typical SHJ devices including all the essential layers (a-Si:H and TCO) and metallic electrodes and either hole collection at the front (left) or the rear (right).

2.1.3 Atomic-layer-deposition

In theory, this technique represents the ultimate layer-by-layer thin film deposition method. It relies on the sequential application of precursor gases on a heated substrate inside an atomic layer deposition (ALD) reactor. The precursor gas molecules adsorb to the surface, forming a monolayer of molecules which reacts with the molecules of a different precursor gas introduced in a second step. This reaction leads to the formation of the first layer of the new material. In practice, however, this layer-by-layer growth mode does not necessarily

[1] Long-wavelength light, which is able to travel through the entire wafer, is reflected and has another chance to be absorbed.

reflect the reality as the deposited materials can have the tendency to grow in an island-like manner [Ohring 2001]. Hence, in order to obtain a coalescent film one has to grow several nanometers, which represents several cycles of precursor gases. Despite this drawback, in contrast to standard physical vapor deposition techniques (*e.g.* sputtering as discussed in section 2.1.2.2, p. 25) the potential of ALD is its softness—ideal for sensitive materials or interfaces—its potentially precise thickness control and its conformal deposition. These properties makes ALD a valuable asset mainly in research with applications reaching from solar cells to electronics.

2.1.4 Front contact

For the standard architecture of c-Si solar cells, with contacts on both sides, screen printing is a standard procedure to define the contacts at the front. Generally, in order to minimize associated shadowing losses the printed lines have to be as thin as possible. State-of-the-art screen printing produces finger widths as narrow as 30 μm [Zicarelli 2010], while using copper-plating lines of down to 15 μm are possible [Geissbühler 2014]. The cells processed in this work exclusively relied on screen-printing for which a low-temperature silver paste was used. The printing is followed by a curing step at 200 °C in which the solvents are evaporated and the silver particles coalesce. The interconnection of the silver particles enables good line resistances contributing to the series resistance in the order of 0.05 Ω cm^2 [Geissbühler 2014].

2.1.5 Cell design

For the fabrication of solar cells we used high-quality FZ *n*-type wafers (~230–250 μm, ~2–3 Ωcm) that were processed as described above. The standard wafer layout used in the present work is depicted in Fig. 2.2(e), with either front or rear hole collection. The cells were defined by using a shadow mask during sputtering. The typical cell structure is as follows: screen-printed Ag front grid/ITO 70 nm/a-Si:H(*p*) 10 nm/a-Si:H(*i*) 5 nm/FZ c-Si(*n*)(see above)/a-Si:H(*i*) 5 nm/a-Si:H(*n*) 10 nm/ITO 150—200 nm/Ag full rear metallization. For cells with hole collection at the rear, the electrodes at the rear were also masked using the same shadow-mask as for the front ITO. Thereby recombination losses in adjacent dark diodes can be avoided.

2.2 Characterization tools

2.2.1 Material characterization

2.2.1.1 Spectroscopic ellipsometry

Spectroscopic ellipsometry (SE) was one of the main tools used for layer characterization. We used a UVISEL from HORIBA Jobin Yvon. The tool measures the changes in polarization of initially linear polarized light after reflection at the sample surface. This can either be a single layer or a stack of layers deposited on a substrate (typically glass or polished wafers).

From the measurement of the change in polarization and the subsequent fitting of the raw data to a model using *DeltaPsi 2.6.8.239*, from HORIBA Jobin Yvon), it is possible to extract information about the optical properties [bandgap (E_g), refractive index (n) and extinction coefficient (k)] of each individual layer but also about the bulk properties (*e.g.* thickness or crystallinity). Fig. 2.3 depicts the models used in this work for both a-Si:H and μc-Si:H layers. For the a-Si:H layers a Tauc-Lorentz model was used, the μc-Si:H layers on the other hand were fitted using a Kato-Adachi model. Note that for the fits of μc-Si:H layers in some instances we obtained better results when introducing an additional a-Si:H layer between the a-Si:H that was deposited directly on the glass—measured individually, prior to μc-Si:H deposition—and the μc-Si:H layer. Although no systematic study was performed, this additional layer could give access to the incubation layer forming before the nucleation of the crystalline phase. For further information on SE see [Stückelberger 2014].

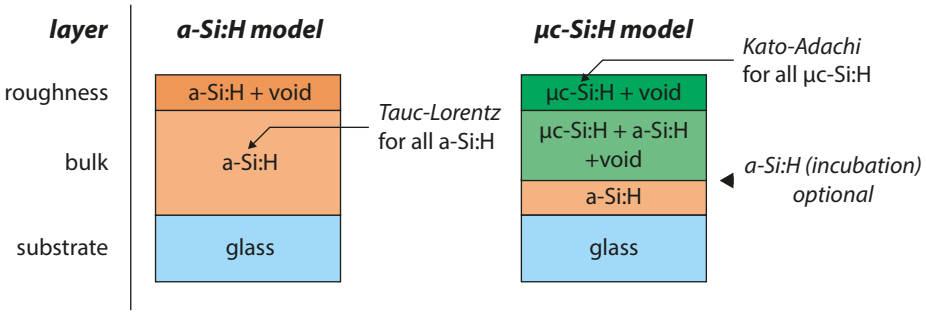

Figure 2.3 – Schematic representation of the SE models used in this work.

2.2.1.2 Raman spectroscopy

Raman spectroscopy was used to characterize the μc-Si:H layers investigated in this work. Measurements were performed with a Renishaw RAMASCOPE, green laser at 514 nm for glass samples (estimated error ±3% absolute) or a Renishaw InVia REXLEX, blue laser at 325 nm, for measurements on textured wafers. In Raman spectroscopy the sample is illuminated with a laser beam of a specified wavelength, which defines the penetration depth into the layers. High-energy photons are absorbed faster than low-energy photons and hence probe only the surface of the sample. The basis of this technique is the interaction of the photons with the material. The light that is reflected may have a shift away from the initial wavelength that was used to probe the sample. This shift is characteristic of the material microstructure and enables the extraction of *e.g.* the crystallinity of a μc-Si:H layer. The Raman spectra were deconvoluted using three Gaussian peaks centered at 480 cm^{-1}, 510 cm^{-1} and 520 cm^{-1}, which are often attributed to the amorphous phase, small-sized grains or grain boundaries and the bulk crystalline phase, respectively [Droz 2004]. The Raman crystallinity (χ_c) was determined

from the following formula (where A denotes the area below the associated Gaussian peak):

$$\chi_c = \frac{A_{510} + A_{520}}{A_{480} + A_{510} + A_{520}} \tag{2.1}$$

2.2.1.3 Electron microscopy

Similar to optical microscopes relying on photons, electron microscopy capitalizes on the shorter De Broglie wavelength of electrons as a probe for imaging materials down to the nanometer scale. Generally speaking, this technique is based on the interaction of electrons—either elastic or inelastic—with matter. It comprises a wealth of different possibilities for material analysis ranging from standard imaging techniques, to high-resolution imaging and chemical analysis. High-resolution transmission electron microscopy (HRTEM) were used to investigate crystalline samples (see chapter 6, p. 99). The Structural investigations using HRTEM, were performed using a FEI Titan microscope equipped with a spherical aberration corrector at the image plane with a beam energy of 300 kV. For this the samples were processed into cross-sectional specimen by focused ion beam milling. A final thinning step was performed with low energy Ar ions (0.5 eV) using a Fischione NanoMill system.

2.2.1.4 Fourier-transform infrared spectroscopy

Fourier-transform infrared spectroscopy (FTIR) enables us to probe thin layers of a given material and study the prevailing bonding configurations of the atoms within. It relies on the analysis of the absorption of IR light leading to characteristic loss spectra. Depending on the needs of the user and the preparation of the sample (thick layers or deposition on prisms), FTIR can be operated in transmission or attenuated-total-reflection (ATR) mode, the latter enabling higher precision. More information can be found in the literature (*e.g.* in [Stückelberger 2014]).

2.2.1.5 Hall measurements

Hall measurements were used for TCO characterization, namely to extract the density and mobility of majority-carriers and the sheet resistance of a given material. We used the Van der Pauw method on an Ecopia HMS-5000 setup, which is described elsewhere [Sze 1981, Ding 2013b].

2.2.1.6 Thermal desorption spectroscopy

Thermal desorption spectroscopy (TDS) relies on the analysis of atoms and molecules emitted by a sample, when heated to temperatures as high as 900 °C in ultra-high vacuum. The analysis is performed by a mass spectrometer, which counts the number of molecules or atoms of a specific mass. We mainly analyzed the effusion of molecular hydrogen which

reveals the structure and bonding configuration of a specific species of molecules. Depending on the prevailing bonding configurations of hydrogen within *e.g.* an a-Si:H layer—be they mono-hydrides or higher hydrides—it is possible to discern different peaks in the effusion spectrum (counts as a function of the temperature). Each of these peaks is associated with one type of hydrogen bonding configuration. Higher hydrides exhibiting a lower bonding energy rupture at lower temperatures, while mono-hydrides release their hydrogen at higher temperatures, as they are more stable. For more information the reader is referred to the literature [Beyer 1983, De Wolf 2007].

2.2.2 Device characterization

2.2.2.1 Current-voltage measurements

For the characterization of finished devices, current-voltage measurements (J-V) enable the assessment of the performance of any type of solar cell. Typically J-V measurements are used in standard operation, namely standard testing conditions (STC), *i.e.* at 25 °C, with a one-sun AM1.5g equivalent illumination, which is the spectrum and intensity at the earth's surface at a latitude of 45°. However, as solar panels deployed in the field are rarely at 25 °C and different types of cells react differently to an increase in temperature, it makes sense to measure the cells temperature-dependently [J-$V(T)$], as we will discuss in chapters 3 (p. 37) and 4 (p. 63).

A probing station consists of a sun simulator, typically with a set of different lamps (halogen and xenon) and filter(s) to mimic the solar spectrum (AM1.5g). In this work three different systems (class AAA) were used: the Wacom (Meyer Burger Research, one xenon lamp), the WXS-220S-L2 ("Wacom II", three halogen lamps, one xenon lamp) and the WXS-90S-L2 ("Malibu", one halogen lamp and one xenon lamp). All of them feature a temperature-controllable vacuum chuck. For the Wacom the temperature is varied by a Peltier element in a range of 25–60 °C, whereas both the Wacom II and the Malibu feature a Peltier-regulated temperature-controllable chuck with active cooling capability and a temperature range of ~15–85 °C.[2] The cells are measured by contacting the busbars at the front using four probes on each end of the latter.

A typical measurement is shown in Fig. 2.4. This is obtained by illuminating the solar cell and sweeping the voltage in a given range (typically −0.1 to 0.8 V) while measuring the generated current. Measuring the diode characteristics of the cell enables the extraction of the relevant parameters (see section 1.2.1, p. 3):

- J_{sc}: The *short-circuit current density* is measured at zero voltage where the entire current is extracted. This value depends mainly on the amount of light entering the cell and contributing to the generation of the current. Effects like *parasitic absorption* can lead to losses (see section 1.2.2.3, p. 13; and chapters 3, p. 37; and 6, p. 99).

[2] For all the measurements presented here, the temperature was kept high enough to avoid water condensation.

- V_{oc}: The *open-circuit voltage* refers to the voltage obtained at one-sun illumination, when no current is extracted. Besides the intrinsic recombination processes (*radiative* and *Auger* recombination), it depends on defect-mediated recombination (*Shockley-Read-Hall*, SRH) and hence on the bulk and the interface passivation quality of the c-Si wafer (see section 1.2.2.2, p. 7). Any of the recombination processes lowers the excess carrier density (Δn) and hence the maximum achievable voltage, as also shown in Fig. 1.4.

- mpp: The *maximum power point* is, the point at which the product of current density and voltage is maximized. J_{mpp} and $V_{mpp}$are the current density and voltage at the maximum power point, respectively. Besides J_{sc}, V_{oc} and *FF*, J_{mpp} and V_{mpp} can also be used to determine the conversion efficiency (η) of a solar cell (see below).

- *FF*: The *fill factor* represents the *squareness* of the *J-V* curve, *i.e.* the ratio between the ideal, square-shaped curve—delimited by the V_{oc} and the J_{sc}—and the actual, measured curve. It gives an indication of transport properties, namely the effect of (ohmic or non-ohmic) R_s or R_{sh}. It is calculated as follows:

$$FF = \frac{V_{mpp} \cdot J_{mpp}}{V_{oc} \cdot J_{sc}} \tag{2.2}$$

- η: The solar cell efficiency (η) is calculated from the power input (P_{in}) and the power output which is obtained from the values given above:

$$\eta = \frac{V_{oc} \cdot J_{sc} \cdot FF}{P_{in}} = \frac{V_{mpp} \cdot J_{mpp}}{P_{in}} \tag{2.3}$$

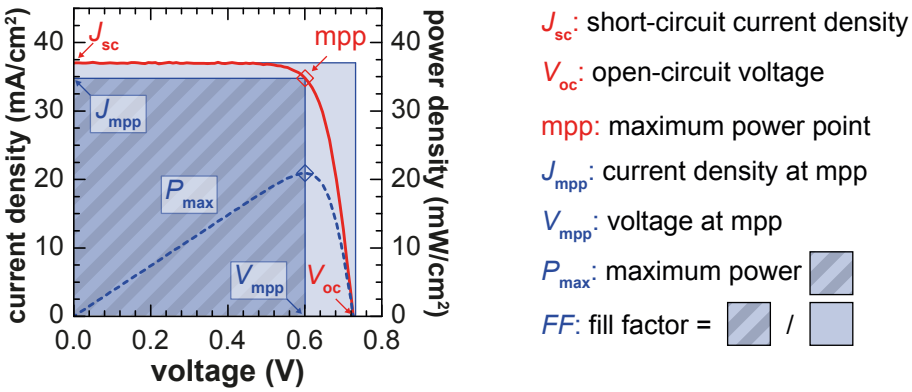

Figure 2.4 – Typical *J-V* curve of a SHJ solar cell with all the relevant parameters.

As can be seen from Fig. 2.4, a solar cell behaves like a diode, to me more precise it is a current-generating diode. The simplest way to describe it is with a single diode as depicted in Fig. 2.5 (black circuit). This model however neglects recombination at the junction, hence,

normally the double-diode model is used (including the second, grey diode in the figure). The current density of such a double-diode is given by:

$$J(V) = J_L - J_{01}\left[\exp\left(\frac{q(V+JR_s)}{n_1 k_B T} - 1\right)\right] - J_{02}\left[\exp\left(\frac{q(V+JR_s)}{n_2 k_B T} - 1\right)\right] - \frac{V+JR_s}{R_{sh}} \quad (2.4)$$

Here J_L is the current generated by the photovoltaic cell, J_{01} and J_{02} are the recombination currents that have an effect on the V_{oc} and the *FF*, V is the voltage, n_1 and n_2 are the ideality factors of either of the diodes, q is the elementary charge, k is the Boltzmann constant and T is the absolute temperature in Kelvin.

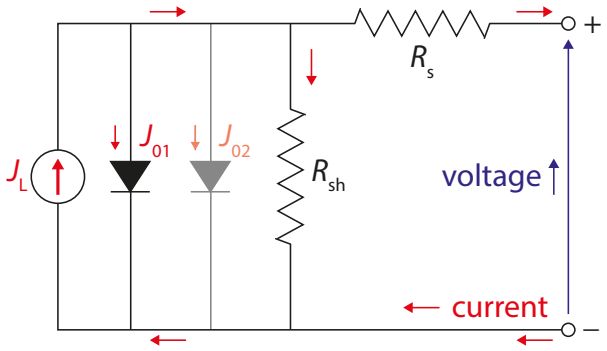

Figure 2.5 – Equivalent circuit for a solar cell for the one-diode model (black) or the two-diode model (including the second diode in grey).

2.2.2.2 Photoconductivity decay measurement

Photoconductivity decay (PCD) measurements were used to quantify the passivation quality of a wafer. For these measurements two types of setups were used: (1) a Sinton Instruments WCT-100 for standard measurements and (2) a WCT-120-TS system for standard or temperature-dependent measurements [Sinton 1996, Schmidt 2003]. This contactless method is based on the inductive measurement of the change in photoconductivity within the wafer after illumination by a flash of a given duration. From the decay of the photoconductivity it is possible to calculate the injection-level-dependent (Δn) effective minority-carrier lifetime [$\tau_{eff}(\Delta n)$], hereafter denoted as τ_{eff} where we implicitly assume its injection-level-dependence. The injection level is directly linked to a voltage and a so-called *implied J-V* curve can be reconstructed. Since the latter is obtained for unfinished devices, a value for the J_{sc} has to be assumed. We typically chose 37 mA cm^{-2} as this is the range of current we usually obtain for finished devices. From this curve we extract the implied open-circuit voltage (iV_{oc}) and

implied fill-factor (*iFF*[3]). For an *n*-type wafer with a doping density of N_D the iV_{oc} is given by [Sinton 1996]:

$$iV_{oc} = \frac{k_B T}{q} \ln\left(\frac{(N_D + \Delta n)\,\Delta n}{n_i^2}\right) \tag{2.5}$$

While the iV_{oc} is associated with the lifetime at higher injection levels which correspond to an illumination of one sun (close to 1×10^{16}), the *iFF* depends more on the lifetime at lower injection levels (around 1×10^{15}). These two figures provide an upper limit to the actual figures (V_{oc} and *FF*) to be expected in a finished device. For the discussion of the *iFF* see section 2.2.2.6 (p. 35).

For further details on this measurement technique, the reader is referred to the literature [Sinton 1996].

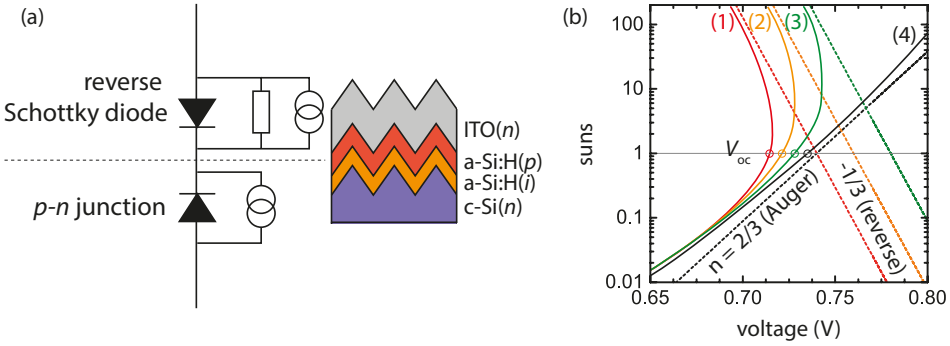

Figure 2.6 – (a) Simplified schematic of the circuit including a reverse Schottky diode forming between the ITO and the a-Si:H(*p*) layer (adapted from [Glunz 2007, Bivour 2012]). (b) Schematic of a typical suns-V_{oc} measurement for four different cases: (1)–(3) represent devices that are influenced by an inverse diode, while (4) represents a case closer to the ideal.

2.2.2.3 Suns-V_{oc}

The measurement called suns-V_{oc} relies on the measurement of the photogenerated voltage of a finished solar cell as a function of the illumination (suns). As no current is extracted from the cell, the measurement is *transport independent* and hence the so-called *pseudo J-V* curve that is obtained does not show any transport-related effects, *e.g.* from the R_s. Hence, one possibility to calculate a value for the R_s is to compare both the standard *J-V* to the suns-V_{oc} measurement [Pysch 2007]. Besides, the so-called *pseudo FF* gives an upper bound to the *FF* that can be expected in a finished cell. In order to understand the difference to *iFF* see section

[3] Note that the *iFF* does not depend on the J_{sc} value that is chosen.

2.2.2.6 (p. 35). See [Sinton 2000] for further details.

Operated at both low and high injection levels, this type of measurement was also used to characterize cells and the effects present at the different interfaces, *e.g.* TCO to a-Si:H, and the presence of Schottky barriers (see section 1.2.2.4, p. 15) that may form there [Glunz 2007, Bivour 2014, Bivour 2013, Tomasi 2015]. The typical signature of these inverse diodes is depicted schematically in Fig. 2.6.

2.2.2.4 External and internal quantum efficiency

This measurement relies on probing the photogenerated current as a function of the wavelength (energy) of the incident photons on a solar cell contacted on both sides. It gives insight into loss mechanisms affecting the J_{sc}. During the course of this work, three different setups were used: (1) QEX10 Solar Cell IPCE (PV Measurements) , (2) IQE-SCAN (pv-tools) and (3) a home-built setup.

The external quantum efficiency [EQE(λ)] corresponds to the ratio of the number of electrons flowing in the device in short-circuit condition and the number of impinging photons, *i.e.* which percentage of electron-hole pairs are created and collected per photon of a specific wavelength. It is useful to identify loss mechanisms in the cell and takes advantage of the nature of light: High-energy photons (short wavelengths, blue light) are absorbed in the first few 10–100 nm of the cell, whereas low-energy photons (longer wavelengths, visible and especially red light) can enter the cell and bounce back and forth between the rear and front before being absorbed or re-emitted. Hence losses showing up in the high-energy range can be mainly related to the front side of the device. Losses in the low-energy range on the other hand include both the front and rear of the device.

In order to gain more insights into what actually happens inside the cell, the internal quantum efficiency [IQE(λ)] can be calculated from the EQE in the following way (where R is the reflectance:

$$\mathrm{IQE}(\lambda) = \frac{\mathrm{EQE}(\lambda)}{1 - R(\lambda)} \tag{2.6}$$

The IQE represents the ratio of electrons flowing in the internal circuit and the number of photons penetrating into the cell, *i.e.* the percentage of electrons (created and collected) per number of photons that actually make it into the cell. This helps to identify other effects apart from reflection issues that lead to a lower current, *e.g.* parasitic absorption at the front or collection issues in general. For the extraction of the IQE the information on the reflectance (R) is needed, which typically was measured using a PerkinElmer Lambda900 UV-vis-IR spectrometer.

2.2.2.5 Photoluminescence

Photoluminescence (PL) was used for qualitative investigations of the global wafer passivation only. The basics of this measurement are the illumination of a sample (a passivated wafer) and the analysis of the light—corresponding to the bandgap energy of c-Si—emitted from the sample, and detected by an IR camera. This way the global passivation of the wafer can be probed in a matter of seconds. Areas of high passivation quality appear brighter as most of the carriers recombine radiatively, in contrast to areas that are dominated by defect-mediated recombination (SRH). Further information can be found elsewhere [Trupke 2006].

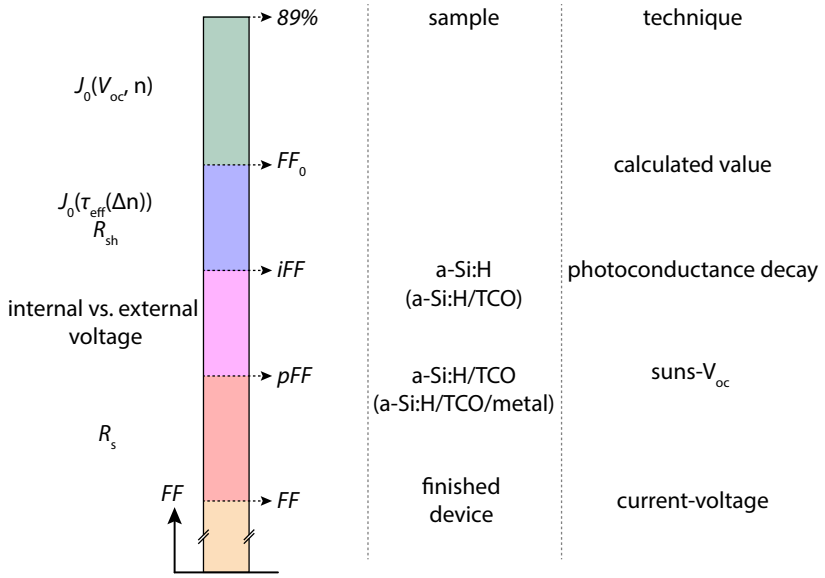

Figure 2.7 – Summary of different fill factor values obtained when including different loss mechanisms. By courtesy of B. Demaurex (EPFL, PV-Lab, Switzerland) [Demaurex 2014a].

2.2.2.6 Fill factor analysis: FF_0, *iFF, pFF and FF*

As described in the sections 2.2.2.2 (*iFF*, p. 32), 2.2.2.1 (*FF*, p. 30) and 2.2.2.3 (*pFF*, p. 33), different values for the *FF* are obtained for each characterization method. Starting from the fundamental limit proposed by Tiedje *et al.* [Tiedje 1984] shown in Fig. 2.7 the different values are obtained when including different loss mechanisms.

***FF*$_0$:** Assuming a specific V_{oc} value and ideality factor the *FF* is reduced by a given amount and FF_0 is obtained as described by the empirical formula proposed by Green [Green 1983], for the *FF* free of R_s, R_{sh} and the recombination current J_{02} based on the two-diode model (see Eq. 2.4, p. 32). Here n is the ideality factor for the one-diode model, k is the Boltzmann

constant, T is the absolute temperature and q is the elementary charge.

$$FF_0 = \frac{v_{oc} - \ln(v_{oc} + 0.72)}{v_{oc} + 1} \quad \text{with } v_{oc} = \frac{V_{oc}}{n k_B T / q} \tag{2.7}$$

The different loss mechanisms were also analyzed by Khanna *et al.*, yet in a more analytical way [Khanna 2013].

***iFF*:** Adding now the contribution of the recombination losses J_0 and the R_{sh} leads to the *iFF* which is accessible by PCD measurements as described in section 2.2.2.2 (p. 32). This measurement, being a non-contact measurement, is still free from losses related to R_s and *iFF* is determined by the internal voltage.

***pFF*:** Advancing one more step in Fig. 2.7 and measuring now the finished device by suns-V_{oc} by contacting it, gives access to the *pFF* determined by the external voltage. Yet, in this measurement it is only the voltage of the device that is measured and no current is flowing (see also section 2.2.2.3, p. 33). This means that the R_s is still not taken into account.

***FF*:** Finally, measuring the device with any standard *J-V* setup includes all the losses in *FF* and the final value is obtained.

3 Silicon oxide layers

Highlights

In the first part of this chapter we discuss the properties of intrinsic amorphous silicon suboxides [a-SiO_x:H(*i*)] and their impact on cell performance when applied in combination with a-Si:H(*i*) as passivating layer. Besides bearing the potential to increase the J_{sc}, we show that a-SiO_x:H layers can severely deteriorate the *FF* values at 25 °C due to a transport barrier for holes that we link to increased valence band offsets (VBO) by numerical simulation. Recently this has been confirmed also experimentally by measurements of the band offsets [Liebhaber 2015]. However, despite the induced drop in *FF*, we evidence a positive temperature coefficient for the *FF* and hence a beneficial effect on the efficiency's temperature coefficient (TC_η). We observe an overall TC_η of −0.1 %/°C, which—compared to the −0.3 %/°C obtained for our reference—results in a superior high temperature performance (for temperature effects see also chapter 4, p. 63). It has to be noted that the difference to the −0.21 to −0.23 %/°C reported in literature [Mishima 2011, Bätzner 2011b] is less pronounced.[1]

The second part discusses the impact associated with the asymmetry of the band offsets inherent to a-Si:H/c-Si interfaces, the offset encountered by holes in the valence band being larger than the one for electrons in the conduction band. For this, we use similar passivation layers as discussed in the first part as these layers can be fabricated with intentionally exacerbated band offset asymmetry. Investigating all topologically possible permutations of these passivation layers, we conclude that to avoid *FF* losses, holes should ideally not be collected through wide-bandgap materials. SHJ devices featuring wide-bandgap window-layers may therefore benefit from hole-collection at the rear. This contrasts with *p-i-n* thin-film devices, for which the combined facts of asymmetry in mobility and drift-driven carrier collection dictates the polarity of the device, namely requiring hole collection at the front.[2]

[1] Parts of this first part are reproduced with permission from [Seif 2014b]. Copyright 2014, AIP Publishing LLC.
[2] This study was done in collaboration with D. Menda (Yıldız Technical University, Turkey).

3.1 Introduction

As discussed in the section 1.2.2.3 (p. 13), one of the limiting factors to the performance of a SHJ solar cell, is parasitic light absorption, *i.e.* absorption within layers from which charge carriers are not efficiently collected [Holman 2012]. Instead of using a material with an indirect bandgap as will be discussed for microcrystalline layers in chapter 6 (p. 99), another well-known strategy to solve this problem is the application of wide-bandgap silicon alloys. These materials show higher transparencies and hence reduced parasitic losses. In the past this was already pursued by several groups and authors and applied to different cell technologies including thin-film devices as window-layers or intermediate reflectors [Sichanugrist 1994, Cuony 2010, Smirnov 2010, Lambertz 2011, Cuony 2012] or in SHJ devices as passivation layers or window-layers as well [Ding 2012, Mueller 2012, Mazzarella 2015].

In a-Si:H/c-Si heterojunction devices, the differences in both bandgap and electron affinity of the different materials, give rise to band offsets in both the electron-conducting conduction band (conduction band offset, CBO: ΔE_c = 0.13–0.28 eV) and the hole-conducting valence band (valence band offset, VBO: ΔE_v = 0.3–0.45 eV) as depicted in Fig. 3.1 [Schulze 2011, Korte 2011, Liebhaber 2015]. Increasing the bandgap of the amorphous layer will have an effect on these band offsets. Notably, for the a-SiO_x:H layers investigated here, the increase in bandgap influences mainly the VBO, while the CBO remains unaffected [Liebhaber 2015], which is likely a fundamental feature of most wide-bandgap materials. These band offsets represent barriers to the charge carriers that have to be either surmounted (thermionic emission) or crossed (tunneling) in order for the carriers to be collected efficiently. Hence, besides their beneficial optical properties—enabling higher J_{sc} values—these wide-bandgap materials can have severe effects on transport, which also raises the question what the ultimate polarity of a SHJ solar cell may be, *i.e.* hole collection at the front or rear.

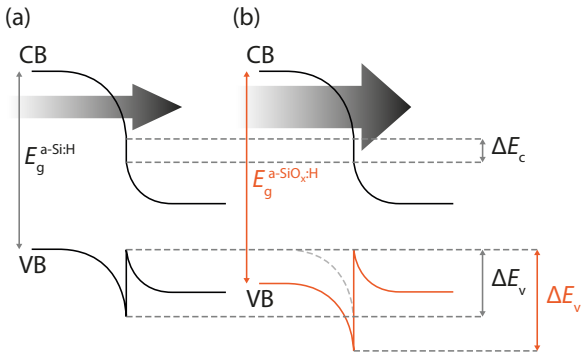

Figure 3.1 – Schematic showing the band structure with the band offsets (CBO: ΔE_v and CBO: ΔE_c) present at the hetero-interface between (a) a-Si:H or (b) a-SiO_x:H with c-Si for the hole-collecting side. The arrows indicated the amount of light transmitted through the amorphous layers.

3.2 Experimental details

The device results discussed in this study were obtained for our standard 2×2 cm^2 cells (see section 2.1.5, p. 27) with the structure depicted in Fig. 3.2. Note that we used either a-Si:H(*i*) or stacks of both a-Si:H(*i*)/a-SiO$_x$:H(*i*) of approximately 5 nm on textured wafers (unless otherwise indicated). Besides this slight deviation from the standard process the remaining steps and layers were according to what is described in section 2.1 (p. 23). For this study, the a-Si:H and a-SiO$_x$:H layers were all deposited at 200 °C in the Octopus I (see Tab. 2.1, p. 25) with all the chambers powered at 13.56 MHz. In addition to the standard gases (see section 2.1.2.1, p. 24), carbon dioxide (CO_2) was used as oxygen source. The layers implemented into devices were co-deposited on both wafers and glass samples for layer characterization. After PECVD, the effective minority-carrier lifetimes (τ_{eff}) of the cell precursors were measured and the implied V_{oc} (iV_{oc}) was extracted [Sinton 1996] (see section 2.2.2.2, p. 32).

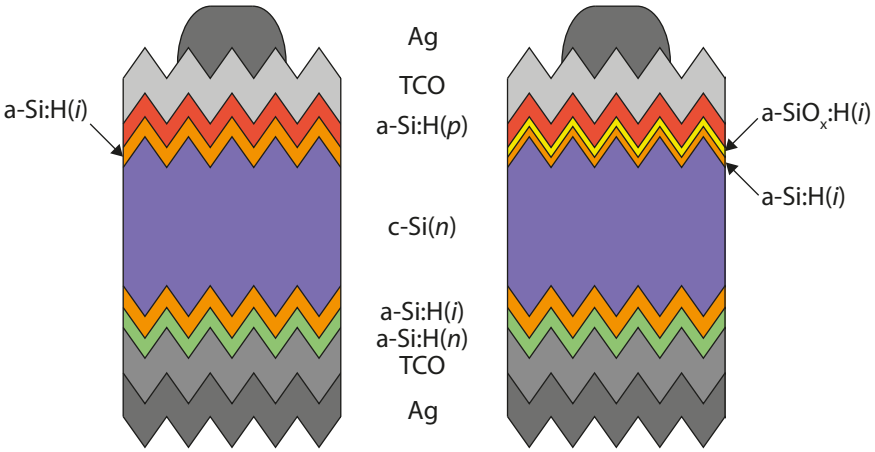

Figure 3.2 – Schematic of reference cell (all a-Si:H) and cell with a stack of a-Si:H and a-SiO$_x$:H at the front (*p*-side).

The cells presented in 3.3 (p. 40), were characterized using standard (AM1.5g) *J*-*V* measurements at ambient or higher temperatures (up to the setup limit of 55 °C). Furthermore, for the samples in this first part, systematic optical characterization was performed to determine EQE, R and IQE. The devices presented in section 3.4 (p. 54) were measured as function of temperature (up to 85 °C) with a different but similar *J*-*V* setup, both in dark and at one-sun illumination.

SE was used to characterize the layers that were co-deposited on glass or on polished wafers and extract both optical but also bulk properties (see section 2.2.1.1, p. 27). Here we chose to extract the optical bandgap defined as E_{04} as it is more representative for alloyed materials. This definition relies on the absorption coefficient (α) and is the energy at which $\alpha = 1 \times 10^4$ cm^{-1}. Furthermore, unless stated differently, the layer thicknesses refer to the thicknesses on a textured wafer, *i.e.* the thicknesses measured on a flat substrate (glass) divided by a geometrical factor of 1.7 [De Wolf 2012b].

Thermal desorption spectroscopy (TDS, see section 2.2.1.6, p. 29) was used to investigate the bonding configuration of hydrogen within a-SiO_x:H(*i*) passivation layers.

Additionally, we used Fourier transform infrared spectroscopy (FTIR) in perpendicular transmittance mode to verify the presence of oxygen for an approximately 95-nm-thick layer. This was done by analyzing the modes of silicon-oxygen bonds centered at around 1000 cm^{-1} and 1150 cm^{-1} [He 2000] as well as the mono-hydride and multi-hydride modes at 2010 cm^{-1} and 2100 cm^{-1}, respectively [Jousse 1985].

3.3 Amorphous silicon suboxides for silicon heterojunction solar cells

3.3.1 Results and discussion

3.3.1.1 Passivation properties of a-SiO_x:H(*i*)

To evaluate the passivation and optical properties of a-SiO_x:H(*i*) films, double-side polished (DSP), (100)-oriented, 300-μm-thick phosphorus-doped wafers with a resistivity of 4 Ω cm were passivated by 16-nm-thick layer stacks deposited on both sides. These stacks consisted of a very thin a-Si:H(*i*) layer (~ 2 nm, from ellipsometry), on which an a-SiO_x:H(*i*) layer of varying composition was deposited. This was done since direct deposition of a-SiO_x:H(*i*) layers on the wafer surfaces systematically resulted in poor passivation. In the remainder of this chapter (section 3.3 and section 3.4), the presence of such thin a-Si:H(*i*) layers is implicitly assumed for the a-SiO_x:H(*i*) devices and we refer to this stack as *i*-layer (or also *I* in section 3.4). The effective minority-carrier lifetime (τ_{eff}) of each passivated sample was measured both in the as-deposited state as well as after annealing at 200 °C for 100 min in air (Fig. 3.3). The approximate effective surface recombination velocity (S_{eff}) was calculated from the following equation for τ_{eff} (with wafer thickness W):

$$\frac{1}{\tau_{eff}} = 2\frac{S_{eff}}{W} \tag{3.1}$$

Equation 3.1 assumes symmetric passivation at the front and rear surfaces and a bulk lifetime of $\tau_{bulk} \rightarrow \infty$. Excellent as-deposited lifetimes of $\tau_{eff} > 5$ ms ($S_{eff} < 3$ cm s^{-1}) are obtained across the entire input gas flow ratio range. Samples passivated by silicon-rich films show a clear further improvement in passivation upon low-temperature annealing, which represents a well-known phenomenon for pure a-Si:H films [De Wolf 2008]. The samples fabricated with $[CO_2]/[SiH_4]$ gas flow ratios higher than 0.8 show a slightly lower τ_{eff} and a smaller increase in passivation quality upon annealing compared to the samples fabricated at lower $[CO_2]/[SiH_4]$ gas flow ratios (Fig. 3.3).

One possible explanation for this slight drop in passivation quality may be the increasingly

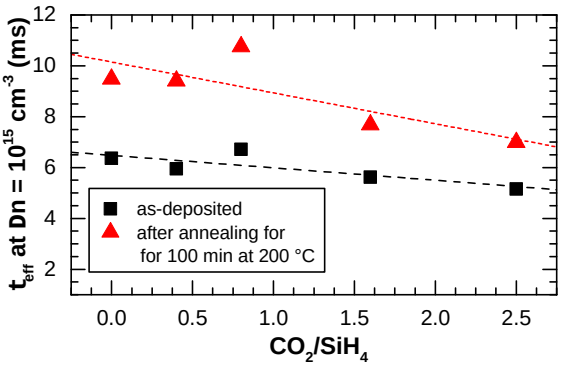

Figure 3.3 – Effective minority-carrier lifetimes (at an excess carrier density of $\Delta n = 10^{15}$ cm^{-3}) before and after annealing for 100 min at 200 °C in air for *n*-type float-zone wafers passivated with approximately 16-nm-thick a-Si:H(*i*)/a-SiO$_x$:H(*i*) stacks deposited with different [CO_2]/[SiH_4] input flow ratios. The trend lines are guides for the eye. Reproduced with permission from [Seif 2014b]. Copyright 2014, AIP Publishing LLC.

porous character of the layers. An indication of such porosity was observed by TDS measurements on layers deposited directly, without a thin a-Si:H(*i*) layer, on DSP wafers (Fig. 3.4). For pure a-Si:H films, typically a high- and a low-temperature H_2 desorption peaks are present and are usually taken, respectively, as signatures for the release of H_2 from mono-hydrides and for the presence of hydrogenated voids in the material [Gupta 1988, Beyer 1991]. Here, for an increasing [CO_2]/[SiH_4] input flow ratio, a clear decrease of the high-temperature peak signal and a simultaneous increase of the low-temperature peak signal is observed, pointing to increased porosity. Similar results have been reported by Einsele *et al.* [Einsele 2012], who show an increasing low-temperature peak with increasing oxygen-content. They also correlate their TDS results with FTIR measurements, with which they could show that an increasing oxygen content indeed changes the layer's microstructure significantly. For higher oxygen contents, they observed an increase in the stretching mode at 2100 cm^{-1}, which is attributed to hydrogen-terminated voids in the material [Cardona 1983, Wagner 1983]. According to Refs. [Schulze 2010] and [Zhao 2010], termination with higher hydrides, which is related to a higher void fraction and defect density, is less favorable for passivation, which explains our results in Fig. 3.3. Besides extracting information about the porosity, the TDS data were also used to study the hydrogen content in the layers. To do this, the H_2 effusion signals (normalized to the volume of the respective layers) shown in Fig. 3.4(a) were integrated from 200 to 800 °C. An increase of [CO_2]/[SiH_4] input flow ratio from 0.4 to 2.5 results in a relative increase in hydrogen content in the layer of 22.5% relative [Fig. 3.4(b)].

3.3.1.2 Optical properties of a-SiO$_x$:H(*i*)

Fig. 3.5(a) shows the evolution of *n* and *k* obtained from SE measurements for an increasing [CO_2]/[SiH_4] input flow ratio. Both parameters decrease, while E_{04} [Fig. 3.5(b)] increases [Ding 2013a]. These effects can be attributed to the increased incorporation of either oxygen

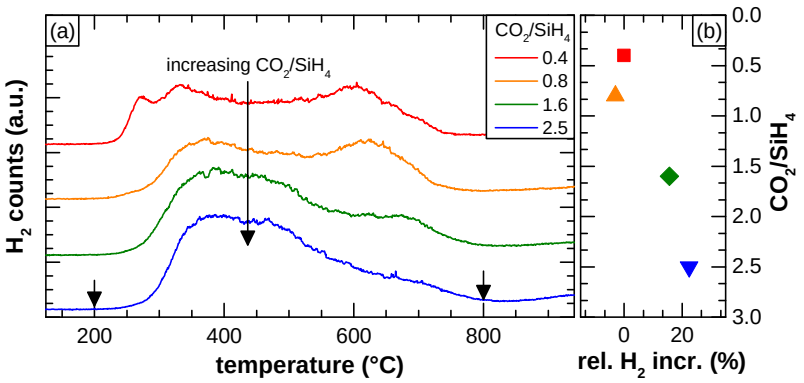

Figure 3.4 – (a) TDS data of H_2 ($m/z = 2$) taken for a-SiO_x:H(*i*) layers deposited directly on polished wafers, *i.e.*, without an a-Si:H(*i*) layer beneath. The measurements were normalized to the volume of the corresponding layer and the curves are offset for clarity. The arrows indicate the range used for integration (200—800 °C). (b) Relative H_2 increase for the layers shown in (a), normalized to the layer deposited with $[CO_2]/[SiH_4]$= 0.4. Reproduced with permission from [Seif 2014b]. Copyright 2014, AIP Publishing LLC.

[Knights 1980] or hydrogen into the silicon matrix (and the associated increase in the void fraction in the layer) [Cuony 2012, Iftiquar 1998, Kageyama 2011, Schulze 2011, Smets 2012]. For our films, both effects likely contribute. With the findings reported in by Schulze *et al.* [Schulze 2011] and the assumption that the trends reported there are also valid for the E_{04} value, we calculated the change in bandgap one would expect from the increase in hydrogen extracted from the TDS data.

We used the bandgap E_{04} = 2.04 eV of the a-SiO_x:H layer deposited at $[CO_2]/[SiH_4]$ = 0.4 as a starting point; this corresponds to approximately 26.8% of hydrogen (atomic). Compared to the standard a-Si:H layer (E_{04} = 1.98 eV), this represents already an increase of approximately 6.4% of hydrogen (atomic) [Schulze 2011]. The 22.5% relative increase from $[CO_2]/[SiH_4]$ = 0.4 to 2.5 (obtained from TDS, see section 3.3.1.1, p. 40) amounts to approximately an additional 5.9% of hydrogen (atomic). However, based on the findings by Schulze *et al.* [Schulze 2011], this is not quite sufficient to explain the total increase of E_{04} to 2.12 eV (measured for the a-SiO_x:H layer deposited at a flow ratio of $[CO_2]/[SiH_4]$ = 2.5), as it leads to an increase of only 60 meV to 2.10 eV. Thus, we attribute the remaining difference between the calculated and measured E_{04} values, of 20 meV, to the effect of the oxygen content in the layer, which we believe to be considerably lower than that of hydrogen.

The incorporation of oxygen into an approximately 94-nm-thick layer deposited on a DSP (100)-oriented wafer at a $[CO_2]/[SiH_4]$ gas ratio of 2.5 was confirmed by FTIR measurements. In contrast to our standard *i*-layers [Geissbühler 2013] we observed a significantly higher absorbance for the mode centered around 2100 cm^{-1} compared to the mode at 2000 cm^{-1} (Fig. 3.6). This points to more hydrogen-terminated voids, which confirms our results obtained from TDS. Note that compared to the standard a-Si:H(*i*) layer, the spectrum for the a-SiO_x:H(*i*) layer exhibits additional peaks at higher wavenumbers [SiH(O3), SiH_2(O2), and SiH_2(SiO), Fig.

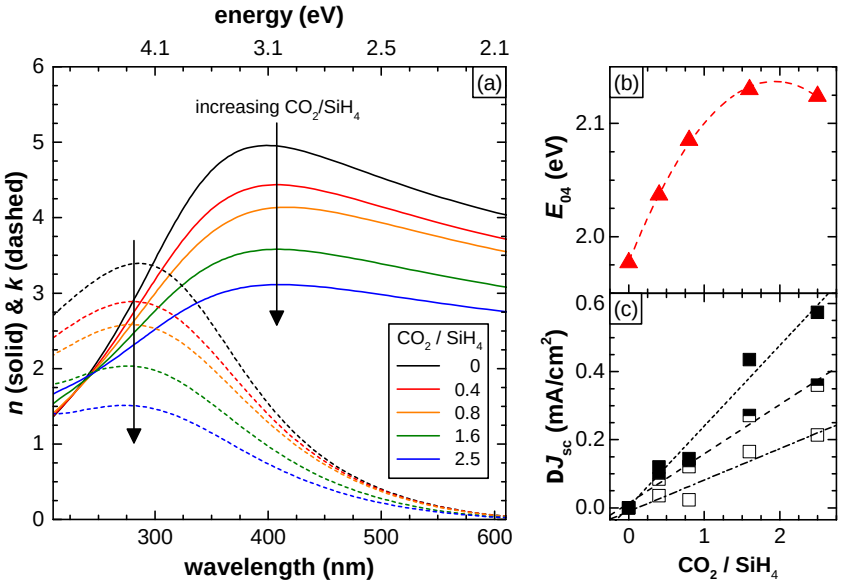

Figure 3.5 – (a) Refractive index n (solid) and extinction coefficient k (dashed) of a-Si:H(i)/a-SiO$_x$:H(i) stacks as a function of the wavelength and energy for layers deposited with increasing [CO_2]/[SiH_4] input flow ratios (direction indicated by arrows). (b) Optical bandgap E_{04} extracted from SE and (c) calculated gain in current density between 300 and 600 nm (half-filled symbols), 600–1200 nm (open symbols) and the total gain (filled symbols), as a function of the [CO_2]/[SiH_4] ratio. Reproduced with permission from [Seif 2014b]. Copyright 2014, AIP Publishing LLC.

3.6]. These can be attributed to oxygen present in the layer [Niwano 1994]. Both the increasing amount of hydrogen and—for our case, to a minor extent—oxygen may lead to an increasing VBO [Bacioğlu 2005, Schulze 2011, Liebhaber 2015]. This can explain the significant effect on carrier collection we observe in our devices, which is discussed in section 3.3.1.3 (p. 46).

To assess the potential current gain (ΔJ_{sc}) that can be expected with such wider bandgap films, we used the n and k values as input for OPAL (version 1.2 & 1.3) [Baker-Finch 2010] simulations. The parasitic absorption in a device-relevant stack of ITO (70 nm, carrier density of 6.1×10^{20} cm^{-1}), a-Si:H(p) (6 nm) and a-Si:H(i) or a-SiO$_x$:H(i) (6 nm) on a textured wafer was calculated for different oxygen contents. We then determined an equivalent short-circuit current density (J_{eq}) lost through parasitic absorption in the three front layers by integrating the product of absorption and photon flux (standard AM1.5g spectrum) from 300 to 600 nm and 600 to 1200 nm. We chose this set of wavelength ranges to assess the effect on the entire range of interest (300–1200 nm), but for shorter and longer wavelengths separately. We thereby obtained a potential total gain of up to 0.81 mA cm^{-2} (300—600 nm: 0.51 mA cm^{-2}, 600—1200 nm: 0.31 mA cm^{-2}) for a layer deposited at a [CO_2]/[SiH_4] ratio of 2.5. However, taking into account that 30% of the carriers generated in the i-layer are collected [Holman 2012]—assuming that this is also the case for a-SiO$_x$:H(i) layers—the effective gain in current is by a factor of 0.7 lower, namely ~ 0.57 mA cm^{-2} [300—600 nm: ~0.36 mA cm^{-2}, 600—1200 nm: ~0.22 mA cm^{-2}, Fig. 3.5(c)]. We attribute this gain to an increase of the optical bandgap [Fig.

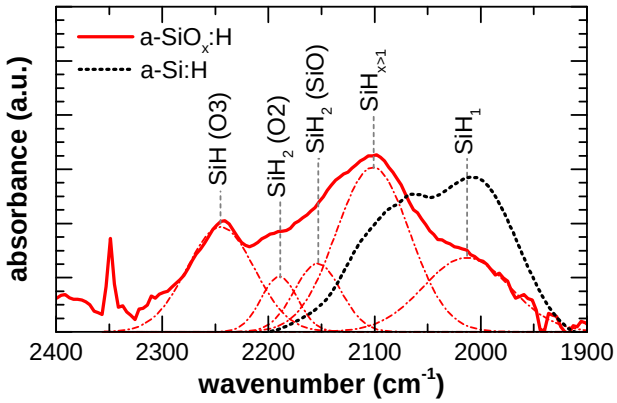

Figure 3.6 – Comparison of FTIR spectra (raw data). The dotted black line shows the spectrum taken for the standard a-Si:H(*i*) layer (7 nm, measured in attenuated total reflection configuration, taken from [Geissbühler 2013]) whereas the solid red line refers to a 95-nm-thick layer of a-SiO$_x$:H(*i*) (measured in transmission mode, thus the need for a thick layer). The dashed-dotted lines represent the peaks used for fitting the a-SiO$_x$:H data. See [Niwano 1994] for more details on the oxide-related peaks. Reproduced with permission from [Seif 2014b]. Copyright 2014, AIP Publishing LLC.

3.5(b)] and a change in reflectance [*R*, see Figs. 3.9(b), 3.9(d) and 3.8]. The latter was also extracted from the same set of simulation data and shows a decrease especially between 300—400 and 600—1200 nm in both experiment (Fig. 3.8) and simulation (Fig. 3.7). This decrease is more pronounced for higher [CO_2]/[SiH_4] ratios and thicker layers, and is caused by the low-*n* a-SiO$_x$:H layer, which acts like an additional anti-reflection coating between the TCO and the silicon.

In a next step, we fabricated solar cells and implemented either standard a-Si:H(*i*) (both sides, standard cell) or a-SiO$_x$:H(*i*) (front only) passivation layers. We varied both the [CO_2]/[SiH_4] gas flow ratio and the layer thickness, and obtained a J_{sc} increase of approximately 0.43 mA cm^{-2} for ~ 6-nm-thick a-SiO$_x$:H passivation layer deposited at [CO_2]/[SiH_4] = 2.5, compared to the reference a-Si:H solar cell. Comparing the EQE and IQE data of both cells, the gain in the range of 300—600 nm is of 0.27 mA cm^{-2} while for the range 600—1200 nm we see a gain of 0.29 mA cm^{-2}, which amounts to a total gain of 0.56 mA cm^{-2}, which matches well the predicted value. The fact that the increase in current is a result of the widening bandgap and an anti-reflective effect is confirmed by these results from real devices [Figs. 3.9(a)–(d)]. While *R* at 400 nm is constant for the standard a-Si:H layers—which have nearly the same refractive index as c-Si—as their thickness is increased, we see a decrease in *R* for all of the a-SiO$_x$:H layers. This explains why at 400 nm the EQE of the cells with oxide layers shows only a weak thickness dependence [Fig. 3.9(b); parasitic absorbance increases but *R* decreases], whereas we see a strong dependence for the standard a-Si:H layers.

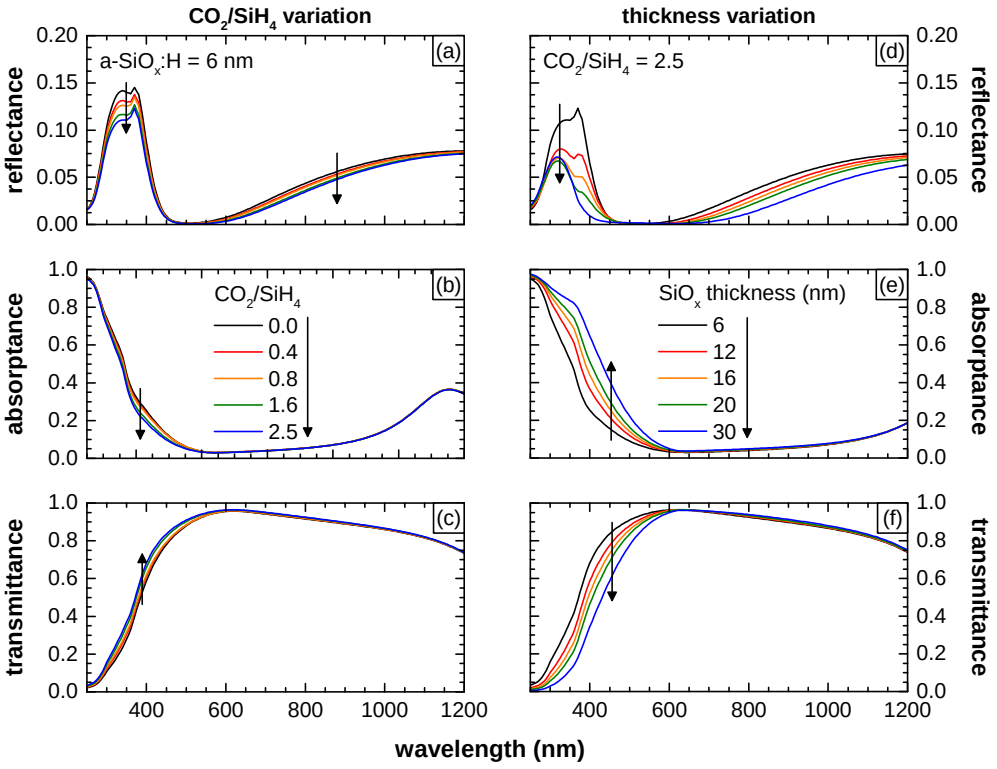

Figure 3.7 – Optical simulation results: (a)–(c) variation in $[CO_2]/[SiH_4]$ (fixed ITO and a-Si:H(*p*) thickness, a-SiO_x:H = 6 nm), (d)–(f) variation in a-Si:H(*i*)/a-SiO_x:H(*i*) thickness (for a layer with $[CO_2]/[SiH_4] = 2.5$). The arrows indicate the variation of the parameters reflectance, absorptance and transmittance of the layers as a function of the wavelength.

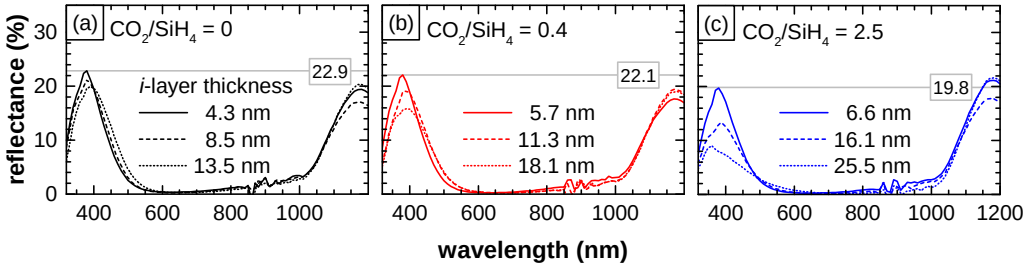

Figure 3.8 – Reflectance as function of the wavelength for the samples exhibiting layers of different thicknesses with a $[CO_2]/[SiH_4]$ ratios of (a) 0, (b) 0.4 and (c) 2.5.

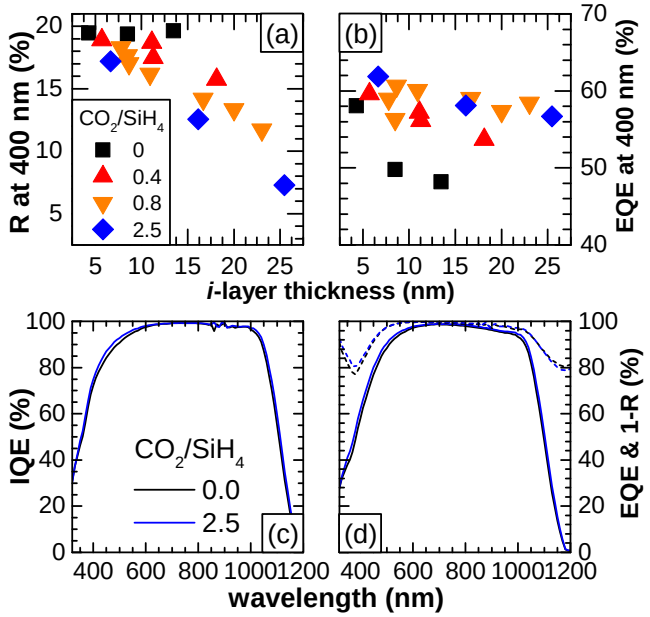

Figure 3.9 – (a) Reflectance and (b) EQE at 400 nm for different *i*-layer thicknesses (stack a-Si:H/a-SiO_x:H) and different $[CO_2]/[SiH_4]$ ratios. (c) and (d) IQE, EQE and 1-*R* as a function of the wavelength. Reproduced with permission from [Seif 2014b]. Copyright 2014, AIP Publishing LLC.

3.3.1.3 Application of a-SiO_x:H(*i*) in solar cells

Fig. 3.10 shows the illuminated *J*-*V* parameters of solar cells featuring a-SiO_x:H(*i*) passivation layers of various thickness and composition. Some of the *J*-*V* curves are s-shaped and the voltage measured at zero current (in some cases above 830 mV) exceeds the theoretical limit for c-Si [Tiedje 1984, De Wolf 2012b]. Hence, rather than reporting the one-sun V_{oc} values, we show the implied V_{oc} values obtained from lifetime measurements as an indication of the level of passivation. Also, in devices, the $[CO_2]/[SiH_4]$ ratio has only a minor influence on the passivation quality [Fig. 3.10(a)], which is high for all of the cells, as evidenced by the implied V_{oc} values in excess of 720 mV.

Note that for the devices exhibiting similar *i*-layer thicknesses below 7.5 nm, J_{sc} is not improved for the cells with a-SiO_x:H(*i*) layers [Fig. 3.10(b)], as would be expected from the EQE values at 400 nm [Fig. 3.9(b)]. This is due to similar or lower EQE values at longer wavelengths compared to the reference sample (thinnest *i*-layer), possibly either due to lower reflection or mere sample-to-sample variations. Hence, for those cells more light is lost in the red than gained in the blue part of the light spectrum, and the J_{sc} is slightly lower than the reference.

For devices with standard a-Si:H(*i*) layers, the *FF* shows a slight dependence on *i*-layer thickness. However, increasing the $[CO_2]/[SiH_4]$ ratio increases the *FF*'s sensitivity to thickness variations significantly, as can be seen in the different trends shown in Fig. 3.10(c). The decrease in *FF* with increasing $[CO_2]/[SiH_4]$ ratio is most likely due to the change in the band

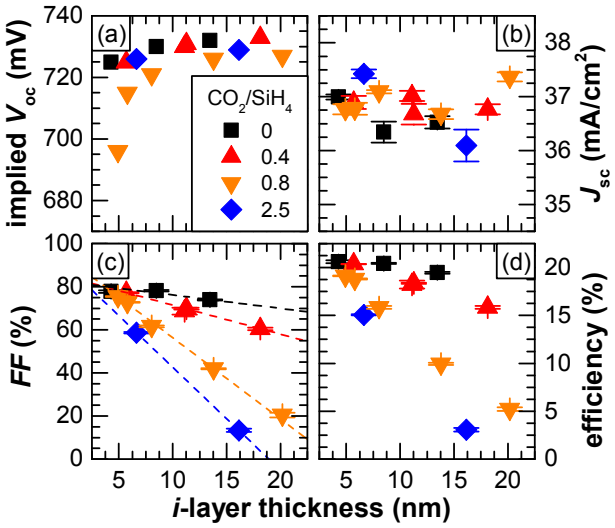

Figure 3.10 – (a) Implied V_{oc}, (b) J_{sc}, (c) *FF* (the dashed lines are linear fits to the data) and (d) cell efficiency as a function of the front *i*-layer thickness (on textured wafers). The data points represent the average of three cells on the same wafer. The error bars indicate the standard error of the mean. Note that the series at a $[CO_2]/[SiH_4]$ ratio of 0.8 featured a different batch of wafers, *i.e.*, different cleaning and texturization, than the others; hence the slight differences in implied V_{oc}. Reproduced with permission from [Seif 2014b]. Copyright 2014, AIP Publishing LLC.

offset at the interface [Schulze 2011] and is in agreement with findings by Shu *et al.* [Shu 2013] and to what is reported by Rath [Rath 2012]. Using simulations, they linked a decrease in *FF* to an increase in passivation layer bandgap. In our case, collecting the holes at the front, an increased VBO at the interface between the wafer and passivation layer may be especially detrimental, as the holes face a higher effective barrier than electrons at the conduction band offset (CBO), making their collection less efficient.

To assess the influence of this barrier on hole transport, we conducted *J*-*V*(*T*) measurements on a standard cell [a-Si:H(*i*) buffer, ~ 6 nm thick, Fig. 3.12(a)] and a cell with an a-SiO_x:H passivation layer [$[CO_2]/[SiH_4]$ = 0.8, ~ 6 nm thick, Fig. 3.12(b)]. When increasing the temperature from 25 °C to 55 °C, the V_{oc} decreases by roughly 50 mV for both cells due to an increase in dark saturation current density through the increase of the intrinsic carrier density (n_i). However, compared to the reference, the a-SiO_x:H cell shows a slightly lower absolute value of the relative change in V_{oc}, −0.22 %/°C instead of −0.25 %/°C. This is also discussed in more detail in chapter 4 (p. 63). Furthermore, besides this effect, the standard cell shows a decrease in *FF* of approximately 2% absolute, whereas the cell with an oxide layer recovers almost 2% for the same temperature range [Fig. 3.12(e)]. This improvement confirms earlier findings for wide-bandgap a-SiC:H passivation layers [Van Cleef 1998]. Due to a more favorable temperature coefficient for the efficiency of −0.1 %/°C (compared to −0.3 %/°C for the reference) in the investigated temperature range, the cell with an implemented oxide passivation layer shows an efficiency which, at high temperatures—those closer to real working conditions in the field—is superior to the reference shown here exhibiting the standard cell design (Fig. 3.11).

At 55 °C, the cell with an oxide passivation layer exhibits an efficiency of 18.0% (18.6% at 25 °C), compared to 17.7% (19.6% at 25 °C) obtained from the reference cell. Yet it is noteworthy, that comparing the a-SiO_x:H device to the calculated values—assuming a TC_η of −0.2 %/°C as reported in [Bätzner 2011a]—the two trends do not cross at temperatures below 60 °C. Measurements up to higher temperatures will be discussed in section 3.4, p. 54.

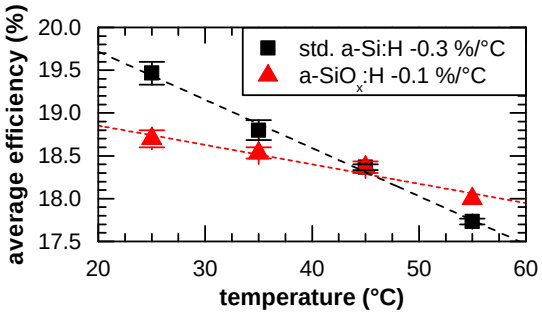

Figure 3.11 – Efficiency as a function of the temperature of a standard cell with a-Si:H(*i*) passivation layers [see Fig. 3.12(a)] and a cell with an a-SiO_x:H(*i*) passivation layer at the front [see Fig. 3.12(b)]. The trend lines represent linear fits to the data. The slopes of −0.056 %/°C and −0.023 %/°C represent the absolute changes in efficiency with temperature, which lead to TC_ηs of −0.3 %/°C and −0.1 %/°C, respectively [Kinoshita 2011]. Reproduced with permission from [Seif 2014b]. Copyright 2014, AIP Publishing LLC.

A similar effect has been reported in a simulation study by Rahmouni *et al.* [Rahmouni 2010], where thicker passivation layers lead to favorable temperature coefficients due to improving *FF*. However, in contrast to our findings for a-SiO_x:H layers, according to [Taguchi 2008], devices with thicker a-Si:H(*i*) passivation layers do not show a better performance at elevated temperatures. Their efficiencies stay below the efficiency of the reference device with a 3-nm-thick a-Si:H(*i*) layer.

3.3.1.4 Band offset simulations

To better understand the observed trends in *FF* for our devices, one-dimensional device simulations were carried out using the software packages *SunShine* [Krč 2003] and *ASPIN2* [Nerat 2009] for the optical and electrical models, respectively. To obtain the generation-rate profile throughout the cell, a 70-nm-thick front ITO layer (anti-reflective coating) and a 150-nm-thick rear ITO layer with 300 nm of Ag (rear reflector) were added. The simulations were done on flat layers, yet in order to simulate a textured wafer and match the measured J_{sc}, the reflection at the front was reduced by 17.5%. Furthermore, the *n* and *k* data of the relevant layers obtained from SE were used [Holman 2013c]. For electrical simulations, the surface defect density at both the front and rear a-Si:H/c-Si interfaces was set to 5×10^{10} cm^{-2} to match the measured V_{oc}. The parameters of the different materials were chosen as described in Tab. 3.1. We assumed the same electron affinity for all of the amorphous layers, *i.e.*, only the VBO [Schulze 2011] varied upon changing the bandgap of the a-SiO_x:H layer from 1.7 eV

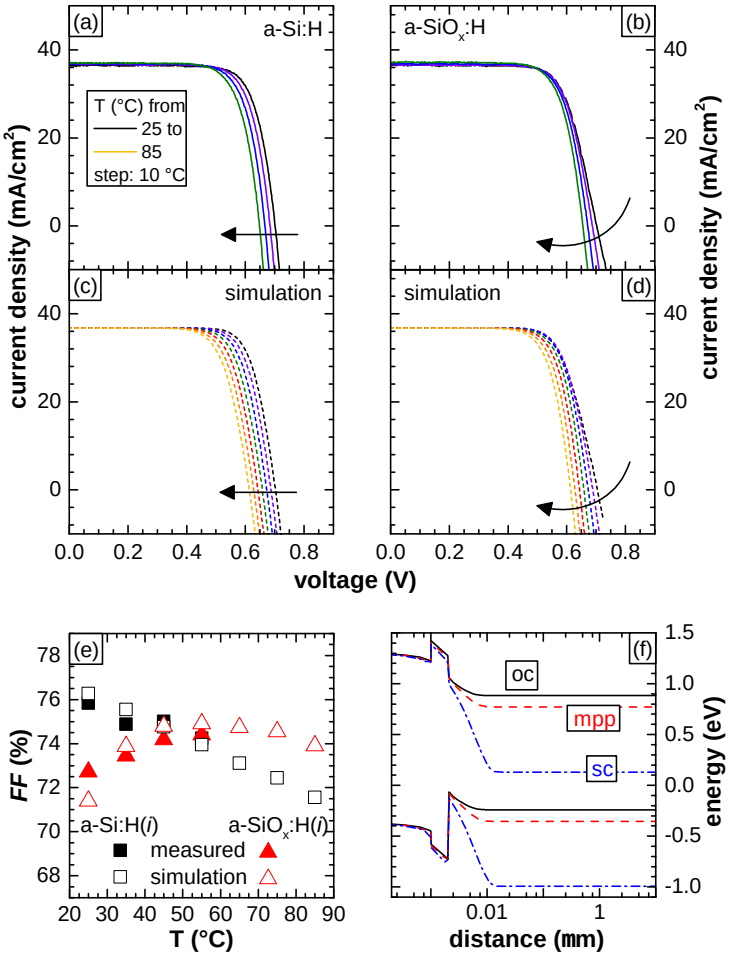

Figure 3.12 – (a), (b) *J-V* measurements (temperature: 25—55 °C in steps of 10 °C) and (c), (d) simulations (25—85 °C, in steps of 10 °C) for devices with an a-Si:H(*i*) or a-SiO_x:H(*i*) front passivation layer. The arrows indicate the increasing temperature and illustrate the different behaviors. (e) *FF* evolution with temperature (filled symbols: *J-V* measurements, open symbols: simulation) for both cells. (f) PC1D [Clugston 1997] simulation of the energy bands close to the a-SiO_x:H/c-Si interface in short-circuit (sc), at maximum power point (mpp) and in open-circuit (oc) conditions. Reproduced with permission from [Seif 2014b]. Copyright 2014, AIP Publishing LLC.

to 1.9 eV, whereas the CBO remained constant. This reflects the assumption we made that mainly the valence band is affected by changing the hydrogen content of the layer thereby widening the bandgap [Schulze 2011]. For simplicity, only thermionic emission across the barrier was included in the simulations; neither the temperature dependence of the bandgaps, Auger recombination, nor tunneling at the heterointerface was taken into account.

Figs. 3.12(c) and 3.12(d) show the simulated *J-V* curves (25—85 °C, step size of 10 °C) corresponding to the measured *J-V* curves in Figs. 3.12(a) and 3.12(b) (25—55 °C, step size of 10 °C). Remarkably, numerical simulations are in good agreement with experimental results, especially for the *FF* [Fig. 3.12(e)]. We therefore conclude that the drop in *FF* we observed

Table 3.1 – Parameters used for simulations of a standard cell with an a-Si:H passivation layer, and of a cell with an a-SiO_x:H front passivation layer.

parameter	a-Si:H(*p*)	a-Si:H(*n*)	a-Si:H(*i*)/a-SiO_x:H(*i*)	c-Si
thickness	10 nm	10 nm	8.5 nm	230 μm
bandgap (eV)	1.7	1.7	1.7 / 1.9	1.124
electron affinity (eV)	3.924	3.924	3.924	4.05
doping (cm^{-3})	1×10^{19}	1×10^{19}	0	1.2×10^{15}
e^-/h^+ mobility (cm^2/Vs)	10 / 2	10 / 2	10 / 2	1320 / 450

in cells with thin a-SiO_x:H passivation layers must indeed be a result of impeded hole collection due to a higher VBO [Rahmouni 2010, Lu 2011] which leads to an accumulation of holes [Rath 2012, Filipič 2013]. The effect, however, depends on the working point of the device and becomes more significant when moving from short-circuit to open-circuit conditions. In short-circuit conditions, there is strong band bending, as indicated in Fig. 3.12(f). Therefore, holes are easily collected across the junction thanks to a high electric field, and hole accumulation at the interface is kept low. However, moving towards open-circuit conditions, the bands flatten [Fig. 3.12(f)], and the accumulation of holes at the interface increases. It has been reported that this accumulation of holes at the interface can lead to a strong increase of recombination and thus to a reduction of the photocurrent [Anderson 1975] and eventually, in our case, of the *FF*. This has also been confirmed by Rath [Rath 2012], who links the accumulation of holes at the interface to a compensation of fixed negative charges and hence a reduction in internal fields. This effect is one possible explanation for the behavior we obtain for our devices.

The increase in *FF* with temperature observed for cells with a-SiO_x:H passivation layers points then to enhanced carrier transport, probably due to thermionic emission of the holes over the barrier at maximum power point. We remark that optimized standard devices are considered to operate in a carrier-diffusion-limited regime, very similar to homojunction devices [Taguchi 2008]. In the latter case, the decrease in *FF* with increasing temperature is a consequence of the temperature-induced drop in V_{oc}(see also 4, p. 63). And this will also have an influence on the *FF* [Green 1983] (Eq. 2.7, p. 36). The increase of the metallic contacts' line resistance with temperature plays only a negligible role due to the small resistivity temperature coefficient of silver.

In order to investigate further the influence of the VBO, we performed another set of simulations using the same model as described before (a-SiO_x:H cell, 3.1, p. 50). However, this time we varied the electron affinity [$q\chi_s$, Fig. 3.13(d)] of the a-SiO_x:H(*i*) passivation layer while keeping the other parameters fixed. Changing its value from 3.72 eV to 3.92 eV, both the CB and VB edge move down in energy and the VBO increases by 0.2 eV from (1) that of the reference cell to (2) that assumed for the oxide cell [Fig. 3.13(a)]. This has the same effect on the *FF* as we observed in our experiments when increasing the [CO_2]/[SiH_4] ratio and confirms that

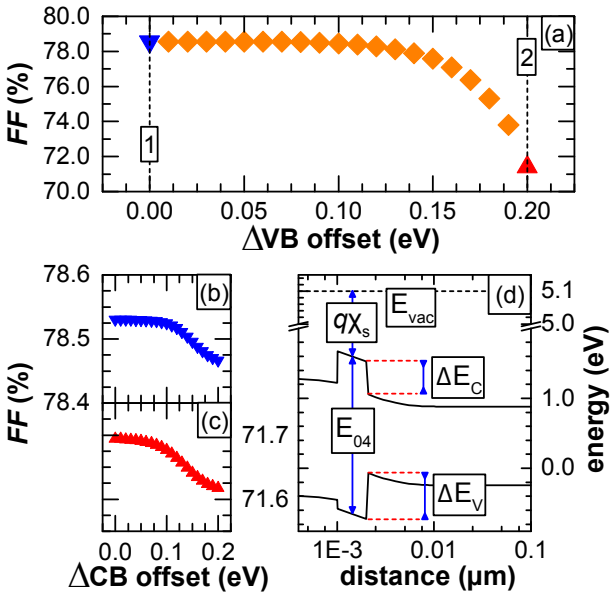

Figure 3.13 – (a) *FF* as a function of the change in VBO (variation of ΔE_V). At position (1), the VBO corresponds to the offset of the reference cell, whereas at position (2), it is approximately equal to the offset of the cell with an oxide passivation layer. (b) and (c) show the *FF* as a function of the change in CBO, keeping the VBO constant at positions (1) and (2), respectively. (d) Schematic band diagram illustrating the energies varied in the simulations (electron affinity $q\chi_s$ and vacuum level E_{vac}). Reproduced with permission from [Seif 2014b]. Copyright 2014, AIP Publishing LLC.

it is the VBO that hinders the carriers from being collected efficiently and that lowers *FF* at room temperature. To further underline this fact, two additional series of simulations were performed. This time the VBO was fixed to the values of positions (1) and (2) in Fig. 3.13(a) and the CBO was varied by changing both the electron affinity and the bandgap at the same time [Figs. 3.13(b) and 3.13(c)]. For both cases, the *FF* shows only a weak dependence on the CBO value. Therefore—even though an increase in CBO or additional effects lowering the *FF* cannot be excluded completely—we believe that it is the VBO which mainly limits carrier (hole) transport. This is corroborated by recent findings of Liebhaber *et al.* who could show that the VBO increases with increasing oxygen content [Liebhaber 2015], while the CBO remains unaffected.

3.3.2 Cell results

Combining our findings, and following further optimization, our best cell with an a-SiO_x:H passivation layer at the front ($[CO_2]/[SiH_4] = 0.4$) showed a V_{oc} of 716 mV, a J_{sc} of 37.1 mA cm^{-2}, a *FF* of 76.8% and an efficiency of 20.4% (Fig. 3.14, dashed line). These values are quite close to those of the reference cell in this experiment with a similar *i*-layer thickness, which reached a V_{oc} of 718 mV, a J_{sc} of 36.9 mA cm^{-2}, a *FF* of 78.5% and an efficiency of 20.8% (Fig. 3.14, solid line). Although the J_{sc} increased by approximately 0.2 mA cm^{-2} by using an

a-SiO_x:H(*i*) passivation layer, the cell efficiency at room temperature decreased due to an absolute reduction in *FF* of 1.7%. Based on our device simulations, this limitation is likely to be fundamental, where an increase in J_{sc} by opening the bandgap of the passivation or hole-collecting layer, and thereby increasing the VBO, is compensated by a drop in *FF* resulting from impeded collection of holes. The difference in TC_η obtained for the two devices (reference a-Si:H(*i*): $TC_\eta = -0.282\,\%/°C$; a-SiO_x:H(*i*): $TC_\eta = -0.278\,\%/°C$) is small and does not lead to a significant difference in the high-*T* behavior of the cells, *i.e.* the cells show the same trends and similar efficiencies.

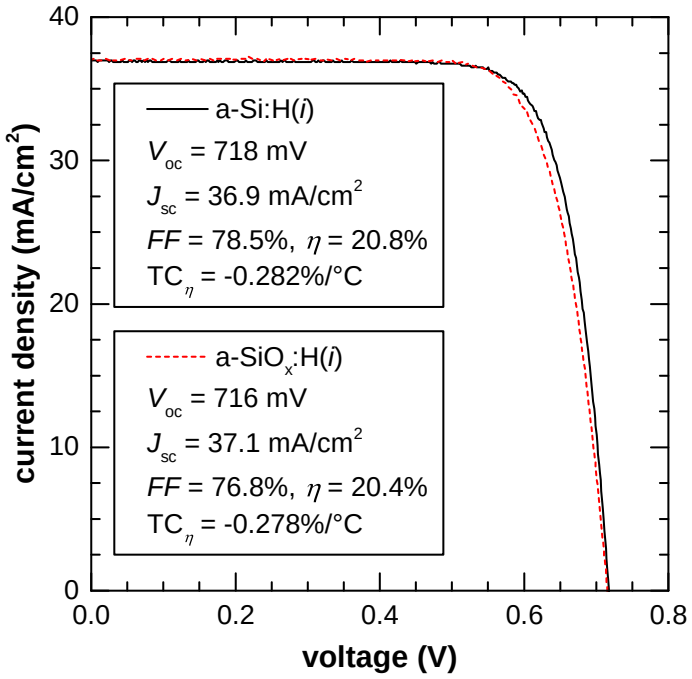

Figure 3.14 – Illuminated *J-V* measurements of our best 2×2 cm^2 cells in these experiments, measured in-house under standard test conditions (Wacom, Meyer Burger Research *J-V* setup). Reproduced with permission from [Seif 2014b]. Copyright 2014, AIP Publishing LLC.

3.3.3 Conclusion

We compared devices with a-SiO_x:H passivation layers at the front—beneath the a-Si:H(*p*) layer—to devices with standard a-Si:H passivation layers. No significant difference in passivation was observed and comparable iV_{oc} values in excess of 720 mV were obtained. An increase in bandgap and a simultaneous decrease in short-wavelength reflection were observed with oxide layers. Both lead to an increase in J_{sc} of up to 0.43 mA cm^{-2} for $[CO_2]/[SiH_4] = 2.5$. Despite this gain—at room temperature—the expected improvement in efficiency is more than compensated for by losses in *FF*. Using simulations, we linked the *FF* losses to an in-

creased VBO at the interface between the amorphous and crystalline phases, which results in a blockade for holes. This raises concerns whether wider bandgap window layers applied to the hole-collecting side of the device, offer potential for improved device performance. However, despite the losses in *FF*, the structure investigated here yields improved high-temperature performance, linked to a positive temperature coefficient for the *FF*. We note that, in many cases, the working conditions for a module in the field are actually in many cases far above room temperature. Hence, these layers may be applied to optimize devices for deployment in hotter climates. However, as we will see in the following section, this effect was not observed for all a-SiO_x:H-containing devices. Furthermore, it may be preferable to collect electrons at the window-layer side. In the next section (3.4, p. 54) this will be discussed in more detail.

Here we focused on the passivation layer and on silicon-based materials only. However, it is important to note that other classes of materials exist that may be used for the same purpose. Recently metal-oxides sparked a lot of interest and *e.g.* molybdenum-oxide has been proposed and applied successfully as hole-collecting layers in SHJ devices [Battaglia 2014, Bullock 2015]. With a bandgap in the range of 3.3 eV—which represents almost double the bandgap of a-Si:H—this material has the potential to completely avoid any parasitic absorption and impressive gains of 1.9 mA cm^{-2} were reported [Battaglia 2014].

3.4 Asymmetric band offsets in silicon heterojunction devices

3.4.1 Experimental details

The experiments described in this second part are based on devices with all topologically possible permutations for the passivation layers, namely implementing either front or rear hole collection in: (1) standard devices, or devices with an a-Si:H/a-SiO_x:H stack below (2) the a-Si:H(*p*) or (3) the a-Si:H(*n*) layer. The structures are depicted in Fig. 3.15 and were fabricated as described in section 3.2 (p. 39). For the layers applied in this study we fixed the $[CO_2]/[SiH_4]$ input gas flow ratio to 0.8 and applied identical a-Si:H(*i*)/a-SiO_x:H(*i*) stacks[3] to each of the devices shown in Fig. 3.15(c)–(f). On textured wafer the a-Si:H(*i*)/a-SiO_x:H(*i*) featured a thickness of ~6 nm. The layer thicknesses were again extracted from a Tauc-Lorentz multi-layer model used to fit SE data taken on planar glass samples. We systematically investigated the cells focusing mainly on light and dark *J*-*V* measurements as a function of the temperature (25—85 °C) and suns-V_{oc} measurements. For simplicity, the stack a-Si:H(*i*)/a-SiO_x:H(*i*) will be denoted by "*I*", so *e.g. ip*/*In* has an a-SiO_x:H(*i*) layer beneath the *n*-layer. The same applies for the *p*-side (*Ip*/*in*).

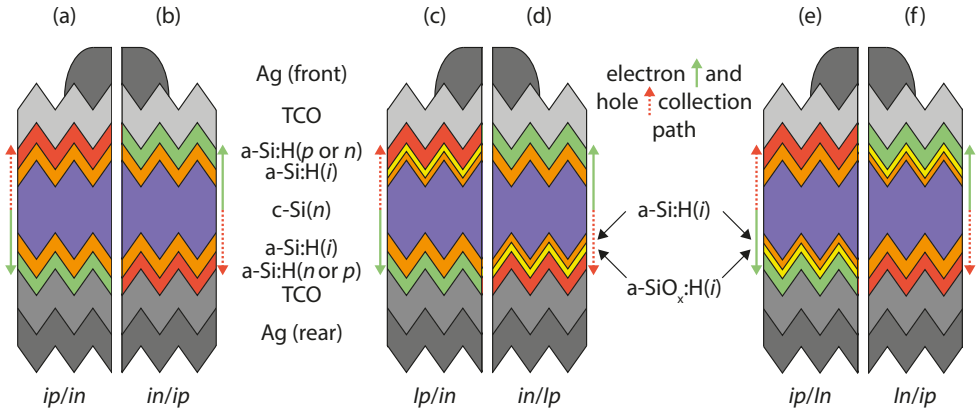

Figure 3.15 – Structure of devices with either front or rear hole collection investigated in this study: (a) and (b): all-a-Si:H devices; (c) and (d): devices with an a-SiO_x:H layer below the hole-collecting a-Si:H(*p*) layer; (e) and (f): devices with an a-SiO_x:H layer below the electron-collecting a-Si:H(*n*) layer. The arrows indicate the direction of the electron and hole flow.

3.4.2 Results and discussion

3.4.2.1 Cell parameters

The light *J*-*V* measurement performed at 25 °C yielded the values listed in Tab. 3.2. All the cells showed V_{oc}s above 700 mV, in particular also for the cells with a-SiO_x:H(*i*) passivation

[3] Again, we decided to stick to this structure due to low lifetime results with a-SiO_x:H directly on the wafer.

layers. For the *Ip*/*in* samples we observe a characteristic drop in *FF* (of approximately 10% absolute at 25 °C) associated with the insertion of an a-SiO_x:H(*i*) layer underneath the a-Si:H(*p*) layer, despite the fact that this passivation layer does not feature yet a sufficiently wide optical bandgap to yield any significant current gain.[4] The fact that we obtain much higher *pFF* values indicates already that this might be an effect linked to the R_s.[5]

Table 3.2 – Illuminated *J*-*V* parameters obtained at standard testing conditions. For the cell description: the stack on the left represents the front-side stack, while the stack on the right refers to the rear.

cell (Fig. 3.15)	**label**	V_{oc} [mV]	J_{sc} [mA cm^{-2}]	***FF*** [%]	**pFF** [%]	η [%]
ip/*in*	*ip*/*in*	726	36.5	76.9	83.6	20.3
in/*ip*	*in*/*ip*	721	36.6	77.0	82.6	20.3
a-SiO_x:H(*i*)*p*/*in*	*Ip*/*in*	719	36.9	66.9	83.2	17.7
in/a-SiO_x:H(*i*)*p*	*in*/*Ip*	701	36.7	65.6	82.5	16.9
ip/a-SiO_x:H(*i*)*n*	*ip*/*In*	724	36.6	76.6	83.4	20.3
a-SiO_x:H(*i*)*n*/*ip*	*In*/*ip*	719	36.4	75.4	82.4	19.8

The presence of this a-SiO_x:H layer results in the occurrence of an s-shaped *J*-*V* curve, which we link to a transport barrier for holes [Seif 2014b, Liebhaber 2015] which leads to an increasing trend in *FF* as we have seen in section 3.3 [Fig. 3.16(a)] [Seif 2014b, Chavali 2014, Rath 2012]. This contrasts with what is observed for the samples exhibiting an a-SiO_x:H(*i*) layer beneath the a-Si:H(*n*) layer [Fig. 3.16(b)] or the oxide-free reference samples [Fig. 3.16(c)]. These two types of samples show similar decreasing *FF* trends in temperature, and—in the case of the *ip*/*In* and *In*/*ip* samples—no overly pronounced transport barrier. This confirms that for the [CO_2]/[SiH_4] input gas flow ratio—determining the barrier (*e.g.* VBO) the holes encounter—and the layer thickness used here, electrons are still efficiently collected, whereas hole collection is impeded [Taguchi 2008]. Hence, in this case it would be beneficial to collect the holes at the rear, to avoid any collection issues while being able to benefit from the improved transparency of the a-SiO_x:H layers.

As we observe identical trends for both the devices with hole collection at the rear and devices with hole collection at the front, we focus on the latter in the remaining discussion.

A straight forward method to investigate the observed trend consists of fitting a two-diode model (see Eq. 2.4, section 2.2.2.1, p. 30) to our experimental light and dark *J*-*V* data. Here, we chose two diodes with fixed ideality factors (1 and 2 for the first and second diode, respectively). Fig. 3.16(a) shows an example of the resulting fits, enabling the extraction of the series

[4] As we have seen in the first part of this chapter (section 3.3, 40), the [CO_2]/[SiH_4] values has to be relatively high in order to be able to gain in current, which is not the case for the value chose for this study.

[5] We note that the *pFF* values for the devices with hole collecting at the rear show systematically smaller values than their counterparts with front-side hole collection. This can be explained by the fact that the three cells on each wafer were not isolated towards the measurement chuck. This is crucial for the measurement of this cell type, in order to avoid neighboring dark diodes.

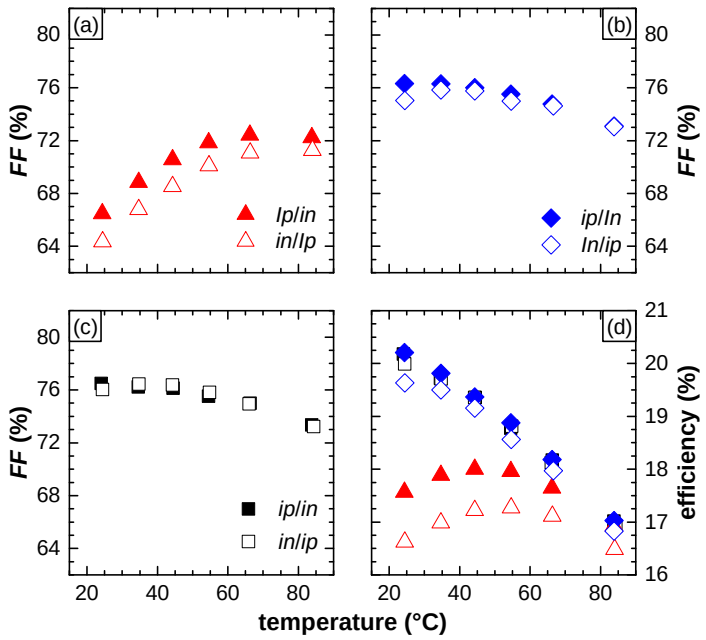

Figure 3.16 – Temperature dependence of the *FF* obtained from light *J*-*V* measurements on (a) *Ip*/*in*, (b) *ip*/*In* and (c) the standard *ip*/*in* devices (described in Fig. 3.15). (d) Efficiency for the cells shown in (a)–(c).

resistance (R_s) from both data sets, which qualitatively show the same trends [Fig. 3.16(b)].[6] Compared to the other samples, the $R_s$values extracted for the *Ip*/*in* device systematically show higher values but also a more pronounced decrease with temperature. This is explained by the exacerbated barrier for holes, its contribution to the series resistance, and the fact that it is overcome at higher temperatures. Yet, interestingly, we note that all our devices show this decreasing trend for their respective R_s values. This suggests, that carrier transport in *ip*/*in* and *ip*/*In* samples is negatively affected by some temperature-dependent contribution to the R_s—likely associated to a small barrier—as well. Since we do not observe any effect of the a-SiO_x:H(*i*) layer on the *n*-side, we suspect the determining barrier is also here to be found at the hole-collecting side. This is also in line with the larger VBO (> 0.3 eV) [Liebhaber 2015] than CBO (~0.13–0.28 eV) [Schulze 2011, Korte 2011]. Yet, we systematically obtain larger R_s values for the *ip*/*In* samples compared to the *ip*/*in* (+8% on average). Hence, an effect of the a-SiO_x:H layers on the electron collection cannot be excluded.

[6] Quantitatively there is a discrepancy between the R_s obtained from light and dark *J*-*V* at temperatures < 55 °C. This is linked to the increasingly s-shaped *J*-*V* curves for the *Ip*/*in* samples which are not reproduced accurately by the fit with a two-diode model. Therefore, in this temperature regime the absolute R_s values obtained from the dark *J*-*V* may be more reliable.

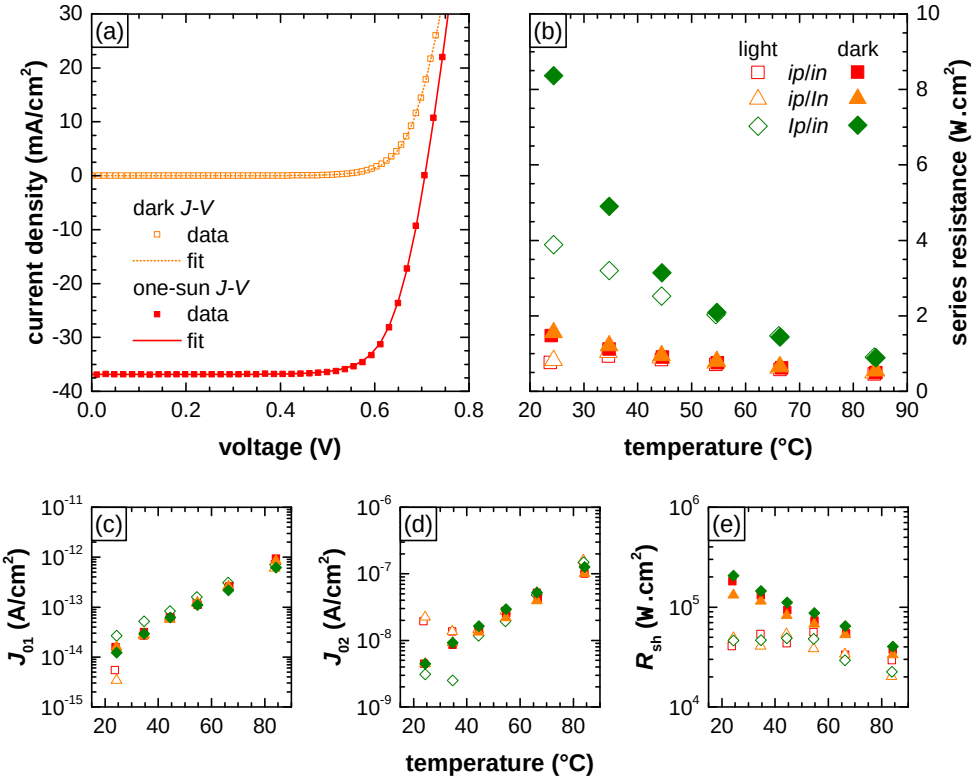

Figure 3.17 – (a) Example of fitted light and dark *J-V* data used to extract the series resistance (R_s) shown in (b) obtained from light *J-V* (Open symbols) and from dark *J-V* (filled symbols) fit. Fitting parameters (c) J_{01}, (d) J_{02} and (e) R_{sh}, from light and dark *J-V* fits.

3.4.2.2 Further dark *J-V* analyses

Keeping in mind what we discussed in section 3.4.2.1, in this section we compare different dark *J-V* analysis methods reported in literature to learn more about the impact of the applied wide-bandgap a-SiO_x:H and confirm the role of the R_s. First, we focus on the bias regime of 0.7–1 V to gain insights into the trap distribution of the amorphous layers [Rose 1955, Marsal 1996b] and finally we turn to the analysis of the local ideality factor [McIntosh 2001].

Bandtail width:

Currents in the high-bias regime were studied by Rose [Rose 1955], who found the following voltage dependence. Later, this formalism has been applied to a-Si:H/c-Si heterojunctions by Marsal *et al.* [Marsal 1996b].

$$J = K \cdot V^m \tag{3.2}$$

Here m is related to the trap distribution (the tail states) in the amorphous silicon layers—including the a-SiO_x:H—that exponentially decreases from the conduction band edge towards midgap. Furthermore, K is a parameter associated with the thickness of the amorphous layers, the trap distribution and the conductivity. The trap distribution is given by [Rose 1955, Marsal 1996b]:

$$g(E) = N_0 \exp\left(\frac{E - E_c}{k_B T_c}\right) \tag{3.3}$$

where N_0 is trap density at the exponential onset of the band tail and T_c is a characteristic temperature. The latter is linked to the m parameter via [Rose 1955, Marsal 1996b]:

$$m = 1 + \frac{T_c}{T} \tag{3.4}$$

Hence, extracting the slope of $m-1$ gives us access to the characteristic temperature T_c and energy $k_B T_c$. The latter scales with the Urbach energy and determines the width of the trap distribution, larger $k_B T_c$ values implying broader distribution [Rose 1955, Lampert 1964, Marsal 1996b, Marsal 1996a, Pallares 2006] (see Fig. 3.18).

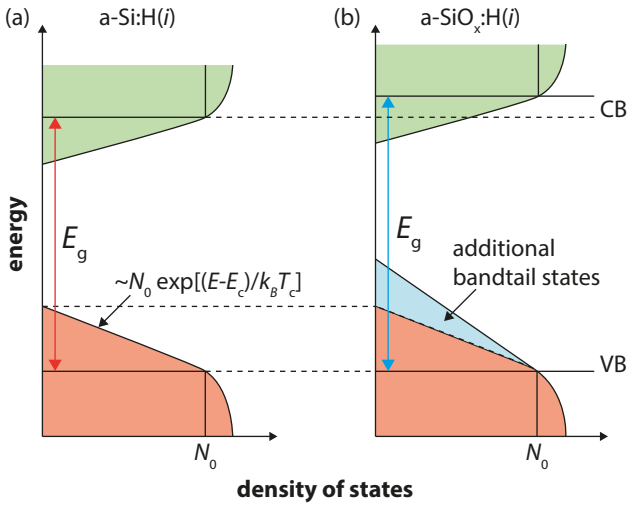

Figure 3.18 – Schematic of the band structure showing the (a) comparably narrow valence band tail of a-Si:H(*i*) and (b) the wider bandtail of a-SiO_x:H(*i*). E_g is the bandgap energy.

Based on Eq. 3.2, we apply a linear fit to the dark *J*-*V* data (log-log plot, not shown here) and extract the slope, which corresponds to the m value. From the $m(T)-1$ data we obtain $k_B T_c$ = 188 meV, 182 meV, and 478 meV, respectively for the *ip*/*in*, *ip*/*In*, and *Ip*/*in* samples [Rafiq 2005,

Xu 2012, Shao 2014]. Note that these values are by a factor of 2–4 too large compared to what is reported in literature [Shah 2010, Schulze 2010, Schulze 2011]. This overestimation of the Urbach energy may be explained by a scaling factor, which to determine will require further investigation. Nevertheless, we can conclude that for the case of an *Ip*/*in* structure, the effective trap distribution of the a-Si:H(*i*)/a-SiO_x:H(*i*) stack—encountered by the holes—is broader compared to the reference as schematically indicated in (Fig. 3.18). This corresponds to what is reported elsewhere, *i.e.* the fact that incorporation of oxygen into the amorphous layer can lead to the formation of voids in the film matrix [Einsele 2012, Seif 2014b] and hence can give rise to an increased trap density [Schulze 2010, Zhao 2010]. The fact that we do not see a broadening of the distribution for the *ip*/*In* device confirms earlier findings that the conduction band tail remains largely unaffected by the presence of oxygen or a surplus of hydrogen [Seif 2014b, Liebhaber 2015], characteristic for our a-SiO_x:H(*i*) layers.

In combination with a larger VBO this broader trap distribution may lead to the observed increase in R_s. The latter also explains the reduction in current within the R_s-dominated high-bias regime [Fig. 3.19(c)].

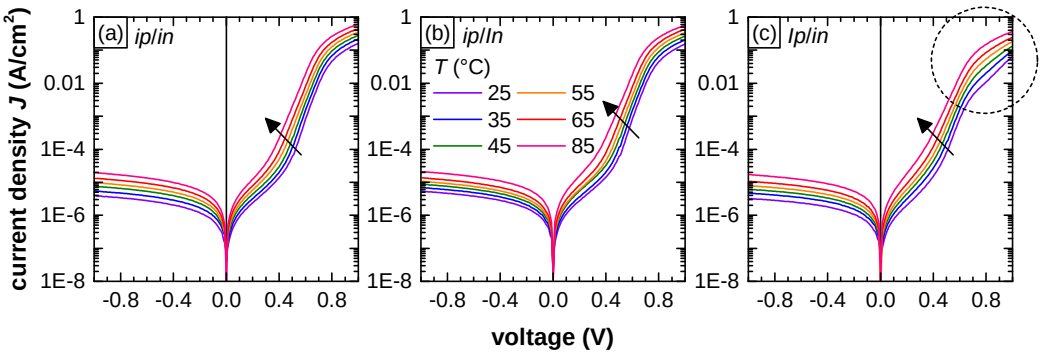

Figure 3.19 – Semi-log plot of the dark *J*-*V*(*T*) results for (a) the *ip*/*in*, (b) the *ip*/*In*, and (c) *Ip*/*in* device. The arrows indicate the temperature increase.

Local ideality factor n_{local}:

Finally, we turn to the analysis of the transport mechanisms with the help of the local ideality factor (n_{local}) as discussed by McIntosh [McIntosh 2001]. We use the dark *J*-*V* data shown in Fig. 3.19 and calculate the slope of the ln(*J*) curve with respect to the voltage. Assuming the following behavior for the current:

$$J = J_0 \exp\left(A(T)V\right) \tag{3.5}$$

$$\ln(J) = \ln(J_0) + A(T)\cdot V \tag{3.6}$$

Assume no voltage dependence of J_0 the slope of the ln(*J*) curve is directly given by $A(T)$ and

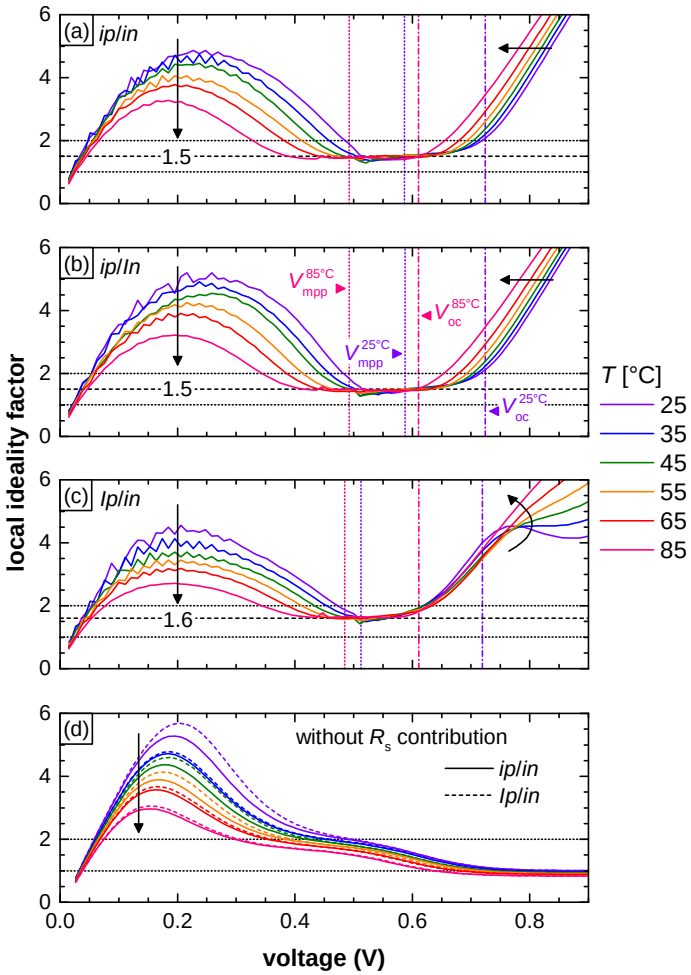

Figure 3.20 – Local ideality factor for various temperatures from 25–85 °C for the (a) *ip*/*in*, (b) the *ip*/*In* and (c) the *Ip*/*in* samples. (d) Local ideality factor without R_s for the same temperature range for the *ip*/*in* (solid) the *Ip*/*in* (dashed) samples. The dotted horizontal lines indicate the values 1 and 2, respectively. The vertical lines indicate the position of both the V_{oc} and V_{mpp} at the indicated temperatures.

n_{local} follows accordingly:

$$\frac{\partial \ln(J)}{\partial V} = A(T) = \frac{q}{n_{local} \cdot k_B \cdot T}, \text{ and hence} \tag{3.7}$$

$$n_{local} = \frac{q}{A(T) \cdot k_B \cdot T} \tag{3.8}$$

The results are shown in Fig. 3.20. Considering the *ip*/*in* and the *ip*/*In* samples [Figs. 3.20(a) and 3.20(b)], we observe a shift of the curves as indicated by the arrows, which is explained by an interplay of the dark saturation current densities J_{01} and J_{02} (two-diode model) as well

as R_s and R_{sh} [McIntosh 2001]. In fact we observe the following variations with increasing temperature (25–85 °C) for the parameters extracted from the dark *J-V* fits. Exponential increase for (J_{01}) ~1.5×10^{-14} to 1×10^{-12} A cm^{-2} and (J_{02}) ~4×10^{-9} to 1×10^{-7} A cm^{-2} and an exponential decrease for (R_{sh}) ~1×10^{5} to 4×10^{4} Ω cm^2. The variation of the different parameters are shown in Fig. 3.17(b)–(e).

Besides showing slightly higher n_{local} values (1.6 instead of 1.5) than the *ip*/*in* reference within the intermediate bias regime (0.4–0.6 V) and showing the same decrease of the peak at bias voltages <0.5 V [Fig. 3.20(c)], the *Ip*/*in* sample exhibits more significant differences at bias voltages between 0.6–0.75 V and an additional feature at voltages >0.75 V. The difference at intermediate bias voltages (<0.6 V) indicates increased recombination, whereas again, the features at higher bias are linked to the high R_s [McIntosh 2001]. This is also corroborated by the data shown in Fig. 3.20(d), where the local ideality factor for both the *ip*/*in* and the *Ip*/*in* device are plotted after removing the R_s contribution from the dark *J-V* data. Besides minor variations between 0.1–0.5 V, it shows almost identical behavior at higher bias and a collapse of the curve to values close to 1 for voltages >0.7 V, without any significant difference.

Double-diode signatures:

A similar analysis method compared to the local ideality factor was proposed by Van Cleef *et al.* [Van Cleef 1996]. Instead of considering n_{local} here it is $A(T)$ that is investigated. Hence, we merely look at the same data from a different perspective. The results are given in Fig. 3.21. For both the *ip*/*in* and the *ip*/*In* device the data features two distinct peaks centered around 0.55 V and 0.7 V (at 25 °C) indicating two different transport paths or diodes [see labels $A_{1,2}$ and $B_{1,2}$ in Fig. 3.21(a)]. From the T-dependence of the peak amplitude it is possible to determine the transport mechanism by extracting the ideality factors according to Eq. 3.7 (Fig. 3.21, right column). The ideality factor n_{local} is simply the inverse slope of $A(q/k_B T)$. The amplitude of peak A shows some temperature dependence, which can be associated with diffusion-limited transport. This is confirmed by n_{local} values obtained from this peak between 1.02 and 1.13.

The amplitude of peak B is temperature-independent, which leads us to conclude that it is associated with tunneling [Rath 2012, Van Cleef 1996]. However, this contrasts with earlier reports [Matsuura 1984, Taguchi 2008] where tunneling is attributed to the low-bias regime (< 0.5 V) and diffusion-dominated transport to the high-bias regime (0.4–0.8 V). This discrepancy with the literature is not clear yet and will have to be investigated further.

For the *Ip*/*in* device on the other hand, at 25 °C we observe only the peak associated with diffusion-limited transport. At 25 °C the second peak, lying in the bias regime between the V_{oc} and V_{mpp} for the other devices is missing completely. Yet, it starts reappearing at $T > 45$ °C. As argued before, this points to a R_s-limited transport. Besides the appearance of peak B, we also witness the disappearance of a third peak between 0.8 and 1 V [denoted by C in Fig. 3.21(c)] and which is the same R_s-related feature as we discussed before with the help of n_{local}.

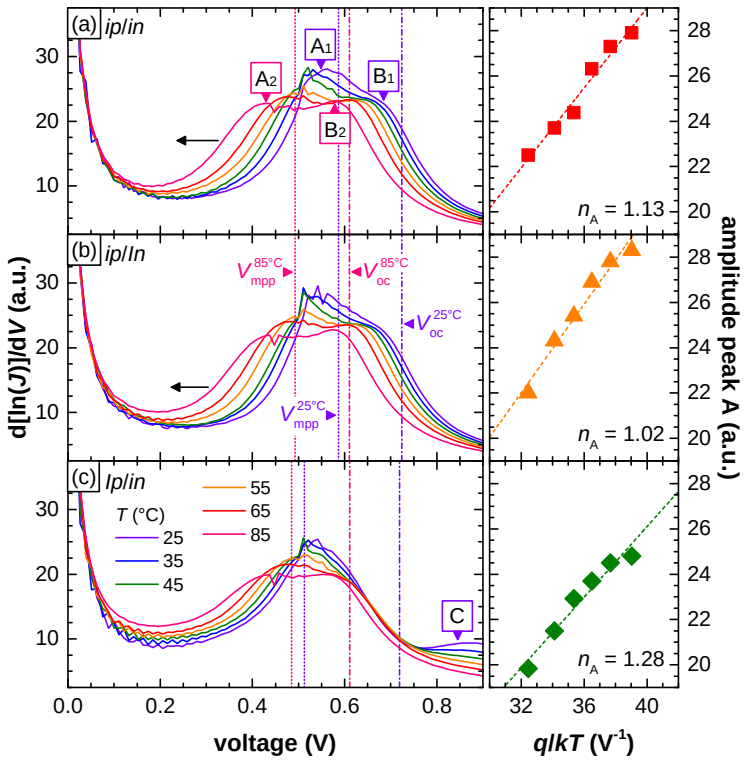

Figure 3.21 – First derivative of ln(J) with respect to V for (a) the *ip*/*in*, (b) the *ip*/*In* and the (c) *Ip*/*in* devices. The labels A1,2 and B1,2, shown as an example in (a), indicate the position of the two peaks for 25 and 85 °C and n_A is the ideality factor extracted from the temperature dependence of peak A.

3.4.3 Conclusion

To summarize, we have seen that a-SiO$_x$:H(*i*) passivation layers in SHJ solar cells exhibit an asymmetric effect on the collection of electrons and holes which we associated with a significant contribution of the R_s. We investigated this aspect by light and dark J-V measurements and conclude that for wide-bandgap materials—to a certain degree also including standard a-Si:H(*i*)—the effect on holes more pronounced than on electrons. For this reason we argue that—irrespective of the device structure—collecting holes at the rear of the device may be the ideal configuration. This also grants more freedom for the design of *p*-collecting layers in particular with respect to thickness and material properties. The layer should be thick enough to shield the interface against the negative influence of the transparent electrode. The latter can lead to losses in *FF* as discussed in chapter 5 (p. 83) and [Seif 2014a]. Furthermore, the VBO should be optimized with respect to transport. A good candidate for a hole-collecting material is therefore high-quality μc-Si:H(*p*). This material exhibits a smaller effective bandgap, potentially reducing barriers for holes, and improved transport properties. We investigated this material as well and discuss the results in chapter 6 (p. 99).

4 Impact of ambient-temperature and irradiance

Highlights

In the first part of this chapter, we unravel the T-dependence of SHJ solar cells, addressing each cell parameter individually. This analysis is based on T-dependent photo-conductance decay measurements [PCD(T)]. Investigating a-Si:H-passivated wafers, we observe a clear T-dependence of τ_{eff}. This dependence—in combination with results obtained by T-dependent current-voltage measurements [J-V(T)]—exposes the limit of the usually assumed simple relation between the V_{oc}'s temperature coefficient ($\text{TC}_{V_{\text{oc}}}$) and the V_{oc} itself. We show that PCD(T) measurements performed on solar cell precursors can be used as indications of the V_{oc} and FF temperature behavior of finished cells.[1] In part two, we compare different cell technologies and their temperature behavior at different illumination conditions. These technologies include the following devices provided by imec (Leuven, Belgium): (1) full Al-BSF, (2) PERC, (3) hybrid SHJ, (4) standard n-PERT, (5) advanced n-PERT and (6) a SHJ cell provided by CSEM (Neuchâtel, Switzerland). The results show a strong influence of surface passivation on the device performance at elevated temperatures, which is not only affecting the V_{oc} but also V_{mpp} and as a result the FF.

4.1 Introduction

Solar cells are generally certified in standard testing conditions (STC, $1000\,\text{W}\,\text{m}^{-2}$, 25 °C, AM1.5g spectrum). This certification procedure, however, could be questioned, as devices encapsulated in modules and deployed in the field can reach operating temperatures (T) as high as 90 °C [Kurtz 2011]. In fact, photovoltaic devices typically show significant performance losses with increasing T. Hence, the temperature coefficient of the conversion efficiency (TC_η) represents an important figure-of-merit for the energy yield of a given photovoltaic technology.[2] In this respect, compared to conventional c-Si homojunction technologies (TC_η

[1] Parts of this first study was published in the IEEE Journal of Photovoltaics, [Seif 2015].

[2] We refer to TC as the relative temperature coefficient, *i.e.* for a solar cell parameter X (V_{oc}, etc.) , $\text{TC}_X = 1/X^0 \partial X/\partial T$ (X^0: value at the reference temperature, if not stated differently at 25 °C) [Green 1985]. The absolute

= −0.45 %/°C for standard homojunction and -0.35 %/°C for homojunctions with passivating contacts [Smith 2012]), SHJ solar cells are less sensitive to increasing operating temperatures (TC_η = −0.23 %/°C [Mishima 2011] to −0.1 %/°C [Seif 2014b] [3]). To underline the importance of a favorable TC_η, starting from a 20%-efficient-cell (at 25 °C), a difference in TC_η of 0.12 or 0.35 %/°C results in ∼ 5.4 or 15.8% relative difference in efficiency at an T of 70 °C. Panasonic—supplier of SHJ modules—claims that compared to conventional c-Si-based solar modules, and thanks to the superior temperature performance of the SHJ devices, their technology yields up to 8% more in terms of cumulative power output throughout the year. According to them, this represents a difference of up to 65.3 kWh/kWp per year [Panasonic 2015].[4]

For an ideal solar cell, the diode equation directly yields an inverse dependence of the absolute value of $TC_{V_{oc}}$ on its V_{oc} [Green 1982b, Green 2003]. Green *et al.* proposed the following equation for the temperature dependence of the V_{oc}:

$$\frac{\partial V_{oc}}{\partial T} = -\frac{V_{g0} - V_{oc} + \gamma k_B T/q}{T} \tag{4.1}$$

Here T is the absolute temperature [K], V_{g0} is the voltage equivalent of the semiconductor bandgap extrapolated to T = 0 K, $k_B T/q$ is the thermal voltage and γ is a parameter that determines the sensitivity of the V_{oc} towards changes in T (smaller value equals lower sensitivity). According to Green *et al.* it typically lies between 1 and 4. However, for SHJ solar cells, the simple diode model may not hold as discussed in [Chavali 2014]. Despite this, the superior high-temperature behavior of this technology is often attributed to high V_{oc}s as well [Taguchi 2008]. For these devices, the high V_{oc} values are a direct consequence of their excellent surface passivation achieved by the intrinsic hydrogenated amorphous silicon [a-Si:H(*i*)] layers deposited on both sides of the wafer. In combination with the electron- and hole-selective contacts—formed by a-Si:H(*n*) or a-Si:H(*p*)—and the TCO—necessary for optical and electrical reasons—they suppress the metal-to-wafer contact carrier recombination, a severe performance-limiting factor for standard homojunction devices [De Wolf 2012b, Tous 2014a].

temperature coefficient, which we denote as 'tc', refers to the absolute value of $\partial X/\partial T$.

[3] This is comparable to thin-film silicon solar cells, which exhibit high V_{oc}s as well [Sriprapha 2007].

[4] The unit Wp (Watt peak) refers to the maximum power output under standard testing conditions (25 °C, AM1.5g spectrum, 0.1 W/cm^2).

4.2 Ambient-temperature impact on passivation & cell performance

4.2.1 Experimental details

C-Si *n*-type float-zone wafers (FZ, 240–280 μm, 2-–3 Ω cm) textured by potassium hydroxide were used to fabricate symmetric passivation samples (*i*/*i*), symmetric test structures (*in*/*in* and *ip*/*ip*), cell precursors (*ip*/*in*) and finished cells. Here *i*, *in* or *ip* refer to a-Si:H layers or layer stacks of either intrinsic (*i*) or doped (*n* or *p*) material.

Following chemical cleaning, finished by dipping the samples in diluted hydro-fluoric acid solution (5%, 60s), a-Si:H layers were deposited on both sides of the wafers by plasma-enhanced chemical vapor deposition (PECVD) in reactors powered at 40 MHz (KAI-M, or Octopus II). Further details can be found in chapter 2 (p. 23) or elsewhere [Descoeudres 2013]. The passivation samples received a symmetric coating of a-Si:H(*i*) (~30 nm), whereas *in*- and *ip*-stacks of ~10 nm (total stack thickness on textured wafers) were used for the other structures. For our investigation of finished cells, pairs of cell precursors were co-deposited, one of which was processed into a cell while the other was used for lifetime characterization only.

To study the electronic properties of the a-Si:H/c-Si interface as a function of T, the samples' $\tau_{\mathrm{eff}}(\Delta n)$ was measured using a Sinton Instruments WCT-120-TS PCD [Schmidt 2003] system with a controllable temperature stage, operated in transient or generalized mode [Kerr 2002]. In order to ensure the thermal stability of the a-Si:H layers during the measurements [De Wolf 2012a], all the samples were pre-cured for ~25 min at ~200 °C in air, the procedure we use to cure the silver paste after screen printing [Descoeudres 2013]. This process may change the electronic properties of the layers [De Wolf 2012a, El Mhamdi 2014]. Enabling hydrogen to diffuse and passivate further defects, thereby increasing the passivation quality [De Wolf 2008], it provides a sample that is stable at temperatures below the curing temperature. Furthermore, to avoid changes during the measurement, the lifetimes were probed while cooling down from 150 to 30 °C (in steps of 5 °C)—temperatures at which the layers are expected to be stable. The thermal stability of our samples was confirmed by similar $\tau_{\mathrm{eff}}(\Delta n)$ values (at room temperature) before and after the PCD(T) measurements.[5]

The performance of the finished cells was characterized with the Wacom II (see section 2.2.2.1, p. 30). Measurements were carried out at an intensity of one sun while T was ramped up from 25 to 85 °C, which again is a range in which no microstructural changes are expected.[6]

Furthermore, T-dependent external quantum efficiency measurements [EQE(T)] were performed to investigate the spectral dependencies, as well as the changes in effective bandgap ($E_{\mathrm{g,\,eff}}$). To extract $E_{\mathrm{g,\,eff}}$ we proceed as follows: (1) we chose the EQE measurement closest

[5] The actual value of T was cross-checked using a thermocouple (type K) glued directly on the wafer using thermal paste for the best thermal contact. No difference to the T measured by the thermocouple integrated into the device was found.

[6] Similar to the PCD(T) measurements a four-point-probe PT-100 sensor was glued directly on the wafer to measure T.

to 25 °C as reference; (2) from this, we extract the EQE value at the wavelength corresponding to the known bandgap at this temperature [Bludau 1974]; and finally for the other EQE measurements (3) we extract the wavelengths at this reference EQE value and convert it to the corresponding bandgap to obtain $E_{g,\,\mathrm{eff}}(T)$. For these measurements T was probed by a temperature sensor integrated into the chuck.

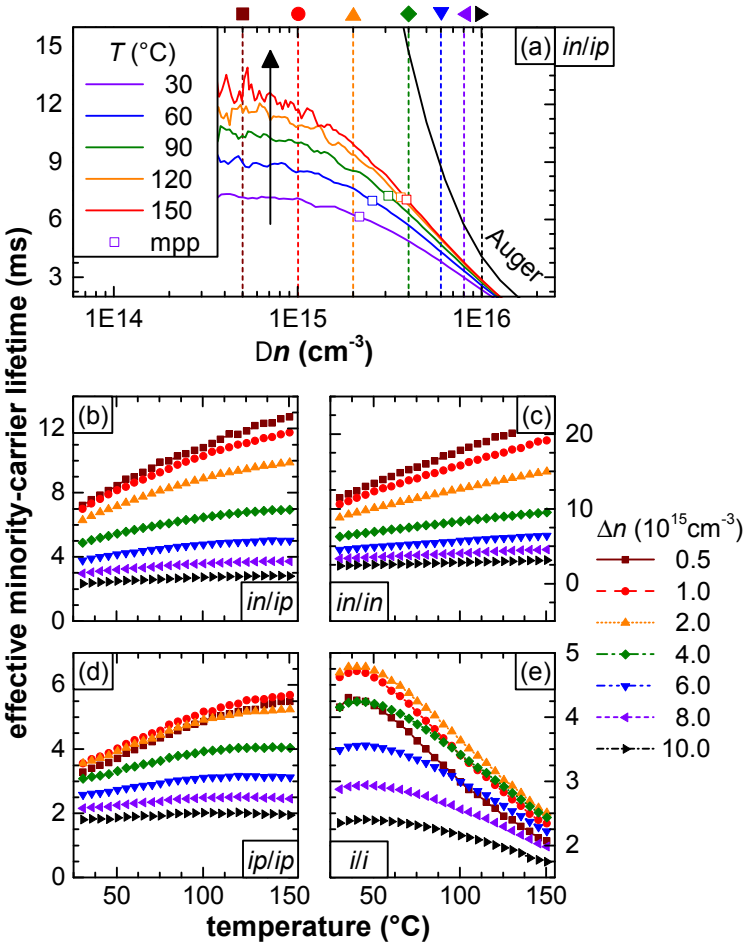

Figure 4.1 – (a) Effective minority-carrier lifetime of an *ip*/*in* solar cell precursor sample for different T (arrow indicates increase). The dashed lines indicate the injection levels (Δn) considered for the lifetime as function of T plots displayed for the (b) *ip*/*in*, (c) *in*/*in*, (d) *ip*/*ip* and (e) *i*/*i* samples. © 2015 IEEE, [Seif 2015]. The open data points in (a) represent the point associated with the mpp. The same is omitted for the point associated with the one-sun open-circuit conditions as the change is not clearly visible on this scale.

4.2.2 Results and discussion

4.2.2.1 Temperature-dependent minority-carrier lifetime

Here, we discuss results obtained from PCD(T) measurements. In Fig. 4.1(a), we notice that the T-dependence of τ_{eff} varies with Δn, the effect being more pronounced at lower Δn. For this reason, for each Δn value, indicated by a dashed line in Fig. 4.1(a), we extract T-traces shown in Fig. 4.1(b). To disentangle the effects of the two different interfaces, we also show T-traces for symmetric *in*/*in*, *ip*/*ip* and *i*/*i* samples [Fig. 4.1(c)–(e)]. It is important to note that the observations discussed here are likely linked to passivation variations at the c-Si *surface* and not the c-Si bulk. This assumption is corroborated by the fact that the variation of a-Si:H passivation stacks changes the lifetime T-dependence. For an effect purely related to the c-Si bulk, no differences between the samples would be expected.

For the *ip*/*in*, *in*/*in* and *ip*/*ip* samples, the T-dependence of τ_{eff} is not very pronounced at elevated Δn (6×10^{15} – 1×10^{16} cm^{-3}) as it is limited by the dominating Auger recombination process in the c-Si bulk (see section 1.2.2.2, p. 9), which is approximately constant for the investigated T-range for FZ wafers [Wang 2012]. This already indicates that the increasing lifetime will have a rather weak influence on the implied V_{oc} (iV_{oc}), as it is related to the lifetime value close to $\Delta n = 1\times10^{16}$ cm^{-3} (see discussion in section 4.2.2.2, p. 69). Judging from the findings of other authors [Trupke 2003, Nguyen 2014], the radiative recombination coefficient exhibits a strong temperature dependence for $T < 250$ K, but seems to reach a stable value for higher T (> 300 K). Due to the lack of data for the T-range investigated here, we assume it to be constant with temperature.

These findings contrast with the trends seen at lower Δn (5×10^{14} - 4×10^{15} cm^{-3}). For this injection range we observe a clear, monotonous increase of τ_{eff} with T [Fig. 4.1(b)–(d)], potentially affecting the (implied) fill factor [(i)*FF*] and the J_{sc}. This is discussed in the sections on *FF* (p. 73) and on J_{sc} (p. 74). Similar trends were recently reported for T below [Courtois 2013] and above [Sinton 2014] room temperature.

Compared to the samples featuring doped layers, the *i*/*i* samples [Fig. 4.1(e)] show a markedly different behavior. After a slight increase, the latter show a strong decrease in τ_{eff} across all injection levels, once T reaches 50 °C. We observed this behavior systematically also for other *i*/*i* samples (from different batches) and tentatively explain this effect by a decreasing internal electrical field close to the a-Si:H/c-Si interfaces at higher T. Without strong field-effect passivation, thermally excited carriers are able to reach the a-Si:H/c-Si interface more easily, where they may recombine and hence lead to a reduction of τ_{eff}. Besides this field-effect, possible explanations for these trends also include temperature-dependent variations of the capture cross-sections for electrons and holes and recombination statistics [Goldie 2013]. A possible way to see this is to consider the fact that with increasing T a shift of E_F towards mid-gap will be induced in the c-Si part of the device, which is likely also true for a-Si:H. This shift changes the occupation level of the different amphoteric defect states (D^0, D^- an D^+) as discussed earlier (section 1.2.2.2, p. 9) [Goldie 2013]. These defect level, however, have

different capture cross-sections for both electrons and holes, while D^0 can capture either an electron, D^+ and D^- can capture *either* electrons *or* holes, respectively. Furthermore, the shift of E_F towards mid-gap also weakens the effective band-bending in the c-Si part, hence, enabling charge carriers to diffuse more easily towards the surfaces, where they recombine. These hypotheses, however, has to be confirmed or rejected by further investigations.

Besides the changes observed in τ_{eff}, we also systematically observe a shift of Δn for the points associated with the iV_{mpp} and the iV_{oc} (hereafter denoted as: $\Delta n_{iV_{\text{mpp}}}$ and $\Delta n_{iV_{\text{oc}}}$). These variations are depicted in Fig. 4.2(a) ($\Delta n_{iV_{\text{mpp}}}$) and 4.2(b) ($\Delta n_{iV_{\text{oc}}}$). The results show, that $\Delta n_{iV_{\text{mpp}}}$ exhibits a linear, monotonic increase for all the samples. Conversely, for the $\Delta n_{iV_{\text{oc}}}$ values, the trends depend on the sample structure. Both the *in*/*in* and the *ip*/*in* samples show an increase in $\Delta n_{iV_{\text{oc}}}$. The *ip*/*ip* sample first shows an increase and then for $T > 120\,^{\circ}\text{C}$ a decreasing trend. Again, the *i*/*i* sample shows a different behavior, namely a decreasing trend starting already at around 50 °C, as discussed before.

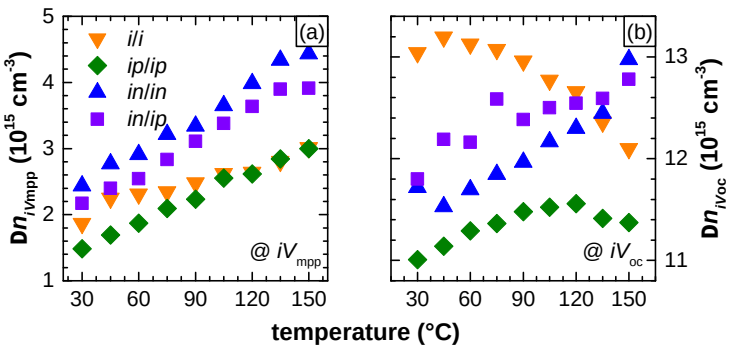

Figure 4.2 – Temperature trends for the Δn values associated with (a) the iV_{mpp} and (b) the iV_{oc}. The data was extracted from same $\tau_{\text{eff}}(T)$-data shown in Fig. 4.1.

We now turn the attention to the device performance at elevated T and discuss the implications of our findings so far.

4.2.2.2 Implications of $\tau_{\text{eff}}(T)$ on cell parameters T-dependence

Conversion efficiency: Fig. 4.3 shows typical T-dependences for a SHJ cell fabricated in our lab (see section 2.1, p. 23 or [Descoeudres 2013]). We observe clear trends for all cell parameters. While both V_{oc} and FF decrease with temperature, J_{sc} increases. From the derivative of η with respect to T, the overall TC_η is obtained simply by summing the contributions of $\text{TC}_{V_{\text{oc}}}$ (−0.27 %/°C), $\text{TC}_{J_{\text{sc}}}$ (+0.08 %/°C) and TC_{FF} (−0.07 %/°C, for $T > 40\,^{\circ}\text{C}$, see footnote):

$$\frac{1}{\eta^0}\frac{\partial \eta}{\partial T} = \frac{1}{V_{\text{oc}}^0}\frac{\partial V_{\text{oc}}}{\partial T} + \frac{1}{J_{\text{sc}}^0}\frac{\partial J_{\text{sc}}}{\partial T} + \frac{1}{FF^0}\frac{\partial FF}{\partial T} \tag{4.2}$$

Considering 4.2 and the TC values obtained, it is evident that the weak contribution of the $TC_{J_{sc}}$ does not counterbalance the dominating $TC_{V_{oc}}$, and a value of $TC_{\eta} = -0.26\,\%/°C$ is obtained. All the values are given in Tab. 4.1, including those for parameters closely associated with the *J-V* parameters, namely the voltage and the current density at the maximum power point (V_{mpp} and J_{mpp}) and the iV_{oc}.[7]

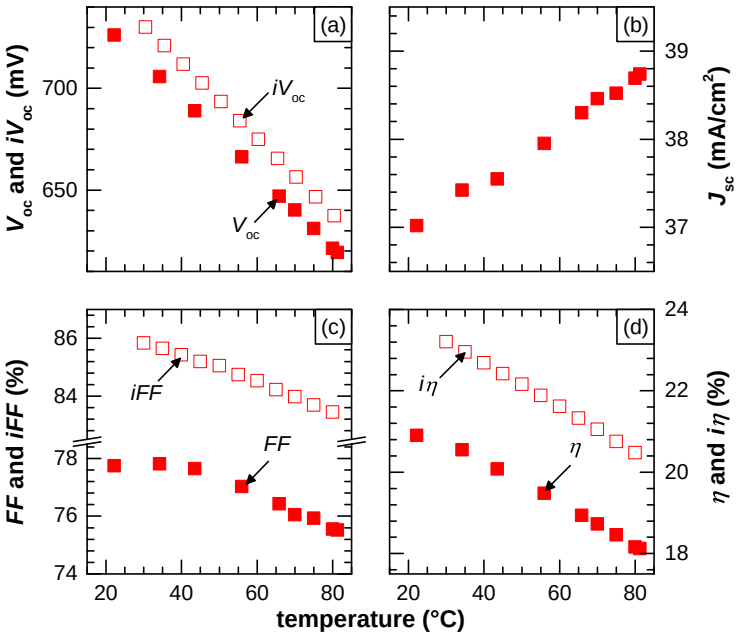

Figure 4.3 – *T*-dependence of (a) V_{oc} and iV_{oc}; (b) J_{sc}; (c) *FF* and *iFF*; and (d) the cell efficiencies η and $i\eta$. These results were obtained by one-sun *J-V*(*T*) (finished cells) and PCD(*T*) measurements (cell precursors, implied values). © 2015 IEEE, [Seif 2015].

(Implied) open-circuit voltage: The fact that both V_{oc} and iV_{oc} show the same *T*-dependence of approximately -1.90 mV/°C [Fig. 4.3(a)], suggests that temperature-related effects observed for the iV_{oc} also apply for the V_{oc}. Therefore, the simplicity of the PCD(*T*) measurement can be exploited to gather information about the V_{oc} and gain preliminary insights without the necessity to fabricate a finished cell. In the following we concentrate therefore on iV_{oc} measurements.

As mentioned in section 4.2.2.1, we observe that the lifetime at an injection level of around 10^{16} cm^{-3}—the one we associate the value of the iV_{oc} to—shows only a weak *T*-dependence as the increase is almost entirely suppressed by Auger recombination, which we assume to be *T*-independent [Wang 2012]. However, as depicted in Fig. 4.2, depending on the sample

[7] Note that we normalized to 40 °C as the TC_{FF} is constant only above 40 °C and varies below (see footnote 1 for the definition of the normalization). This is likely due to a slight transport barrier. Such barrier effects may be aggravated by the presence of wide-bandgap passivation films [Seif 2014b].

Table 4.1 – Absolute tcs and relative TCs for the relevant cell parameters: Extracted from the data shown in Fig. 4.3 by applying linear fits to the T-range 40–80 °C and, for the values of TC_X, by normalizing to the value at 40 °C for the cell and 30 °C for the precursor.

X	tc_X	TC_X [%/°C]
V_{oc}	−1.85 mV/ °C	−0.27
iV_{oc}	−1.90 mV/ °C	−0.26
V_{mpp}	−1.66 mV/ °C	−0.29
J_{sc}	+0.03 mA cm^{-2}/ °C	+0.08
J_{mpp}	+0.01 mA cm^{-2}/ °C	+0.03
FF	−0.06%/ °C	−0.07
iFF	−0.05%/ °C	−0.05
η	−0.05%/ °C	−0.26
$i\eta$	−0.05%/ °C	−0.24

structure, we observe an additional effect namely an increase of $\Delta n_{iV_{\mathrm{oc}}}$ (Fig. 4.2). Both effects seem to influence the $\mathrm{TC}_{iV_{\mathrm{oc}}}$ as depicted in Fig. 4.4(a) and 4.4(b), in which we show the $\mathrm{TC}_{iV_{\mathrm{oc}}}$ as a function of the $\mathrm{TC}_{\tau_{\mathrm{eff}}}$ at 10^{16} cm^{-3} and as a function of the $\mathrm{TC}_{\Delta n_{iV_{\mathrm{oc}}}}$, respectively. Even though both effects improve the $\mathrm{TC}_{iV_{\mathrm{oc}}}$, they are by far not the dominant effects. As discussed by Taguchi *et al.* [Taguchi 2008], the V_{oc} depends on the dark saturation current J_0 which is given by the following equation:

$$J_0 = q \cdot n_{\mathrm{i}}^2 \left(J_{\mathrm{n0}} + J_{\mathrm{p0}}\right) \tag{4.3}$$

$$n_i^2 = N_{\mathrm{C}} N_{\mathrm{V}} \exp\left(-\frac{E_{\mathrm{g}}}{k_{\mathrm{B}} T}\right) \tag{4.4}$$

Here q is the elementary charge, n_{i} the intrinsic carrier concentration and $J_{0\mathrm{n}}$ and $J_{0\mathrm{p}}$ are the saturation current densities on either side of the p-n junction, J_0 represents the total saturation current density, n_i is the intrinsic carrier density of the material, and N_{C} and N_{V} are the effective densities of states in the conduction and valence band respectively.

Among other parameters these J_0 values depend on the diffusion coefficients (D) of each carrier type and their diffusion lengths ($L = \sqrt{\tau \cdot D}$, where τ is the effective carrier lifetime). For more details see [Taguchi 2008]. Considering now equation 4.3 it is clear that both n_{i} and the J_0s are independent of each other. This means that even though there might be a beneficial effect of the temperature on τ_{eff} resulting in an increase of L—which is partly compensated by a decreasing carrier mobility (μ) and $D = \mu q / k_{\mathrm{B}} T$ with T [Schindler 2014]—the increase of n_{i} with T dominates the trends in V_{oc}. This becomes even clearer considering the formula for the iV_{oc} given for an n-type wafer with doping density N_{D} by [Sinton 1996]:

$$iV_{\mathrm{oc}} = \frac{k_{\mathrm{B}} T}{q} \ln\left(\frac{(N_{\mathrm{D}} + \Delta n)\,\Delta n}{n_i^2}\right) \tag{4.5}$$

Obviously the ratio of $\Delta n^2/n_i^2$ (here: Δn is equivalent to $\Delta n_{iV_{oc}}$) will be dominated by n_i, as it increases exponentially with temperature, while $\Delta n_{iV_{oc}}$ varies linearly. Note that the increase in n_i is associated with a decreasing bandgap—enhancing thermal excitation across the same—and to an increase of the effective densities of states within the electronic bands, both leading to an increase of the J_0 [Sze 1981].

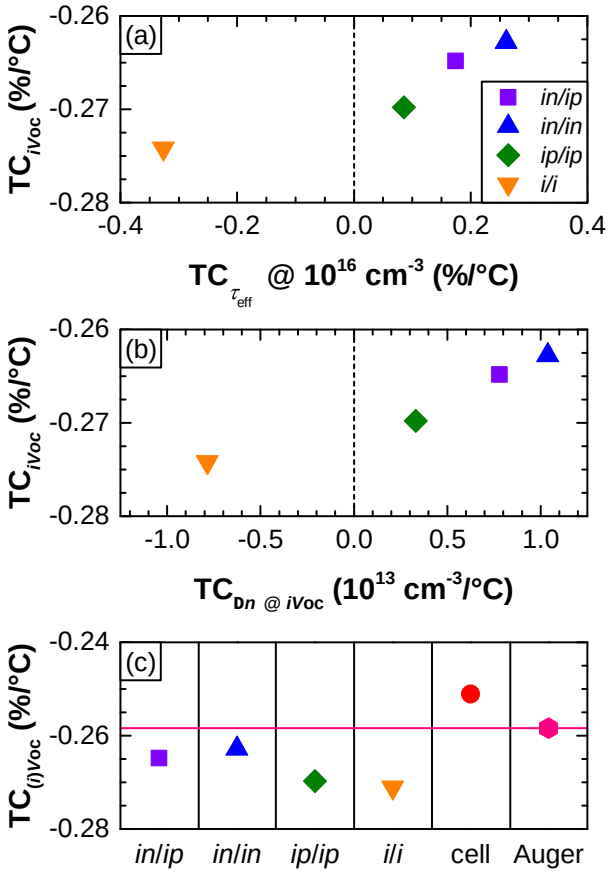

Figure 4.4 – (a) $TC_{iV_{oc}}$ as a function of $TC_{\tau_{eff}}$ extracted from Fig. 4.1(b)—(e) for τ_{eff} at $\Delta n = 10^{16}$ cm^{-3} and (b) $TC_{iV_{oc}}$ as a function of $TC_{\Delta n_{iV_{oc}}}$, extracted from the same data. (c) Comparison of $TC_{iV_{oc}}$ obtained for the different samples to the hypothetical case of assuming Auger recombination only (see text for details). To obtain the TC values, linear fits were applied to the data in the entire T-range. © 2015 IEEE, [Seif 2015].

In the following we compare the $TC_{(i)V_{oc}}$ values of the different structures studied here, to the case of a hypothetical structure limited by Auger recombination only, which unveils interesting differences. For this hypothetical device, we reconstruct the so-called implied J-V (iJ-V) curve for each point of the investigated T-range. We calculate the iV_{oc} using $n_i(T)$ and the Auger model described by Richter *et al.* [Richter 2012] and combine it with the implied current density (iJ), which depends on the wafer specifications (n-type wafer; thickness: 242 μm; doping: 2×10^{15} cm^{-3}), the injection level and the Auger lifetime as well as the temperature.

We assume a J_{sc} of 37 mA cm^{-2} (at 30 °C, as our PCD measurements only went down to 30 °C) based on our cell results [see Fig. 4.3(b)] and calculate the iJ accordingly, correcting it with respect to its increase with T, which we had previously derived from J-$V(T)$ measurements.

While the entire set of samples with a-Si:H layers only shows less favorable $TC_{iV_{oc}}$ values, the cell (Fig. 4.3) shows a better temperature performance than the Auger-limited device [Fig. 4.4(c)]. This shows that the passivation alone might not be the only aspect to be considered when assessing the T-dependencies at cell level as we discuss in the following. Note that the iV_{oc} is measured inductively and represents an internal voltage—depending only on the splitting of the quasi-Fermi-levels of the electrons and holes—while the V_{oc} is measured at external metallic electrodes, where a potential drop in the layers present between the electrodes and the wafer surface may occur. Furthermore, the passivated samples do not exhibit any TCO layer. All this may explain the discrepancy in TC values.

To assess the effect of the absolute value of the iV_{oc} (at 25 °C) on the $TC_{iV_{oc}}$, we fabricated a symmetrically passivated i/i sample [30 nm a-Si:H(i)], which we thermally degraded by annealing it at temperatures of up to 350 °C (in air). Within this T-range the thermal desorption of hydrogen eventually ensues an increase in unpassivated surface defects and hence a reduction in passivation quality [De Wolf 2009]. After each annealing step the sample was measured on the PCD(T) stage. The results are shown in Fig. 4.5. From each $iV_{oc}(T)$ curve [Fig. 4.5(a)] we extracted the $TC_{iV_{oc}}$ from a linear fit and plot the result as a function of the (extrapolated) iV_{oc} value at 25 °C [Fig. 4.5(b)]. Even though the changes of the iV_{oc} (at 25 °C) are relatively small (variation less than 20 mV), the repercussions for the $TC_{iV_{oc}}$ are large. This result shows the importance for high passivation quality, *i.e.* high V_{oc}s at room temperature. This value is one aspect determining the $TC_{V_{oc}}$ and hence directly influences the performance of the device at high T, as argued in section 4.2.2.1, and as was originally proposed by Green *et al.* [Green 1985] and reported by Taguchi *et al.* [Taguchi 2008] as well as more recently by Mishima *et al.* [Mishima 2011].

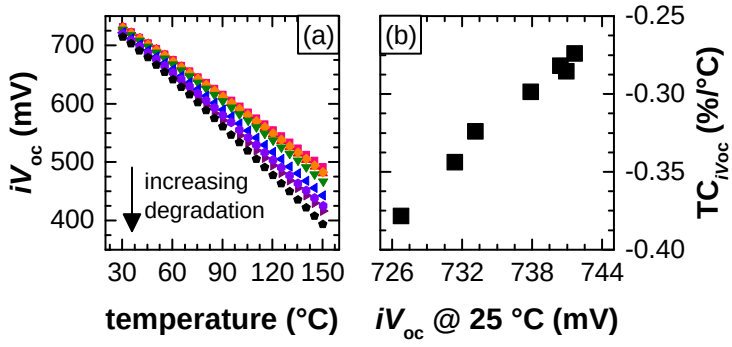

Figure 4.5 – (a) iV_{oc} as a function of T for different stages after thermal degradation. (b) $TC_{iV_{oc}}$ values as a function of the measured iV_{oc}(25 °C) extracted from (a) by extrapolation. © 2015 IEEE, [Seif 2015].

However, besides the effect on the passivation quality, the hydrogen content in the a-Si:H(*i*) layer determines the bandgap of the material [Schulze 2011]. Hence, its effusion from the layer can entail the changes of the passivation quality [De Wolf 2009] and have an influence on the $TC_{iV_{oc}}$. We observe this effect on finished cells with wide-bandgap hydrogenated amorphous silicon oxide (a-SiO_x:H) passivation layers, as described in chapter 3 (p. 37) and 3.4 (p. 54). In contrast with the standard *in*/*ip* device with a V_{oc} of ~724 mV,[8] exhibiting a $TC_{V_{oc}}$ of ~-0.262 %/°C, the cell with a wide-bandgap a-SiO_x:H passivation layer below the hole collecting a-Si:H(*p*) layer shows a lower V_{oc} of ~713 mV, but intriguingly a more favorable $TC_{V_{oc}}$ of ~-0.253 %/°C. This underlines the fact that the $TC_{V_{oc}}$ is influenced not only by the V_{oc} value at 25 °C, but also by the materials used in the device and the band offsets (transport barriers) associated with the same. This reduced sensitivity of the V_{oc} with respect to temperature can be explained by a lower γ value (see equation 4.1, p. 64)[9] for this type of device. However, it is surprising that the structure of the device can play a role for the $TC_{V_{oc}}$, as in open-circuit conditions no carrier transport takes place and hence $TC_{V_{oc}}$ should be transport independent. A possible explanation could be an impeded recombination of charge carriers associated with the presence of the a-SiO_x:H layers. These may be either be caused by unintentional *n*-type doping of the a-SiO_x:H(*i*) that would lead to an enhanced field effect, or impeded recombination of holes on the a-Si:H(*p*) side due to the barrier represented by the a-SiO_x:H(*i*) layer. Future work has to clarify this point, as it was not possible to do it during the course of this thesis.

Fill factor: We now turn to the trends observed for the *FF*. Using again PCD(*T*) measurements, we extract *iJ*-*V* curves as discussed before and as shown in Fig. 4.6(a). This time however, instead of considering only the Auger lifetime, we take the measured τ_{eff} values into account. This gives us access to the *iFF*.

The *iFF* trends obtained are given in Fig. 4.6(b). The latter are not linear which is directly linked to the trends of τ_{eff} extracted corresponding to the implied maximum power point (*i*-mpp) [Fig. 4.6(c)] and the shift of $\Delta n_{iV_{mpp}}$ towards higher values [Fig. 4.2(a)]. Below 80 °C, both effects mitigate the decrease in iV_{mpp} and hence the *iFF* decrease is slower. This is also the reason, why all test samples (except the *i*/*i*) show a more favorable TC_{iFF} in this *T*-range compared to the hypothetical Auger-limited case (see Fig. 4.7). For *T* beyond 80 °C, however, $\tau_{eff,\ i\text{-mpp}}$ remains stable or decreases even slightly and TC_{iFF} decreases and approaches—at least for *ip*/*in* and *in*/*in* samples—the value for the Auger-limited case.

Comparing the $TC_{(i)FF}$ of both the *ip*/*in* cell precursor [Fig. 4.6(b)] and the actual cell (Fig. 4.3) it is noteworthy that for the same *T* range (30 – 80 °C) they show slightly different TCs (TC_{iFF}- TC_{FF} = 0.02 %/°C). This may be explained by the fact that for contactless PCD(*T*) measurements, transport-related effects (ohmic or non-ohmic) are unaccounted for. This is also corroborated by comparing the TC_{iFF} of the Auger-limited case to the TC_{FF} of the cell,

[8] Note that the values we report here are the averages over three cells on the same wafer.

[9] According to Green *et al.*, γ refers to the temperature sensitivity of mechanisms limiting the V_{oc} [Green 1985].

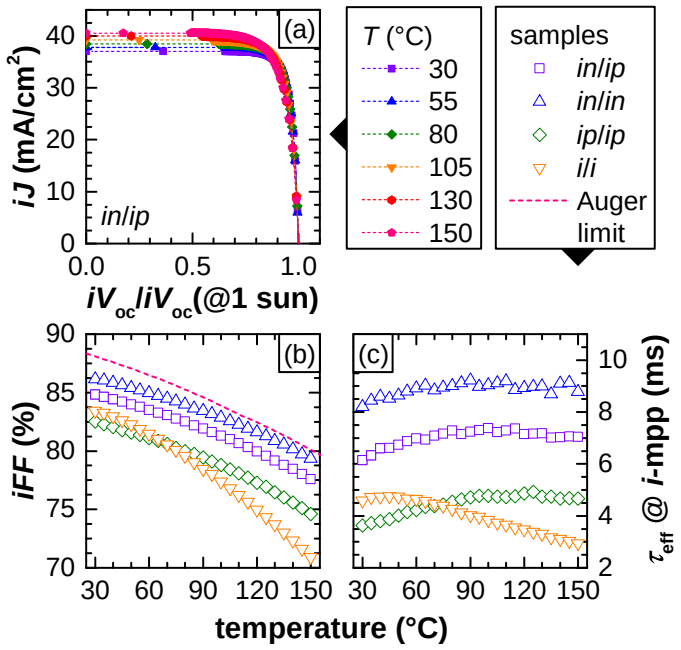

Figure 4.6 – (a) Implied *J*-*V* curves extracted from PCD(*T*) measurements on the *in*/*ip* sample. The implied current density (*iJ*) has been corrected with respect to *T* according to the results given in Tab. 4.1. Note that the voltage values are normalized for easier comparison of the curves. (b) Implied *FF* (*iFF*) for the test structures as function of *T*. The dashed line indicates the limit obtained for a device limited by Auger recombination only. (c) Effective minority-carrier lifetime extracted at the implied maximum power point (*i*-mpp). © 2015 IEEE, [Seif 2015].

the latter displaying a more favorable value (Fig. 4.7). These effects amount to approximately 30% of the TC_{FF}.

Furthermore, as discussed in the previous section for the $TC_{V_{oc}}$, the TC_{FF} can as well be influenced by transport barriers. These barriers may even lead to positive TC_{FF} values and hence to TC_{η} as low as -0.1 %/°C, enabling improved performance at higher *T* compared to standard devices [Seif 2014b]. Yet, this phenomena is not exclusive to a-SiO_x:H but has also been observed for instance by using thicker a-Si:H layers [Taguchi 2008] or different materials, such as metal oxides [Battaglia 2014].

Short-circuit current density: Finally, we turn to the trends observed for the J_{sc} [Fig. 4.3(b)]. These can be explained by a decreasing effective bandgap and the resulting increased, phonon-assisted, absorption in the red part of the solar spectrum [Fig. 4.8(a)]. In Fig. 4.8(b) we compare the values obtained for $E_{g,\,eff}(T)$ (as described in section 4.2.1), and the bandgap's *T*-dependence known from literature [Bludau 1974]. We observe that $E_{g,\,eff}$ values yield a variation $\Delta E_{g,\,eff}$ of 35 meV when increasing the *T* from 20–75 °C [Fig. 4.8(b)]. This accounts for more than what is expected [Bludau 1974], which is linked to the increased probability for phonon-mediated indirect transitions with *T* [Sin 1984]. The variation in effective surface

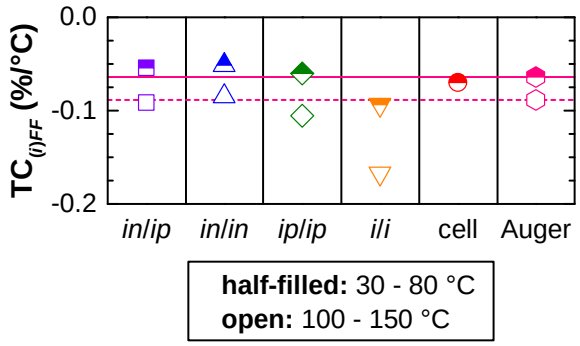

Figure 4.7 – Comparison of TC_{iFF} obtained for the different samples to the hypothetical case of assuming Auger recombination only (horizontal lines). To obtain the TC values, linear fits were applied to the data in the specified T-ranges. © 2015 IEEE, [Seif 2015].

recombination velocity on the other hand is too small (< 1 cm/s, across all injection levels) to explain an enhancement of the collection probability and can therefore be neglected.

The influence of an increase in J_{sc} on the V_{oc}, is negligible as well. For a standard SHJ cell we recently reported a variation of only 0.7 mV/ mA cm^{-2} close to one sun [Seif 2014a]. This leads to a variation of only 1.1 mV (corresponding to +0.02 mV/°C) for the observed T range (25–80 °C).

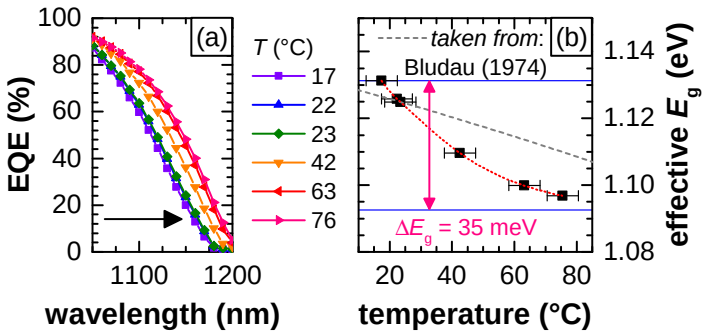

Figure 4.8 – (a) EQE(T) at wavelengths above 1050 nm for different T. (b) $E_{g,\,eff}$ extracted from EQE(T) as a function of T. Comparison to temperature dependence reported by Bludau [Bludau 1974]. © 2015 IEEE, [Seif 2015].

4.2.3 Conclusion

Performance losses associated with increasing T are detrimental to the energy yield of a photovoltaic cell. Typically, TC_η is closely linked to the V_{oc} measured at room temperature. In the present study we investigated the implications of τ_{eff} on the solar cell parameters of

silicon heterojunction devices.

First, we found that—depending on the injection level and sample structure—τ_{eff} changes with increasing T. This is tentatively explained by variations in the capture cross-section for electrons and holes or the structure inherent field-effect passivation. Further investigations are necessary to pinpoint the dominant physical effects.

Based on these results we investigated their impact on the cell parameters, which—for our standard devices—lead us to the following results:

1. The V_{oc} decreases with T; The increasing τ_{eff} shows a minor effect on the $\text{TC}_{iV_{\text{oc}}}$, yet, it does not counterbalance the decrease imposed by the increase in saturation current density (diode equation); Thermally degraded samples clearly show the beneficial influence of higher initial iV_{oc} values (at 25 °C) on $\text{TC}_{iV_{\text{oc}}}$. However, a high V_{oc} is not the only aspect for favorable $\text{TC}_{V_{\text{oc}}}$ values, the structure of and materials used in the device have to be considered as well, even though the V_{oc} should not directly be affected by the latter as no transport takes place in open-circuit conditions. Future work has to clarify this point.

2. The *FF* decreases with T; Similar to the iV_{oc}, the *iFF* is influenced by the variation in τ_{eff} and shows a more favorable TC compared to the *FF* for the investigated T range. This is likely linked to the negative influence transport-related T effects. As we have seen in chapter 3 layers that impede carrier transport can have a strong effect on the *FF*—*i.e.* lowering its value in standard test conditions—but also on the TC_{FF}, which—instead of yielding negative values—can be positive for a certain temperature range.

3. The J_{sc}, increases with T; The dominant effects are the decrease of the bandgap and the enhanced phonon-assisted excitation; Increasing lifetimes do not affect the J_{sc}.

4. The conversion efficiency η, is clearly dominated by the V_{oc} and hence decreases with temperature. J_{sc} influences the efficiency only to a lesser extent whereas devices with no transport problem exhibit a weak variation of *FF* with T.

4.3 Temperature behavior of different c-Si technologies at a glance

4.3.1 Experimental details

To assess the variations of the TC among different device technologies, we performed standard J-$V(T)$ measurements on a set of samples provided by Loic Tous (imec, Interuniversity Microelectronics Center, Leuven, Belgium) and CSEM (Swiss Center for Electronics and Microtechnology, Neuchâtel, Switzerland). These include: (1) a cell with a full aluminum back-surface field [BSF, Fig. 4.9(a)]; (2) a passivated emitter and rear cell [PERC, Fig. 4.9(b)]; (3) a standard passivated emitter, rear totally-diffused cell [PERT, Fig. 4.9(c)]; (4) an advanced PERT cell [Fig. 4.9(d)]; and (5) a hybrid homojunction-heterojunction cell [hybrid SHJ, Fig. 4.9(e)]. The cell fabrication is partly described elsewhere: see [Dullweber 2011] for the fabrication of a full-BSF cell; [Cornagliotti 2015] for the *p*-PERC; [Tous 2014a] for a description of the standard *n*-PERT; [Aleman 2014] and [Cornagliotti 2014] for the advanced *n*-PERT;[10] [Tous 2014b] for the hybrid cell and [Tous 2013] for the metallization by copper-plating. The SHJ cell measured here (supplied by CSEM) is a bi-facial SHJ, *i.e.* it does not feature full rear metallization [Fig. 4.9(f)]. Since we are interested in the electrical performance—*i.e.* mainly in V_{oc} and *FF*—we neglect this fact for the discussion presented here as illumination from both sides of the wafer mainly influences the J_{sc}.

The cell parameters obtained for these cells at 25 °C are listed in Tab. 4.2. Besides sweeping T we also used different filters or a Fresnel lens to vary the light intensity. The different filters are listed in Tab. 4.3. These measurements were performed on the Wacom II sun simulator at CSEM (see section 2.2.2.1, p. 30).[11]

Table 4.2 – Cell parameters of the cells used in this study, measured at 25 °C and one sun. [a]Values given here, measured at imec.

cell	**size** [cm^2]	V_{oc} [mV]	J_{sc} [$mA\,cm^{-2}$]	***FF*** [%]	η [%]
full BSF D03[a]	238.95	639.4	38.2	78.7	19.2
PERC D51[a]	238.95	652.4	38.8	79.3	20.0
hybrid SHJ[a]	227.06	676.7	38.8	79.4	20.9
n-PERT D49 (standard)[a]	227.06	674.1	39.7	81.3	21.7
n-PERT D06 (advanced)[a]	227.06	684.8	40.1	80.6	22.2
SHJ cell	243.36	731.1	37.4	78.3	21.4

[10] The advanced *n*-PERT features a combination of a selective front-surface-field [Aleman 2014] and rear aluminum-oxide passivation [Cornagliotti 2014].

[11] The measurements were done in collaboration with Jonathan Champilaud (CSEM), whereas the data was processed by Jacques Levrat (CSEM). Note that due to dust in the system the light intensity at longer wavelengths was reduced. This was compensated by increasing the contribution of the shorter wavelengths.

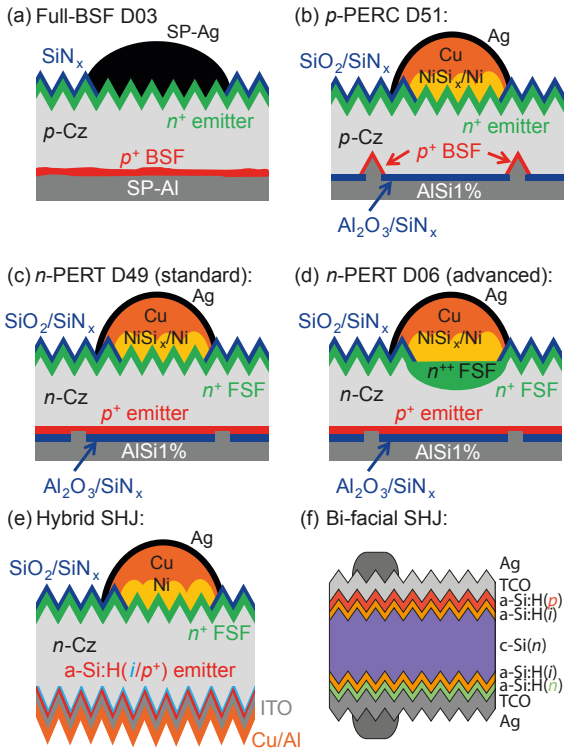

Figure 4.9 – Structures of the devices used for this study: (a) Cell with cell full aluminum back-surface field, (b) passivated emitter and rear cell, (c) standard and (d) advanced passivated emitter, rear totally-diffused cell, and (d) hybrid homojunction-heterojunction cell. Sketches by courtesy of Loïc Tous (imec) © imec (Leuven, Belgium). (f) Bi-facial SHJ solar cell with hole collection at the front.

Table 4.3 – Irradiances at which the cells were measured with different filters or lenses.

suns	filter/lens
1.96	Fresnel lens
1.67	Fresnel lens + transparent plastic sheet
1	no filter
0.5	neutral density filter 50%
0.14	one sheet of paper
0.06	two sheets of paper
0.036	three sheets of paper

4.3.2 Results and discussion

First, we focus on the results obtained at one-sun illumination. For this irradiance, Tab. 4.4 summarizes the TC values for the different cell structures ordered according to their V_{oc} value measured at 25 °C and one-sun irradiance. Note that the TC values were extracted fitting the T-dependent data with linear fits above 40 °C. Considering the structure of each of the devices

(Fig. 4.9, and in section 1.2.3 Fig. 1.10) these differences are easily explained. For the cells listed in Tab. 4.4, the passivation schemes become increasingly efficient following the order of the list, the 'full BSF' cell being the least and the SHJ cell being the best passivated device. From these values alone it is already possible to see that there is indeed a trend towards better temperature performance with increasing passivation [V_{oc}(25 °C, one sun) value]. This is especially true for the $TC_{V_{oc}}$, the $TC_{V_{mpp}}$, the TC_{FF} and therefore for the TC_{η}.

Table 4.4 – Temperature coefficients calculated from J-$V(T)$ data at one-sun illumination.

	V_{oc}(25 °C, one sun) [mV]	$TC_{V_{oc}}$	$TC_{V_{mpp}}$	$TC_{J_{sc}}$ [%/ °C]	TC_{FF}	TC_{η}
full BSF	639.4	−0.32	−0.39	0.05	−0.14	−0.41
PERC	652.4	−0.30	−0.37	0.04	−0.13	−0.38
n-PERT (standard)	674.1	−0.30	−0.37	0.04	−0.10	−0.35
hybrid SHJ	676.7	−0.29	−0.36	0.04	−0.12	−0.37
n-PERT (advanced)	684.8	−0.28	−0.34	0.04	−0.11	−0.34
SHJ cell	731.1	−0.26	−0.29	0.04	−0.07	−0.29

Fig. 4.10 summarizes the results obtained for the J-$V(T)$ and J-V(suns) measurements. Here we show the $TC_{V_{oc}}$, $TC_{V_{mpp}}$, TC_{FF} and TC_{η} as a function of the irradiance applied to the cells. The values for the $TC_{J_{sc}}$ for one-sun illumination are given in Tab. 4.4. But since they do not show a strong dependence with irradiation we do not show them in the figure. Furthermore, the data below 0.2 suns shows some noise related to measurement artifacts.

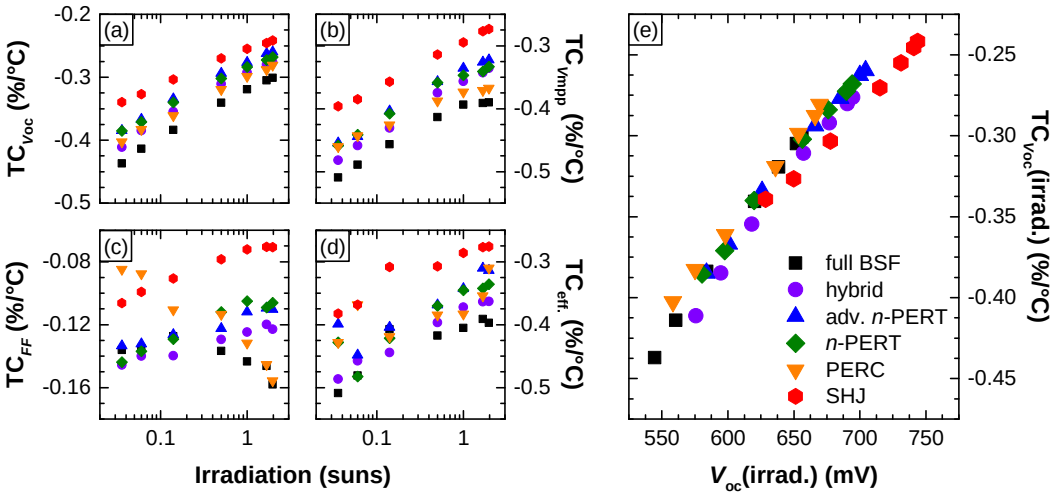

Figure 4.10 – Temperature coefficients of different technologies for (a) the V_{oc}, (b) the J_{sc}, (c) the FF, and (d) the conversion efficiency (for T> 40 °C). (e) $TC_{V_{oc}}$ as a function of the V_{oc} both taken the same irradiation.

Considering the trends shown in Fig. 4.10(a) for the $TC_{V_{oc}}$, all the cells yield an amelioration of the $TC_{V_{oc}}$ with increasing irradiance. Correlating the $TC_{V_{oc}}$, to the V_{oc} at the same irradiance we obtain the results shown in Fig. 4.10(e). The data gathered for the different technologies all show a linear behavior of the $TC_{V_{oc}}$ with irradiance-dependent V_{oc} [Green 2003]. This again shows the importance of the V_{oc} values a certain technology yields at 25 °C and at a given irradiance, as argued in section 4.2.2.2 (p. 69). It is interesting to note that the SHJ cell exhibits a worse $TC_{V_{oc}}$ for a given V_{oc} at lower irradiance. The reason for this will have to be investigated further, but was beyond the scope of this work.

Next we turn to Fig. 4.10(b), which depicts the results for the $TC_{V_{mpp}}$. Here it is interesting to note that—compared to the full BSF and the PERC cell—the $TC_{V_{mpp}}$ of the SHJ device shows an ever increasing trend, even beyond one-sun irradiation. This is also seen for the standard and advanced *n*-PERT, as well as for the hybrid SHJ cells, although they show lower $TC_{V_{mpp}}$ values. For the full BSF and the PERC cells, the $TC_{V_{mpp}}$ reaches a maximum at approximately one sun. Considering the TC_{FF} data [Fig. 4.10(c)], we observe intriguing differences. The SHJ cell exhibits a steady increase of the TC_{FF}, as do the advanced *n*-PERT, the standard *n*-PERT cells and the hybrid devices, however, for them the increase is less pronounced. Yet, these trends strongly contrast with the results obtained for the full BSF and the PERC cells. For these devices we observe the opposite trend and the TC_{FF} degrades with increasing irradiance. Possible reasons for this device-specific T- and irradiance-dependent behavior may be the already mentioned differences in passivation or the device architecture, in particular also the doping type of the absorber, the full BSF and the p-PERC cells being the only cells based on *p*-type c-Si. Further work is necessary to investigate this further and clarify this phenomenon. The TC_{η} values are shown in Fig. 4.10(d). Similar to the steady increase in $TC_{V_{oc}}$ these values also increase with irradiance. The strong increase of the TC_{η} of the PERC device beyond one sun is explained by measurement artifacts, *i.e.* T-trends exhibiting offsets.

In the following we compare the TC values ($TC_{V_{oc}}$, TC_{FF} and TC_{η}) and *FF* values obtained for the different technologies and their dependence on the $V_{oc}(25\,°C)$. Fig. 4.11 summarizes these results. As already mentioned the $TC_{V_{oc}}$ shown in Fig. 4.11(a) exhibits a clear dependence on the $V_{oc}(25\,°C)$. The SHJ devices exhibit much higher V_{oc} values, hence their $TC_{V_{oc}}$s are superior to the other devices. The slope obtained from a linear fit to the data yields 5.9×10^{-4}(%/ °C)/mV, whereas for the TC_{FF} trend shown in Fig. 4.11(b) a value of 8.2×10^{-4}(%/ °C)/mV is found. This shows that the TC_{FF} is more sensitive to high V_{oc} values. Here the difference between the SHJ and diffused-junction devices is also more pronounced. The improved TC_{FF} values for SHJ solar cells, however, might not only be linked to the high V_{oc} but also the presence of a small transport barrier—inherent to this device structure—as discussed in chapter 3.4 (p. 54). An increase in temperature fosters better carrier transport and hence a reduced decrease in *FF* is observed.

Despite the superior V_{oc} and temperature performance, the SHJ cell is outperformed by the diffused-junction devices, in terms of *FF*. This is clearly seen in Fig. 4.11(d). Judging by the

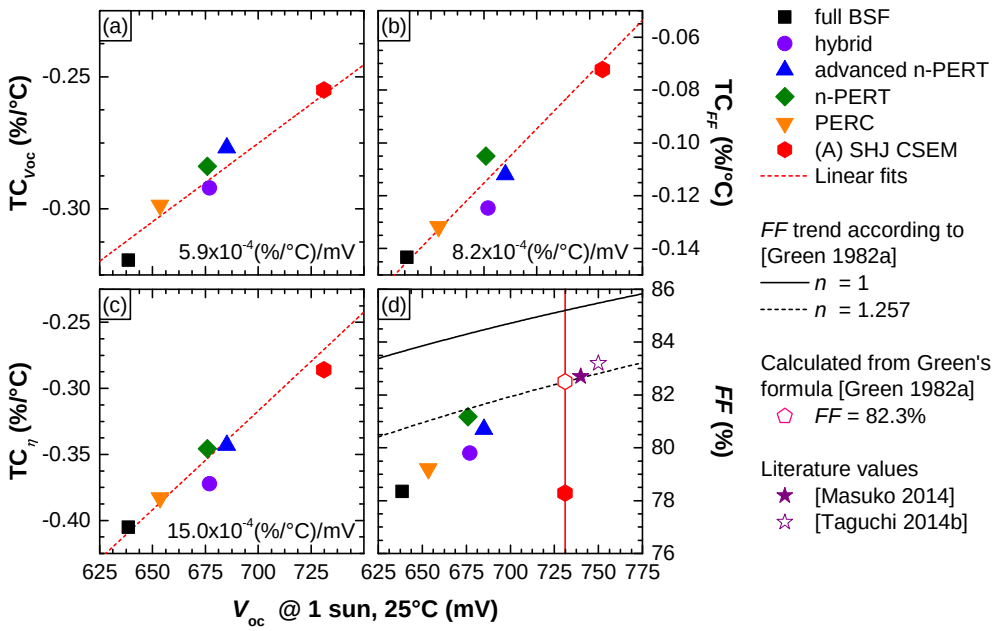

Figure 4.11 – (a)–(c): $TC_{V_{oc}}$, TC_{FF}, and TC_{η} as a function of the V_{oc} (taken at 25 °C and one sun). Note that the TC values were calculated for data > 40 °C. The straight lines are linear fits to the data. (d) *FF* data as a function of V_{oc} with literature values [Taguchi 2014] and [Masuko 2014] as well as the *FF* trends given by Green's empirical formula [Green 1982a].

V_{oc}(25 °C) value of 731.1 mV, and assuming the validity of Green's formula [Green 1982a]:

$$FF = \frac{v_{oc} - \ln(v_{oc} + 0.72)}{v_{oc} + 1} \quad \text{with } v_{oc} = \frac{qV_{oc}}{k_B T}, \tag{4.6}$$

the SHJ should in principle be able to reach a *FF* value as high as 82.5% respectively, a value that is indeed possible to reach as confirmed by Panasonic [Masuko 2014, Taguchi 2014]. This shows that the devices presented here are not limited by passivation but the by transport-related effects, *e.g.* barriers. As we will see in chapter 6, section 6.4 on p. 119, μc-Si:H layers can mitigate these transport losses at least to some extent.

4.3.3 Conclusion

The different behaviors we observe for the cells investigated here have to be linked to the differences in structure. It seems that the better the passivation, the better the performance of the device at higher temperature. This, however, is not exclusive for the trends in $TC_{V_{oc}}$, but also for the $TC_{V_{mpp}}$ and hence also for the TC_{FF}. The SHJ devices—the ones exhibiting

the best passivation and highest V_{oc}s—show the best temperature performance for all the parameters (V_{oc}, V_{mpp}, *FF*, and η) as function of irradiance (Fig. 4.10). The next devices in line are the advanced and standard *n*-PERT cells as well as the hybrid SHJ devices. The PERT cells, exhibiting a full area p^+ emitter and an Al_2O_3/SiN_x stack—passivating via field-effect—yield an even better temperature performance. However, they are limited by the direct metal contacts applied on both sides of the device. The hybrid, with a fully a-Si:H-passivated rear, shows similar trends than seen for the *n*-PERT cells. And finally, we turn to the PERC and full BSF cells. Both have less efficient passivation schemes and hence show marked differences especially in the $TC_{V_{mpp}}$ and TC_{FF} trends with irradiance. However, it is noteworthy that the PERC device reaches the same TC_{FF} values as the SHJ at low illumination. Furthermore we confirm that the standard SHJ devices used for this study are limited by transport-related losses in *FF* and not by a lack of passivation.

5 Alternative transparent electrodes

Highlights

This chapter is divided into two parts. Keeping the long-term goal of enhancing the J_{sc} in mind, here we present preliminary studies on the impact of ALD ZnO:Al[1] and organic semiconductor layers—meant as replacement for commonly used TCOs—on the *FF*, which, like the current, represents an equally important aspect for high device performance. Applying simple lifetime measurements we see significant differences in the behavior of τ_{eff}, when applying either of these materials on the a-Si:H(*ip*)- or a-Si:H(*in*)-side of a symmetrically passivated *n*- or *p*-type wafers. For the deposition of ALD ZnO:Al on the a-Si:H(*in*) stack or organic semiconductors on the a-Si:H(*ip*) stack of *n*-type wafers we observe promising enhancements of τ_{eff}, in particular at low injection levels—the range that affects the final *FF* the most. This shows the potential of work function engineering.

Note that the work on organic semiconductors, even though it matches very well with the needs for better hole-collecting contacts, was a side-project in this thesis. Therefore we limit ourselves to the presentation of the results without discussing organic semiconductors in detail.

5.1 Atomic-layer-deposited transparent electrodes: *impact on FF*

5.1.1 Introduction

Even though μc-Si:H and a-SiO_x:H can help to enhance the J_{sc}, their application in SHJ devices can be challenging as we have discussed in the previous chapters (μc-Si:H: chapter 6, p. 99 and a-SiO_x:H: chapter 3, p. 37). An even easier way is to minimize the thickness of the standard a-Si:H layers so as to reduce the associated optical losses (section 1.2.2.3, p. 13

[1] These results were gathered in a study conducted in collaboration with B. Demaurex (EPFL, PV-Lab, Switzerland) during the course of this thesis. The preceding study was published in the IEEE Journal of Photovoltaics, [Seif 2014a].

[Holman 2012]). Yet, this is limited by the necessity for high passivation quality and good carrier selectiveness, which are two indispensable ingredients for high-quality contacts. The surface passivation in particular can be strongly affected by the deposition of TCO layers by sputtering. Demaurex *et al.* [Demaurex 2012] showed that the use of this technique can induce damage to the a-Si:H/c-Si interface, and could link it to ion-bombardment but also to the irradiation by UV light emitted by the plasma during sputtering. For sufficiently thick a-Si:H layers, this sputtering-induced damage can be recovered to a large extent during the subsequent curing step (section 2.1.4, p. 27). Yet, thinner layers can give rise to permanent damage and hence lead to a reduction in V_{oc} and as a result in conversion efficiency. Therefore, in order to be able to benefit from reduced parasitic absorption with thinner a-Si:H layers, a soft deposition technique for TCO layers, such as ALD, is indispensable to form at least a thin protective TCO layer (~10–20 nm) against subsequent sputter-deposition. A few nanometers of sputtered material already has been shown to efficiently shield the underlying a-Si:H layers from further damage [Demaurex 2012].

Hence, in the first phase of this development, set apart the current-related objectives, we concentrated on the assessment of the suitability of protective ALD ZnO:Al layers and their impact on cell performance. This work has been published in [Seif 2014a] (see also [Demaurex 2014a]) and shall not be discussed in detail here. Instead we briefly summarize the main findings and concentrate on follow-up experiments focusing on the impact of similar ALD layers on the *iFF* of SHJ devices. The results are presented in the first part of this chapter.

In the preceding study we could show that the drop in τ_{eff}—observed for TCO deposition on the *ip*-side [Bivour 2013, Favre 2013, Rößler 2013]—is process-independent and results from the mere presence of the TCO, *i.e.* its work function mismatch to the layer beneath. However, a 20-nm-thick protective ALD ZnO:Al layer effectively shields the underlying a-Si:H layers and the a-Si:H/c-Si interface against sputter damage. Furthermore, higher *pFF* values were obtained for these samples due to lower recombination losses at low injection levels. We argued that these improvements are on one hand linked to the protection of the ALD film against subsequent sputter damage. However, the thinnest ALD-prepared layers—offering the least protection—yield the lowest recombination losses, likely, due to a detrimental effect of the work function of the TCO on the field effect passivation of the *ip* stack. This is evidenced by increasingly poorer passivation at low injection for increasingly thick ZnO films. As a consequence, the higher *pFF* values could indeed be linked to the protection, but the benefits may be offset due to the poorly matched ALD ZnO:Al. Increased R_s lead to important *FF* losses which outweigh the potential gain linked to the higher *pFF* values. This confirms again what we described in the introduction (section contacts, 1.2.2.4, p. 15)—namely that contacts have to be passivating, carrier-selective and majority-carrier conductive [Cuevas 2013, Bullock 2014, Wurfel 2015, Holman 2015]. The increased R_s is partly explained by the presence of a thin a-SiO_x:H layer acting as transport barrier for electrons and holes, formed at the a-Si:H/ZnO:Al interface during the fabrication process. Therefore, future goal to avoid any of these drawback while maintaining the benefits of lower recombination losses at low injection levels. The assessment of the limits of a-Si:H layer thickness and hence the

potential gain in J_{sc} when using thin layers in combination with ALD TCO layers was beyond the scope of the experiments presented here and requires further investigations in the future.

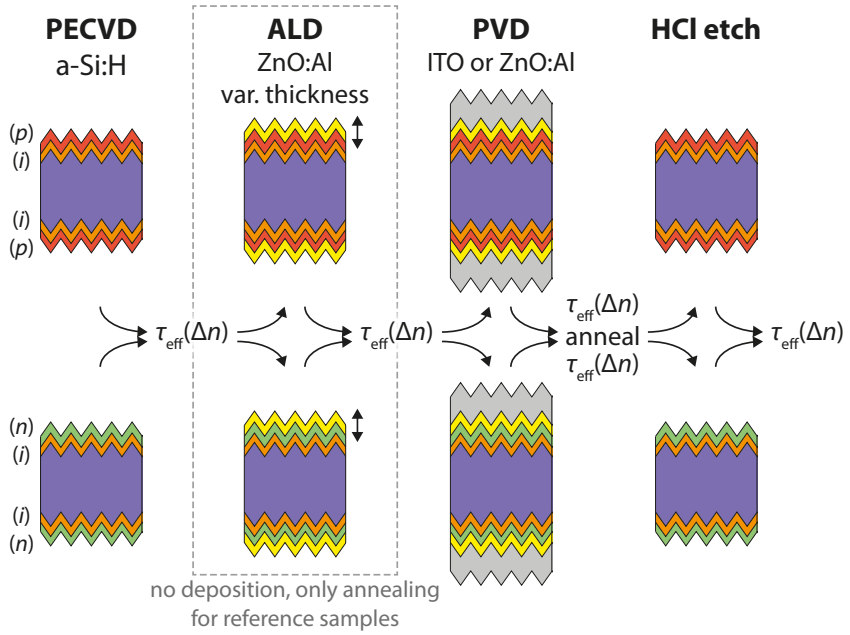

Figure 5.1 – Process flow.

5.1.2 Experimental details

For the experiments discussed here, we employed the same techniques as presented in [Seif 2014a]. However, compared to these preceding experiments, we focused exclusively on lifetime measurements of symmetric samples (*ip*/*ip* and *in*/*in*). The a-Si:H layers for these samples (textured, FZ, *n*-type, 2–3 Ω cm, 230 μm) were deposited in the Octopus II (see Tab. 2.1, p. 25). After PECVD, but prior to the ALD ZnO:Al depositions (see section 2.1.3, p. 26), the wafers were scribed by a laser and cleaved in half. The samples were then coated with ZnO:Al of nominal thicknesses: 5, 10, 20 and 40 nm at the *Eindhoven University of Technology*. Putting them upright into the ALD reactor, both sides of the wafers received the same coating. To ensure the same thermal budget for all samples, they were kept in the ALD reactor for the same amount of time. This was done not only for the samples that received an ALD ZnO:Al layer, but also for the reference samples that received a sputtered layer directly on the a-Si:H layers. Subsequently, ~65 nm of ITO or ZnO:Al was sputtered on both sides (for ALD and reference samples) and the samples were annealed at 200 °C for 25 min. Eventually, the TCO layers were stripped using HCl. Along the entire processing chain, τ_{eff} of the samples was

monitored to assess the passivation quality in each sample state. The process flow for the samples presented here is also shown in Fig. 5.1.

5.1.3 Results and discussion

As discussed in [Seif 2014a] and illustrated in Fig. 5.2(a) and (b), sputtering a TCO directly on either *ip* or *in* stacks shows differences in resulting τ_{eff}. For both types of samples τ_{eff} drops to lower values due to a degradation induced by the plasma's luminescence and ion bombardment [Demaurex 2012] [see Fig. 5.2(a), a.ITO]. However, this damage is mostly recovered by annealing [see Fig. 5.2(b), a.Ann]. Yet, as argued before, the work function mismatch between the TCO and the a-Si:H(*p*) layer suppresses the recovery of τ_{eff} at $\Delta n < 10^{15}$ cm^{-3}. This effect is normally not observed on the *in*-side. Yet, removing the TCO layers, re-establishes the same lifetime curve as before the TCO deposition proving the effect being linked to the mere presence of the TCO. As can clearly be seen from the figures, both iV_{oc} and iV_{mpp} are influenced by the different processing steps as indicated by the data points. This sequence of depositions and sample treatments therefore gives access to the effects implied by the TCO layers. Minor deviations are the result of the other processing steps.

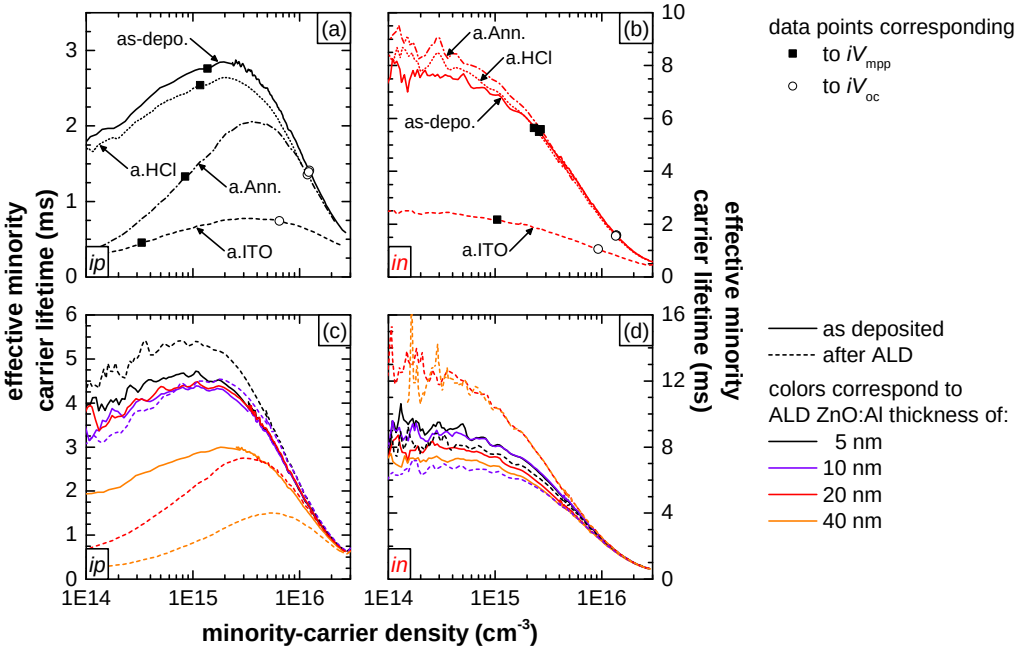

Figure 5.2 – (a) and (b) lifetime results for the reference samples (*ip*/*ip* and *in*/*in*) covered directly with ITO layers by sputtering. (c) and (d) results obtained after deposition of ZnO:Al layers of different thickness by ALD.

We focus now on Fig. 5.2(c) and 5.2(d), where τ_{eff} is given for *ip*/*ip* and *in*/*in* samples before and after the deposition of ALD ZnO:Al. Depositing ZnO:Al layers of ≥20 nm on *ip*/*ip* samples

yield similar trends as seen for *ip*/*ip* samples exhibiting ITO layers [data with ITO shown in Fig. 5.2(a)]. The same is true for the *in*/*in* samples with ITO, where τ_{eff} at low injection levels is not suppressed. Instead, the *in*-samples with ZnO:Al layers ≥20 nm show even a marked increase of τ_{eff} for injection levels up to 4×10^{15} cm^{-3}. As discussed in [Seif 2014a], this is the signature of an effect associated with the work function of the TCO. However, as depicted in Fig. 5.3(b), this time the TCO has a favorable effect on the band bending in both the a-Si:H(*n*) layer and the c-Si wafer. The enhanced field-effect passivation and the resulting increase in τ_{eff}, could potentially lead to higher *FF* in a finished device. For a different type of TCO the opposite might happen as shown in Fig. 5.3(c), where the TCO or TCO-replacing material—just as for the *ip*/*ip* case—depletes the a-Si:H(*n*) layer and lead to enhanced recombination due to a weaker band banding in the c-Si wafer. This is also discussed in chapter 5.2 (p. 90).

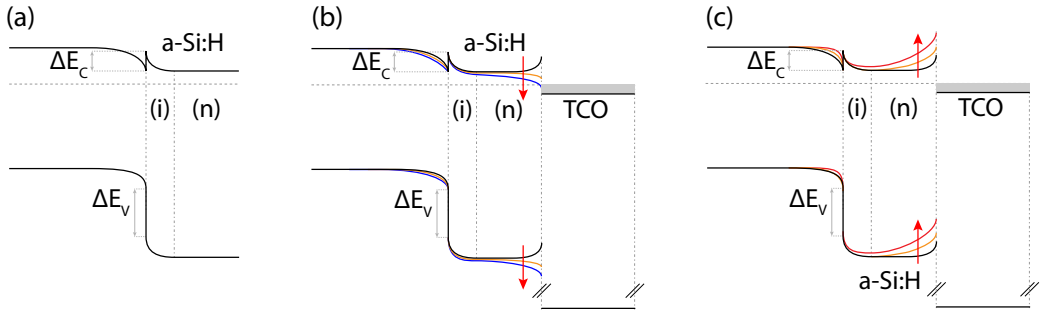

Figure 5.3 – Schematic representation of the band alignment for (a) the case without TCO on the *in* stack; as well as for a TCO with a work function (b) lower or (c) higher than that of a-Si:H(*n*). The arrows indicate the increasing work function mismatch. By courtesy of B. Demaurex (EPFL, PV-Lab, Switzerland) [Demaurex 2014a].

To evaluate the benefits of using a protective ALD layer in terms of τ_{eff} and resulting potential gain in *FF* in a finished device, the *iFF* values were extracted from the lifetime data. For the calculation of the latter the J_{sc} was set to 37 mA cm^{-2}, which is representative for actual J_{sc} values. The results are shown in Fig. 5.4, for *ip*/*ip* (top row) and *in*/*in* samples (bottom row). The variations are given with respect to the preceding processing step, *i.e.* variation between the as-deposited state (after PECVD) and the deposition of the ALD ZnO:Al layers (0–40 nm) or annealing inside the ALD reactor; between ALD and sputter deposition of ITO or ZnO:Al; between the TCO deposition by sputtering and the annealing step; and between annealing of the samples and the TCO removal by HCl.

In line from what has been already discussed above [Fig. 5.2(c) and 5.2(d)], the data shown in Fig. 5.4 makes the connection between τ_{eff} and *iFF*. First, we want to consider Figs. 5.4(a) and Fig. 5.4(e). Here we observe only minor changes for the thin ALD ZnO:Al layers (0–10 nm). However, layers ≥20 nm have a visible influence on *iFF*. For the *ip*/*ip* samples [Fig. 5.4(a)], the thick ALD ZnO:Al layer induces a severe drop in *iFF* (> −8% absolute for 40 nm ZnO:Al). This contrasts with the *in*/*in* samples for which a slight improvement is seen [> +1.5% absolute for 40 nm ZnO:Al, Fig. 5.4(e)]. This can be explained by the influence of the TCO on the a-Si:H

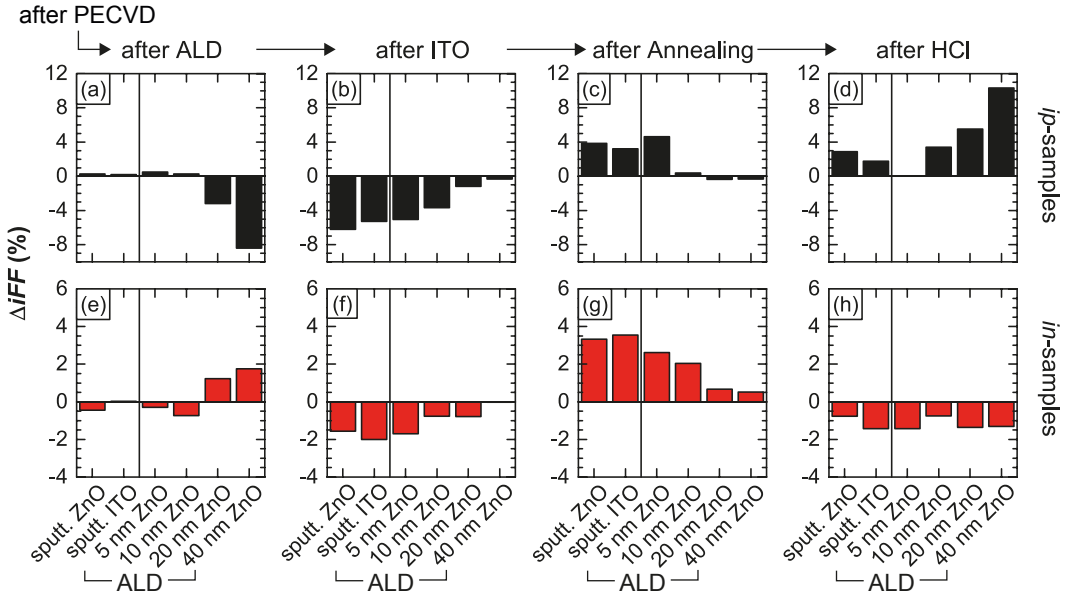

Figure 5.4 – Evolution of the *iFF* (relative changes, with respect to preceding step) seen for the *ip*- (top row) and *in*-samples (bottom row) along different stages: (a)+(e) after ALD, (b)+(f) after sputter deposition of ITO, (c)+(g) after annealing and (d)+(h) after TCO removal by HCl. The variation in *iFF* (ΔiFF) is calculated with respect to the previous processing step, which is the state after PECVD for the first column.

and in particular also the band bending within the c-Si wafer (Fig. 5.3 and [Seif 2014a]). It is also important to note that the reference samples do not exhibit any significant change in *iFF* after annealing in the ALD reactor. This shows that annealing at 180 °C does not significantly change the layers.

We now turn to Figs. 5.4(b) and 5.4(f) showing the relative *iFF* change between ALD and sputtering. They show that with increasing thickness of the protective ALD ZnO:Al layer the losses in *iFF*—which are associated with sputtering-induced damage—are less severe, as compared to the reference samples with sputtered ZnO:Al and sputtered ITO layers but without protective ALD ZnO:Al layer. This is more detrimental for the *ip*-samples than for the *in*-samples. We relate this to the accumulation of sputter damage and the effect of the work function, which is stronger for the *ip* case than for the *in* case, as discussed before [Fig. 5.2(a) and 5.2(b)]. Furthermore it is to note that the changes for the samples exhibiting a 40-nm-thick protective layer are low or not present at all. However, this is not necessarily due to protection but likely due to the fact that the work function effect of the ALD ZnO:Al itself already induced a strong suppression of τ_{eff} at low injection levels.

Annealing the samples, as shown in Figs. 5.2(c) and 5.2(g), leads to an increase in *iFF* for the two references (plain, sputtered ITO or ZnO:Al) as well as for the samples with thinner ALD layers. This contrasts with the samples with thick ALD layers, for which a slight increase [*in*, Fig. 5.2(g)] or even a slight decrease [*ip*, 5.2(c)] is observed. For the *ip*-samples, this can again

be explained by the effect of the work function. The increase in lifetime that is seen for the other samples is screened by this effect.

Finally, removing the TCO stacks by dipping the samples in HCl shows a clear recovery from the work function effect for the *ip*-samples and hence an increase in *iFF*, whereas the *in*-samples show a systematic decrease, which again points to the beneficial effect of the TCO layers on the *in*-side.

Comparing the as-deposited *iFF* values for both sets of samples to the values of the annealed state—the one corresponding closest to a finished device—we do not see any improvement on the *ip*-side (data not shown here) since the influence of the work function is too strong, as mentioned above. Yet for the *in*-side, interestingly, the 40-*in*-sample shows a slight increase in *iFF* compared to the reference (~0.7% absolute).

For ZnO:Al deposited on solar cell precursors by ALD, we do not observe a vertical downshift of the lifetime curves—as expected—whereas the decrease of carrier lifetime at low injection levels remains [Fig. 5.2(b)]. The latter confirms that the responsible recombination centers are not formed by the TCO-specific deposition process but are merely activated by the presence of an overlayer with a given work function. Notably, we observe an ALD thickness dependence for the lifetime curves at low injection levels. This could either be explained by gradient effects in the build-up of the bulk ZnO, *i.e.* decreasing work function starting from a high value at the interface, or by the presence of adsorbed species at the ZnO:Al surface, affecting the work function of the ZnO:Al films at its interface with a-Si:H. On the a-Si:H(*n*) side, no low-injection decrease is observed, indicating that no recombination centers are activated by the presence of the TCO. In fact, the opposite is the case, and τ_{eff} increases.

5.1.4 Conclusion

Here, we presented a method—relying on the high sensitivity of wafer passivation to the effects of any possible work function mismatch—to evaluate the suitability for application of any kind of material in a SHJ solar cell. This could prove particularly useful for the optimization of transparent electrode layers. Furthermore, we find that ALD as a soft deposition technique can be beneficial in terms of *iFF* and V_{oc} and hence for device performance.

Trying to maximize the J_{sc} by applying thinner a-Si:H layers, the application of the ALD ZnO:Al layers could prove essential to prevent sputter-induced damage. When applied to the *in*-side of a symmetrically-passivated *n*-type wafer they show a potentially beneficial effect. However, when deposited on the *ip*-side of a device we observe a severe effect on the low-injection τ_{eff}. This effect is likely impaired for thinner a-Si:H(*p*) layers. Therefore, to avoid this effect, it is necessary to optimize the doping and hence the work function of the materials discussed here. Another possibility is to collect holes at the rear of the device, which would allow for thicker a-Si:H(*p*) layers and hence a mitigation of the work function effect on the c-Si part, *i.e.* improving the *iFF* [Tomasi 2015].

This however might not be sufficient, due to the following reasons: (1) the a-SiO_x:H transport barrier—which we evidenced in the preceding study [Seif 2014a]—which has to be avoided and (2) the likely formation of an inverse diode at the a-Si:H(*p*)/TCO interface—as we have discussed in the experimental part (section 2.2.2.3, p. 33, Fig. 2.6)—which can have an impact on the contact resistivity (section 1.2.2.4, p. 15). An alternative route, could be the application of transparent electrodes deposited by low-pressure chemical vapor deposition or the application of a different material that does not degrade the hole contact in terms of low-injection τ_{eff} and that exhibits good contacting properties, which ensure low contact resistivities. Possible candidates are presented in the following section.

5.2 Organic semiconductors as transparent electrodes

5.2.1 Introduction

Hole-collecting, low-refractive-index organic semiconductors may prove beneficial both optically *and* electronically. It has been found that low-refractive-index materials may be applied at the interface to the metallic electrode and reflector at the rear to mitigate plasmon-related J_{sc}-losses [Holman 2013b]. Furthermore, as they may be used to replace both the a-Si:H(*p*) layer and the TCO, they could mitigate or even completely avoid any work function mismatch effect—helping increasing the *FF*—and with an evaporated metal contact also sputter-induced damage. Before applying these materials in a device, we investigated their impact on the electrical properties and the *iFF* in particular as we did for ALD ZnO:Al layers in section 5.1 (p. 83).

As we have seen in section 5.1 (p. 83), there is still room for improvement of the *p*-type contact of SHJ devices. We have seen that the direct deposition of common TCO materials (*e.g.* ITO or ZnO:Al) on the a-Si:H(*ip*) stack of an *n*-type wafer can have a severely negative effect on the low-injection τ_{eff}, which can degrade the *FF* in a finished device [Seif 2014a]. Unfortunately, the lack of *p*-type TCO materials sets strong restrictions to the optimization of the TCO/a-Si:H(*p*) contact. The only viable option is to tune the work function of these TCO layers is by changing their doping level. Achieving a better work function matching to the adjacent a-Si:H(*p*) layers in particular could help to reduce these losses (discussed in section 5.1.3, p. 86). This explains the interest in hole-conducting organic semiconductors, which have the potential to mitigate any work function-related reduction of τ_{eff} at low injection levels and hence could help increase the *FF*. Furthermore, another aspect is the ease and low-cost method of processing these materials. Compared to more sophisticated techniques like PECVD or sputtering, spin-coating—which can be used to apply films or organic semiconductors—is applicable to a variety of different devices and surfaces and does not rely on expensive high-vacuum equipment.

Semiconducting polymers have found application in optoelectronic devices such as organic light-emitting diodes [Kido 1994, Lamansky 2001] and solar cells [Kippelen 2009, Dennler 2009,

Table 5.1 – PVK specifications.

organic semiconductor	doping	dopant concentration [μl/ml]	thickness [nm]
PVK # 01	no doping	0	~54
PVK # 02	low doping	1.8	~51
PVK # 03	high doping	17.5	—
Spiro-MeOTAD	—	—	~300

Deibel 2010, Voroshazi 2011, Thompson 2008]. So far, however, these materials were used mainly for thin-film photovoltaic devices. Recently promising results were reported on c-Si(n) wafer-based hybrid cells with hole collection through PEDOT:PSS films[2] deposited either at the front or the rear of the device [Schmidt 2013, Zielke 2014]. Even though PEDOT:PSS has been successfully applied as a hole-collecting layer in silicon-based solar cells, significant parasitic absorption losses due to the strong FCA limits its application on the front side of the cell.[3] For this reason the main interest lies in applying semiconducting polymers in devices with hole-collection at the rear. As we already discussed in chapter 3 (p. 54), this might be the most favorable way to collect holes in both-sides-contacted SHJ devices.[4]

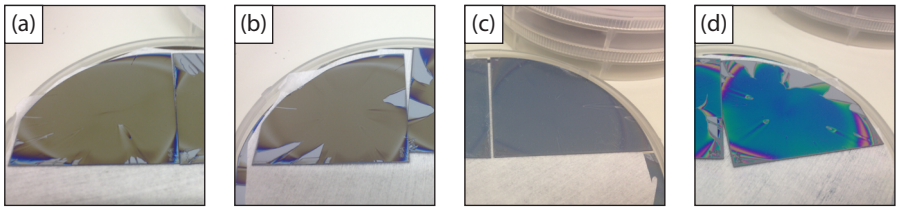

Figure 5.5 – Photos of the different organic semiconductors applied in this study: (a) undoped, (b) lowly-doped (c) highly-doped PVK (polymer) as well as (d) Spiro-MeOTAD (molecule) on c-Si samples.

5.2.2 Experimental

For the experiments presented in this chapter, we used DSP n-type (FZ, (111), 255–305 μm, 1–5 Ωcm) and p-type (FZ, (100)-oriented, 255–305 μm, 1–5 Ωcm) c-Si wafers. The samples received symmetric passivation layers (i/i, ~ 8 nm on the DSP) or stacks (in/in, ~ 15 nm or ip/ip, ~ 12 nm) deposited in the KAI-M (see Tab. 2.1, p. 25). Note that in the following the different samples are labeled as [*layer type*]-[*wafer type*]. So for instance a sample based on a

[2] Technical term: poly(3,4-ethylenedioxythiophene):poly(styrenesulfonate).

[3] As polymers typically exhibit low carrier mobilities the have to be strongly doped to enable good transport properties. This, however, leads to strong FCA, which is much lower in undoped polymers.

[4] This study was conducted in collaboration with B. Niesen, who helped with preparation of polymer solutions and spin-coating.

p-type wafer with a-Si:H(*in*) layers on both sides is referred to as '*in-p*'. The different sample types and the different processing steps are also depicted in Fig. 5.6.

Following the PECVD, the samples were cleaved into quarters and four different organic semiconductors were applied by spin-coating on one side only. Here we used poly(N-vinylcarbazole) (PVK), dissolved in chlorobenzene at a concentration of 10 mg/ml, of three different levels of lithium bis-trifluoromethanesulfonimidate, which acts as dopant and 2,2',7,7'-tetrakis(N,N-di-p-methoxyphenylamine)-9,9'-spirobifluorene (Spiro-MeOTAD). The latter is a small molecule used as hole transporter *e.g.* in lead iodide perovskite thin film solar cells [Kim 2012] or solid-state dye-sensitized solar cells [Krüger 2001, Campbell 2007, Snaith 2007]. For further details on the organic semiconductors see table 5.1. Each time 150–200 μl of the respective organic semiconductor solution was dispensed on the wafer and spun at 1000 rpm for 5 s and for 60 s at 2000 rpm. After spin-coating, the samples (except the Spiro-MeOTAD samples) were annealed on a hotplate at 100 °C for ~5 min to evaporate the solvents. Both the spin-coating and the annealing were performed in a glove box under nitrogen atmosphere. It is noteworthy that compared to the undoped and lowly-doped material, the highly-doped PVK showed a formation of clusters of the different constituents in the polymer solution and hence is likely not applicable to devices [see Fig. 5.5(c)].

The organic semiconductor layers thicknesses were determined by profilometry. However, this technique was only applicable to the undoped and lowly-doped PVK (# 01 and 02) as well as for the Spiro-MeOTAD samples. It was not possible to determine the thickness of the highly-doped PVK sample (# 03) as the film was not homogeneous. All the samples were measured after PECVD and after processing the organic semiconductors (spin-coating and annealing) by PCD.

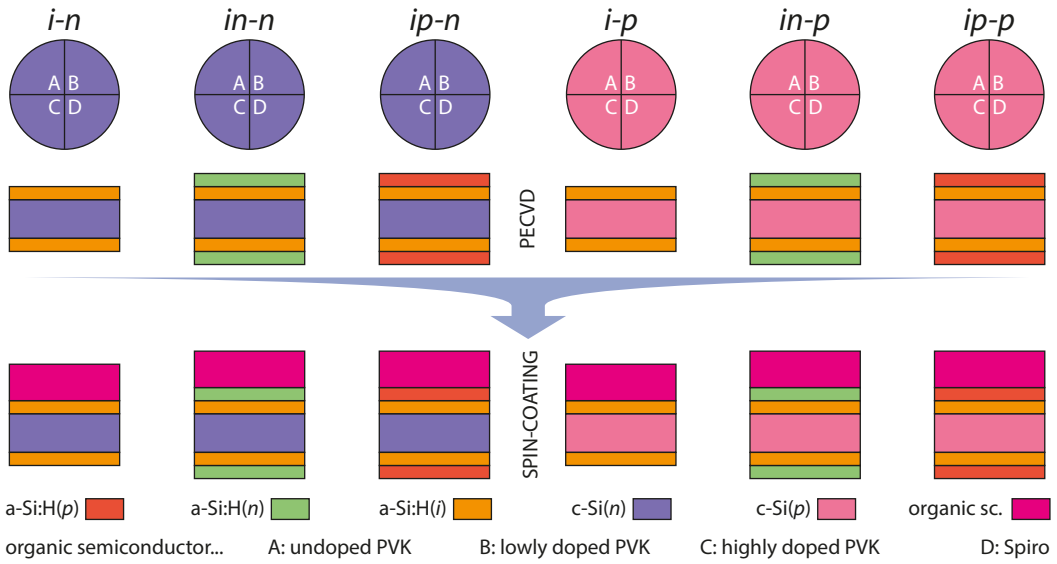

Figure 5.6 – Overview over the samples processed in this study.

5.2.3 Results and discussion

Before discussing qualitatively the lifetime results of the *p*-type or *n*-type samples processes in this work, we want to draw the attention to a general fact. Comparing the lifetime values obtained for *p*-type and *n*-type—that is discussed in section 5.2.3.2—wafers directly after PECVD shown in Figs. 5.7 and 5.9, we already see a significant difference. While the *n*-type samples exhibit high lifetime values at low injection levels, the *p*-type samples already show lower values. This can be related to the asymmetric of defect capture cross-sections for electrons and holes [Descoeudres 2013] or the different terminations of (111) and (100) c-Si wafers, the latter exhibiting twice as many dangling bonds at the surface.

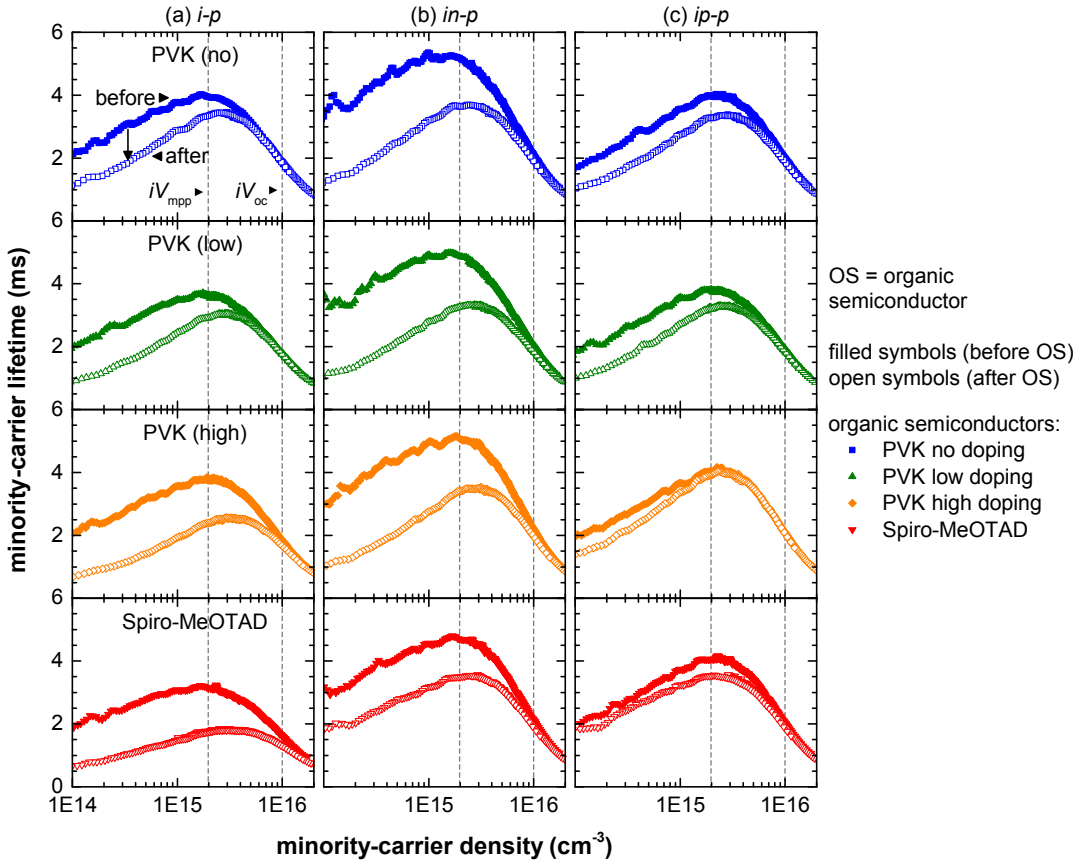

Figure 5.7 – Minority-carrier lifetime as a function of the minority-carrier density obtained for *p*-type wafers with symmetric (a) *i*/*i*, (b) *in*/*in* or (c) *ip*/*ip* a-Si:H layers.

5.2.3.1 Organic semiconductors on *p*-type wafers

We now turn to the lifetime results obtained on *p*-type wafers after the deposition of the different organic semiconductors by spin-coating (Fig. 5.7). In addition to the already mentioned

low τ_{eff} values at lower injection levels, both the *i-p* and the *in-p* samples show a significant additional decrease in lifetime. This decrease is seen for injection levels below 8×10^{15} cm^{-3}. Furthermore, a clear trend is observed with increasing organic film doping for the *i-p* samples [Fig. 5.7(a)]. In this particular case Spiro-MeOTAD affects the passivation even up $\Delta n = 1\times10^{16}$ cm^{-3}, injection levels associated with the iV_{oc}. Comparing these results to the *ip-p* samples a clear difference is apparent as these samples show a much less pronounced effect. As argued in section 5.1 (p. 83) for either ZnO:Al and ITO deposited on a-Si:H(*ip*) side of c-Si(*n*), this reduction in τ_{eff} is related to an effect of the organic semiconductors on the band bending within the c-Si bulk. The same leads to a reduction of the field-effect passivation and hence to an increase in recombination.

In comparison to the *n*-type TCOs discussed in section 5.1—applied symmetrically to the samples—the results obtained for organic, *p*-type materials, applied on one side only in the *i-p* and *in-p* samples, confirm what we expected. However, following the same reasoning, we would expect an increase of τ_{eff} at low injection levels for the *ip-p* samples. What we rather observe, is a slight decrease, though the variation is much less pronounced compared to the other samples. This is especially true for the highly-doped PVK and Spiro-MeOTAD samples. The fact that we do not see an increase might be associated to the already low lifetime values after PECVD, linked to the less efficient passivation of *p*-type wafers by a-Si:H(*i*) layers [Descoeudres 2013]. This may screen any potential improvement these layers could bring.

To relate the effects we see to real devices and assess their potential impact on the *FF* we compare the *iFF* values before and after the deposition of the organic materials extracted from the lifetime data shown in Fig. 5.7 (see also section 5.1). For *i-p* and—slightly less so—for *in-p* samples the *iFF* exhibit decreasing trends with increasing dopant concentration. The *ip-p* samples on the other hand show an *iFF* decrease after the deposition of the organic semiconductors, but even though the highly-doped PVK shows only a slight decrease, we do not observe a clear trend with doping (Fig. 5.8).

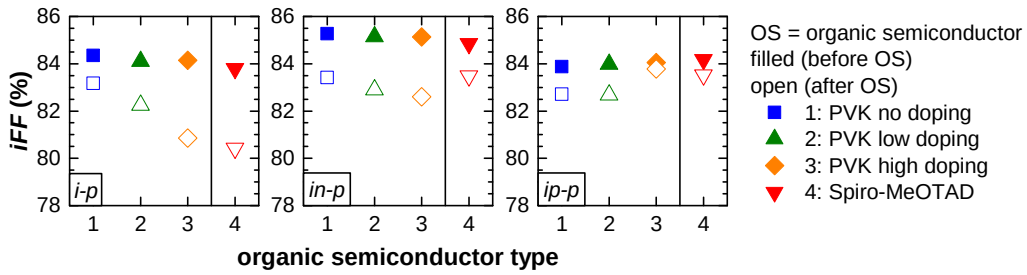

Figure 5.8 – *iFF* data for each of the *p*-type samples covered with different organic semiconductors. The data was extracted from the lifetime data shown in Fig. 5.7.

To summarize, we do not see an improvement of the *iFF*, depositing the here-investigated organic materials on *ip*/*ip*-passivated *p*-type wafers. However, we do not see a strong decrease

either. Yet, due to the lack of a sufficiently good statistic, it is too early to conclude that the application of organic semiconductors on *p*-type wafers is not possible. Nevertheless, the results obtained here, do not raise high expectations.

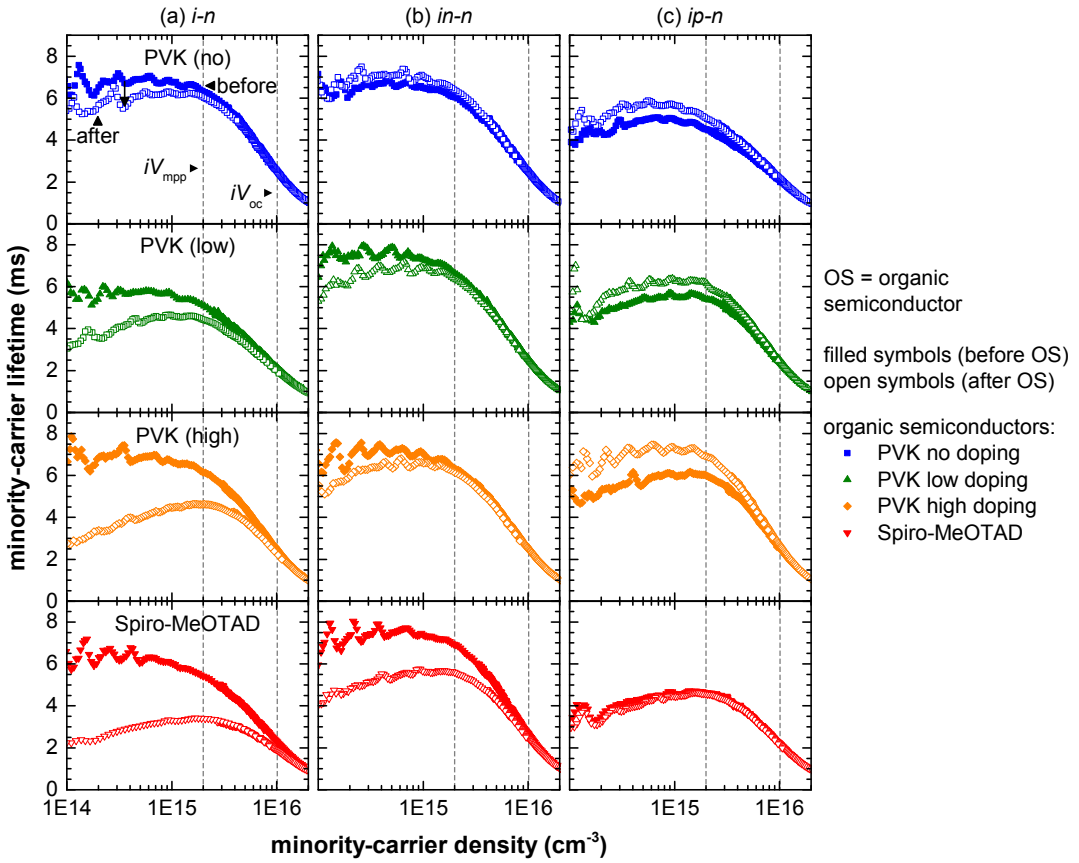

Figure 5.9 – Minority-carrier lifetime as a function of the minority-carrier density obtained for *n*-type wafers with symmetric (a) *i*/*i*, (b) *in*/*in* or (c) *ip*/*ip* a-Si:H layers.

5.2.3.2 Organic semiconductors on *n*-type wafers

After the discussion of the results obtained on c-Si(*p*)-based samples, we now turn to the data collected for samples based on *n*-type wafers (see Fig. 5.9). For organic semiconductors deposited on the *i*-*n* samples, we observe a similar trend as for the *i*-*p* samples discussed in the section before or for samples exhibiting *n*-type TCO layers deposited on similar samples (section 5.1, p. 83). Yet, the *i*-*n* samples *exhibit* a decreasing τ_{eff} at low carrier injection [Fig. 5.9(b)], which in contrast to their *i*-*p* counterparts is less steep [5.7(a)]. The trends for the *in*-*n* samples on the other hand are less clear as the lifetime stays almost stable compared to the other cases discussed so far. While for the lowly-doped PVK a slight increase in lifetime is achieved, the lifetime decreases for the samples with higher dopant concentration or Spiro-

MeOTAD. Since we are dealing with *p*-type organic semiconductors, this effect is expected and likely represents to analog work function effect we observe for *n*-type TCOs on *p*-type layers. The fact that the effect is more pronounced for the *i*-*n* samples than for the *in*-*n* samples may be explained by the difference in a-Si:H layer thickness. The sample with the simple *i*-layer—being only approximately half as thick as the *in* stack—will be more sensitive to the work function effect than the thicker *in*-stack. The most interesting observation for this set of samples, however, is the increase in lifetime seen for the *ip*-*n* samples. Again following the same reasoning as in section 5.1 for *n*-type TCOs, the *p*-type organic semiconductors are expected to have the inverse effect, which indeed seems to be the case. Instead of deteriorating τ_{eff} at low injection levels, τ_{eff} is enhanced by the presence of the PVK, except for the Spiro-MeOTAD sample for which τ_{eff} remains stable.

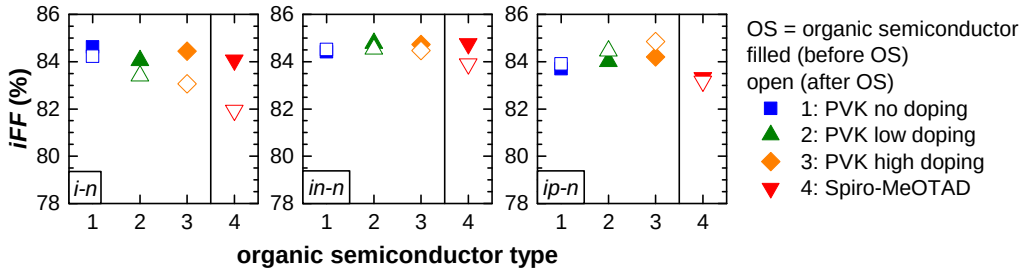

Figure 5.10 – *iFF* data for each of the *n*-type samples covered with different organic semiconductors. The data was extracted from the lifetime data shown in Fig. 5.9.

We now turn again to the *iFF* results. A negative influence on the *iFF* (Fig. 5.10) is observed only for the *i*-*n* samples as expected from the lifetime results. And while for the *in*-*n* samples *iFF* stays virtually stable, the *ip*-*n* samples show a distinct increase. In a device this could enable better hole-collecting contacts and improved *FF* values.

5.2.4 Conclusion

Deposited on *in*-*n* samples the *p*-type organic semiconductors, investigated here, show the same behavior as observed for *n*-type TCOs deposited on *ip*-*n* samples (section 5.1, p. 83), namely they induce a reduction of low-injection τ_{eff}. The same effect is also particularly pronounced for *in*-*p* samples. The *ip*-*p* samples are less affected. Furthermore, we have shown that in terms of application to the *ip*-*n* interface, PVK could indeed be an interesting alternative to replace the standard TCO layers. However, the replacement of the whole stack (a-Si:H(*p*) / *n*-type TCO) might not be viable, as we have seen that the organic materials strongly deteriorate the lifetime when deposited directly on the a-Si:H(*i*) layer.

Hence, given the fact that organic semiconductors provide sufficiently good charge transport properties—enabling good carrier collection and high *FF* values—they could be applied to

a-Si:H(*ip*) stacks to mitigate the recombination losses on one hand and optical losses associated with plasmon absorption on the other. Their application would entail a change in the process procedure, in particular the deposition of the metallic rear reflector and contact. This layer is typically deposited by sputtering, which could be potentially harmful to the organic materials. A possible alternative could be the application of this metallic layer by evaporation. Benefits for the conversion efficiency of SHJ solar cells, ensuing from the application of organic semiconductor layers, are yet to be proven.

Besides the electrical and optical aspects briefly discussed here, future studies will also have to investigate the stability of the materials tested here with respect to long term application. In this respect, the hygroscopic nature of certain organic semiconductors may play an important role, as the saturation of the layers with water can result in impaired carrier transport [Voroshazi 2011]. This in combination with their optical properties, provide an additional argument for their application at the rear of the SHJ device. There, the transparent electrode is completely covered by a metal, severing as electrode but also to protect the layer beneath against water ingress. Furthermore, the conductivity of the organic layer has to ensure transversal transport only.

6 Microcrystalline layers for silicon heterojunction solar cells

Highlights

This chapter is divided into three parts. First, we discuss the requirements for the implementation of microcrystalline (μc-Si:H) layers in SHJ solar cells, strategies how to obtain these layers and assess their suitability for application in SHJ devices. Then, we focus on the impact of different deposition conditions for μc-Si:H material on the τ_{eff} of passivated wafers. As discussed in chapter 1.2.2.2 (p. 7) and 1.2.2.4 (p. 14) this it is of great importance for the performance of a device. And finally, we turn to cell results obtained in different deposition regimes, clearly showing the potential of μc-Si:H layers for SHJ solar cells that enable significant gains in *FF* and J_{sc} compared to our standard all-a-Si:H devices. Here we report up to +2.1% absolute and +1 mA cm^{-2}.[1]

6.1 Introduction

The interest in μc-Si:H as replacement for the standard a-Si:H charge-selective contacts in SHJ solar cells is manifold. In terms of optical properties, the most interesting aspect is the fact that it exhibits an indirect bandgap of 1.1 eV in the crystalline part. This ensues a reduction of the absorption in the high-energy photon range [Vetterl 2000]. Hence, applying μc-Si:H to the front of a SHJ device can potentially help to increase in J_{sc} [Madani Ghahfarokhi 2014, Watahiki 2015, Mazzarella 2015]. The low-energy absorption obtained for μc-Si:H—even though it is higher than for a-Si:H—may only play a subordinate role for device-relevant layer thicknesses of a few nanometers [Vetterl 2000]. For this reason the μc-Si:H bottom cell in micromorph thin-film silicon solar cell devices has to exceed a few hundred nm up to several μm in order to absorb the red light efficiently.

Besides this optical advantage, μc-Si:H also exhibits better transport properties thanks to its more ordered phase and higher doping efficiency. This renders it a promising material

[1] The results reported here were obtained with the help of S. Hänni, M. Boccard, G. Nogay and J. Geissbühler (EPFL, PV-Lab, Switzerland), contributions are gratefully acknowledged.

for carrier-selective contacts and as contacting material to the TCO layers in particular. The a-Si:H/TCO interface, as we have seen in chapter 5 (p. 83), is very sensitive and prone to the formation of inverse Schottky diodes [Glunz 2007, Bivour 2014, Bivour 2013, Seif 2014a], an effect that is claimed to be mitigated by μc-Si:H [Madani Ghahfarokhi 2014]. Another explanation is the amelioration of the contact resistance enabled by μc-Si:H carrier collecting layers. This issue has been analyzed in detail for IBC devices, clearly showing the potential of low contact resistances on either of the two carrier-selective contacts [Tomasi 2014]. An additional aspect is the narrower bandgap leading to smaller effective band offsets. This of particular interest for the hole-collecting layer, as it would enable more efficient collection (see chapter 3, p. 3).

All these benefits give a strong incentive to take on the challenges the implementation of μc-Si:H layers into SHJ solar cells holds. They are related to the following requirements: (1) the thickness of the μc-Si:H layers should be in the range of the typical a-Si:H thicknesses used in SHJ devices (on the order of 10 nm) in order to maximize the optical gain. This requires fast nucleation and hence avoidance of a-Si:H incubation layers [Vetterl 2000]; (2) to ensure good transport and contacting properties they should be sufficiently doped; but, at the same time (3) be highly microcrystalline. The difficulty is, to meet all these requirements without damaging the essential passivation layers [De Wolf 2012b] which are known to be very sensitive to post-passivation processing [Demaurex 2012, Geissbühler 2013]. So the main goal in this work was to optimize the deposition conditions according to these requirements.

The substrate's surface morphology and chemistry play an important role [Vallat-Sauvain 2005, Zhang 2011, Roca i Cabarrocas 1995] and—deposited on an a-Si:H layer—the μc-Si:H films tend exhibit an incubation layer, which—depending on the deposition conditions—can be on the order of tens of nanometers. But besides the substrate, microcrystalline growth strongly depends on the deposition conditions. One of the main parameters is the SiH_4 concentration in the plasma, which is determined by the SiH_4 depletion and hydrogen dilution [Strahm 2007a, Strahm 2007b]. Depending on the application, the SiH_4 concentration in the plasma is strongly influenced by different deposition parameters: pressure, power, gas flows and frequency [Finger 1994, Strahm 2007b, Smets 2008]. Conversely, μc-Si:H growth is very sensitive to doping introduced into the film [Saleh 2002]. Phosphorous and—even more so—boron lead to increased disorder in the growing film and hence to a thicker incubation layer or even complete amorphous growth [Chou 1992]. However, they are indispensable for the formation of carrier-collecting layers.

Different models have been proposed to explain μc-Si:H growth, but one thing they all have in common, which is the influence of hydrogen on the growing film: (1) The *selective etching model* refers to H_2 etching the a-Si:H phase more efficiently than the μc-Si:H phase, thereby fostering order within the silicon layer [Tsai 1989, Schmitt 1989, Asano 1990, Boland 1992]; (2) According to the *surface diffusion model* [Matsuda 1983], the diffusion length of the SiH_3 radicals—that lead to the film growth—is enhanced by the presence of hydrogen at the surface, leading to an increased probability for them to find an adequate site to attach. For this to

happen the deposition rate of the material has to be sufficiently slow; and finally (3) the *chemical annealing model*—in which the energy emitted by the formation of molecular H_2 within the film, leads to reorganization of the structure which may lead to nucleation of crystallites. These models are discussed *e.g.* in [Matsuda 1999, Terasa 2002, Matsuda 2004, Strahm 2007b]. It is important to note that these models depend on the deposition regime—*e.g.* at high deposition rates, the surface diffusion model fails, as too much material arrives before the radicals can find a suitable place—and that likely a combination of the phenomena described lead to μc-Si:H growth. Furthermore, it has been shown that μc-Si:H grows more easily on substrate layers exhibiting compressive stress [Fujiwara 2004] as well as on oxidized [Ross 2000, Pellaton Vaucher 1997] or even a-SiO_x:H layers [Choong 2009].

Despite the fact that there are numerous techniques to grow μc-Si:H layers, not all of them are equally suitable for application in SHJ devices. The first part of this chapter focuses therefore on different strategies and discusses their suitability for this type of solar cells. The second part is dedicated to the impact of μc-Si:H(n) and μc-Si:H(p) layers on the passivation quality of the c-Si interface and the potential damage associated with sputtering of TCO layers. And eventually, in the third part we discuss the impact of μc-Si:H layers on devices based on cell results.

6.1.1 Experimental details

All the experimental results shown in this chapter were obtained with either the KAI-M or Octopus I (see section 2.1.2.1, p. 24), or combining both (*e.g.* a-Si:H layers in KAI-M and μc-Si:H layers in Octopus I). The gases used for the depositions were SiH_4, Si_2H_6, SiF_4, H_2, D_2, $B(CH_3)_3$ (diluted in H_2 at 500 ppm), PH_3 (diluted in H_2 at 20'000 ppm) and Ar. The latter was reported to have a beneficial effect on the crystalline growth but was not used if not explicitly mentioned [Das 1996].

First, the μc-Si:H layers were either deposited directly on glass or on glass coated with a-Si:H for characterization purposes. In a later step they were applied to passivated wafers and eventually implemented into SHJ devices. The solar cells fabricated in this study all received the standard ITO layers at both the front and rear, a silver back contact and a screen-printed front contact. Further details on the deposition equipment and the processes used for fabrication of layers and cells are discussed in chapter 2 (p. 23).

For the characterization of the μc-Si:H layers, both SE and Raman spectroscopy were used.[2] The Raman crystallinity (χ_c) was extracted as described in section 2.2.1.2 (p. 28). For layers thicker than 20 nm, the thickness was also measured by profilometry (Ambios XP-2). Note that the thickness values given here correspond to the thickness on flat substrates if not mentioned differently.

[2] The Raman measurements on textured wafers were conducted by M. Ledinsky (Institute of Physics, Czech Academy of Sciences, Prague, Czech Republic) using the Renishaw InVia REXLEX. See chapter 2 for more details.

Besides applying the standard measurement techniques (*J*-*V*, lifetime, PL, suns-V_{oc}, EQE, see chapter 2, p. 23), we also used HRTEM to investigate the growth of selected μc-Si:H layers deposited by SiF_4 plasma chemistry on a-Si:H(*i*)-coated (111) oriented DSP wafers. These samples were processed as described in section 2.2.1.3 (p. 29).[3]

6.2 Strategies for thin, doped and microcrystalline layers

In this section we focus specifically on how to integrate boron-doped [μc-Si:H(*p*)] and phosphorous-doped [μc-Si:H(*n*)] layers into SHJ solar cells, while satisfying the requirements mentioned above. We outline strategies to obtain ultrathin microcrystalline silicon films applicable for SHJ solar cell fabrication.

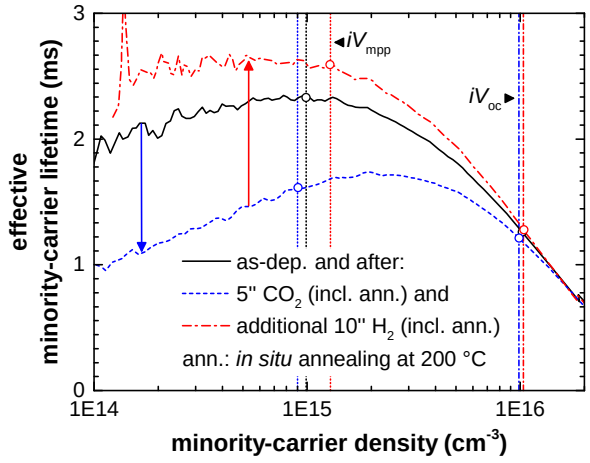

Figure 6.1 – Effective minority carrier lifetime as a function of the minority carrier density, for different sample states: (black solid) c-Si(*n*) with as-deposited *i*/*i* passivation, (blue dashed) after a 5 s CO_2 plasma treatment (including ~10 min *in situ* annealing at 200 °C), and (red dashed-dotted) after additional 10 s H_2 plasma treatment (including ~10 min *in situ* annealing at 200 °C). The vertical lines indicate the ranges associated to the implied voltages at the mpp and in oc conditions.

6.2.1 Surface treatments and nucleation layers

6.2.1.1 CO_2 plasma treatment and intrinsic a-SiO_x:H nucleation layer

Using a CO_2 plasma pretreatment prior to the deposition of a μc-Si:H layer has already been proven to facilitate nucleation of both *p*- and *n*-type layers [Pellaton Vaucher 1997, Pernet 2000]. However, in contrast to silicon thin-film solar cells, the passivation layer of an SHJ solar cell and the crystalline surface can be extremely sensitive to subsequent plasma treatments [Geissbühler 2013]. Fig. 6.1 shows the results of exposing one side of a symmet-

[3] The HRTEM analysis was performed by M. Duchamp (Forschungszentrum, Jülich, Germany).

rically a-Si:H(*i*)/a-Si:H(*i*) passivated wafer to a CO_2 plasma ignited at 40.68 MHz. Using a power density of 0.125 W/cm^2 at a pressure of 0.7 mbar, we observed a drop in minority carrier lifetime. Even though this drop does not affect the iV_{oc} too much, it is especially pronounced at low injection levels (see data points in Fig. 6.1)—the ones associated to the iV_{mpp}—which can potentially have a negative effect on the *FF* of a device [Seif 2014a]. However, the lifetime recovers after a subsequent H_2 plasma treatment and *in situ* annealing at 200 °C, which points to the creation of defects which can be re-passivated by plasma-induced hydrogenation or thermal diffusion of hydrogen [De Wolf 2008]. Since μc-Si:H layers are deposited from highly H_2-diluted plasmas, this drop in effective minority-carrier lifetime may not be a limiting effect here. However, as we discuss in the following, the introduction of a barrier associated to an a-SiO_x:H layer can have a detrimental effect on transport.

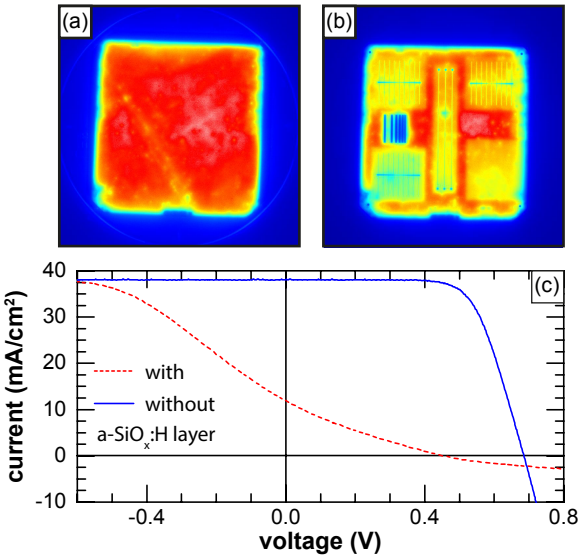

Figure 6.2 – PL images (a) as-deposited (μc-Si:H(*p*)/a-SiO_x:H buffer/a-Si:H(*i*)//a-Si:H(*n*)) and (b) after ITO deposition, screen-print and curing. (c) *J-V* results for a cell with (red dashed line) and a cell without a-SiO_x:H buffer beneath the hole-collecting μc-Si:H(*p*) layer.

An alternative approach to modify the surface of the a-Si:H layer prior to μc-Si:H(*p*) layer deposition is the use of an a-SiO_x:H buffer layer. Here we used SiH_4 and CO_2, highly diluted in H_2 ([SiH_4/H_2] = 0.003) [Bugnon 2014]. This approach was tested starting from a μc-Si:H(*p*) process at 40.68 MHz yielding a layer with a χ_c of approximately 50% for a thickness of 60 nm, when deposited directly on glass (reference sample). Direct deposition on a-Si:H(*i*)-coated glass yielded no microcrystalline material, yet, the insertion of an a-SiO_x:H buffer leads to comparable crystalline fractions as obtained for deposition directly on glass. From ellipsometry measurements only a small thickness difference (< 1 nm) for the a-Si:H(*i*) layer and the a-Si:H(*i*)/a-SiO_x:H(*i*) stack was measured, which can be explained by the high hydrogen dilution. This small difference or the impact on the a-Si:H(*i*) layer seem however sufficient to

improve the nucleation [Vallat-Sauvain 2005]. Despite this promising result, the implementation into devices showed a severely detrimental effect on the passivation as shown in Figs. 6.2(a) and 6.2(b). This may be explained by a stack of layers that for an unknown reason is less resilient to sputter damage. In conclusion, the low passivation quality and likely the presence of an a-SiO_x:H barrier for the holes explains the s-shaped *J*-*V* curve seen in Fig. 6.2(c), as we discussed in chapter 3 (p. 3).

6.2.1.2 Microcrystalline nucleation layer deposited by SiF_4 plasma chemistry

Motivation

Microcrystalline silicon deposited by SiF_4 and H_2 highly diluted in Ar has been found to exhibit very high χ_c values, due to the very specific growth mechanisms induced by this plasma chemistry [Kasouit 2002, Dornstetter 2013]. In our laboratory, such layers were developed for thin-film Si solar cells using plasma regimes at higher pressure and 13.56 MHz excitation at 200 °C. The best layers were obtained at low deposition rate (below 1 Å/s) [Hänni 2014] and were also applied in thin-film solar cells, details are reported elsewhere [Meillaud 2015]. These low deposition rates allow for the precise deposition-control of μc-Si:H(*i*) nucleation layers [hereafter referred to as μc-Si:H(i_{SiF4})] that potentially help to ensure immediate nucleation of the following doped μc-Si:H layers. This is of particular interest for highly sensitive interfaces as found in SHJ solar cells, however less for applications requiring layer thicknesses typical for thin-film silicon solar cells [Hänni 2013].

Impact on passivation

Knowing that fluorine is a strong etching agent—used also for standard reactor cleaning—we first assessed the impact of layers deposited by SiF_4 on the effective minority-carrier lifetime. For this purpose, we used textured wafers symmetrically passivated with standard a-Si:H(*i*) layers of various device-relevant thicknesses (10, 12.5 and 16 nm nominal). After this first step we obtained very high iV_{oc} values in excess of 740 mV. This was not changed significantly by the deposition of a 2-nm-thick (based on the deposition rate) μc-Si:H(i_{SiF4}) nucleation layer. In fact, we saw even an increase in effective minority-carrier lifetime either related to the deposition or due to *in situ* annealing (at 200 °C), especially in the low and medium injection range (Δn= 5×10^{14} and 1×10^{15} cm^{-3}). The lifetime at higher injection levels (5×10^{15} cm^{-3}) remained almost unchanged. This result already proves that our process using SiF_4 does not harm the passivation. This being said, further experiments will have to show, whether thicker μc-Si:H(i_{SiF4}) layers—longer deposition times—can have an effect.

Microstructure analysis with TEM

In a next step, we fabricated three test samples with the following stacks of layers deposited on polished (111)-oriented wafers: (1) a sandwich structure a-Si:H(*i*)/μc-Si:H(i_{SiF4})/a-Si:H(*i*) with

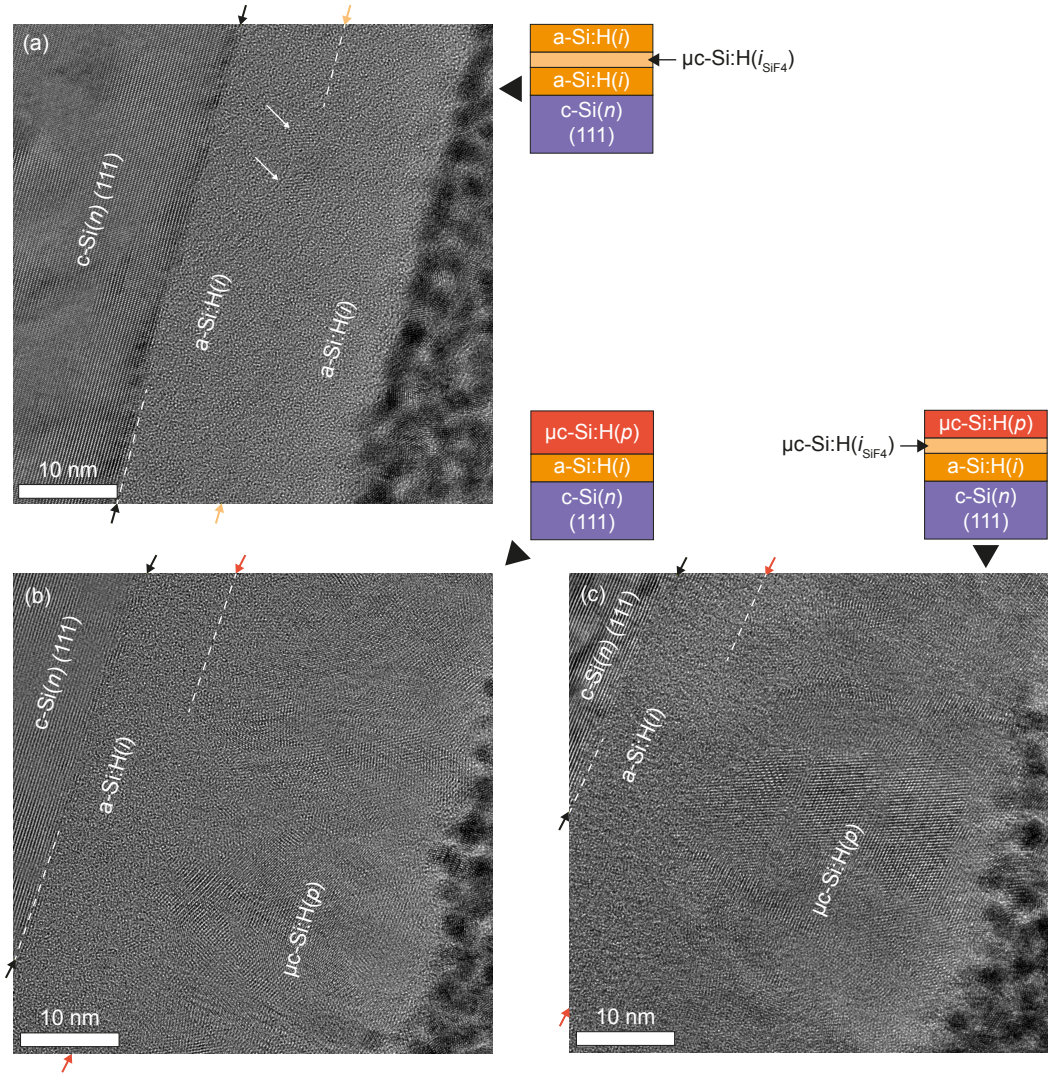

Figure 6.3 – TEM micrographs for samples with the following layers: (a) a-Si:H(i)/μc-Si:H(i_{SiF4})/a-Si:H(i) (nominal thicknesses 10/2/10 nm), (b) a-Si:H(i)/μc-Si:H(p) (10/30 nm nominal) and (c) a-Si:H(i)/μc-Si:H(i_{SiF4})/μc-Si:H(p) (10/2/30 nm nominal), all deposited on c-Si(n) (111). The cell results obtained for co-deposited textured wafers [(b) and (c)] are presented in section 6.4.2 (p. 121). The white arrows in (a) indicate crystallites formed during the μc-Si:H(i_{SiF4}) deposition, whereas the colored arrows outside the micrographs and the dashed white lines indicate the approximate location of the interfaces.

nominal thicknesses of 10/2/10 nm [Fig. 6.3(a)]; (2) a-Si:H(*i*)/μc-Si:H(*p*) (10/30 nm nominal) [Fig. 6.3(b)]; and (3) a-Si:H(*i*)/μc-Si:H(i_{SiF4})/μc-Si:H(*p*) (10/2/30 nm nominal) [Fig. 6.3(c)]. We used these samples to assess the growth mode of the μc-Si:H(i_{SiF4}) nucleation layer and the μc-Si:H(*p*) with and without nucleation layer. The TEM micrograph in Fig. 6.3(a) shows a clear rupture between the two a-Si:H(*i*) layers and it is possible to discern first crystallites forming at the interface (indicated by white arrows). It has been claimed that for SiF_4-based processes, crystallites may form within the plasma [Kasouit 2004]. However, this was not investigated here. Nevertheless, this shows the potential of these highly crystalline nucleation layers. Yet, it is hard to highlight the difference between Figs. 6.3(b) and 6.3(c), as both samples show a clear microcrystalline phase. Further experiments are needed to assess whether the μc-Si:H(i_{SiF4}) layer clearly enhances the quality of the μc-Si:H(*p*) layers. The cell results obtained with these layers (co-deposited on textured wafers) are discussed in section 6.4.2 (p. 121).

6.2.2 Variation of precursor & dilution gases

6.2.2.1 Silane vs. disilane

As discussed before, the SiH_4 concentration in the plasma is one of the factors determining the growth mode of silicon layers, *i.e.* either μc-Si:H or a-Si:H [Strahm 2007b]. Similar results have been reported for the growth of epitaxial layers [Demaurex 2014b]. Therefore, a simple approach to facilitate the nucleation of μc-Si:H layers is the use of Si-precursor gases that are easier to dissociate compared to SiH_4 and therefore enable to reach high depletion regimes more easily. Si_2H_6 is known to be less stable than SiH_4 and is therefore a good candidate [Arkles 2000]. Furthermore, in these experiments Ar was used in the gas mixture, to facilitate the microcrystalline growth of the layer [Das 1996].

Starting with a process for a μc-Si:H(*p*) layer at 40.68 MHz in the KAI-M, exhibiting χ_c of 40% on glass [Bugnon 2012], the SiH_4 flow was gradually reduced while the Si_2H_6 flow was increased accordingly, keeping the total flow of atomic Si ($[SiH_4] = [SiH_4]_{init} - 2\times[Si_2H_6]$) and all the other deposition parameters constant.

The layers were deposited on glass substrates. The reactor walls were coated before each deposition with an intrinsic amorphous layer, to ensure the same starting conditions for all experiments and avoid an offset in χ_c after several subsequent depositions. We observed an increase in χ_c of approximately 20% absolute [Fig. 6.4(a)] for layer thicknesses of approximately 60 nm (measured by profilometry) deposited from a plasma with Si_2H_6 instead of SiH_4. This indicates a beneficial effect of Si_2H_6 on the crystalline growth.

6.2.2.2 H_2 vs D_2

Hydrogen plays an essential role in the growth process of μc-Si:H layers as we have discussed in the introduction of this chapter. Replacing H_2 by D_2 has two potential advantages: (1) it etches a-Si:H tissue faster than H_2 [Geissbühler 2013], which—according to the selective

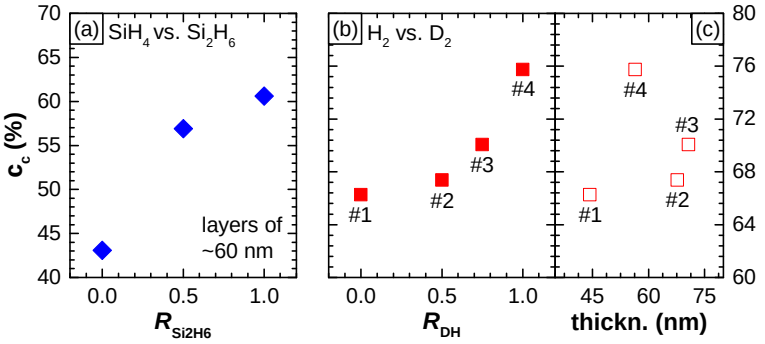

Figure 6.4 – χ_c as a function of the input gas flow ratios: (a) $R_{Si2H6} = Si_2H_6/(SiH_4+Si_2H_6)$ and (b) $R_{DH} = D_2/(D_2+H_2)$. (c) Thickness measured by profilometry for the D_2 series.

etching model [Tsai 1989]—can be beneficial; (2) the higher mass of D_2 might increase the compressive stress in the layer by ion bombardment, which was reported to be beneficial for nucleation as well [Fujiwara 2002]. Therefore, this might be a good approach to enhance crystalline growth.

We deposited μc-Si:H(p) layers from a $SiH_4/H_2/D_2$/TMB/Ar plasma (Octopus I, 40.68 MHz) on glass samples coated with the a-SiO_x:H buffer layer discussed in section 6.2.1.1. All the deposition parameters were kept constant while the ratio between D_2 and H_2 [$R_{DH} = D_2/(D_2+H_2)$] was varied. The results are shown in Fig. 6.4(b). We observe a χ_c increase of more than 10% absolute comparing the layers prepared without D_2 (#1; $R_{DH} = 0$; thickness: 45 nm) and without H_2 (#4; $R_{DH} = 1$; thickness: 55 nm). Samples #2 and #3 showed slightly higher thicknesses [Fig. 6.4(c)] but lower χ_c which corroborates the beneficial effect of D_2 for μc-Si:H growth.

6.2.3 Impact of temperature on microcrystalline growth

To assess the impact of the deposition temperature (T_{dep}) on the μc-Si:H growth, a series of experiments was carried out in the Octopus I. The starting point for this series was a process at 40.68 MHz yielding crystalline fractions of ~50% for > 70 nm thick layers, deposited at 200 °C. The gas mixture included SiH_4, H_2, TMB (500 ppm in H_2) and Ar.

Keeping all the other deposition parameters constant, T_{dep} was varied while both χ_c and the layer thickness were monitored. Fig. 6.5(a) shows a clear trend towards lower χ_c with increasing T_{dep}. Fig. 6.5(b) shows the same χ_c data as in Fig. 6.5(a) but as a function of the layer thickness. Here we see that cutting down the deposition time by half (open symbols) does not have a strong effect on the χ_c of layers deposited at lower temperatures, while at high temperatures χ_c decreases. This is corroborated further by layer-by-layer depositions as proposed by [Asano 1990] (half-filled symbols in Fig. 6.5). While at lower temperature (175 °C) the layer thickness could be reduced even more without losing χ_c, the layer deposited at higher temperature (200 °C) shows the same χ_c as the layer with 5 instead of 10 min. This indicates a

reduced incubation layer thickness for the low-temperature deposition. The higher χ_c values obtained for layers deposited at lower T_{dep} could be explained by more efficient etching of the a-Si:H phase [Kaïl 2004]—necessary for nucleation according to the selective etching model [Tsai 1989]—or by facilitated nucleation at lower temperatures [Robertson 2003].

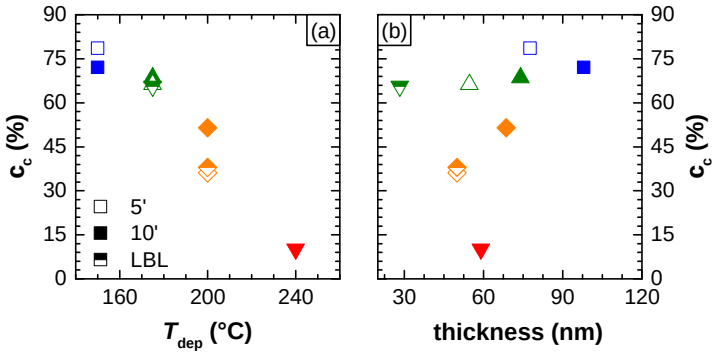

Figure 6.5 – χ_c (a) as a function of the sample temperature during deposition and the same data (b) as a function of the layer thickness. The open symbols correspond to 5 min deposition time, the solid symbols to 10 min. The half-filled symbols refer to layers deposited with several interruptions by hydrogen plasmas as proposed by [Asano 1990].

6.2.4 Deposition frequency: *impact on microcrystalline growth*

Motivation

Higher plasma excitation frequencies have several known beneficial effects. First, it has been shown that the nucleation of μc-Si:H material on a-Si:H is facilitated [Finger 1994], and second, increasing the frequency lowers the ion energy [Heintze 1996]. As reported elsewhere [Geissbühler 2013] and shown above (see section 6.2.1.1, p. 102), ion bombardment induced by a plasma can be potentially harmful to the c-Si interface and its passivation. Therefore, reducing the ion energy is especially interesting for SHJ as it can reduce the potential damages. Despite these benefits, it has been argued that increasing the excitation frequency can have a negative effect on the material quality, leading to an increase in porosity of the deposited layer [Bugnon 2013]. The latter effects of this were investigated further using PCD measurements of passivated wafers at different stages of the fabrication chain of our devices (see section 6.3, p. 110).

Impact of excitation frequency on μc-Si:H growth

We tested processes at different plasma excitation frequencies ranging from RF to VHF (13.56 to 81.36 MHz), in order to identify the most suitable deposition regime for the application of μc-Si:H layers in SHJ solar cells. In a first phase, the layers were deposited either directly on

glass or on a-Si:H(*i*)-coated glass and only later implemented into devices. The results that were obtained using the Octopus I are summarized in Tab. 6.1. For the low pressure (2 mbar) deposition regimes investigated at 13.56 MHz, the onset of crystalline growth was found to be strongly suppressed and the thickness of the incubation layer of material amounted to ~20–30 nm, even for undoped material. This is incompatible with the application to SHJ solar cell as argued in the introduction. Typically the layer thicknesses used in SHJ devices amounts to ~10 nm. Yet, by increasing the pressure and power as well as adapting the dilution, and introducing a μc-Si:H(*i*) nucleation layer deposited in the same deposition regime, *p*- and *n*-doped μc-Si:H layers could be obtained with device-relevant thicknesses and χ_c values on the order of 50% (obtained from SE data). More information on this regime are given in section 6.3.3 (p. 117), where we investigate its impact on lifetime samples. The cell results for this regime are reported in section 6.4.3 (p. 122).

Table 6.1 – Deposition of μc-Si:H(*p*) directly on glass or on a-Si:H(*i*)-coated glass in the Octopus I (estimated error margin of ±3% absolute for χ_c obtained with Raman).

substrate	**frequency** [MHz]	**pressure** [mbar]	**thickness** [nm]	χ_c [%]
glass	13.56	2	~20–30	0
glass/a-Si:H(*i*)	13.56	>2	~15	50 (from SE)
glass	40.68	>2	~13	65 ± 3
glass/a-Si:H(*i*)	81.36	2	~10	55 ± 3

By increasing the frequency to 40.68 MHz, very thin but highly crystalline layers were obtained on glass. However, applying those layers to an a-Si:H(*i*)-coated substrate did not yield μc-Si:H layers without using the surface treatments as described in section 6.2.1.1 (p. 102). Hence, we increased the frequency even further to 81.36 MHz, at which μc-Si:H was obtained also on an a-Si:H(*i*)-coated substrate after depositing again a thin nucleation layer of μc-Si:H(*i*) in the same deposition conditions. This lead to the cell results discussed in section 6.4.1 (p. 119). The results presented here confirm earlier findings that VHF enables the deposition of highly crystalline material [Finger 1994].

6.2.5 Conclusion

The following table summarizes the results obtained for the different methods tested in this section with respect to benefits on layer level and their suitability for the application in SHJ devices. All the methods tested here were successful in terms of layer growth, however the application of a CO_2 plasma or an a-SiO_x:H(*i*) buffer layer can potentially lead to reduced cell performance due to the introduction of transport barriers. Furthermore, for the transfer to industry the more exotic gases (SiF_4, Si_2H_6 and D_2) may not be an option.

Table 6.2 – Suitability of tested methods for layers and for application in SHJ devices. [a]If applied to the hole-collecting contact; [b]To be investigated further.

method	layer crystallinity / nucleation speed	application in SHJ devices
CO_2 plasma	✓	✗
a-SiO_x:H(i) buffer	✓✓	✗✗[a]
SiF_4 nucleation layer	✓✓	✓
Si_2H_6 (instead of SiH_4)	✓	✓
D_2 (instead of H_2)	✓	✓
Deposition temperature	✓✓	✓
Deposition frequency	✓✓✓	✓[b]

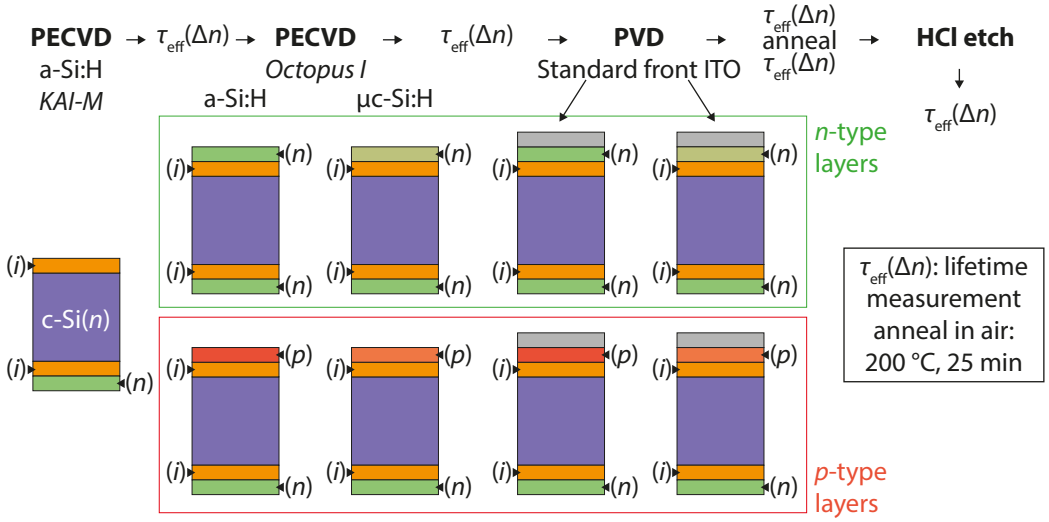

Figure 6.6 – Process flow for the lifetime samples investigated here.

6.3 The impact of microcrystalline deposition on lifetime

High-quality passivation enabling both high V_{oc} *and* high V_{mpp} are essential for the application in devices. Therefore, before discussing device-related results in section 6.4 (p. 119), we discuss how the deposition and presence of microcrystalline layers impact the passivation of a c-Si wafer. For this we limited ourselves to two deposition regimes (details given in Tab. 6.3). These deposition regimes were optimized in terms of crystallinity and homogeneity of the μc-Si:H layer deposited on top of an a-Si:H(i)-coated glass substrate. For this, the dilution, pressure and power were adapted. Best results were obtained for layers with homogeneous deposition on the a-Si:H(i)-coated glass, but little or no deposition on a bare glass substrate.

6.3.1 Experimental details

For each of these regimes we conducted a series of experiments on DSP (100)-oriented *n*-type wafers that were passivated by a-Si:H layers (*in*/*i*) in the KAI-M using our standard process as described in section 2.1 (p. 23). After the PECVD layers of the KAI-M, the samples received either a doped a-Si:H or μc-Si:H(*i*)/μc-Si:H(*p* or *n*) stack[4] deposited in the Octopus I. Then, the standard front ITO was sputtered on the Octopus layer only, the samples are annealed (25 min at 200 °C in air) and the ITO stripped (for selected samples) by dipping the wafers in hydrochloric acid ([H_2O]:[HCl] = 1:2) for 2.5–3 min. The process flow is summarized in Fig. 6.6. For the experiments presented here, we either varied the doping or thickness of the Octopus-deposited layers.

Table 6.3 – Deposition regimes for μc-Si:H in Octopus I.

regime	**pressure** [mbar]	**frequency** [MHz]	**temperature** [°C]	**SiH_4/(SiH_4+ H_2)** [%]
(A)	1.4–2.0	81.36	175	0.83
(B)	> 2	13.56	180	0.1–1

6.3.2 High-frequency, low-pressure regime

In the following we discuss results obtained for layers deposited in regime (A) (Tab. 6.3).

6.3.2.1 Doping variation

Here we investigate the effect of differently doped μc-Si:H layers on the passivation and compare it to the a-Si:H reference. To do so we varied the input doping gas flow to SiH_4 ratio while keeping the [H_2]/[SiH_4] ratio constant for the μc-Si:H deposition. The samples were processed as depicted in Fig. 6.6.

Lifetime results with *p*-type layers

The results for wafers that received *in* [a-Si:H(*n*), KAI-M] on one side and *ip* [a-Si:H(*i*) from KAI-M, a-Si:H(*p*) or μc-Si:H(*p*) from Octopus I] stacks on the other side are shown in Fig. 6.7(a)–(d). For the a-Si:H reference sample shown in Fig. 6.7(a) we see a significant increase in τ_{eff} after the deposition of the a-Si:H(*p*) layer, which is likely due to *in situ* annealing. This increase is followed by a severe decrease upon sputter deposition of the ITO [Demaurex 2012]. However, the annealing step recovers this loss at least partly at high injection levels. In contrast to this, at lower minority-carrier densities the lifetime remains lower. This has been

[4] Note that the thin μc-Si:H(*i*) layer is applied as a nucleation layer for the doped μc-Si:H layer.

explained by the work function mismatch between the ITO and the a-Si:H(*p*) layer, leading to a change in recombination statistics [Bivour 2012, Rößler 2013, Seif 2014a]. Other authors have linked this effect to a defective layer at the a-Si:H/TCO interface leading to increased recombination [Favre 2013]. Similar behavior is observed for the medium and highly-doped μc-Si:H(*p*) layers, which points to the same effects. For the sample exhibiting a lowly-doped μc-Si:H(*p*) layer, however, we see slight differences. The deposition of the μc-Si:H(*p*) layer already leads to a reduction in τ_{eff}, which might be linked to the fact that the strongly hydrogen-diluted plasma provokes more severe etching and hence the interface might be permanently damaged [Geissbühler 2013]. Nevertheless, in the annealed state—the one that is closest to a real device—the lifetime of all the samples is comparable, which is also seen in the similar iV_{oc} values given in Tab. 6.4. In terms of *iFF* the microcrystalline layers show similar results as the a-Si:H(*p*) reference and values on the order of 86% are obtained for all the samples.

Table 6.4 – iV_{oc} [mV] / *iFF* [%] values obtained from lifetime measurements for samples with μc-Si:H(*p*) layers of different doping levels.

sample state	**a-Si:H(*p*)**	**μc-Si:H(*p*) low**	**μc-Si:H(*p*) medium**	**μc-Si:H(*p*) high**
in/*i*	722 / 83.9	729 / 86.1	728 / 86.1	728 / 85.9
in/*ip* or *in*	728 / 86.3	728 / 85.8	727 / 86.1	728 / 86.3
after ITO	666 / 76.9	669 / 80.0	710 / 82.0	690 / 78.3
after annealing	**737 / 86.3**	**737 / 86.6**	**736 / 86.0**	**732 / 85.8**
after HCl etch	729 / 86.4	739 / 84.8	728 / 86.1	725 / 85.9

Lifetime results with *n*-type layers

Turning now to the results obtained for the samples that received a *in* (a-Si:H(*n*) from KAI-M) and *in* (a-Si:H(*i*) from KAI-M, a-Si:H(*n*) or μc-Si:H(*n*) from Octopus I). Compared to the results presented for *p*-type layers, the samples with *n*-type layers reveal a distinct difference between a-Si:H(*n*) and μc-Si:H(*n*). After the deposition of the μc-Si:H(*n*) layers the lifetime is strongly increased, as it is the case for the deposition of the a-Si:H(*n*) layer. This increase is likely related to *in situ* annealing but may also be related to enhanced field effect passivation. The difference between the initial *in*/*i* state and the *in*/*in* state seems to increase with doping gas flow. However, this might also be an effect linked to the layer thickness, as the same also increases in parallel. Yet, the most interesting result here is the comparison of the annealed state. While a-Si:H(*n*) in contrast to the a-Si:H(*p*) layers do not show the typical lifetime reduction at low carrier densities (see also chapter 5, p. 83), the μc-Si:H(*n*) layers show this kind of behavior, even though less than the μc-Si:H(*p*) layers. Since a work function effect is unlikely, a possible explanation could be a higher sensitivity of the μc-Si:H(*n*) layer to sputter-induced damage. This increased sensitivity may be associated with poor material quality possibly obtained VHF deposition regimes [Bugnon 2013, Smets 2008].

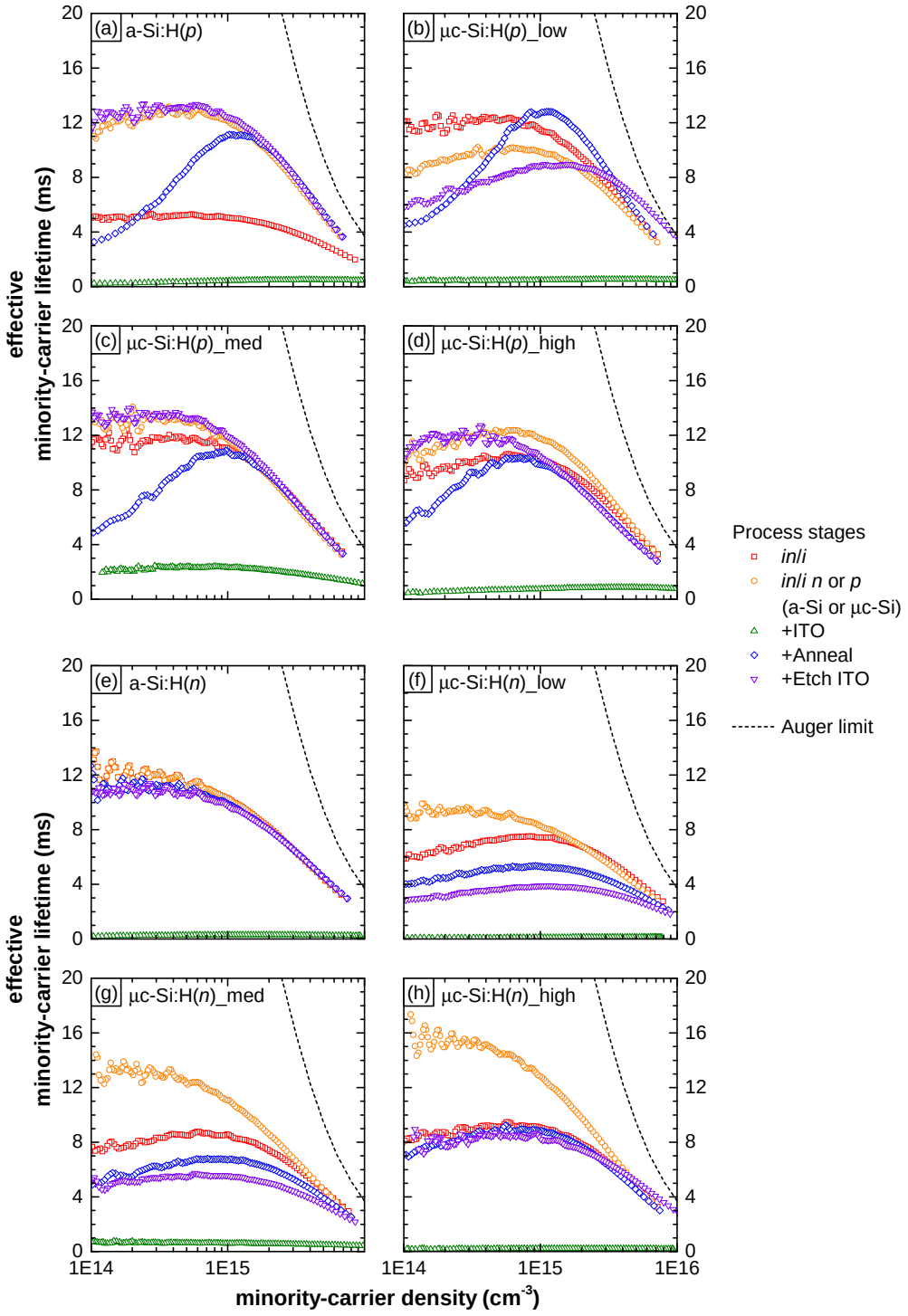

Figure 6.7 – **Doping variation results:** Effective minority-carrier lifetime data, at different process stages, for (a) a-Si:H(*p*), (b)–(d) *µ*c-Si:H(*p*), (e) a-Si:H(*n*) and (f)–(h) *µ*c-Si:H(*n*) layers. The doping (*low* - *high*) of the *µ*c-Si:H layers was varied changing the doping gas flow.

Compared to the μc-Si:H(p) samples, for which the reduction in lifetime affects only injection levels below 1×10^{15} for μc-Si:H(n) the lifetime is reduced beyond this point. In a finished device, this can have a negative effect on the *FF* as argued in section 1.2.2.2 (p. 12), in severe cases even on the V_{oc}. Here, however, the application of μc-Si:H(n) layers does not degrade the passivation at high injection levels and comparable iV_{oc} values are obtained (Tab. 6.5).

Table 6.5 – iV_{oc} [mV] / *iFF* [%] values obtained from lifetime measurements for samples with μc-Si:H(n) layers of different doping levels.

sample state	a-Si:H(n)	μc-Si:H(n) low	μc-Si:H(n) medium	μc-Si:H(n) high
in/i	724 / 83.8	728 / 84.9	728 / 85.3	728 / 85.5
in/ip or in	727 / 85.8	726 / 85.2	727 / 86.0	728 / 86.3
after ITO	646 / 79.4	603 / 81.2	670 / 81.7	634 / 81.6
after annealing	**735 / 85.6**	**732 / 83.8**	**734 / 84.6**	**736 / 85.2**
after HCl etch	727 / 85.7	722 / 82.9	724 / 84.1	735 / 84.5

6.3.2.2 Thickness variation

In addition to this doping series we performed a series of experiments varying the layer thicknesses. Here, we concentrated on the p-type layers only. Fig. 6.8 summarizes the results obtained for samples of various a-Si:H(p) [Fig. 6.8(a)–(d)] and various μc-Si:H(p) [Fig. 6.8(e)–(h)] layer thicknesses. First thing to note is that after the deposition of in/i the samples showed similar τ_{eff} values. The first significant difference is seen after the deposition of the p layers. Here the a-Si:H(p) clearly outperforms the μc-Si:H(p). The most significant difference however is seen for the data after the ITO deposition. While the a-Si:H(p) layers seem to protect reasonably well against sputter damage, the μc-Si:H(p) layers deposited in the regime barely protect the underlying layers. One possible explication for this might be the fact that due the lower absorption at shorter wavelengths, high-energy photons—the ones that have been shown to be harmful for passivation [Demaurex 2012]—are able to reach the sensitive a-Si:H/c-Si interface more easily and hence create an increased amount of defects. These defects, however, are mostly recovered by the subsequent annealing step. Comparing the a-Si:H(p) and μc-Si:H(p) samples at this stage reveals an additional marked difference, which is seen at lower injection levels. In contrast to the a-Si:H(p) samples—for which a strong *tailing* is observed systematically (work function mismatch, section 6.3.2.1, p. 111 and chapter 5, p. 83)—the lifetime of the μc-Si:H(p) samples seem to be more resilient to this kind of effect.

Raman analysis

Analyzing these samples by Raman spectroscopy (Renishaw InVia REXLEX, section 2.2.1.2, 28) we obtained the data given in Fig. 6.9. The data clearly shows a thickness dependence of the

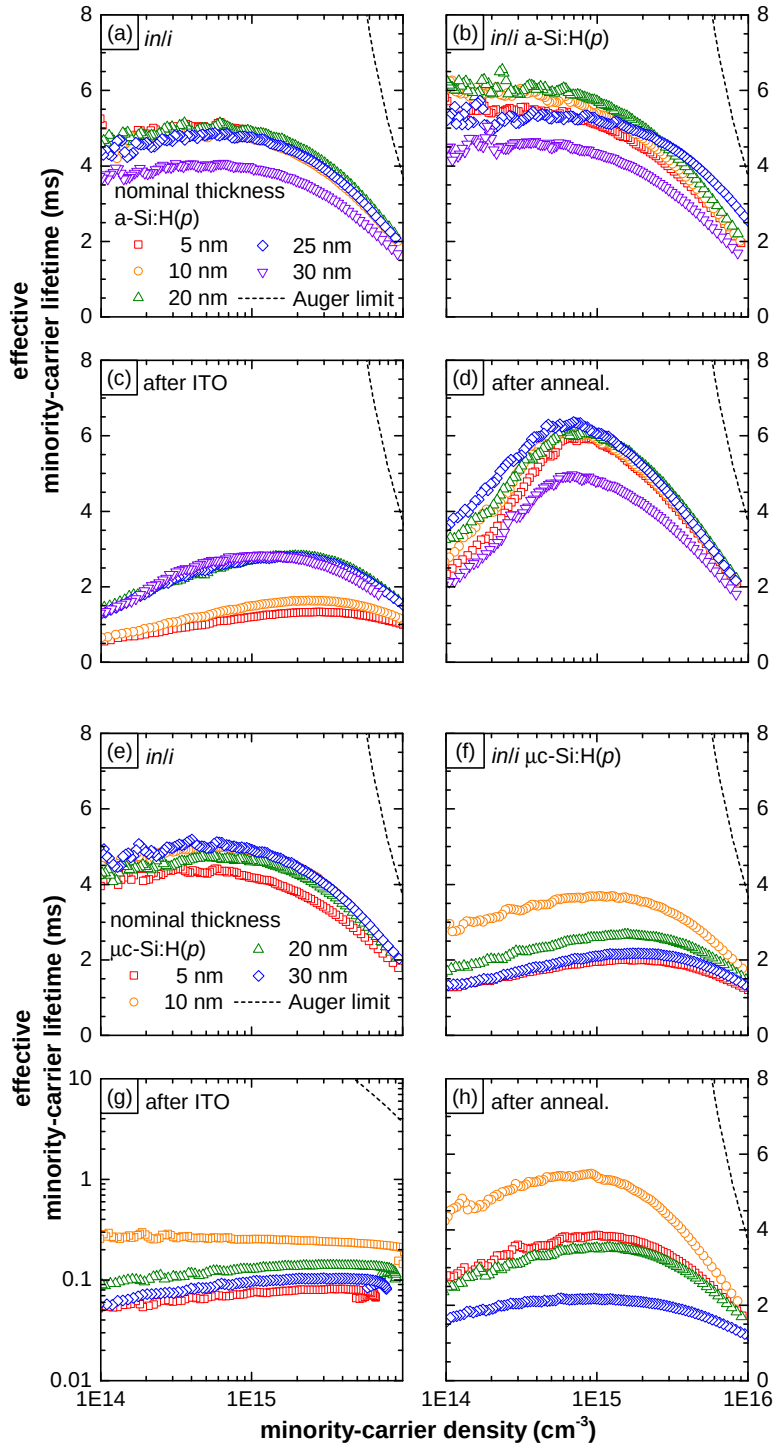

Figure 6.8 – Lifetime data for passivated wafers after the deposition of (a) a-Si:H *in*/*i*, (b) a-Si:H(*p*), (c) ITO and after (d) annealing at 200 °C in air for 25 min. The remaining figures show same data for another set of samples after the deposition of (e) a-Si:H *in*/*i*, (f) μc-Si:H(*p*), (g) ITO and (h) again after annealing at 200 °C in air for 25 min.

crystalline fraction. For the layer with a nominal thickness of 5 nm we do not see the presence of any crystalline phase. Yet, the lifetime curve obtained for this nominally 5-nm-thick layer shows a difference to the a-Si:H(p) reference, which points to the fact that the material is different even though it is amorphous. The layers with nominal thicknesses beyond 5 nm show an increasing crystalline fraction reaching up to 80%. Hence the trend seen in Fig. 6.8(h)—thicker layers yield lower lifetimes—could be explained by an increase in crystallinity or simply deposition time (up to 16 min for the layer of nominally 30 nm) and therefore longer exposure to the harsh μc-Si:H plasma or to over-annealing of the samples leading to lower lifetime values. Furthermore, comparing the *iFF* data of both the a-Si:H(p) and μc-Si:H(p) samples (Fig. 6.9) we see that in the case of the μc-Si:H(p) layers it is affected by the layer thickness and shows a decreasing trend as well, going from 84.0% (μc-Si:H(p) 10 nm nominal) down to 81.3% (μc-Si:H(p) 30 nm nominal). This contrasts with what is observed for the a-Si:H(p) samples. Here the *iFF* is not affected by the layer thickness and remains on average at around 84.2%. This is in line with the fact that τ_{eff} at around 1×10^{15} cm^{-1} remains high and the low τ_{eff} values at low injection levels do not play a role for the *iFF* in this case. As a consequence, for this deposition regime the deposition time should be kept short to avoid this degradation.

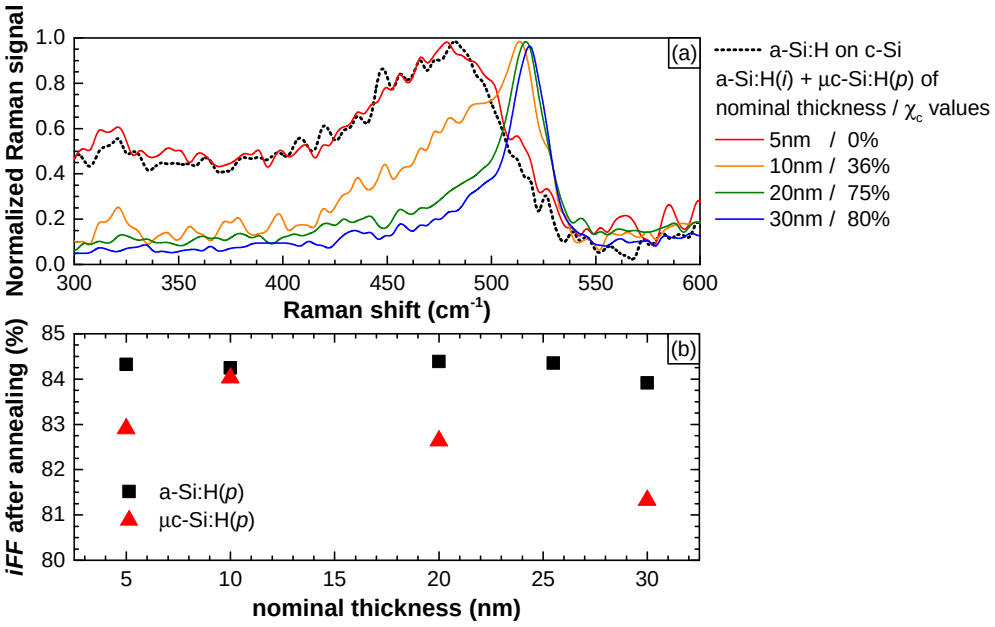

Figure 6.9 – (a) Raman signals, normalized to their maxima, for the layers of different thickness investigated in this section. (b) *iFF* values obtained for the a-Si:H(p) and μc-Si:H(p) samples as a function of the nominal layer thickness.

6.3.3 High-power & higher-pressure, and low-frequency regime

In the following we compare the lifetime results obtained at very high frequency [81.36 MHz, regime (A), see Tab. 6.3] and discussed in section 6.3.2 (p. 6.3.2), to the ones obtained for μc-Si:H(n) layers developed in a high-power and higher-pressure regime at 13.56 MHz [regime (B), see Tab. 6.3] in the Octopus I. For this regime we mixed both H_2 and D_2 to obtain very high equivalent H_2 dilutions. Again we changed the doping gas flow ratio $[PH_3]/[SiH_4]$ while keeping the total flow constant.

Lifetime results with μc-Si:H(n) layers

The lifetime data collected from *in*/ *i*μc-Si:H(n) samples, processed as described above (Fig. 6.6: *in*/ *i* in KAI-M, μc-Si:H(n) in Octopus, front ITO on μc-Si:H(n) and subsequent HCl etching), are gathered in Fig. 6.10. Comparing these, to the ones depicted in Fig. 6.7 a striking difference is apparent. Unlike their high-frequency counterparts, the layers prepared at lower frequency—yet much higher pressure and power—exhibit no or only minor lifetime losses at carrier injection levels below 1×10^{15} cm^{-3}. The application of the μc-Si:H(n) layer with the lowest doping, however, reduces the lifetime at higher injection levels. The origin of this effect is not yet clear and has to be investigated further. A possible explanation, however, could again be the aggressive nature of the highly diluted plasma. Decreasing the flow of dopant gas might lead to an enhanced availability of hydrogen—as known for boron [Chou 1992]—which in turn could lead to enhanced etching of the a-Si:H(i) layer, making it more susceptible to sputter-induced damage.

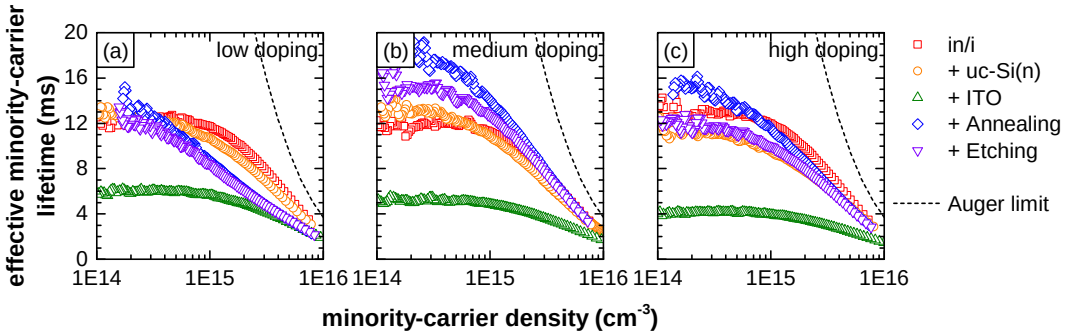

Figure 6.10 – Lifetime data for passivated wafers after various processing steps for three different doping gas flow ratios (see Tab. 6.6, p. 118): (a) low doping, (b) medium doping and (c) high doping.

From SE we extracted the thickness and an estimate of the crystalline fraction. These results are given in Tab. 6.6 along with the gas flow ratios used for the deposition. Even though we did not use the same gas flows for regime (B), we obtained comparable layer thicknesses, yet lower crystalline fractions. Hence, one hypothesis to explain the reduction in low-injection lifetime is the χ_c value. From the application of μc-Si:H layers on rough ZnO layers in thin-film solar

cells it is known that sharp features of the texture can lead to porous regions emerging from the v-shaped valleys between the pyramids that lowers the cell performance, as for instance shown by Bugnon *et al.* [Bugnon 2012]. Even though for the study presented here flat wafers were used, the same could apply here, namely that the layers deposited at higher frequencies [regime (A), section 6.3.2, p. 111] are less dense—hence more susceptible to sputter-induced damage—than the layers deposited in regime (B). Whether this is the case has to be shown in future studies with the help of more in-depth microstructural analysis as *e.g.* TEM.

Table 6.6 – Comparison for the parameters used at 81.36 MHz (A) (see section 6.3.2.1, p. 111) and 13.56 MHz (B).

regime	**[PH_3]/[SiH_4]**	**dilution (w. H_2 or D_2)**	**μc-Si:H(*n*) thickness** [nm]	**χ_c(from SE)** [%]
(A)	low	standard dilution	13.7	61.19
	medium		14.2	56.48
	high		14.8	51.96
(B)	low	higher dilution	15.3	23.05
	medium		14.6	19
	high		9.6	0

6.3.4 Conclusion

In this study we have seen that the deposition regime of the μc-Si:H layers can have a significant influence on the material properties, hence leading to a resilience to sputter damage or the drop in low-injection τ_{eff} that is more or less pronounced. This may be linked to both doping, layer thickness or material microstructure. Our best results were obtained in regime (B) at higher pressures and low deposition frequency. The reason for this will have to be investigated further in the future.

6.4 Implementation of microcrystalline layers into devices

In the following we present results for devices with doped μc-Si:H layers deposited in the different deposition regimes, with different structures—with or without nucleation layers and hole-collecting layer at the front or rear—fabricated in different systems (KAI-M or Octopus I). First, we focus on the results obtained with layers deposited at high frequency: regime (A) in the Octopus I at 81.36 MHz (see Tab. 6.3, p. 111) and at 40.68 MHz in the KAI-M using SiF_4 plasma chemistry to deposit highly crystalline μc-Si:H(*i*) nucleation layers. Then we turn to the results obtained for regime (B) at 13.56 MHz (see Tab. 6.3, p. 111). All the devices are based on textured FZ wafers.

6.4.1 *p*-doped microcrystalline layers at 81.36 MHz

Experimental details & information on layers

In this deposition regime we deposited the μc-Si:H(*p*) layers at low temperature (175 °C) and introduced D_2 to the gas mix to obtain the highest crystallinity at a pressure of 2 mbar. The results for the best cell obtained in this regime are shown in Tab. 6.7 (p. 120). The thickness of the two different *p*-type layers [a-Si:H(*p*) deposited at 13.56 MHz: 8.7 nm and μc-Si:H(*p*) deposited at 81.36 MHz: 9.8 nm], applied to the front of the cells, differs by only ~1 nm. The thickness of the a-Si:H(*p*) was measured by SE, whereas the thickness of the μc-Si:H(*p*) was estimated from the maximum deposition rate [Strahm 2007b], assuming a hydrogen content of 10%, and represents therefore only an upper bound. The obtained deposition rate amounts to 0.3Å/s, which is typical for these highly microcrystalline regimes.

Cell results

Applying both of these layers to cells yielded the same V_{oc} values of 720 mV [a-Si:H(*p*) and μc-Si:H(*p*)]. Measuring the iV_{oc} before and after the deposition of the *p*-type layers revealed a more severe drop for the device exhibiting a μc-Si:H(*p*) layer (~20 mV) while the device with an a-Si:H(*p*) layer exhibited only a small drop (~5 mV). However, comparable V_{oc} values for both devices have been obtained, which shows that both the damages induced by the PECVD deposition as well as those induced by the TCO sputter deposition were recovered to a high degree during the curing of the screen-printed silver paste. This is in line with what we discussed before (section 6.3.2, p. 111). More importantly, the μc-Si:H(*p*) layer shows a significant increase in J_{sc} of 0.8 mA cm^{-2} leading to an increase of 0.4% absolute in conversion efficiency. The crystallinity of the *p*-layer was confirmed by Raman spectroscopy (Renishaw InVia REXLEX, blue laser at 325 nm) and a χ_c of 55% was measured [see Fig. 6.11(a)]. Furthermore, the cell's optical performance was characterized by quantum efficiency measurements. As expected, this analysis clearly identifies the gain at short wavelengths as the reason for higher J_{sc} values [approximately +4.8% relative in EQE and IQE for the microcrystalline cell, see Fig. 6.11(c) and 6.11(d)]. The low *FF* values are likely due to the inhomogeneous passiva-

tion, in particular a ring-like defect in the center but also towards the edges [see Figs. 6.11(e) and 6.11(f); three cells indicated by dashed squares], thereby screening the expected gain in *FF*.

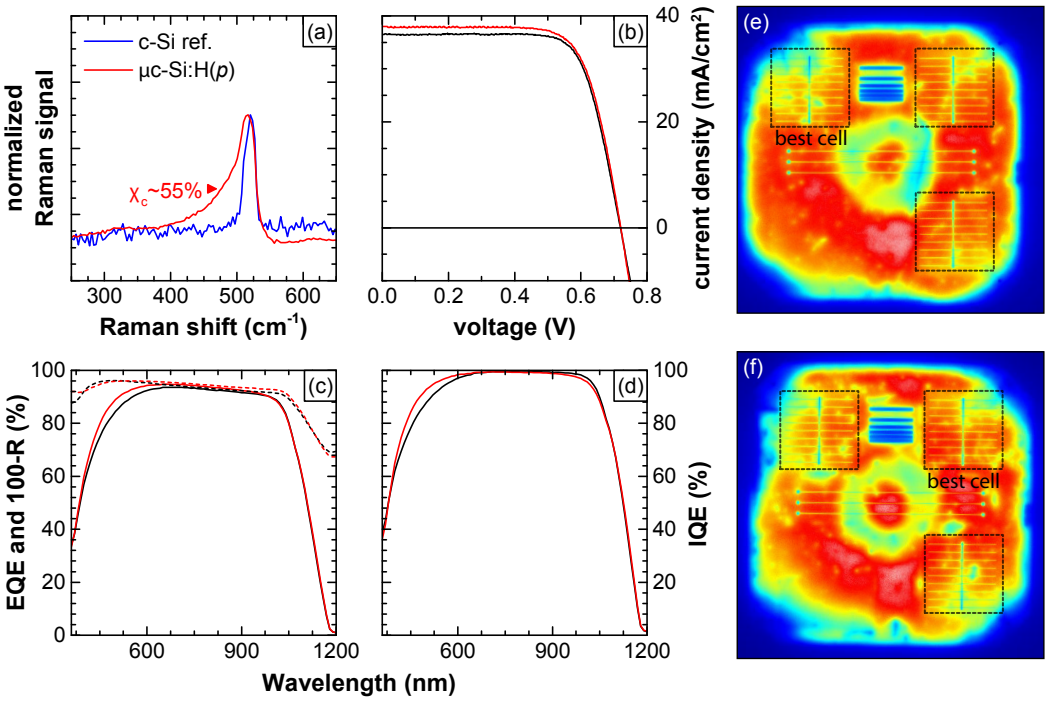

Figure 6.11 – (a) Raman spectra for c-Si reference and the a-Si:H(*i*)/µc-Si:H(*p*) layer stack measured directly on the c-Si wafer. The data are normalized to their peak value. (b) *J*-*V* curves for the reference cell (standard design, black line) and a cell with µc-Si:H(*p*) hole collector (red line). (c) EQE, 100-R (dashed) and (d) IQE as a function of the wavelength. (e) and (f) show PL mappings of the cell with a µc-Si:H(*p*) and a-Si:H(*p*) hole-collecting layer, respectively. A ring-like defect in the middle and other inhomogeneities in passivation are clearly visible. Red and orange indicate high lifetime, whereas the other colors indicate defective regions. The three individual cells are marked by dashed squares. The best cells who's *J*-*V* data is plotted in (b) are indicated.

Table 6.7 – Deposition regime and cell parameters of the best cells: µc-Si:H(*p*)/a-Si:H(*i*)/c-Si(*n*)/a-Si:H(*in*) and [all-a-Si:H reference] processed in the same run in the Octopus I.

µc-Si:H regime **[reference a-Si:H regime]**	V_{oc} **[ref.]** [mV]	J_{sc} **[ref.]** [mA cm^{-2}]	***FF*** **[ref.]** [%]	η **[ref.]** [%]
81.36 MHz µc-Si:H(*p*)	720	37.6	73.3	19.8
[13.56 MHz a-Si:H(*p*)]	[720]	[36.8]	[73.3]	[19.4]

6.4.2 Intrinsic microcrystalline nucleation layers deposited from SiF_4

Experimental details

We now turn to the results obtained for cells fabricated in parallel with the layers discussed in section 6.2.1.2 (p. 104), *i.e.* μc-Si:H(i_{SiF4}) nucleation layers, deposited at 13.56 MHz in the KAI-M by SiF_4 plasma chemistry that were subsequently covered by a μc-Si:H(p) layer (30 nominal thickness), deposited in the same system at 40.68 MHz. For these devices the μc-Si:H(p) layer is situated at the front.

Cell results

In line with what was discussed earlier, the cells with μc-Si:H(p) layers do not show any significant difference to the all-a-Si:H reference in terms of V_{oc} and values of around 720 mV were achieved. The improvement of J_{sc} on the other hand is screened by the fact that the μc-Si:H(p) layers were chosen too thick in order to ensure microcrystalline growth. From the TEM micrographs [Fig. 6.3(c)] we extract a thickness of roughly 26–30 nm, *i.e.* depending on where to define the starting point of the crystalline cones. This represents approximately double the thickness of a standard a-Si:H(p) layer. Yet, judging from the TEM micrographs, there is still room to thin down these layers to some extent without sacrificing the crystallinity. These results set aside, compared to the a-Si:H(p) reference cell, the *FF* values of the cells exhibiting μc-Si:H(p) layers were increased by up to 2.1% absolute. This represents a significant improvement, which is likely linked to the thick μc-Si:H(p) layer and therefore high crystalline fraction of the layer. Yet, due to the low current, the conversion efficiencies were all lower than the reference. Furthermore, it is important to note that the difference in current—even though it can affect the *FF*—does not account for this differences we see in *FF*. Optimizing the layer thickness and reaching the same J_{sc} as the all-a-Si:H cell (lower bound) would lead to a further enhancement in conversion efficiency of up to 0.6% absolute, assuming that the same *FF* could be reached, which has yet to be shown. The results for the two cells processed in this study are given in Tab. 6.8.

Table 6.8 – Deposition regime and cell parameters of the best cells: μc-Si:H(i_{SiF4} p)/a-Si:H(i)//a-Si:H(in), μc-Si:H(p)/a-Si:H(i)//a-Si:H(in) and the [all-a-Si:H reference] processed in the same run (in the KAI-M).

μc-Si:H regime [reference a-Si:H regime]	**V_{oc} [ref.]** [mV]	**J_{sc} [ref.]** [mA cm^{-2}]	***FF* [ref.]** [%]	**η [ref.]** [%]
13.56 MHz μc-Si:H(i_{SiF4}) 40.68 MHz μc-Si:H(p)	718	36.0	78.4	20.3
40.68 MHz μc-Si:H(p)	722	35.8	78.8	20.3
[40.68 MHz a-Si:H(p)]	[718]	[37.1]	[76.7]	[20.4]

6.4.3 Layers deposited at 13.56 MHz, high power & higher pressure

Experimental details & information on layers

Finally we present results obtained for two cells with either μc-Si:H(p) at the rear or μc-Si:H(n) at the front, both deposited at above 2 mbar with power densities of $> 0.1\,\mathrm{W/cm^2}$ in the Octopus I. The layers were deposited from a highly diluted $SiH_4/H_2/D_2/$(TMB or PH_3) plasma at a temperature of 180 °C. For both devices, a thin μc-Si:H(i) layer was deposited as nucleation layer prior to the doped μc-Si:H layers, using the same deposition conditions without the dopant gases. These layers were not optimized in terms of thickness, doping or crystallinity, yet. The thickness and crystallinity of the layers were determined from ellipsometry measurements performed on co-deposited a-Si:H/μc-Si:H coated flat glass samples. This yields 9.9 nm and a crystallinity of 32.1% for the μc-Si:H(n) and 13.6 nm and 48.8% for the μc-Si:H(p) layers.

Cell results

The cells processed with these layers yield similar high V_{oc} values of around 720 mV, whereas the current is slightly increased for the cell with the μc-Si:H(n). However, the most impressive results obtained are the high *FF* values: 78.7% for the cell exhibiting a μc-Si:H(n) layer at the front and up to 79.2% for the device with a μc-Si:H(p) layer at the rear. From the comparison of *J-V* and suns-V_{oc} measurement [Pysch 2007] we extracted the R_s values and obtained 1.02 and $0.83\,\Omega\,\mathrm{cm^2}$, for the μc-Si:H(n) and μc-Si:H(p) cells, respectively. The reason for these low R_s values are yet to be assessed, but may be linked to the high material quality—high crystallinity and hence high resulting doping—and the resulting low contact resistance associated with the silicon/TCO interface. The results obtained from lifetime test point to the same direction, *i.e.* the materials deposited in regime (B) (see Tab. 6.3, seem to be more insensitive towards subsequent sputtering. All the results are given in Tab. 6.9. The microstructure of the layers might give more information in that respect.

Table 6.9 – Cell parameters of the best cells obtained in the higher-pressure, high-power regime at 13.56 MHz processed in the same run (in the Octopus I). Unfortunately for this run no all-a-Si:H device was available.

cell structure	V_{oc} [mV]	J_{sc} [$\mathrm{mA\,cm^{-2}}$]	*FF* [%]	η [%]
a-Si:H(in)//a-Si:H(i)/μc-Si:H(ip)	720	36.5	79.2	20.8
μc-Si:H(in)/a-Si:H(i)//a-Si:H(p)	719	37.0	78.7	20.9

Assessment of optical gain using μc-Si:H(n)

To further assess the optical potential of μc-Si:H(n) layers applied to the front of a SHJ device, we conducted a set of experiments and compare cells with different layer thicknesses of either μc-Si:H(n) or a-Si:H(n) as electron-collecting layers at the front. The thicknesses of the layers

were extracted by fitting SE data. Even though the μc-Si:H(n) layers were slightly thicker than the a-Si:H(n) layers the results shown in Fig. 6.12 clearly show different trends. The slope of the J_{sc} values as a function of the n-layer thickness is 1.8 times steeper for the a-Si:H(n) layers (-0.11 mA cm^{-2}/nm) than the slope obtained for the μc-Si:H(n) layers (-0.06 mA cm^{-2}/nm). Reducing the thickness of the μc-Si:H(n) layers to the same thickness as obtained for the a-Si:H(n) layers would yield a current-density gain of up to 0.3 mA cm^{-2}. From SE we determined the crystalline fraction for the layers applied here to approximately 30–50%, increasing with layer thickness as expected. Further investigations will have to show whether it is possible to minimize the μc-Si:H(n) thickness while maintaining a high crystalline fraction.

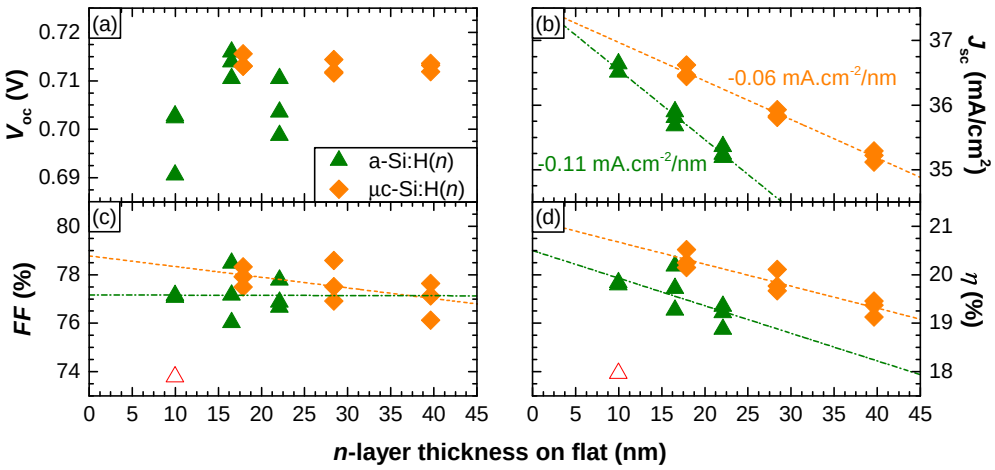

Figure 6.12 – Comparison of cells exhibiting different thicknesses of either a-Si:H(n) or μc-Si:H(n) layers. The lines are linear fits to the data. The open symbols were excluded from the fit.

6.5 Conclusion

In this chapter we have investigated a variety of different techniques to obtain thin μc-Si:H layers, ranging from plasma pre-treatments to nucleation layers and variations in precursor gases. These techniques enabled us to transfer μc-Si:H-processes to a-Si:H(i)-coated substrates maintaining high crystalline fractions. The most promising approach ensuing from this study is the deposition of μc-Si:H layers in a high-power and higher-pressure regime—at an excitation frequency of 13.56 MHz—and their combination with μc-Si:H(i) nucleation layers. Comparing lifetime results, we find that—in contrast to material deposited at higher excitation frequency—the layers deposited at higher pressure and power at 13.56 MHz are more resilient to post-PECVD fabrication processes and high lifetime values are maintained also at low carrier injection levels. A possible explanation for this improvement could be a denser material—reduced porosity—enabled by very low deposition rates. Microstructure analysis will have to clarify this point.

With respect to devices, we could prove that besides showing clear optical benefits (J_{sc} gain of up to 1 mA cm^{-2})—which we strived to achieve with a-SiO$_x$:H layers (chapter 3, p. 37)—these high-quality μc-Si:H layers have the potential to improve both the optical *and* the electrical performance of SHJ devices. We fabricated cells with hole collection at the rear and either μc-Si:H(*n*) or μc-Si:H(*p*) layers that yielded *FF*s of 78.7% and 79.2%, respectively. These are a result of the very low R_s values of 1.02 and 0.83 Ωcm^2. Notably, these promising results were achieved while maintaining high V_{oc} values in excess of 720 mV, resulting in good conversion efficiencies of 20.9 and 20.8%. Note that this is a preliminary result and that even higher efficiencies can be expected implementing the layers reported here into our best devices. With respect to IBC devices, exhibiting a reduced contacting area, the layers developed in this work may be of even more important as changes of the transport properties of the carrier-collecting layers can have an even greater effect.[5]

To conclude, the process giving the highest χ_c value might not be the best in terms of device performance. Furthermore, instead of introducing materials that may act as potential transport barriers, or treating the substrate surface with potentially harmful plasmas, it may be best to stick to nucleation layers of the same material, namely plain μc-Si:H(*i*). The TCO material optimization for the specific μc-Si:H layer may help to improve the performance of these μc-Si:H-based devices even further.

[5] See work of A. Tomasi *et al.*, who applied these layers to IBC (not published yet).

7 Summary and perspectives

7.1 Summary

The results obtained for μc-Si:H layers clearly show the potential of this non-traditional material for SHJ solar cells. As we have seen, their implementation, however, is not necessarily always trivial as it can be potentially harmful to the device performance, as we were able to show comparing material deposited in different regimes. We assessed the suitability of different processes for the deposition of μc-Si:H material on the highly sensitive a-Si:H(*i*)-passivated c-Si wafer surface. Identifying and applying the most promising approaches—namely deposition in higher-pressure and high-power regimes combined with μc-Si:H(*i*) nucleation layers deposited in the same regime—we were able to successfully apply both μc-Si:H(*p*) and μc-Si:H(*n*) layers in devices. Notably, this was achieved maintaining high V_{oc} values in excess of 720 mV, increasing the J_{sc} values by up to 0.5–1 mA cm^{-2} and yielding very good *FF* values as high as 79.2%. Their excellent transport properties renders μc-Si:H layers also an interesting candidate for carrier-collecting layers in IBC devices that may benefit even more in terms of *FF*, due to their reduced contacting area.

Furthermore, we have seen that the application of a-SiO$_x$:H layers—inserted between the a-Si:H(*i*) and a-Si:H(*p*) layers—can have a severe impact on hole collection which we relate to a wider valence band offset (VBO). We were able to confirm this by applying a-SiO$_x$:H layers beneath the a-Si:H(*n*), which showed only a negligible influence, as the conduction band offset (CBO) remains virtually unchanged when increasing the bandgap in these materials. This shows that a-SiO$_x$:H(*i*) passivation layers could be a viable solution to increase the J_{sc} for devices with electron collection at the front. Despite the negative effect of a-SiO$_x$:H applied to the *p*-side of a device—resulting in a strong reduction in *FF* at 25 °C—this structure yields better temperature coefficients (TC$_{V_{oc}}$ and TC$_\eta$) which may be interesting to optimize cells for warm climates [Seif 2014b]. From the findings presented here, we conclude that care has to be taken when collecting holes through a window layer as minor gains in J_{sc} can easily be outweighed by losses in *FF* induced by this same layer. In fact we evidence that the standard VBO of a-Si:H already represents a transport-limiting barrier. Therefore, we argue that SHJ

solar cells might benefit from hole collection at the rear of the device. This grants more freedom on the design of the hole-collecting layers especially in terms of bandgap, band offsets, and thickness. The latter can be particularly advantageous for the implementation of μc-Si:H(p) layers as the material properties improve with thickness.

In a more fundamental study—inspired by the results obtained from a-SiO_x:H layers—we unraveled the effect of the operating temperature on each cell parameter individually [Seif 2015]. Exploiting simple temperature-dependent lifetime measurements, we observed a distinct increase in τ_{eff} with temperature across the entire injection range. Even though it was not possible to pin down the physical effect inducing this behavior—we suspect changes in recombination statistics linked to the temperature-dependent occupation of defect levels or temperature-dependent capture cross-sections—we were able to show the impact on both the $TC_{V_{\text{oc}}}$ and the TC_{iFF}. However, in contrast to the potential beneficial effect of an increased lifetime on the recombination current—via the carrier diffusion length—the increase in n_{i} outweighs the increasing τ_{eff}.

Even though the results were not discussed in detail in this thesis (see [Seif 2014a]), we assessed the benefits of protective ALD ZnO:Al layers against sputter damage. These layers may be indispensable when moving towards even thinner a-Si:H layers that can help to maximize the J_{sc} by reducing the parasitic losses to a minimum. We found that ALD ZnO:Al can indeed be used for this purpose if the formation of an a-SiO_x:H layer can be avoided. Here, we reported the results gathered during a subsequent study on the impact of such ALD ZnO:Al layers on τ_{eff} and *iFF*. Applying these layers to the hole-collecting side of the device did not yield better results in terms of *iFF*. However, after depositing them on top of the a-Si:H(n) layers, we observed a slight improvement of τ_{eff} at low injection levels and hence a gain in *iFF*. This indicates the importance of work function engineering for optimized TCO materials or finding new materials that can be used as transparent conductive electrodes. To this end we investigated the potential of p-type polymers as a replacement for the standard n-type TCOs. The potential benefit of these materials for SHJ solar cells is twofold: optically, due to reduced plasmon absorption in the rear reflector, and electrically, due to the improved contact to a-Si:H(p). Indeed we were able to obtain promising results applying PVK to the a-Si:H(p) side, which yielded an increase in low-injection τ_{eff} and as a result in *iFF*. Applied to a device this could enable higher *FF* values, given that the polymer does not introduce additional hurdles to carrier transport and that the parasitic absorption associated with it can be maintained at a low level.

7.2 Perspectives

Recent developments on SHJ solar cells have shown excellent results for devices fully based on a-Si:H layers (Tab. 7.1). Even though, these results are hard to beat on the lab-scale, the materials investigated during the course of this work—μc-Si:H in particular—may prove valuable for next-generation SHJ devices and enable even higher conversion efficiencies. From

Table 7.1 – Current record devices (101.8 cm^2) fully based on a-Si:H layers reported by Panasonic, Japan.

	contact design	**c-Si wafer thickness** [μm]	V_{oc} [mV]	J_{sc} [$mA\,cm^{-2}$]	***FF*** [%]	η [%]
[Taguchi 2014]	both-sides	98	750	39.5	83.2	24.7
[Masuko 2014]	IBC	98	740	41.8	82.7	25.6

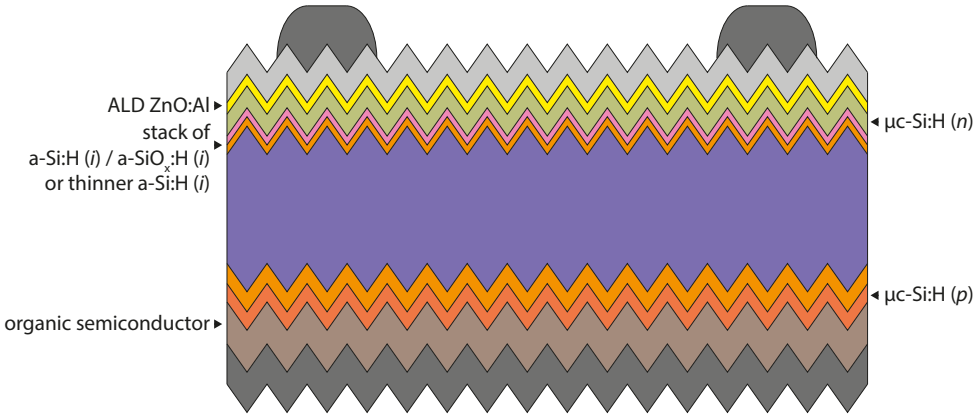

Figure 7.1 – Suggestion for next-generation SHJ solar cells, applying the methods investigated in this work.

the results we obtained on both-side-contacted devices, we can state that a cell with μc-Si:H carrier-collecting layers likely performs best with hole collection at the rear as this poses fewer constraints on the μc-Si:H(p) layer. Increasing the thickness of the μc-Si:H(p) ensures a high crystalline fraction and hence reduces the contact resistance to the TCO by suppressing the Schottky barrier, thereby assuring high *FF* values. As we have seen here (using non-optimized layers), applying μc-Si:H(n) layers at the front can be beneficial for the J_{sc} and also the *FF*, yet, to a smaller extent compared to the effect observed when using μc-Si:H(p). Furthermore, we were able to show that wide-bandgap materials can potentially be applied to the electron-collecting contact to gain in current. An alternative would be to thin down the a-Si:H(i) layer as much as possible, using a non-destructive way to deposit the transparent electrode, to avoid *permanent* sputtering-induced damage. As to the hole contact at the rear, organic semiconductors may help increase both the *FF* and J_{sc}, thanks to reduced recombination losses at low injection and an improved reflection at longer wavelengths associated with the high refractive index of the organic semiconductor.

A structure combining all these changes is depicted in Fig. 7.1 and the estimated variations of the cell parameters are given in Tab. 7.2. As starting point, we assume a $2 \times 2\,cm^2$ device with hole collection at the rear with a V_{oc} of 720 mV, a J_{sc} of 37 $mA\,cm^{-2}$, a *FF* of 77% and

a conversion efficiency of 20.5%—which represents an average cell fabricated in our lab (standard a-Si:H layers, standard ITO). Applying the suggested changes would lead to a device with: 720 mV (assuming the passivation does not change), 39 mA cm^{-2}, 80.5% and a conversion efficiency of 22.6%.

Table 7.2 – Extrapolation of device efficiencies with processes investigated in this work.

	ΔJ_{sc} [mA cm^{-2}]	ΔFF [%]	ΔV_{oc} [mV]	**gain** [%]
μc-Si:H(n) & μc-Si:H(p) layers	1	2	0	
oxides or thinner a-Si:H(i) & ALD	0.5	1	0	
organic semiconductor	0.5	0.5	0	
total variation	2	3.5	0	2.09

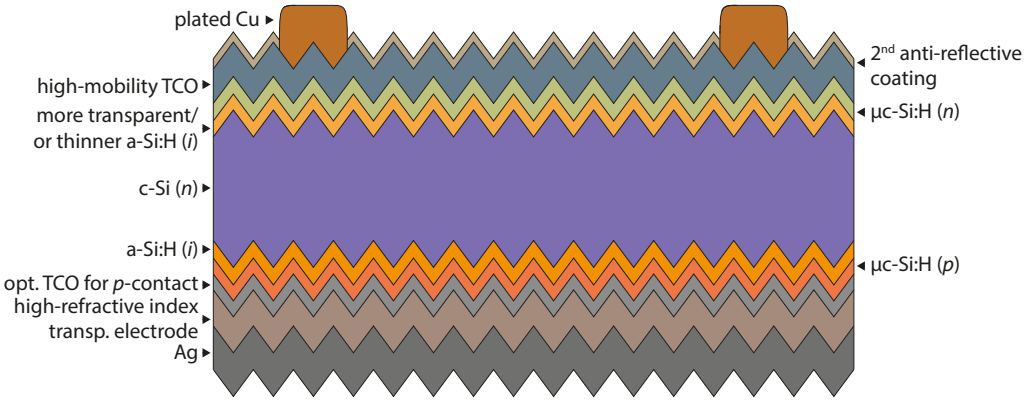

Figure 7.2 – Suggestion for next-generation SHJ solar cells, applying methods beyond this work.

Going beyond the methods investigated in this work the device could be improved even further as described in the following and depicted in Fig. 7.2. Again we start from the same reference cell as before and list the estimated changes (Tab. 7.3). Starting from the top of the device, applying a second anti-reflective coating as well as plated copper contacts, with a high aspect ratio and hence reduce shadow losses [Geissbühler 2014], the J_{sc} of the device could be improved. The latter in combination with a high-mobility front TCO (*e.g.* hydrogenated indium oxide, IO:H [Koida 2009, Barraud 2013])—optimized for the electron-contact—also have the potential to improve the *FF*. For the carrier-selective layers, again we suggest μc-Si:H(p or n) (μc-Si:H(n) at the front and μc-Si:H(p) at the rear), which, as discussed above, are beneficial for both J_{sc} and *FF*. A more transparent or thinner a-Si:H(i) layer at the front

and a high-refractive-index transparent electrode at the rear may boost the J_{sc} even more. The latter could *e.g.* be an organic semiconductor as discussed above or a stack of ITO and magnesium fluoride (MgF_2) minimizing plasmon-related losses [Holman 2013b]. In addition these changes, reducing the wafer thickness would enable higher V_{oc}, increase the *FF* with acceptable losses in J_{sc}. And finally, increasing the cell size from $2 \times 2\,cm^2$ to *e.g.* full-sized $15.6 \times 15.6\,cm^2$ may help to increase the *FF*.

In Tab. 7.3 we summarize the estimated gains in J_{sc}, *FF* and V_{oc} from what has just been discussed. As starting point, we assume the same device as before. V_{oc} of 720 mV, a J_{sc} of $37\,mA\,cm^{-2}$, a *FF* of 77% and a conversion efficiency of 20.5%. With all the changes applied we would in theory reach a V_{oc} of 750 mV, a J_{sc} of $40.1\,mA\,cm^{-2}$, a *FF* of 83.0% and a conversion efficiency of 24.96%.

Table 7.3 – Extrapolation of device efficiencies with processes available at PV-Lab.

	ΔJ_{sc} [$mA\,cm^{-2}$]	ΔFF [%]	ΔV_{oc} [mV]	**gain** [%]
plated contacts	1.3	1	0	
second anti-reflective coating	0.6	0	0	
high-μ front TCO & optimized n-contact	0.6	1	0	
μc-Si:H(n) & μc-Si:H(p) layers	1	2	0	
more transparent or thinner a-Si:H(i)	0.5	0	0	
high-refractive-index rear TCO	0.5	0	0	
optimized p-contact	0	0.5	0	
thinner wafer	−1.4	0.5	30	
large area cell	0	1	0	
total variation	3.1	6.0	30	4.45

These estimates show that there is still some room for improvement for this type of device architecture and that the materials proposed here could indeed be part of this roadmap. In order to reach even higher efficiencies the device architecture has to be changed as well. A promising concept here is to remove the metallic contacts from the front and contact the cell from the rear (IBC design). Combining all the solutions presented here, the next world record for silicon-based solar cells is within reach.

Radiative recombination

In order to calculate the lifetimes for the different recombination processes one starts with the *recombination rate U*. This rate depends on the process: *radiative*, *Auger* or *Shockley-Read-Hall*. The following shows the way from recombination rate U to the lifetime τ in *high* and *low injection* for the example of *radiative recombination*. The recombination rate for this process is given by:

$$U_{\text{rad.}} = r_{\text{ec}}\left(np - n_{\text{i}}^2\right) \tag{1}$$

For the illuminated case the free carrier densities increase by $\Delta n = \Delta p$ and thus $n = n_0 + \Delta n$. Inserted into the equation above this leads to:

$$\begin{aligned} U_{\text{rad.}} &= r_{\text{ec}}\left(n_0 p_0 + n_0 \Delta p + p_0 \Delta n + \Delta n \Delta p - n_{\text{i}}^2\right) \\ &= r_{\text{ec}}\left(n_0 \Delta p + p_0 \Delta n + \Delta n \Delta p\right) \end{aligned} \tag{2}$$

Keeping in mind that $n_0 p_0 = n_{\text{i}}^2$ the first and the last term in the brackets cancel each other out. Now considering *low injection, i.e.* $\Delta n = \Delta p \ll n_0$ for an n-type material, this leads to the following, neglecting all the terms that do not contain n_0.

$$\begin{aligned} U_{\text{rad.}} &= r_{\text{ec}} n_0 \Delta p = \frac{\Delta p}{\tau_{\text{p}}} \text{ and thus} \\ \tau_{\text{p}} &= \frac{1}{r_{\text{ec}} n_0} \end{aligned} \tag{3}$$

For *high injection* the situation changes and $\Delta n = \Delta p \gg n_0$ and p_0. This relation plugged into equation 2 results in the following. This time neglecting the terms with either n_0 or p_0.

$$\tau_{\text{n}} = \tau_{\text{p}} = \frac{1}{r_{\text{ec}} \Delta n} \tag{4}$$

Programming

To facilitate and accelerate the extraction of measurement data or have an easy-to-use system logbook, various programs were written during the course of this thesis, either in Excel using Visual Basic for Applications or in MATLAB. These macros included the following:

- **IV-Summary (light and dark)**: enabling the extraction and treatment of standard *J-V* data at room temperature as well as the calculation of temperature coefficients for temperature-dependent measurements.
- **Lifetime-Summary**: enabling the extraction of lifetime data and the calculation of *iFF* values.
- **Suns-V_{oc}-Summary**: for the extraction of suns-V_{oc} data, the extraction of voltage, lifetime and ideality factor values at different injection/illumination levels (developed together with Andrea Tomasi).
- **R_s from suns-V_{oc} vs. IV**: for the calculation of the series resistance R_s as proposed by Pysch [Pysch 2007].
- **Spectral Response**: for the extraction of spectral response data.
- **GetEllipso**: program coded in MATLAB for the extraction of ellipsometry data.
- **PL**: program coded in MATLAB for the conversion of photoluminescence images from TIF to PNG or JPG with the same scale for an arbitrarily large set of images.
- **Octopus Logger**: enables the easy import of pre-defined process recipes of the Octopus I PECVD system with comments on samples, pre-treatments etc.

Bibliography

[Agostinelli 2006] G Agostinelli, A Delabie, P Vitanov, Z Alexieva, H F W Dekkers, S De Wolf and G Beaucarne. *Very low surface recombination velocities on p-type silicon wafers passivated with a dielectric with fixed negative charge.* Solar Energy Materials and Solar Cells, vol. 90, no. 18–19, pages 3438–3443, 2006.

[Aleman 2014] M Aleman, A Uruena de Castro, P Choulat, B Hallam, C Dang, R Russell, F Duerinckx, E Cornagliotti and J Szlufcik. *Reducing Front Recombination Losses to Improve the Efficiency of Rear Junction Cu-Plated n-Si Cells.* In 29th European Photovoltaic Solar Energy Conference and Exhibition, pages 528–531, 2014.

[Altermatt 2005] P P Altermatt, F Geelhaar, T Trupke, X Dai, A Neisser and E Daub. *Injection dependence of spontaneous radiative recombination in c-Si: experiment, theoretical analysis, and simulation.* In Numerical Simulation of Optoelectronic Devices, 2005. NUSOD '05. Proceedings of the 5th International Conference on, pages 47–48, 19 2005.

[Anderson 1975] R L Anderson. *Photocurrent suppression in heterojunction solar cells.* Applied Physics Letters, vol. 27, no. 12, pages 691–693, 1975.

[Arkles 2000] Barry Arkles. *Kirk-Othmer Encyclopedia of Chemical Technology.* In Kirk-Othmer Encyclopedia of Chemical Technology. John Wiley & Sons, Inc., 2000.

[Asano 1990] A Asano. *Effects of hydrogen atoms on the network structure of hydrogenated amorphous and microcrystalline silicon thin films.* Applied Physics Letters, vol. 56, no. 6, pages 533–535, 1990.

[Auger 1923] P Auger. *Sur les rayons beta secondaires produits dans un gaz par des rayons X.* C.R.A.S., vol. 177, pages 169–171, 1923.

[Bacioğlu 2005] A Bacioğlu, A O Kodolbaş and Ö Öktü. *Deposition of highly photoconductive wide band gap a-SiO:H thin films at a high temperature without H-dilution.* Solar Energy Materials and Solar Cells, vol. 89, no. 1, pages 49–59, 2005.

[Baker-Finch 2010] S C Baker-Finch and K R McIntosh. *A Freeware Program for precise optical Analysis of the front Surface of a Solar Cell.* In 35th IEEE Photovoltaic Specialists Conference, pages 002184–002187, Honolulu, HI, USA, 2010.

[Barraud 2013] L Barraud, Z C Holman, N Badel, P Reiss, A Descoeudres, C Battaglia, S De Wolf and C Ballif. *Hydrogen-doped indium oxide/indium tin oxide bilayers for high-efficiency silicon heterojunction solar cells.* Solar Energy Materials and Solar Cells, vol. 115, pages 151–156, 2013.

[Battaglia 2014] C Battaglia, S Martín de Nicolás, S De Wolf, X Yin, M Zheng, C Ballif and A Javey. *Silicon heterojunction solar cell with passivated hole selective MoOx contact.* Applied Physics Letters, vol. 104, no. 11, pages 1139021–1139025, 2014.

[Bätzner 2011a] D L Bätzner, Y Andrault, L Andreetta, A Büchel, W Frammelsberger, C Guérin, N Holm, D Lachenal, J Meixenberger, P Papet, B Rau, B Strahm, G Wahli and F Wünsch. *Characterisation of over 21% efficient Silicon Heterojunction Cells developed at Roth & Rau Switzerland.* In 26th European Photovoltaic Solar Energy Conference and Exhibition, pages 1073–1075, Hamburg, Germany, 2011.

[Bätzner 2011b] D L Bätzner, Y Andrault, L Andreetta, A Büchel, W Frammelsberger, C Guérin, N Holm, D Lachenal, J Meixenberger, P Papet, B Rau, B Strahm, G Wahli and F Wünsch. *Properties of high efficiency silicon heterojunction cells.* Energy Procedia, vol. 8, pages 153–159, 2011.

[Beyer 1983] W Beyer and H Wagner. *The role of hydrogen in a-Si:H — results of evolution and annealing studies.* Journal of Non-Crystalline Solids, vol. 59–60, Part 1, no. 0, pages 161–168, 12 1983.

[Beyer 1991] W Beyer. *Hydrogen effusion: a probe for surface desorption and diffusion.* Physica B: Condensed Matter, vol. 170, pages 105–114, 1991.

[Bivour 2012] M Bivour, C Reichel, M Hermle and S W Glunz. *Improving the a-Si:H(p) rear emitter contact of n-type silicon solar cells.* Solar Energy Materials and Solar Cells, vol. 106, pages 11–16, 2012.

[Bivour 2013] M Bivour, S Schröer and M Hermle. *Numerical Analysis of Electrical TCO / a-Si:H(p) Contact Properties for Silicon Heterojunction Solar Cells.* Energy Procedia, vol. 38, pages 658–669, 2013.

[Bivour 2014] M Bivour, M Reusch, S Schröer, F Feldmann, J Temmler, H Steinkemper and M Hermle. *Doped Layer Optimization for Silicon Heterojunctions by Injection-Level-Dependent Open-Circuit Voltage Measurements.* IEEE Journal of Photovoltaics, vol. 4, no. 2, pages 566–574, 2014.

[Bludau 1974] W Bludau, A Onton and W Heinke. *Temperature dependence of the band gap of silicon.* Journal of Applied Physics, vol. 45, no. 4, pages 1846–1848, 1974.

[Boland 1992] J J Boland and G N Parsons. *Bond Selectivity in Silicon Film Growth.* Science, vol. 256, no. 5061, pages 1304–1306, 1992.

[Bugnon 2012] G Bugnon, G Parascandolo, T Söderström, P Cuony, M Despeisse, S Hänni, J Holovsky, F Meillaud and C Ballif. *A New View of Microcrystalline Silicon: The Role of Plasma Processing in Achieving a Dense and Stable Absorber Material for Photovoltaic Applications.* Advanced Functional Materials, vol. 22, no. 17, pages 3665–3671, 2012.

[Bugnon 2013] G Bugnon. *High-Quality Microcrystalline Silicon for Efficient Thin-Film Solar Cells: Insights into Plasma and Material Properties.* Ecole Polytechnique Fédérale de Lausanne, 2013.

[Bugnon 2014] G Bugnon, G Parascandolo, S Hänni, M Stückelberger, Mathieu Charrière, M Despeisse, F Meillaud and C Ballif. *Silicon oxide buffer layer at the p–i interface in amorphous and microcrystalline silicon solar cells.* Solar Energy Materials and Solar Cells, vol. 120, pages 143–150, 2014.

[Bullock 2014] J Bullock, A Cuevas, D Yan, B Demaurex, A Hessler-Wyser and S De Wolf. *Amorphous silicon enhanced metal-insulator-semiconductor contacts for silicon solar cells.* Journal of Applied Physics, vol. 116, no. 16, page 163706, 2014.

[Bullock 2015] J Bullock, D Yan, A Cuevas, Y Wan and C Samundsett. *n- and p-type silicon solar cells with molybdenum oxide hole contacts.* Energy Procedia, 2015.

[Campbell 2007] Wayne M Campbell, Kenneth W Jolley, Pawel Wagner, Klaudia Wagner, Penny J Walsh, Keith C Gordon, Lukas Schmidt-Mende, Mohammad K Nazeeruddin, Qing Wang, M Grätzel and David L Officer. *Highly Efficient Porphyrin Sensitizers for Dye-Sensitized Solar Cells.* The Journal of Physical Chemistry C, vol. 111, no. 32, pages 11760–11762, 2007 2007.

[Cardona 1983] M Cardona. *Vibrational Spectra of Hydrogen in Silicon and Germanium.* Physica Status Solidi B Basic Solid State Physics, vol. 118, no. 2, pages 463–481, 1983.

[Chavali 2014] R V K Chavali, J R Wilcox, B Ray, J L Gray and M A Alam. *Correlated Nonideal Effects of Dark and Light I-V Characteristics in a-Si/c-Si Heterojunction Solar Cells.* IEEE Journal of Photovoltaics, vol. 4, no. 3, pages 763–771, 2014.

[Choong 2009] G Choong, N Wyrsch, M Python and C Ballif. *High mobility bottom gate microcrystalline silicon TFT deposited by VHF PECVD.* In 5th International TFT Conference, 2009.

[Chou 1992] J S Chou, W J Sah, S C Lee, T C Chang and J C Wang. *Microcrystalline silicon deposited by glow discharge decomposition of heaviliy diluted silane.* Materials Chemistry and Physics, vol. 32, pages 273–279, 1992.

[Clugston 1997] D A Clugston and P A Basore. *PC1D Version 5: 32-Bit Solar Cell Modeling on personal Computers.* In 26th IEEE Photovoltaic Specialists Conference, pages 207–210, Anaheim, CA, USA, 1997.

[Cornagliotti 2014] E Cornagliotti, A Sharma, A Uruena, M Aleman, L Tous, R Russell, P Choulat, J Chen, J John, F Duerinckx, B Dielissen, R Görtzen, L Black and J Szlufcik. *Large Area n-type c-Si Solar Cells Featuring rear Emitter and Efficiency beyond 21%.* In The 6th World Conference on Photovoltaic Energy Conversion, Kyoto, Japan, 2014.

[Cornagliotti 2015] E Cornagliotti, A Uruena, B Hallam, L Tous, R Russell, F Duerinckx and J Szlufcik. *Large area p-type PERL cells featuring local p+ BSF formed by laser processing of ALD Al2O3 layers.* Solar Energy Materials and Solar Cells, vol. 138, no. 0, pages 72–79, 7 2015.

[Courtois 2013] G Courtois, B Bruneau, I P Sobkowicz, A Salomon and P Roca i Cabarrocas. *Carrier Lifetime Measurements by Photoconductance at Low Temperature on Passivated Crystalline Silicon Wafers.* MRS Online Proceedings Library, vol. 1536, pages 119–125, 2013.

[Cousins 2010] P J Cousins, D D Smith, Luan Hsin-Chiao, J Manning, T D Dennis, A Waldhauer, K E Wilson, G Harley and W P Mulligan. *Generation 3: Improved performance at lower cost.* In 38th IEEE Photovoltaic Specialists Conference, pages 000275–000278, 20 2010.

[Cuevas 2013] A Cuevas and D Yan. *Misconceptions and Misnomers in Solar Cells.* IEEE Journal of Photovoltaics, vol. 3, no. 2, pages 916–923, April 2013.

[Cuony 2010] P Cuony, M Marending, D T L Alexander, M Boccard, G Bugnon, M Despeisse and C Ballif. *Mixed-phase p-type silicon oxide containing silicon nanocrystals and its role in thin-film silicon solar cells.* Applied Physics Letters, vol. 97, no. 21, page 213502, 2010.

[Cuony 2012] P Cuony, D T L Alexander, I Perez-Wurfl, M Despeisse, G Bugnon, M Boccard, T Söderström, A Hessler-Wyser, C Hebert and C Ballif. *Silicon filaments in silicon oxide for next-generation photovoltaics.* Advanced Materials, vol. 24, no. 9, pages 1182–1186, March 2012.

[Das 1996] U K Das, P Chaudhuri and S T Kshirsagar. *Effect of argon dilution on the structure of microcrystalline silicon deposited from silane.* Journal of Applied Physics, vol. 80, no. 9, page 5389, 1996.

[Davis 1980] J R Jr Davis, A Rohatgi, R H Hopkins, P D Blais, P Rai-Choudhury, J R McCormick and H C Mollenkopf. *Impurities in silicon solar cells.* Electron Devices, IEEE Transactions on, vol. 27, no. 4, pages 677–687, 1980.

[De Wolf 2007] S De Wolf and M Kondo. *Boron-doped a-Si:H/c-Si interface passivation: Degradation mechanism.* Applied Physics Letters, vol. 91, no. 11, page 112109, 2007.

[De Wolf 2008] S De Wolf, Sara Olibet and C Ballif. *Stretched-exponential a-Si:H/c-Si interface recombination decay.* Applied Physics Letters, vol. 93, no. 3, pages 0321011–0321013, 2008.

[De Wolf 2009] S De Wolf and M Kondo. *Nature of doped a-Si:H/c-Si interface recombination.* Journal of Applied Physics, vol. 105, no. 10, pages 1037071–1037076, 2009.

[De Wolf 2012a] S De Wolf, C Ballif and M Kondo. *Kinetics of a-Si:H bulk defect and a-Si:H/c-Si interface-state reduction.* Physical Review B, vol. 85, no. 11, pages 1133021–1133024, 2012.

[De Wolf 2012b] S De Wolf, A Descoeudres, Z C Holman and C Ballif. *High-efficiency Silicon Heterojunction Solar Cells: A Review.* Green, vol. 2, no. 1, pages 7–24, 2012.

[Deibel 2010] C Deibel and V Dyakonov. *Polymer–fullerene bulk heterojunction solar cells.* Reports on Progress in Physics, vol. 73, no. 9, page 096401, 2010.

[Demaurex 2012] B Demaurex, S De Wolf, A Descoeudres, Z C Holman and C Ballif. *Damage at hydrogenated amorphous/crystalline silicon interfaces by indium tin oxide overlayer sputtering.* Applied Physics Letters, vol. 101, no. 17, page 171604, 2012.

[Demaurex 2014a] B Demaurex. *Passivating contacts for homojunction solar cells using a-Si:H/c-Si hetero-interfaces.* EPFL, 2014.

[Demaurex 2014b] B Demaurex, R Bartlome, J P Seif, J Geissbühler, D T L Alexander, Q Jeangros, C Ballif and S De Wolf. *Low-temperature plasma-deposited silicon epitaxial films: Growth and properties.* Journal of Applied Physics, vol. 116, no. 5, page 053519, 2014.

[Dennler 2009] Gilles Dennler, Markus C Scharber and Christoph J Brabec. *Polymer-Fullerene Bulk-Heterojunction Solar Cells.* Advanced Materials, vol. 21, no. 13, pages 1323–1338, 2009.

[Descoeudres 2011] A Descoeudres, L Barraud, S De Wolf, B Strahm, D Lachenal, C Guérin, Z C Holman, F Zicarelli, B Demaurex, J P Seif, J Holovsky and C Ballif. *Improved amorphous/crystalline silicon interface passivation by hydrogen plasma treatment.* Applied Physics Letters, vol. 99, no. 12, page 123506, 2011.

[Descoeudres 2013] A Descoeudres, Z C Holman, L Barraud, S Morel, S De Wolf and C Ballif. *>21% Efficient Silicon Heterojunction Solar Cells on n- and p-Type Wafers Compared.* IEEE Journal of Photovoltaics, vol. 3, no. 1, pages 83–89, 2013.

[Ding 2012] K Ding, U Aeberhard, F Finger and U Rau. *Silicon heterojunction solar cell with amorphous silicon oxide buffer and microcrystalline silicon oxide contact layers.* Physica Status Solidi - Rapid Research Letters, vol. 6, no. 5, pages 193–195, 2012.

[Ding 2013a] K Ding, U Aeberhard, F Finger and U Rau. *Optimized amorphous silicon oxide buffer layers for silicon heterojunction solar cells with microcrystalline silicon oxide contact layers.* Journal of Applied Physics, vol. 113, no. 13, page 134501, 2013.

[Ding 2013b] L Ding. *Low-Pressure Chemical Vapor Deposited Zinc Oxide Films: Toward Decoupled Opto-Electrical and Morphological Properties for More Efficient Electrodes.* EPFL, 2013.

[Dornstetter 2013] J C Dornstetter, S Kasouit and P R I Cabarrocas. *Deposition of High-Efficiency Microcrystalline Silicon Solar Cells Using SiF4/H-2/Ar Mixtures.* IEEE Journal of Photovoltaics, vol. 3, no. 1, pages 581–586, January 2013.

[Droz 2004] C Droz, E Vallat-Sauvain, J Bailat, L Feitknecht, J Meier and A Shah. *Relationship between Raman crystallinity and open-circuit voltage in microcrystalline silicon solar cells.* Solar Energy Materials and Solar Cells, vol. 81, no. 1, pages 61–71, 2004.

[Dullweber 2011] T Dullweber, S Gatz, H Hannebauer, T Falcon, R Hesse, J Schmidt and Brendel R. *19.4% -Efficient Large Area Rear-Passivated Screen-Printed Silicon Solar Cells.* In 26th European Photovoltaic Solar Energy Conference and Exhibition, pages 811–816, Hamburg, Germany, 2011.

[Dziewior 1977] J Dziewior and W Schmid. *Auger coefficients for highly doped and highly excited silicon.* Applied Physics Letters, vol. 31, no. 5, pages 346–348, 1977.

[Einsele 2012] Florian Einsele, Wolfhard Beyer and U Rau. *Analysis of sub-stoichiometric hydrogenated silicon oxide films for surface passivation of crystalline silicon solar cells.* Journal of Applied Physics, vol. 112, no. 5, page 054905, 2012.

[El Mhamdi 2014] E M El Mhamdi, J Holovsky, B Demaurex, C Ballif and S De Wolf. *Is light-induced degradation of a-Si:H/c-Si interfaces reversible?* Applied Physics Letters, vol. 104, no. 25, pages 2521081–2521084, 2014.

[Favre 2013] W Favre, J Coignus, N Nguyen, R Lachaume, R Cabal and D Muñoz. *Influence of the transparent conductive oxide layer deposition step on electrical properties of silicon heterojunction solar cells.* Applied Physics Letters, vol. 102, no. 18, page 181118, 2013.

[Filipič 2013] M Filipič, Z C Holman, F Smole, S De Wolf, C Ballif and Marko Topič. *Analysis of lateral transport through the inversion layer in amorphous silicon/crystalline silicon heterojunction solar cells.* Journal of Applied Physics, vol. 114, no. 7, page 074504, 2013.

[Finger 1994] F Finger, P Hapke, M Luysberg, R Carius, H Wagner and M Scheib. *Improvement of grain size and deposition rate of microcrystalline silicon by use of very high frequency glow discharge.* Applied Physics Letters, vol. 65, no. 20, page 2588, 1994.

[Fraunhofer ISE 2014] Fraunhofer ISE. *Photovoltaics Report.* Rapport technique, 2014.

[Fujiwara 2002] Hiroyuki Fujiwara, M Kondo and A Matsuda. *Stress-Induced Nucleation of Microcrystalline Silicon from Amorphous Phase.* Japanese Journal of Applied Physics, vol. 41, no. Part 1, No. 5A, pages 2821–2828, 2002.

[Fujiwara 2004] Hiroyuki Fujiwara, M Kondo and A Matsuda. *Nucleation mechanism of microcrystalline silicon from the amorphous phase.* Journal of Non-Crystalline Solids, vol. 338-340, pages 97–101, 2004.

[Fujiwara 2009] Hiroyuki Fujiwara, Hitoshi Sai and M Kondo. *Crystalline Si Heterojunction Solar Cells with the Double Heterostructure of Hydrogenated Amorphous Silicon Oxide.* Japanese Journal of Applied Physics, vol. 48, no. 6, page 064506, 2009.

[Geissbühler 2013] J Geissbühler, S De Wolf, B Demaurex, J P Seif, D T L Alexander, L Barraud and C Ballif. *Amorphous/crystalline silicon interface defects induced by hydrogen plasma treatments.* Applied Physics Letters, vol. 102, no. 23, page 231604, 2013.

[Geissbühler 2014] J Geissbühler, S De Wolf, A Faes, N Badel, Q Jeangros, A Tomasi, L Barraud, A Descoeudres, M Despeisse and C Ballif. *Silicon Heterojunction Solar Cells With Copper-Plated Grid Electrodes: Status and Comparison With Silver Thick-Film Techniques.* IEEE Journal of Photovoltaics, vol. 4, no. 4, pages 1055–1062, 2014.

[Glunz 2007] S W Glunz, J Nekarda, H Mäckel and A Cuevas. *Analyzing Back Contacts of Silicon Solar Cells by Suns-Voc-Measurements at High Illumination Densities.* In 22nd European Photovoltaic Solar Energy Conference and Exhibition, pages 849–853, Milan, Italy, 2007.

[Goldie 2013] D M Goldie. *Hole Dangling Bond Capture Cross-Sections in a-Si:H.* American Journal of Material Science, vol. 3, no. 4, pages 70–76, 2013.

[Green 1982a] M A Green. Solar Cells: Operating Principles, Technology and System Applications. University of New South Wales, 1982.

[Green 1982b] M A Green, K Emery and A W Blakers. *Silicon solar cells with reduced temperature sensitivity.* Electronics Letters, vol. 18, no. 2, pages 97–98, 1982.

[Green 1983] M A Green. *Accuracy of analytical expressions for solar cell fill factors.* Solar Cells, vol. 7, pages 337–340, 1983.

[Green 1985] M A Green, A W Blakers and C R Osterwald. *Characterization of high-efficiency silicon solar cells.* Journal of Applied Physics, vol. 58, no. 11, pages 4402–4408, 1985.

[Green 2003] Martin A Green. *General temperature dependence of solar cell performance and implications for device modelling.* Progress in Photovoltaics: Research and Applications, vol. 11, no. 5, pages 333–340, 2003.

[Green 2009] Martin A Green. *The path to 25% silicon solar cell efficiency: History of silicon cell evolution.* Progress in Photovoltaics: Research and Applications, vol. 17, no. 3, pages 183–189, 2009.

[Gupta 1988] P Gupta, V L Colvin and S M George. *Hydrogen desorption kinetics from monohydride and dihydride species on silicon surfaces.* Physical Review B, vol. 37, no. 14, pages 8234–8243, 1988.

[Hall 1952] R N Hall. *Electron-Hole Recombination in Germanium.* Phys. Rev., vol. 87, 1952.

[Hänni 2013] S Hänni, G Bugnon, G Parascandolo, M Boccard, J Escarré, M Despeisse, F Meillaud and C Ballif. *High-efficiency microcrystalline silicon single-junction solar cells*. Progress in Photovoltaics: Research and Applications, vol. 21, pages 821–826, 2013.

[Hänni 2014] S Hänni. *Microcrystalline Silicon for High-Efficiency Thin-Film Photovoltaic Devices*. Ecole Polytechnique Fédérale de Lausanne (EPFL), 2014.

[He 2000] L N He, D M Wang and S Hasegawa. *A study of plasma-deposited amorphous SiOx:H (0<x<2.0) films using infrared spectroscopy*. Journal of Non-Crystalline Solids, vol. 261, pages 67–71, 2000.

[Heintze 1996] M Heintze and R Zedlitz. *New diagnostic aspects of high rate a-Si:H deposition in a VHF plasma*. Journal of Non-Crystalline Solids, vol. 198-200, pages 1038–1041, 1996.

[Hernández 2012] J L Hernández, D Adachi, K Yoshikawa, D Schroos, E Van Assche, A Feltrin, N Valckx, N Menou, J Poortmans, M Yoshimi, T Uto, H Uzu, M Hino, H Kawasaki, M Kanematsu, K Nakano, R Mishima, T Kuchiyama, G Koizumi, C Allebé, T Terashita, M Hiraishi, N Nakanishi and K Yamamoto. *High Efficiency Copper Electroplated Heterojunction Solar Cells*. In 27th European Photovoltaic Solar Energy Conference and Exhibition, Frankfurt, Germany, 2012.

[Hoex 2006] B Hoex, S B S Heil, E Langereis, M C M van de Sanden and W M M Kessels. *Ultralow surface recombination of c-Si substrates passivated by plasma-assisted atomic layer deposited Al2O3*. Applied Physics Letters, vol. 89, no. 4, pages 042112 1–3, July 2006.

[Holman 2012] Z C Holman, A Descoeudres, L Barraud, F Zicarelli Fernandez, J P Seif, S De Wolf and C Ballif. *Current Losses at the Front of Silicon Heterojunction Solar Cells*. IEEE Journal of Photovoltaics, vol. 2, no. 1, pages 7–15, 2012.

[Holman 2013a] Z C Holman, S De Wolf and C Ballif. *Improving metal reflectors by suppressing surface plasmon polaritons: a priori calculation of the internal reflectance of a solar cell*. Light: Science & Applications, vol. 2, no. 10, page e106, 2013.

[Holman 2013b] Z C Holman, A Descoeudres, S De Wolf and C Ballif. *Record Infrared Internal Quantum Efficiency in Silicon Heterojunction Solar Cells With Dielectric/Metal Rear Reflectors*. IEEE Journal of Photovoltaics, vol. 3, no. 4, pages 1243–1249, 2013.

[Holman 2013c] Z C Holman, M Filipič, A Descoeudres, S De Wolf, F Smole, M Topič and C Ballif. *Infrared light management in high-efficiency silicon heterojunction and rear-passivated solar cells*. Journal of Applied Physics, vol. 113, no. 1, page 013107, 2013.

[Holman 2015] Z C Holman, P Koswatta and M Boccard. *A Theory of Passivating, Carrier-Selective, and Majority-Carrire-Conductive Contacts for Silicon Solar Cells*. In 5th SiliconPV, Konstanz, Germany, 2015.

[Iftiquar 1998] S M Iftiquar. *The roles of deposition pressure and rf power in opto-electronic properties of a-SiO:H films.* Journal of Physics D: Applied Physics, vol. 31, pages 1630–1641, 1998.

[Jousse 1985] D Jousse, E Bustarret and F Boulitrop. *Disorder and Defects in Sputtered a-SiH from Subgap Absorption Measurements.* Solid State Communications, vol. 55, no. 5, pages 435–438, 1985.

[Kageyama 2011] Shota Kageyama, Masataka Akagawa and Hiroyuki Fujiwara. *Dielectric function of a-Si:H based on local network structures.* Physical Review B, vol. 83, no. 19, page 195205, 2011.

[Kaïl 2004] F Kaïl, A Fontcuberta I Morral, A Hadjadj, P Roca i Cabarrocas and A Beorchia. *Hydrogen-plasma etching of hydrogenated amorphous silicon: a study by a combination of spectroscopic ellipsometry and trap-limited diffusion model.* Philosophical Magazine, vol. 84, no. 6, pages 595–609, 2004.

[Kasouit 2002] S Kasouit, S Kumar, R Vanderhaghen, P Roca i Cabarrocas and I French. *Fluorine and hydrogen effects on the growth and transport properties of microcrystalline silicon from SiF4 precursor.* Journal of Non-Crystalline Solids, vol. 299-302, pages 113–117, 2002.

[Kasouit 2004] S Kasouit, J Damon-Lacoste, R Vanderhaghen and P Roca i Cabarrocas. *Contribution of plasma generated nanocrystals to the growth of microcrystalline silicon thin films.* Journal of Non-Crystalline Solids, vol. 338-340, pages 86–90, 2004.

[Kerr 2002] M J Kerr, A Cuevas and R A Sinton. *Generalized analysis of quasi-steady-state and transient decay open circuit voltage measurements.* Journal of Applied Physics, vol. 91, no. 1, pages 399–404, 2002.

[Khanna 2013] A Khanna, T Mueller, R A Stangl, B Hoex, P K Basu and A G Aberle. *A Fill Factor Loss Analysis Method for Silicon Wafer Solar Cells.* IEEE Journal of Photovoltaics, vol. 3, no. 4, pages 1170–1177, 2013.

[Kido 1994] J Kido, K Hongawa, K Okuyama and K Nagai. *White light-emitting organic electroluminescent devices using the poly(N-vinylcarbazole) emitter layer doped with three fluorescent dyes.* Applied Physics Letters, vol. 64, no. 7, pages 815–817, 1994.

[Kim 2012] H S Kim, C R Lee, J H Im, K B Lee, T Moehl, A Marchioro, S J Moon, R Humphry-Baker, J H Yum, J E Moser, M Gratzel and N G Park. *Lead iodide perovskite sensitized all-solid-state submicron thin film mesoscopic solar cell with efficiency exceeding 9%.* Sci Rep, vol. 2, page 591, 2012.

[Kinoshita 2011] T Kinoshita, D Fujishima, A Yano, Akiyoshi Ogane, Satoshi Tohoda, K Matsuyama, Yuya Nakamura, Nozomu Tokuoka, Hiroshi Kanno, H Sakata, M Taguchi and E Maruyama. *The Approaches for High Efficency HIT Solar Cell with very thin (<100 um)*

Silicon Wafer Over 23%. In 26th European Photovoltaic Solar Energy Conference and Exhibition, pages 871–874, Hamburg, Germany, 2011.

[Kippelen 2009] Bernard Kippelen and Jean-Luc Bredas. *Organic photovoltaics*. Energy & Environmental Science, vol. 2, no. 3, pages 251–261, 2009.

[Knights 1980] J C Knights, R A Street and G Lucovsky. *Electronic and structural Properties of Plasma-deposited a-Si:O:H - The Story of O2*. Journal of Non-Crystalline Solids, vol. 35 & 36, pages 279–284, 1980.

[Koida 2009] T Koida, H Fujiwara and M Kondo. *High-mobility hydrogen-doped In2O3In2O3 transparent conductive oxide for a-Si:H/c-Si heterojunction solar cells*. Solar Energy Materials and Solar Cells, vol. 93, no. 6-7, pages 851–854, 2009.

[Korte 2011] L Korte and M Schmidt. *Doping type and thickness dependence of band offsets at the amorphous/crystalline silicon heterojunction*. Journal of Applied Physics, vol. 109, no. 6, page 063714, 2011.

[Krč 2003] Janez Krč, F Smole and Marko Topič. *Analysis of light scattering in amorphous Si:H solar cells by a one-dimensional semi-coherent optical model*. Progress in Photovoltaics: Research and Applications, vol. 11, no. 1, pages 15–26, 2003.

[Krüger 2001] Jessica Krüger, Robert Plass, Le Cevey, Marco Piccirelli, M Grätzel and Udo Bach. *High efficiency solid-state photovoltaic device due to inhibition of interface charge recombination*. Applied Physics Letters, vol. 79, no. 13, page 2085, 2001.

[Kurtz 2011] Sarah Kurtz, Kent Whitfield, G TamizhMani, M Koehl, David Miller, James Joyce, John Wohlgemuth, Nick Bosco, M Kempe and Timothy Zgonena. *Evaluation of high-temperature exposure of photovoltaic modules*. Progress in Photovoltaics: Research and Applications, vol. 19, no. 8, pages 954–965, 2011.

[Lamansky 2001] Sergey Lamansky, Raymond C Kwong, Matthew Nugent, Peter I Djurovich and Mark E Thompson. *Molecularly doped polymer light emitting diodes utilizing phosphorescent Pt(II) and Ir(III) dopants*. Organic Electronics, vol. 2, no. 1, pages 53–62, July 2001.

[Lambertz 2011] A Lambertz, T Grundler and F Finger. *Hydrogenated amorphous silicon oxide containing a microcrystalline silicon phase and usage as an intermediate reflector in thin-film silicon solar cells*. Journal of Applied Physics, vol. 109, no. 11, page 113109, 2011.

[Lampert 1964] M A Lampert. *Volume-controlled current injection in insulators*. Reports on Progress in Physics, vol. 27, no. 1, pages 329–367, 1964.

[Leendertz 2010] C Leendertz, R Stangl, T F Schulze, M Schmidt and L Korte. *A recombination model for a-Si:H/c-Si heterostructures*. physica status solidi (c), pages 1005–1010, 2010.

[Liebhaber 2015] M Liebhaber, M Mews, T F Schulze, L Korte, B Rech and K Lips. *Valence band offset in heterojunctions between crystalline silicon and amorphous silicon (sub)oxides (a-SiOx:H, 0 < x < 2).* Applied Physics Letters, vol. 106, no. 3, pages –, 2015.

[Loper 2014] P Loper, B Niesen, Moon Soo-Jin, S Martin de Nicolas, J Holovsky, Z Remes, M Ledinsky, F J Haug, Yum Jun-Ho, S De Wolf and C Ballif. *Organic-Inorganic Halide Perovskites: Perspectives for Silicon-Based Tandem Solar Cells.* IEEE Journal of Photovoltaics, vol. 4, no. 6, pages 1545–1551, 2014.

[Lu 2011] Meijun Lu, Ujjwal Das, Stuart Bowden, Steven Hegedus and Robert Birkmire. *Optimization of interdigitated back contact silicon heterojunction solar cells: tailoring hetero-interface band structures while maintaining surface passivation.* Progress in Photovoltaics: Research and Applications, vol. 19, no. 3, pages 326–338, 2011.

[Madani Ghahfarokhi 2014] Omid Madani Ghahfarokhi, Karsten von Maydell and Carsten Agert. *Enhanced passivation at amorphous/crystalline silicon interface and suppressed Schottky barrier by deposition of microcrystalline silicon emitter layer in silicon heterojunction solar cells.* Applied Physics Letters, vol. 104, no. 11, page 113901, 2014.

[Mark 2002] J Kerr Mark and Cuevas Andres. *Very low bulk and surface recombination in oxidized silicon wafers.* Semiconductor Science and Technology, vol. 17, no. 1, page 35, 2002.

[Marsal 1996a] L F Marsal, J Pallares, X Correig, J Calderer and R Alcubilla. *Electrical characterization of n-amorphous/p-crystalline silicon heterojunctions.* Journal of Applied Physics, vol. 79, no. 11, page 8493, 1996.

[Marsal 1996b] L F Marsal, J Pallares, X Correig, J Calderer and R Alcubilla. *Electrical model for amorphous/crystalline heterojunction silicon diodes (n a-Si:H/p c-Si).* Semiconductor Science and Technology, vol. 11, no. 8, page 1209, 1996.

[Masuko 2014] K Masuko, M Shigematsu, T Hashiguchi, D Fujishima, M Kai, N Yoshimura, T Yamaguchi, Y Ichihashi, T Mishima, N Matsubara, T Yamanishi, T Takahama, M Taguchi, E Maruyama and S Okamoto. *Achievement of More Than 25% Conversion Efficiency With Crystalline Silicon Heterojunction Solar Cell.* IEEE Journal of Photovoltaics, vol. 4, no. 6, pages 1433–1435, 2014.

[Matsuda 1983] A Matsuda. *Formation Kinetics and Control of Microcrystalline in uc-Si:H from Glow Discharge Plasma.* Journal of Non-Crystalline Solids, vol. 59 & 60, pages 767–774, 1983.

[Matsuda 1999] A Matsuda. *Growth mechanism of microcrystalline silicon obtained from reactive plasmas.* Thin Solid Films, vol. 337, pages 1–6, 1999.

[Matsuda 2004] A Matsuda. *Microcrystalline silicon. Growth and device application.* Journal of Non-Crystalline Solids, vol. 338-340, pages 1–12, 2004.

[Matsuura 1984] H Matsuura, T Okuno, H Okushi and K Tanaka. *Electrical properties of n-amorphous/p-crystalline silicon heterojunctions*. Journal of Applied Physics, vol. 55, no. 4, pages 1012–1019, 1984.

[Mazzarella 2015] L Mazzarella, S Kirner, B Stannowski, L Korte, B Rech and R Schlatmann. *p-type microcrystalline silicon oxide emitter for silicon heterojunction solar cells allowing current densities above 40 mA cm^{-2}*. Applied Physics Letters, vol. 106, no. 2, page 023902, 2015.

[McIntosh 2001] K R McIntosh. *Lumps, humps and bumps: Three detrimental effects in the current-voltage curve of silicon solar cells*. UNSW, 2001.

[McIntosh 2015] K McIntosh, M Abbott and S Baker-Finch. *PV LIGHTHOUSE, http://www.pvlighthouse.com.au/, 2015*, 2015.

[Meillaud 2015] F Meillaud, M Boccard, G Bugnon, M Despeisse, S Hänni, F J Haug, J Persoz, J W Schüttauf, M Stückelberger and C Ballif. *Recent advances and remaining challenges in thin-film silicon photovoltaic technology*. Materials Today, no. 0, 2015.

[Mishima 2011] T Mishima, M Taguchi, H Sakata and E Maruyama. *Development status of high-efficiency HIT solar cells*. Solar Energy Materials and Solar Cells, vol. 95, no. 1, pages 18–21, 2011.

[Mueller 2010] T Mueller, S Schwertheim and W R Fahrner. *Crystalline silicon surface passivation by high-frequency plasma-enhanced chemical-vapor-deposited nanocomposite silicon suboxides for solar cell applications*. Journal of Applied Physics, vol. 107, no. 1, page 014504, 2010.

[Mueller 2012] T Mueller, J Wong and Armin G Aberle. *Heterojunction Silicon Wafer Solar Cells using Amorphous Silicon Suboxides for Interface Passivation*. Energy Procedia, vol. 15, pages 97–106, 2012.

[Nakamura 2014] J Nakamura, N Asano, T Hieda, C Okamoto, H Katayama and K Nakamura. *Development of Heterojunction Back Contact Si Solar Cells*. IEEE Journal of Photovoltaics, vol. 4, no. 6, pages 1491–1495, 2014.

[Nerat 2009] M Nerat, G Cernivec, F Smole and Marko Topič. *One- and Two-dimensional Analysis of CIGSS Solar Cells using an advanced Solar Cell Simulator ASPIN*. In 24th European Photovoltaic Solar Energy Conference, pages 2433–2438, Hamburg, Germany, 2009.

[Nguyen 2014] Hieu T Nguyen, Simeon C Baker-Finch and Daniel Macdonald. *Temperature dependence of the radiative recombination coefficient in crystalline silicon from spectral photoluminescence*. Applied Physics Letters, vol. 104, no. 11, pages 1121051–1121053, 2014.

[Niwano 1994] Michio Niwano, Jun-ichi Kageyama, Koji Kinashi, Nobuo Miyamoto and Koji Honma. *Infrared spectroscopic study of initial stages of ultraviolet ozone oxidation of Si(100) and (111) surfaces.* Journal of Vacuum Science & Technology A: Vacuum, Surfaces, and Films, vol. 12, no. 2, pages 465–470, 1994.

[NREL 2015] NREL. *Best Research-Cell Efficiencies.* Rapport technique, 2015.

[OECD 2014] IEA OECD. *Key World Energy Statistics.* Rapport technique, 2014.

[Ohring 2001] M Ohring. Materials Science of Thin Films. Elsevier Science, 2001.

[Olibet 2007] Sara Olibet, Evelyne Vallat-Sauvain and C Ballif. *Model for a-Si:H/c-Si interface recombination based on the amphoteric nature of silicon dangling bonds.* Physical Review B, vol. 76, no. 3, 2007.

[Pallares 2006] J Pallares, R Cabré, L F Marsal and R E I Schropp. *A compact equivalent circuit for the dark current-voltage characteristics of nonideal solar cells.* Journal of Applied Physics, vol. 100, no. 8, page 084513, 2006.

[Panasonic 2015] Panasonic. *http://panasonic.net/ecosolutions/solar/hit/, 2015.* 2015.

[Papet 2013] P Papet, J Hermans, T Söderström, M Cucinelli, L Andreetta, D Bätzner, W Frammelsberger, D Lachenal, J Meixenberger, B Legradic, B Strahm, G Wahli, W Brok, J Geissbühler, A Tomasi, C Ballif, E Vetter and S Leu. *Heterojunction solar cells with electroplated Ni/Cu front electrode.* In 28th European Photovoltaic Solar Energy Conference and Exhibition, Paris, France, 2013.

[Paviet-Salomon 2015] B Paviet-Salomon, A Tomasi, A Descoeudres, L Barraud, S Nicolay, M Despeisse, S De Wolf and C Ballif. *Back-contacted silicon heterojunction solar cells : Optical-loss analysis and mitigation.* IEEE Journal of Photovoltaics, vol. submitted, 2015.

[Pellaton Vaucher 1997] N Pellaton Vaucher, B Rech, D Fischer, S Dubail, M Goetz, H Keppner, N Wyrsch, C Beneking, O Hadjadj, V Shklover and A Shah. *Controlled nucleation of thin microcrystalline layers for the recombination junction in a-Si stacked cells.* Solar Energy Materials and Solar Cells, vol. 49, pages 27–33, 1997.

[Pernet 2000] P Pernet. *Développement de cellules solaires en silicium amorphe de type "n-i-p" sur substrats souples.* Ecole Polytechnique Fédérale de Lausanne (EPFL), 2000.

[Pysch 2007] D Pysch, A Mette and S W Glunz. *A review and comparison of different methods to determine the series resistance of solar cells.* Solar Energy Materials and Solar Cells, vol. 91, no. 18, pages 1698–1706, 2007.

[Rafiq 2005] M A Rafiq, Y Tsuchiya, H Mizuta, S Oda, Shigeyasu Uno, Z A K Durrani and W I Milne. *Charge injection and trapping in silicon nanocrystals.* Applied Physics Letters, vol. 87, no. 18, page 182101, 2005.

[Rahmouni 2010] M Rahmouni, A Datta, P Chatterjee, J Damon-Lacoste, C Ballif and P Roca i Cabarrocas. *Carrier transport and sensitivity issues in heterojunction with intrinsic thin layer solar cells on N-type crystalline silicon: A computer simulation study.* Journal of Applied Physics, vol. 107, no. 5, page 054521, 2010.

[Rath 2012] J K Rath. *Electrical Characterization of HIT Type Solar Cells.* In W G J H M van Sark, L Korte and F Roca, editeurs, Physics and Technology of Amorphous-Crystalline Heterostructure Silicon Solar Cells. 2012.

[Richter 2012] A Richter, S W Glunz, F Werner, J Schmidt and A Cuevas. *Improved quantitative description of Auger recombination in crystalline silicon.* Physical Review B, vol. 86, no. 16, pages 1652021–1652014, 2012.

[Richter 2013] A Richter, M Hermle and S W Glunz. *Reassessment of the Limiting Efficiency for Crystalline Silicon Solar Cells.* IEEE Journal of Photovoltaics, vol. 3, no. 4, pages 1184–1191, 2013.

[Robertson 2003] J Robertson. *Thermodynamic model of nucleation and growth of plasma deposited microcrystalline silicon.* Journal of Applied Physics, vol. 93, no. 1, pages 731–735, 2003.

[Roca i Cabarrocas 1995] P Roca i Cabarrocas, N Layadi, T Heitz, B Drévillon and I Solomon. *Substrate selectivity in the formation of microcrystalline silicon: Mechanisms and technological consequences.* Applied Physics Letters, vol. 66, no. 26, page 3609, 1995.

[Rose 1955] A Rose. *Space-Charge-Limited Currents in Solids.* Physical Review, vol. 97, no. 6, pages 1538–1544, 1955.

[Ross 2000] Ch Ross, J Herion and H Wagner. *Nucleation and growth analysis of microcrystalline silicon by scanning probe microscopy: substrate dependence, local structural and electronic properties of as-grown surfaces.* Journal of Non-Crystalline Solids, vol. 266–269, Part 1, no. 0, pages 69–73, 5 2000.

[Rößler 2013] R Rößler, C Leendertz, L Korte, N Mingirulli and B Rech. *Impact of the transparent conductive oxide work function on injection-dependent a-Si:H/c-Si band bending and solar cell parameters.* Journal of Applied Physics, vol. 113, no. 14, page 144513, 2013.

[Saint-Cast 2009] Pierre Saint-Cast, Daniel Kania, M Hofmann, Jan Benick, J Rentsch and R Preu. *Very low surface recombination velocity on p-type c-Si by high-rate plasma-deposited aluminum oxide.* Applied Physics Letters, vol. 95, no. 15, page 151502, 2009.

[Saleh 2002] R Saleh and N H Nickel. *Structural and Electrical Characterization of B-Doped Microcrystalline Silicon Thin Films.* In Marterials Research Society Symposium, pages A20.6.1–A20.6.6, 2002.

[Schindler 2014] Florian Schindler, Maxime Forster, Juliane Broisch, J Schön, J Giesecke, Stefan Rein, Wilhelm Warta and Martin C Schubert. *Towards a unified low-field model for carrier mobilities in crystalline silicon.* Solar Energy Materials and Solar Cells, vol. 131, no. 0, pages 92–99, 12 2014.

[Schmidt 2003] J Schmidt and R A Sinton. *Defect characterization by temperature and injection-dependent lifetime spectroscopy.* In K Kurokawa, L L Kazmerski, B McNelis, M Yamaguchi, C Wronski and W C Sinke, editeurs, 3rd World Conference on Photovoltaic Energy Conversion, pages 947–950, Tokyo, Japan, 2003. INst Solarenergieforsch Hameln Emmerthal, ISFH, D-31860 Emmerthal, Germany. Schmidt, J (reprint author), INst Solarenergieforsch Hameln Emmerthal, ISFH, Ohrberg 1, D-31860 Emmerthal, Germany., Wcpec-3 Organizing Committee.

[Schmidt 2013] J Schmidt, Valeriya Titova and Dimitri Zielke. *Organic-silicon heterojunction solar cells: Open-circuit voltage potential and stability.* Applied Physics Letters, vol. 103, no. 18, page 183901, 2013.

[Schmitt 1989] J P M Schmitt. *Amorphous Silicon Deposition. Inustrial and Technical Challenges.* Thin Solid Films, vol. 174, pages 193–202, 1989.

[Schulze 2010] T F Schulze, H N Beushausen, C Leendertz, A Dobrich, B Rech and L Korte. *Interplay of amorphous silicon disorder and hydrogen content with interface defects in amorphous/crystalline silicon heterojunctions.* Applied Physics Letters, vol. 96, no. 25, page 252102, 2010.

[Schulze 2011] T F Schulze, L Korte, F Ruske and B Rech. *Band lineup in amorphous/crystalline silicon heterojunctions and the impact of hydrogen microstructure and topological disorder.* Physical Review B, vol. 83, no. 16, pages 1653141–1653111, 2011.

[Seif 2014a] J P Seif, B Demaurex, S Smit, B Macco, W M M E Kessels, J Geissbühler, S De Wolf and C Ballif. *Atomic-Layer-Deposited Transparent Electrodes for Silicon Heterojunction Solar Cells.* IEEE Journal of Photovoltaics, vol. 4, no. 6, pages 1387–1396, 2014.

[Seif 2014b] J P Seif, A Descoeudres, M Filipič, F Smole, M Topič, Z C Holman, S De Wolf and C Ballif. *Amorphous silicon oxide window layers for high-efficiency silicon heterojunction solar cells.* Journal of Applied Physics, vol. 115, no. 2, pages 0245021–0245028, 2014.

[Seif 2015] J P Seif, G Krishnamani, B Demaurex, C Ballif and S De Wolf. *Amorphous/Crystalline Silicon Interface Passivation: Ambient-Temperature Dependence and Implications for Solar Cell Performance.* IEEE Journal of Photovoltaics, 2015.

[Shah 2010] A Shah. Thin-Film Silicon Solar Cells. EPFL Press, 2010.

[Shao 2014] Ye Shao, Jongwon Yoon, Hyeongnam Kim, Takhee Lee and Wu Lu. *Analysis of surface states in ZnO nanowire field effect transistors.* Applied Surface Science, vol. 301, no. 0, pages 2–8, 5 2014.

[Shockley 1952] W Shockley and W T Read. *Statistics of the Recombinations of Holes and Electrons.* Physical Review, vol. 87, 1952.

[Shockley 1961] W Shockley and H J Queisser. *Detailed Balance Limit of Efficiency of p-n Junction Solar Cells.* Journal of Applied Physics, vol. 32, no. 3, pages 510–519, 1961.

[Shu 2013] Zhan Shu, Ujjwal Das, John Allen, Robert Birkmire and Steven Hegedus. *Experimental and simulated analysis of front versus all-back-contact silicon heterojunction solar cells: effect of interface and doped a-Si:H layer defects.* Progress in Photovoltaics: Research and Applications, 2013.

[Sichanugrist 1994] P Sichanugrist, T Sasaki, A Asano, Y Ichikawa and H Sakai. *Amorphous silicon oxide and its application to metal/n-i-p/ITO type a-Si solar cells.* Solar Energy Materials and Solar Cells, vol. 34, no. 1–4, pages 415–422, 9 1994.

[Sin 1984] E H Sin, C K Ong and H S Tan. *Temperature-Dependence of Interband Optical-Absorption of Silicon at 1152, 1064, 750, and 694 nm.* Physica Status Solidi a-Applied Research, vol. 85, no. 1, pages 199–204, 1984.

[Sinton 1987] R A Sinton and R M Swanson. *Design criteria for Si point-contact concentrator solar-cells.* Electron Devices, IEEE Transactions on, vol. 34, no. 10, pages 2116–2123, October 1987.

[Sinton 1996] R A Sinton and A Cuevas. *Contactless determination of current–voltage characteristics and minority-carrier lifetimes in semiconductors from quasi-steady-state photoconductance data.* Applied Physics Letters, vol. 69, no. 17, pages 2510–2512, 1996.

[Sinton 2000] R A Sinton and A Cuevas. *A Quasi-Steady-State Open-Circuit Voltage Method for Solar Cell Characterization.* In 16th European Photovoltaic Solar Energy Conference, pages 1–4, Glasgow, UK, 2000.

[Sinton 2014] R A Sinton, A L Blum and J S Swirhun. *Overview and Latest Developments in Photoconductance Lifetime Measurements in Silicon.* Solid State Phenomena, vol. 205-206, pages 103–109, 2014.

[Smets 2008] A H M Smets, T Matsui and M Kondo. *High-rate deposition of microcrystalline silicon p-i-n solar cells in the high pressure depletion regime.* Journal of Applied Physics, vol. 104, no. 3, page 034508, 2008.

[Smets 2012] A H M Smets, M A Wank, B Vet, Marinus Fischer, R A C M M van Swaaij, Miro Zeman, D C Bobela, C R Wronski and R M C M van de Sanden. *The Relation Between the Bandgap and the Anisotropic Nature of Hydrogenated Amorphous Silicon.* IEEE Journal of Photovoltaics, vol. 2, no. 2, pages 94–98, 2012.

[Smirnov 2010] V Smirnov, W Böttler, A Lambertz, H Wang, R Carius and F Finger. *Microcrystalline silicon n-i-p solar cells prepared with microcrystalline silicon oxide (μc-SiOx:H) n-layer.* physica status solidi (c), pages NA–NA, 2010.

[Smith 1995] D Smith. Thin-Film Deposition: Principles and Practice. McGraw-Hill Education, 1995.

[Smith 2012] D D Smith, P J Cousins, A Masad, A Waldhauer, S Westerberg, M Johnson, Tu Xiuwen, T Dennis, G Harley, G Solomon, Rim Seung, M Shepherd, S Harrington, M Defensor, A Leygo, P Tomada, Wu Junbo, T Pass, L Ann, L Smith, N Bergstrom, C Nicdao, P Tipones and D Vicente. *Generation III high efficiency lower cost technology: Transition to full scale manufacturing.* In 38th IEEE Photovoltaic Specialists Conference, pages 001594–001597, Austin, TX, USA, 3 2012.

[Snaith 2007] Henry J Snaith, Adam J Moule, Cédric Klein, Klaus Meerholz, Richard H Friend and M Grätzel. *Efficiency Enhancements in Solid-State Hybrid Solar Cells via Reduced Charge Recombination and Increased Light Capture.* Nano Letters, vol. 7, no. 11, pages 3372–3376, 2007 2007.

[Sriprapha 2007] Kobsak Sriprapha, Ihsanul Afdi Yunaz, Seung Yeop Myong, Akira Yamada and M Konagai. *Temperature Dependence of Si-Based Thin-Film Solar Cells Fabricated on Amorphous to Microcrystalline Silicon Transition Phase.* Japanese Journal of Applied Physics, vol. 46, no. 11, pages 7212–7216, 2007.

[Stückelberger 2014] M Stückelberger. *Hydrogenated Amorphous Silicon: Impact of Process Conditions on Material Properties and Solar Cell Efficiency.* EPFL, 2014.

[Strahm 2007a] B Strahm, A Howling, L Sansonnens, C Hollenstein, U Kroll, J Meier, C Ellert, L Feitknecht and C Ballif. *Microcrystalline silicon deposited at high rate on large areas from pure silane with efficient gas utilization.* Solar Energy Materials and Solar Cells, vol. 91, no. 6, pages 495–502, 2007.

[Strahm 2007b] B Strahm, A A Howling, L Sansonnens and Ch Hollenstein. *Plasma silane concentration as a determining factor for the transition from amorphous to microcrystalline silicon in SiH4/H2 discharges.* Plasma Sources Science and Technology, vol. 16, no. 1, pages 80–89, 2007.

[Swanson 2005] R M Swanson. *Approaching the 29% limit efficiency of silicon solar cells.* In 38th IEEE Photovoltaic Specialists Conference, pages 889–894, Lake Buena Vista, FL, USA, 3 2005.

[Sze 1981] S M Sze. Physics of Semiconductor Devices. John Wiley & Sons, 1981.

[Sze 2002] S M Sze. Semiconductor Devices - Physics and Technology (2nd edition). John Wiley & Sons, Inc., 2002.

[Taguchi 2008] M Taguchi, E Maruyama and M Tanaka. *Temperature Dependence of Amorphous/Crystalline Silicon Heterojunction Solar Cells.* Japanese Journal of Applied Physics, vol. 47, no. 2, pages 814–818, 2008.

[Taguchi 2014] M Taguchi, A Yano, S Tohoda, K Matsuyama, Y Nakamura, T Nishiwaki, K Fujita and E Maruyama. *24.7 % Record Efficiency HIT Solar Cell on Thin Silicon Wafer*. IEEE Journal of Photovoltaics, vol. 4, no. 1, pages 96–99, 2014.

[Tanaka 1992] M Tanaka, M Taguchi, Takao Matsuyama, Toru Sawada, Shinya Tsuda, Shoichi Nakano, Hiroshi Hanafusa and Yukinori Kuwano. *Development of New a-Si/c-Si Heterojunction Solar Cells: ACJ-HIT (Artificially Constructed Junction-Heterojunction with Intrinsic Thin-Layer)*. Japanese Journal of Applied Physics, vol. 31, no. 11, pages 3518–3522, 1992.

[Terasa 2002] R Terasa, M Albert, J W Bartha, H Brechtel and A Kottwitz. *Time-resolved layer thickness behavior of microcrystalline and amorphous silicon samples after switching on a hydrogen/silane VHF plasma*. Journal of Non-Crystalline Solids, vol. 299-302, pages 58–62, 2002.

[Thompson 2008] Barry C Thompson and Jean M J Fréchet. *Polymer–Fullerene Composite Solar Cells*. Angewandte Chemie International Edition, vol. 47, no. 1, pages 58–77, 2008.

[Tiedje 1984] T Tiedje, E Yablonovitch, G D Cody and B G Brooks. *Limiting Efficiency of Silicon Solar Cells*. IEEE Transactions on Electron Devices, vol. ED-31, no. 5, pages 711–716, 1984.

[Tomasi 2014] A Tomasi, B Paviet-Salomon, D Lachenal, S Martin de Nicolas, A Descoeudres, J Geissbühler, S De Wolf and C Ballif. *Back-Contacted Silicon Heterojunction Solar Cells With Efficiency >21%*. IEEE Journal of Photovoltaics, vol. 4, no. 4, pages 1046–1054, 2014.

[Tomasi 2015] A Tomasi, F Sahli, L Fanni, J P Seif, S Martin de Nicolas, N Holm, J Geissbühler, P Loper, S Nicolay, S De Wolf and C Ballif. *Transparent Conductive Oxides in Silicon Heterojunction Solar Cells: Influence on Carrier Recombination*. In 42nd IEEE Photovoltaic Specialists Conference, New Oerleans, LA, USA, 2015.

[Tous 2013] L Tous, R Russell, J Beckers, J Bertens, E Cornagliotti, P Choulat, J John, F Duerinckx, J Szlufcik, J Poortmans and R Mertens. *A Simple Copper Based Plating Process Resulting in Efficiencies above 20.5% Using Pilot Processing Equipment*. In 28th European Photovoltaic Solar Energy Conference and Exhibition, pages 1008–1012, Paris, France, 2013.

[Tous 2014a] L Tous, M Aleman, R Russell, E Cornagliotti, P Choulat, A Uruena, S Singh, J John, F Duerinckx, J Poortmans and R Mertens. *Evaluation of advanced p-PERL and n-PERT large area silicon solar cells with 20.5% energy conversion efficiencies*. Progress in Photovoltaics: Research and Applications, pages n–a–n–a, 2014.

[Tous 2014b] L Tous, S N Granata, A Rouhi, J F Lerat, T Emeraud, S Martin de Nicolas, T M Pletzer, R Labie, M Aleman, R Russell, J John, F Duerinckx, J Szlufcik, S De Wolf, C Ballif, R Mertens and J Poortmans. *Large-area Hybrid Silicon Heterojunction Solar Cells with Ni/Cu Plated Front Contacts*. Energy Procedia, vol. 55, no. 0, pages 715–723, 2014.

[Trupke 2003] T Trupke, M A Green, P Würfel, P P Altermatt, A Wang, J Zhao and R Corkish. *Temperature dependence of the radiative recombination coefficient of intrinsic crystalline silicon.* Journal of Applied Physics, vol. 94, no. 8, pages 4930–4937, 2003.

[Trupke 2006] T Trupke, R A Bardos, M C Schubert and W Warta. *Photoluminescence imaging of silicon wafers.* Applied Physics Letters, vol. 89, no. 4, pages 044107 1–3, July 2006.

[Tsai 1989] C C Tsai, G B Anderson, R Thompson and B Wacker. *Control of Silicon Network Structure in Plasma Deposition.* Journal of Non-Crystalline Solids, vol. 114, pages 151–153, 1989.

[Tung 2014] Raymond T Tung. *The physics and chemistry of the Schottky barrier height.* Applied Physics Reviews, vol. 1, no. 1, pages –, 2014.

[Vallat-Sauvain 2005] E Vallat-Sauvain, J Bailat, J Meier, X Niquille, U Kroll and A Shah. *Influence of the substrate's surface morphology and chemical nature on the nucleation and growth of microcrystalline silicon.* Thin Solid Films, vol. 485, no. 1-2, pages 77–81, 2005.

[Van Cleef 1996] M W M Van Cleef, M W H Philippens, F A Rubinelli, M Kolter and R E I Schropp. *Electrical Transport Mechanismss in p+a-SiC:H/c-Si Heterojunctions: Dark J-V-T characteristics.* In MRS Spring Meeting, page 239, 1996.

[Van Cleef 1998] M W M Van Cleef, R E I Schropp and F A Rubinelli. *Significance of tunneling in p[sup +] amorphous silicon carbide n crystalline silicon heterojunction solar cells.* Applied Physics Letters, vol. 73, no. 18, page 2609, 1998.

[van der Hoeven 2014] M van der Hoeven. *Medium-Term Renewable Energy Market Report 2014.* Rapport technique, 2014.

[Vetterl 2000] O Vetterl, F Finger, R Carius, P Hapke, L Houben, O Kluth, A Lambertz, A Mück, B Rech and H Wagner. *Intrinsic microcrystalline silicon: A new material for photovoltaics.* Solar Energy Materials and Solar Cells, vol. 62, no. 97, pages 97–108, 2000.

[Voroshazi 2011] Eszter Voroshazi, Bregt Verreet, Andrea Buri, Robert Müller, Daniele Di Nuzzo and Paul Heremans. *Influence of cathode oxidation via the hole extraction layer in polymer:fullerene solar cells.* Organic Electronics, vol. 12, no. 5, pages 736–744, 5 2011.

[Wagner 1983] H Wagner and W Beyer. *Reinterpretation of the Silicon-Hydrogen Stretch Frequencies in amorphous Silicon.* Solid State Communications, vol. 48, no. 7, pages 585–587, 1983.

[Wang 2012] Sisi Wang and Daniel Macdonald. *Temperature dependence of Auger recombination in highly injected crystalline silicon.* Journal of Applied Physics, vol. 112, no. 11, pages 1137081–1137084, 2012.

[Watahiki 2015] Tatsuro Watahiki, Takeo Furuhata, Tsutomu Matsuura, Tomohiro Shinagawa, Yusuke Shirayanagi, Takayuki Morioka, Tetsuro Hayashida, Yohei Yuda, Shintaro Kano, Yuichi Sakai, Hidetada Tokioka, Yoshihiko Kusakabe and Hiroyuki Fuchigami. *Rear-emitter Si heterojunction solar cells with over 23% efficiency*. Applied Physics Express, vol. 8, no. 2, page 021402, 2015.

[Wurfel 2015] U Wurfel, A Cuevas and P Würfel. *Charge Carrier Separation in Solar Cells*. IEEE Journal of Photovoltaics, vol. 5, no. 1, pages 461–469, 2015.

[Xu 2012] Wei Xu, Alan Chin, Laura Ye, C Z Ning and Hongbin Yu. *Charge transport and trap characterization in individual GaSb nanowires*. Journal of Applied Physics, vol. 111, no. 10, page 104515, 2012.

[Zhang 2011] Xiaodan Zhang, Xinxia Zheng, Guanghong Wang and Ying Zhao. *Initial growth of intrinsic microcrystalline silicon thin film: Dependence on pre-hydrogen glow discharge and substrate surface morphology*. Applied Surface Science, vol. 257, no. 7, pages 3014–3019, 2011.

[Zhao 1999] Jianhua Zhao, Aihua Wang and Martin A Green. *24·5% Efficiency silicon PERT cells on MCZ substrates and 24·7% efficiency PERL cells on FZ substrates*. Progress in Photovoltaics: Research and Applications, vol. 7, no. 6, pages 471–474, 1999.

[Zhao 2010] L Zhao, H Diao, X Zeng, C Zhou, H Li and W Wang. *Comparative study of the surface passivation on crystalline silicon by silicon thin films with different structures*. Physica B: Condensed Matter, vol. 405, no. 1, pages 61–64, 2010.

[Zicarelli 2010] F Zicarelli, A Descoeudres, G Choong, P Bôle, L Barraud, S De Wolf and C Ballif. *Metallisation for Silicon Heterojunction Solar Cells*. In 25th European Photovoltaic Solar Energy Conference and Exhibition, pages 1669–1672, Valencia, Spain, 2010.

[Zielke 2014] D Zielke, A Pazidis, F Werner and J Schmidt. *Organic-silicon heterojunction solar cells on n-type silicon wafers: The BackPEDOT concept*. Solar Energy Materials and Solar Cells, vol. 131, pages 110–116, 2014.

Publication list

Last update: June 15, 2015
(*): authors contributed equally to this work.
(P): presenting author.

Publications as first author

1 J. P. Seif, A. Descoeudres, M. Filipič, F. Smole, M. Topič, Z. C. Holman, S. De Wolf, and C. Ballif, "*Amorphous silicon oxide window layers for high-efficiency silicon heterojunction solar cells*," Journal of Applied Physics vol. **115**, pp. 024502-1–8, 2014.

2 J. P. Seif**(*)**, B. Demaurex**(*)**, S. Smit, B. Macco, W. M. M. E. Kessels, J. Geissbühler, S. De Wolf, and C. Ballif, "*Atomic-Layer-Deposited Transparent Electrodes for Silicon Heterojunction Solar Cells*," IEEE Journal of Photovoltaics, vol. **4**, pp. 1387–1396, 2014.

3 J. P. Seif, G. Krishnamani, B. Demaurex, C. Ballif, and S. De Wolf, "*Amorphous/Crystalline Silicon Interface Passivation: Ambient-Temperature Dependence and Implications for Solar Cell Performance*," IEEE Journal of Photovoltaics, 2015.

4 J. P. Seif, A. Descoeudres, G. Nogay, S. Hänni, S. Martin de Nicolas, N. Holm, J. Geissbühler, M. Duchamp, M. Ledinsky, A. Hessler-Wyser, S. De Wolf, and C. Ballif, "*Thin Microcrystalline Silicon doped Layers for Silicon Heterojunction Solar Cells*," manuscript in preparation, 2015.

5 J. P. Seif, D. Menda, O. Özdemir, L. Barraud, A. Descoeudres, S. De Wolf, and C. Ballif, "*Asymmetric Band Offsets in Silicon Heterojunction Solar Cell: Impact on Cell Performance*" (working title), manuscript in preparation, 2015.

Publications as co-author

1 A. Descoeudres, L. Barraud, S. De Wolf, B. Strahm, D. Lachenal, C. Guérin, Z. C. Holman, F. Zicarelli, B. Demaurex, J. P. Seif, J. Holovsky, and C. Ballif, "*Improved amorphous/crystalline silicon interface passivation by hydrogen plasma treatment*," Applied Physics Letters, vol. **99**, p. 123506, 2011.

2 Z. C. Holman, A. Descoeudres, L. Barraud, F. Zicarelli Fernandez, J. P. Seif, S. De Wolf, and C. Ballif, "*Current Losses at the Front of Silicon Heterojunction Solar Cells*," IEEE Journal of Photovoltaics, vol. **2**, pp. 7–15, 2012.

3 B. Demaurex, R. Bartlome, J. P. Seif, J. Geissbühler, D. T. L. Alexander, Q. Jeangros, C. Ballif, and S. De Wolf, "*Low-temperature plasma-deposited silicon epitaxial films: Growth and properties*," Journal of Applied Physics, vol. **116**, p. 053519, 2014.

4 J. Geissbuühler, S. De Wolf, B. Demaurex, J. P. Seif, D. T. L. Alexander, L. Barraud, and C. Ballif, "*Amorphous/crystalline silicon interface defects induced by hydrogen plasma treatments*," Applied Physics Letters, vol. **102**, p. 231604, 2013.

5 A. Tomasi, F. Sahli, L. Fanni, J. P. Seif, S. Martin de Nicolas, J. Geissbühler, B. Paviet-Salomon, S. Nicolay, S. De Wolf, and C. Ballif, "*Transparent Conductive Oxides in Silicon Heterojunction Solar Cells: Influence on Charge Carrier Recombination*", IEEE Journal of Photovoltaics, manuscript in preparation, 2015.

Oral presentations

1 J. P. Seif, A. Descoeudres, Z. C. Holman, S. De Wolf, and C. Ballif, "*Thin microcrystalline layers for application in silicon heterojunction solar cells*," presented at the 25th International Conference on Amorphous and Nano-crystalline Semiconductors, Toronto, Ontario, Canada, 2013.

2 J. P. Seif, A. Descoeudres, M. Filipič, M. Topič, F. Smole, Z. C. Holman, S. De Wolf, and C.Ballif, "*Amorphous silicon oxide layers: Improving Silicon Heterojunction Solar Cell Performance*," presented at the MRS Spring Meeting, San Francisco, California, United States of America, 2014.

3 B. Demaurex **(*)**, **(P)**, J. P. Seif **(*)**, S. Smit, B. Macco and E. Kessels, S. De Wolf and C. Ballif, "*Transparent Electrodes for Silicon Heterojunction Solar Cells Fabricated by Atomic Layer Deposition*," presented at the 40th IEEE Photovoltaic Specialists Conference, Denver, Colorado, United States of America, 2014.

4 J. P. Seif, G. Krishnamani, B. Demaurex, S. Martin de Nicolas, N. Holm, C. Ballif and S. De Wolf, "*Silicon Heterojunction Solar Cells: Ambient-Temperature Impact on Passivation and Performance*," presented at the 5th SiliconPV, Konstanz, Germany, 2015.

5 J. P. Seif **(*)**, B. Demaurex **(*)**, S. Martin de Nicolas, N. Holm, J. Geissbühler, S. Smit, B. Macco and E. Kessels S. De Wolf **(P)**, and C. Ballif, "*Fill-Factor Loss Analysis of Silicon Heterojunction Solar Cells with Atomic-Layer-Deposited Transparent Electrodes*," presented at the MRS Spring Meeting, San Francisco, California, United States of America, 2015.

Contribution as co-author to presentations

1 A. Descoeudres **(P)**, L. Barraud, P. Bôle Rothen, S. De Wolf, B. Demaurex, Z. C. Holman, J. P. Seif, J. Geissbühler "*21% efficiency silicon heterojunction solar cells produced with very high frequency PECVD*," presented at the 21st International Photovoltaic Science and Engineering Conference, Fukuoka, Japan, 2011.

2 Z. C. Holman **(P)**, A. Descoeudres, L. Barraud, J. P. Seif, F. Zicarelli, S. De Wolf, and C. Ballif, "*Increasing short-circuit current in silicon heterojunction solar cells*," presented at the 37th IEEE Photovoltaic Specialists Conference, 2011, pp. 001448–001452.

3 A. Descoeudres **(P)**, L. Barraud, S. De Wolf, B. Demaurex, J. Geissbühler, Z. C. Holman, S. V. Morel, J. P. Seif, and C. Ballif, "*Silicon heterojunction solar cells on n- and p-type wafers with efficiencies above 20%*," presented at the 27th European Photovoltaic Solar Energy Conference and Exhibition, Frankfurt, Germany, 2012.

4 S. De Wolf **(P)**, B. Demaurex, J. Geissbuehler, P. Löper, S. Martin de Nicolas, B. Paviet-Salomon, J. P. Seif, A. Tomasi, and C. Ballif, "*High-efficiency Silicon Heterojunction Solar Cells: Status and Perspectives*," presented at the 40th IEEE Photovoltaic Specialists Conference, Denver, Colorado, United States of America, 2014.

5 S. Martin de Nicolas **(P)**, B. Demaurex, J. Geissbühler, N. Holm, P. Löper, B. Paviet-Salomon, J. P. Seif, A. Tomasi, S. De Wolf, and C. Ballif, "*Increase the photogenerated current in amorphous/crystalline silicon solar cells*," presented at the 6th World Conference on Photovoltaic Energy Conversion, Kyoto, Japan, 2014.

6 B. Demaurex, R. Bartlome, J. P. Seif, J. Geissbühler, D. T. L. Alexander, Q. Jeangros, C. Ballif, and S. De Wolf **(P)**, "*PECVD silicon homo-epitaxy: interface and bulk properties*," presented at the MRS Spring Meeting, San Francisco, Califronia, United States of America, 2015.

7 A. Tomasi **(P)**, F. Sahli, L. Fanni, J. P. Seif, S. Martin de Nicolas, N. Holm, J. Geissbühler, Philipp Löper, S. Nicolay, S. De Wolf and C. Ballif, "*Transparent Conductive Oxides in Silicon Heterojunction Solar Cells: Influence on Carrier Recombination*," presented at the 42th IEEE Photovoltaic Specialists Conference, New Orleans, Louisiana, United States of America, 2015.

8 A. Tomasi **(P)**, B. Paviet-Salomon, S. Nicolay, A. Tajalli, J. P. Seif, J. Geissbühler, S. Martin de Nicolas, N. Holm, S. De Wolf1, M. Despeisse, and C. Ballif, "*Efficient Electrodes for Back-Contacted Silicon Heterojunction Solar Cells*," presented at the 27th European Photovoltaic Solar Energy Conference and Exhibition, Hamburg, Germany, 2015.

9 S. De Wolf **(P)**, J. Geissbühler, P. Löper, S. Martin de Nicolas, J. P. Seif, A. Tomasi, and C. Ballif, "*High-Efficiency Silicon Heterojunction Solar cells: Achievements and Perspectives*," presented at the E-MRS: Conference & Exhibit, Lille, France, 2015.

Acknowledgements

The journey I undertook these last four years was not only a time for scientific discoveries but also for professional and personal development. Looking back, this thesis was built *step-by-step* and wouldn't have been possible to realize without the help, support and encouragements of many people.

First of all I would like to thank my supervisors, Christophe, Antoine and Stefaan. Thank you for giving me the chance to work in an inspiring environment at the cutting edge of photovoltaic research. Thank you for your guidance and support (especially also in the more difficult times), your availability but also for helping me tackle challenges along the way and encouraging me to explore new fields.
I would also like to thank the members of my jury, Prof. Erwin Kessels, Prof. Paul Muralt and Dr. Benjamin Strahm, for accepting to take the time to read and evaluate my thesis, being present at my defense and giving me precious feedback on the manuscript.
Also, I gratefully acknowledge my funding sources: the EuroTech Universities Alliance (Interface Science for Photovoltaics Initiative), the Swiss Commission for Technology and Innovation (CTI), Axpo Naturstrom Fonds, the Office fédérale de l'énergie (OFEN), the Fonds National Suisse (FNS), the US Department of Energy (DOE, FPaceII project), and the European Commission (projects: FAST-TRACK, HERCULES, and CHEETAH).

During my time at PV-lab I saw a lot people arriving and leaving, which makes it hard to remember all of them, but among all the nice people I did meet, I would especially thank the following. Thanks to the (current and former) members of the heterojunction group: Andrea T., Antoine, Bénédicte, Bertrand, Deneb, Fernando, Florent, Gopal, Jakub, Jonas, Loris, Luc, Philipp, Priscille, Martin, Miha, Nicolas, Niels, Silvia, Sophie, Stefaan, and Zachary. Thank you all for your daily support with sample fabrication, characterization, reading manuscripts, pot lucks, helpful discussions and encouragements. It was a pleasure to work with you and to have been part of the heterojunction team.
Besides, my gratitude is also due to all the members of the PV-Lab, the PV-Center at CSEM, people at Microcity, as well as external co-workers, that contribute(d) to make Neuchâtel a unique place for high-quality research with a culture of mutual aid and respect, without forgetting also the social and leisure activities (parties, apéros, pétanque,...). So thank you Adrien, Aïcha, Ali D., Ali N., Amadou, Ana, Andrea F., Antonin, Arnaud, Benoit, Björn, Christian, Christophe Bo., Corsin, Eleonora, Elmar, Esteban, Etienne, Fabien, Fanny, Federica, Franz,

Gaetano, Gizem, Gregory, Jacques, Jan-Willem, Jason, Jérémie W., Jonathan, Josua, Karin, Laura, Laure, Laurent, Linus, Lorenzo, Martial, Mathieu B., Mathieu C., Matthieu D., Max, Michael, Monica, Mohssen, Mustapha, Patrick H., Patrick S., Peter, Rémi, Saeed, Sara, Simon, Sylvain D., Sylvain N., Valentin, Vincenzo, Quentin, Xavier, Yannick...
And where would we all be without our technical team? A big THANK YOU goes to Cédric, Jérémie F., Joël, Lionel, and Reto without whom the numerous experiments presented here would not have run as smoothly as they did, who were always there to solve the problems with the equipment and for not giving up getting the lab running again after the BIG move.
Thanks go also to the Meyer Burger Research team Benjamin, Boris, Damien, Damien Jr., Derk, Guillaume, Jérôme, Ludovic, Pierre, Walter, Frank, Yoann..., for their technical support (wafer processing and characterization) but also for the good time spent in the cleanroom at Breguet and the apéros at Maladière 23.

Some special thanks go to: Lara, for editing part of this thesis on very short notice; Aïcha, Antoine, Bertrand, Björn, Jonas and Simon for reading some parts of my thesis and for your very helpful and fast feedback; my brother Philipp for proofreading my thesis, and support with the list of abbreviations and regular expressions until late at night the days before handing in the thesis; Bertrand, Antoine and Loris for taking the time to listen to and discuss my defense presentation; Mary-Claude, Brigitte, Christelle, Joël, Rosario and Sandrine for your support with administrative affaires, reaching from helping with sending packages, to arranging travel plans, to organizing workshops, to booking hotels or restaurants,...; Hassan, for IT-support and letting me keep a second screen during the writing period; Silvia, Niels and Bertrand, for your support and for supplying samples during the *great drought*; Gizem, for helping out with depositions towards the end and achieving some very nice last minute results; Ali, Andreas, Andrea & Vittoria, Berthold & Rebecca, Christine & Karl, David & Sabine, Eleonora, Golo, Hannah, Hannes & Claudia, Jess, Laura & Mathieu, Marc, Markus & Fenna, Max, Monica & Marcelo, Mohamed, Sarah & Bastian, Winfried & Helen, Yannick & Florine, Zachary & Lara, for excellent food during travelling feasts, bike tours, camping, jam sessions, canyoning, concerts, hikes, travels,... and for reminding me that there's more to life than work, helping me to keep a good work-life balance and simply for all the good time we shared. Thank you also Linus & Darya, for giving me shelter, for taking good care to keep me well-nourished and distracted with games, movies, hikes, guitar sessions, and travels. And of course thanks to you, Bénédicte & Jonas, for pulling me up when I was down, for all the help you offered (until the very end... the printing session and the drinks), for bringing me up to 4000 m (incl. fondue) and for so many other things. I am glad to have had you both as close companions (office mates) on this journey!

And finally I would like to thank my family, my parents, Isabelle & Peter, for their support during all my studies, my brothers, Philipp & Daniela and Etienne. Thank you all for your faithful support and simply for being there for me.

Neuchâtel, June 15, 2015 Johannes P. Seif

Curriculum Vitae

Johannes Peter Seif

E-Mail: johannes.seif@gmail.com

Date of birth	**June 30th 1984**
Place of birth	**Tübingen / Germany**
Citizenship	**German and French**

Education

10/2010 - present	Swiss Federal Institute of Technology (Lausanne, Switzerland) PhD candidate in material science, thesis: *Window Layers for Silicon Heterojunction Solar Cells: Properties and Impact on Devices Performance*
09/2007 - 07/2009	Swiss Federal Institute of Technology (Zürich, Switzerland) Master studies in Physics (focus on Nanophysics) Master thesis: *Time-resolved single electron counting in a graphene quantum dot*
10/2006 - 09/2007	Swiss Federal Institute of Technology (Zürich, Switzerland) Bachelor studies in Physics
10/2004 - 07/2006	Eberhard Karls University Tübingen (Tübingen, Germany) Introductory studies in Physics
06/1994 - 06/2003	'Katholisches freies Gymnasium Sankt Meinrad' (Rottenburg a. N., Germany)

Internships

01/2010 - 07/2010	Oerlikon Solar AG (Trübbach, Switzerland)
Department	PECVD $(^2)$ and Reactor Development
Activity	Characterization of microcrystalline layers (ellipsometry and Raman)
10/2008 - 01/2009	Swiss Federal Laboratories for Materials Testing & Research (EMPA, Dübendorf, Switzerland)
Department	Nanoscale Materials Science, Group for magnetic thin films
Activity	Fabrication of magnetic thin films by sputter deposition and sample characterization via X-ray reflectometry and vibrating sample magnetometry

Languages & Computer Skills

German (native), French (native), English (proficient), Spanish (basic)
MS Office; Visual Basic for Applications (Excel); MATLAB; Python (basics);
Adobe Acrobat, Illustrator and Photoshop; LaTeX

Activities & Interests

Assistant at workshops for high-school graduates who consider studies at ETH Zürich (part of the *Academic and Career Advisory Program*, pilot project until end of 2009 - now *'Studies Orientation & Coaching'*)

Enjoy all sports especially hiking, swimming, snowboarding and windsurfing

Movies, Photography and digital art, guitar (acoustic and electric), singing (former member of the '*Rottenburger Domsingknaben*' and the '*Chorale de l'université de Neuchâtel*' (choirs)

Former member of the *German Red Cross* (voluntary)